ENERGY STORAGE RESEARCH AND DEVELOPMENT

VEHICLE TECHNOLOGIES PROGRAM

Less dependence on foreign oil today, and transition to a petroleum-free, emissions-free vehicle tomorrow.

2007

annual progress report

U.S. Department of Energy
Energy Efficiency
and Renewable Energy
Bringing you a prosperous future where energy
is clean, abundant, reliable, and affordable

U.S. Department of Energy
Office of Vehicle Technologies
1000 Independence Avenue S.W.
Washington, D.C. 20585-0121

FY 2007

Progress Report for Energy Storage Research and Development

Energy Efficiency and Renewable Energy
Vehicle Technologies

David Howell
Manager, Energy Storage R&D

January 2008

TABLE OF CONTENTS

TABLE OF CONTENTS (CONT.)

I. INTRODUCTION

In 2007, US consumers experienced the highest sustained gasoline prices in recent history, in real terms, including those seen in the early 1980s[1]. Partially as a result of the $3/gallon gasoline prices, sales of hybrid electric vehicles (HEVs) increased almost 60% in 2007[2], and several automakers announced plans to develop plug-in hybrid electric vehicles (PHEVs)[3]. However, total sales of HEVs remained in the 2-3 percent range of all vehicle sales. An important step for continued HEV market penetration, as well as electrifying the nation's personal transportation, is the development of cost effective, long lasting, and abuse tolerant Li-ion batteries.

The United States Department of Energy's (DOE) continuing research and development into the use of batteries for motive transportation offers the possibility of reducing our dependence on foreign sources of oil. The work also directly supports the President's Advanced Energy Initiative, released in February 2006, which calls for the development of PHEVs with 40 mile all electric range. In FY2007, the work in this area continued to focus on the development of high power batteries for HEVs. In addition, the Department received additional funding resources to develop higher energy batteries for PHEVs.

I.A Vehicle Technologies Program

The DOE's Vehicle Technologies (VT) Program office[4] works with industry to develop advanced transportation technologies that reduce the nation's use of imported oil (96% of the US transportation fleet uses oil). Technologies being supported by VT include hybrid drive technologies, advanced energy storage devices (batteries and ultracapacitors), power electronics and motors, advanced structural materials, and advanced combustion engines and fuels.

Collaboration with automakers enhances the potential for success and the relevance of these programs. Thus, the department works in partnership with the U.S. automakers through the United States Council for Automotive Research (USCAR)—an umbrella organization for collaborative research among Chrysler LLC, Ford Motor Company, and General Motors Corporation[5]. This partnership is focused on funding high-reward/high-risk research that promises improvements in critical components needed for more fuel efficient, cleaner vehicles.

I.B Energy Storage Research & Development Overview

Energy storage technologies, including batteries and ultracapacitors, have been identified as critical enabling technologies for advanced, fuel-efficient, vehicles. The Energy Storage Research and Development effort within the VT Program is responsible for researching and improving advanced batteries and ultracapacitors for a wide range of vehicle applications, including HEVs, PHEVs, battery electric vehicles (EVs), as well as fuel cell vehicles (FCVs). The office is working in close partnership with the automotive industry, represented by the United States Advanced

---

[1] http://zfacts.com/p/35.html

[2] http://www.hybridcars.com/market-dashboard.html

[3] http://www.greencarcongress.com/2007/07/toyota-to-obtai.html, http://www.gm-volt.com/

[4] See http://www.eere.energy.gov/vehiclesandfuels/.

[5] For more information, please see http://www.uscar.org/guest/view_partnership.php?partnership_id=1.

Battery Consortium (USABC). The current effort is comprised of three major activities, battery development, applied battery research, and long-term exploratory research.

Battery Development is organized into three related sets of activities: benchmark testing, technology assessment, and full system development.

- *Benchmark Testing* - Benchmark testing of emerging technologies is important for remaining abreast of the latest industry developments. Working with the national laboratories, VT purchases and independently tests hardware against the manufacturer's specifications and the most applicable technical targets.

- *Technology Assessment* - Technology assessments are conducted on newly emerging technologies prior to full system development, and are often cost-shared with the developer. These 12-month projects assess a developer's overall capabilities and validate technical claims through independent testing.

- *Full System Development* - In cooperation with industry, efforts are focused on developing and evaluating lithium-battery and ultracapacitor technologies and designs for vehicles. Specifically, this work is focused on the development of batteries for HEVs, PHEVs, and on the development of ultracapacitor technologies for the 42 Volt start/stop application.

Applied Battery Research is focused on addressing the cross-cutting barriers that face Li-ion systems which are closest to meeting all of the energy and power requirements for vehicle applications. Five national laboratories participate in this activity, each bringing its own expertise to the critical barrier areas of life, abuse tolerance, low-temperature performance, and cost.

Focused Long-term Battery Research addresses fundamental problems of chemical instabilities that impede the development of advanced batteries. This research provides a better understanding of why systems fail, develops models that predict system failure and permit system optimization, and investigates new and promising materials. Five national laboratories and 12 universities participate in this activity.

Contributors to the work described in this document are presented in Appendix A, a list of acronyms is provided in Appendix B, and 2007 highlights from the applied and exploratory research programs are provided in Appendix C. For a color version of this report, please visit http://www1.eere.energy.gov/vehiclesandfuels/resources/fcvt_reports.html.

This report highlights the activities and progress in the Energy Storage Research and Development effort during FY2007. We are pleased with the progress made during the year and look forward to continued work with our industrial, government, and scientific partners to overcome the challenges that remain to delivering advanced energy storage systems for vehicle applications.

David Howell
Manager, Energy Storage Research and Development
Vehicle Technologies Program

II. BATTERY TECHNOLOGY DEVELOPMENT

One of the primary objectives of the Energy Storage effort is the development of durable and affordable advanced batteries and ultracapacitors for use in a full range of vehicle applications, from start/stop to full-power hybrid-electric, electric, and plug in HEVs. This activity is subdivided into four mission areas: *system development*, focused on developing full battery systems; *technology assessment*, to evaluate developers' current capabilities and validate technical claims*; benchmark testing* of emerging technologies in order to remain abreast of the latest industry developments; and *Small Business Innovative Research (SBIR),* that provides funding for early-stage R&D to small technology companies or individual entrepreneurs.

II.A System Development

System Development is focused on the development of batteries and ultracapacitors for both high power applications such as HEVs and 42 Volt start/stop systems and high energy applications such as PHEVs. All system development for light duty vehicles is conducted in collaboration with industry through the USABC. All of the USABC subcontracts are awarded competitively and are cost-shared by the developer at a minimum of 50 percent.

Introduction

Work on new battery technologies is organized into High-Power Energy Storage and High-Energy Storage. Both of these efforts are part of a multifaceted effort within VT to develop the technologies needed to encourage the adoption of advanced, cleaner, more fuel-efficient light-duty vehicles in the commercial marketplace.

High Power Energy Storage

High-power energy storage devices are among the critical technologies essential for the development and commercialization of HEVs. This effort is focused on overcoming the technical barriers associated with commercialization of high-power batteries, namely:

- **Cost -** The current cost of Li-based batteries (the most promising high-power battery chemistry) is approximately a factor of two too high on a kW basis. The main cost drivers being addressed are the high cost of raw materials and materials processing, the cost of cell and module packaging, and manufacturing costs.

- **Performance -** The barriers related to battery performance are the reduced discharge pulse power that is available at low temperatures and the loss of available power over time due to use and aging.

- **Abuse Tolerance -** Many high-power batteries are not intrinsically tolerant to abusive conditions such as short circuits (including internal short circuits), overcharge, over-discharge, crush, or exposure to fire and/or other high temperature environments.

- **Life -** Hybrid systems with conventional engines have a life target of 15 years, and battery life goals have been set to meet these targets. The cycle life goal of 300,000 cycles has been attained in laboratory tests but the 15-year calendar life has not yet been demonstrated.

The high-power energy storage activity was created to develop solutions to these challenges. Battery requirements for HEVs were developed in close coordination with industry through the USABC technical teams and are shown in Table II-1. (For more details and for other goals, see http://www.uscar.org/guest/view_team.php?teams_id=11.)

Table II-1. Energy Storage Targets for Power Assist Hybrid Electric Vehicles

Characteristics	Minimum value	Maximum value
Pulse discharge power (kW)	25 (for 10 seconds)	40 (for 10 seconds)
Maximum regenerating pulse (10 s; kW)	20 (50 Wh pulse)	35 (97 Wh pulse)
Total available energy (kWh)	0.3	0.5
Round trip efficiency (%)	>90–25 Wh cycle	>90–50 Wh cycle
Cycle life (cycles)	300k 25-Wh cycle (7.5 MWh)	300k 50-Wh cycle (15 MWh)
Cold-cranking power at −30ºC (three 2-sec pulses, 10-s rests between; kW)	5	7
Calendar life (years)	15	15
Maximum weight (kg)	40	60
Maximum volume (liters)	32	45
Production price @ 100k units/year ($)	500	800
Maximum operating voltage (Vdc)	<400 maximum	<400 maximum
Minimum operating voltage (Vdc)	$>0.55 \times V_{max}$	$>0.55 \times V_{max}$
Maximum self-discharge (Wh/d)	50	50
Operating temperature (ºC)	−30 to +52	−30 to +52
Survival temperature (ºC)	−46 to +66	−46 to +66

Specific objectives of this activity include:

- By 2010, develop an electric drive train energy storage device with a 15-year life at 300Wh with a discharge power of 25 kW for 18 seconds and a cost of $20/kW.
- Develop hardware for specific applications that can be tested against respective performance targets and used for subsystem benchmarking.

In the past, two candidate battery chemistries were identified as the most likely to meet the performance and cost targets: NiMH and Li-based technology. NiMH batteries offer relatively good power capability as a result of the good ionic conductivity of the electrolyte. Li-based batteries offer excellent energy density that can be traded for higher power. The USABC has supported development of these two technologies since the early 1990s by awarding subcontracts to a number of developers. Significant progress has been made as has been summarized in past annual reports. The USABC is continuing to support the development of Li-ion technology through contracts with Johnson Controls-Saft (Li-ion), CPI/LG Chem (Li-ion polymer), EnerDel (Mn spinel/Lithium titanate), and A123Systems (iron phosphate). Details on these contracts and on development work on ultracapacitors follows.

Li-ion Battery Development (40kW HEV)

In May of 2006, the USABC awarded a contract to the joint venture JCS for development of a 40 kW Li-ion battery with significantly reduced cost and improved abuse tolerance. Johnson Controls Inc. and Saft Batteries created this joint venture to complement the two companies' strengths in high-volume manufacturing (specifically for the auto industry) and Li-ion electrochemistry respectively.

The contract is 24 months in duration, and is concentrating on establishing state of the art cell making capability at the Milwaukee location, and on leveraging JCI's high-volume manufacturing expertise to enable the best possible system cost. Development in Milwaukee has yielded electrodes that are nearly identical to those produced at Saft's facility in Bordeaux, France and recent projections of the high volume production price look promising.

Li-ion Polymer Battery Development (25kW HEV)

In September 2006, CPI was awarded an 18-month, $6.2M contract to continue development of Li-ion polymer cell technology for HEV applications using a $LiMn_2O_4$ spinel-based cathode. $LiMn_2O_4$ spinel is an attractive cathode for HEV batteries due to the fact that Mn is abundant, environmentally benign, potentially abuse-tolerant, and capable of high-rates of discharge. Major problems to be overcome in this effort are the historically poor calendar life, particularly at elevated temperatures, and the poor cold cranking and low-temperature charging characteristics that plague many Li-ion chemistries.

CPI has recently achieved significant gains in calendar life estimates, which are currently being validated through testing at national laboratories. In addition, they are in the process of demonstrating the ability of their pouch packaging to attain 15-year calendar life.

Nano-Phase Iron Phosphate Battery Development (25kW HEV)

In December 2006, A123Systems of Watertown MA was awarded a 36-month, $15M contract to modify their doped, iron nano-phosphate ($LiFePO_4$) based power tool cell for HEV vehicle use. This cathode material is particularly attractive for automotive use due to its intrinsic abuse tolerance (although the anode reactivity remains to be mitigated), high power capabilities, and stable cycling.

A123 will manufacturer larger Ahr cells, improve their specific power through electrode engineering, and demonstrate their abuse tolerance characteristics. Finally, they will deliver fully functional 25kW modules for USABC testing and report on their efforts to approach the challenging USABC cost target of $20/kW.

High Rate Low Cost Li-Ion Battery Development (25kW HEV)

In late 2006, EnerDel was awarded a 12-month contract to scale up a nano-phase lithium titanate (LTO)/Mn spinel cell that promises extremely high rate capability along with low cost, good abuse tolerance as well as good low-temperature performance. The nano-phase LTO is characterized by extremely small primary particles (10 to 20 nm) agglomerated into 1 to 2 μμ, secondary particles that can be more easily processed into electrodes and can provide higher electrode density.

This proof in concept phase was successfully completed, with Enerdel delivering 2Ahr cells with commercial LTO and with the Argonne National Laboratory (ANL) supplied LTO which met initial performance goals (note that calendar and cycle life and cost targets were not included in this phase). Enerdel has applied for and been awarded a follow on development contract in September 2007 worth $6.5M over 18 months to scale up their materials and demonstrate their performance, life, and cost, in full sized (4-6Ahr) cells, as well as in modules (multi-cell configuration).

Low-cost Separator Development

Studies at the national laboratories have shown that the cost of the separator dominates the cost of the non-active materials in a high-power Li-ion battery. To reduce this cost, research and development is taking place into lower-cost materials and improved processing techniques. The goal is to develop a replacement separator (which costs $\$1/m^2$ or less) for current materials (which cost more than $\$2/m^2$):

Celgard, Inc., in a contract that ended on March 31, 2007, reported progress in developing a low-cost separator material that was meant to provide high-temperature melt integrity, an important quality for improved abuse tolerance. Celgard believes that the aggressive cost target may be achievable in high enough manufacturing volumes, and proposes to continue work on a high temperature melt integrity (HTMI) separator material.

Ultracapacitor Research and Development

Ultracapacitors (symmetric carbon-carbon double layer type) have been extensively tested at the Idaho National Laboratory (INL) and appear capable of attaining about 50% of the energy density requirements for HEVs in power-assist mode. Full requirements are shown in Table II-2.

Table II-2. Ultracapacitor Requirements

Energy Storage Goals		**Ultracapacitors[4]**		
Characteristics	**Unit**	**12V Start-Stop**	**42V Start-Stop**	**42V Transient Power Assist**
Discharge Pulse Power	kW	4.2 for 2 sec	6 for 2 sec	13 For 2 sec
Regen Pulse Power	kW			8 for 2 sec
Recharge Rate	kW	0.4	2.4	2.6
Cold cranking power @ -30°C (3 pulses)	kW	4.2 @ ≥7V for 2 sec	8 @ ≥21V for 2 sec	
Available Energy	Wh	15 @ 1 kW	30 @ 1 kW	60 @ 1 kW
Calendar Life	year	15		
Cycle Life	cycle	750k cycles or 150k miles		
Energy Efficiency (on Cycle-Life/Load Profile)	%	95 for UC10		
Maximum Self-discharge	var.	4% (72 hours from V_{max})		
Maximum Operating Voltage	Vdc	17	48	
Minimum Operating Voltage	Vdc	9	27	
Maximum System Weight	kg	5	10	20
Maximum System Volume	liter	4	8	16
Operating Temperature Range	°C	-30 to +52		
Survival Temperature Range	°C	-46 to +66		
Selling Price @ 100,000 units/year	$	40	80	130

However, their very high-power capability makes them a candidate technology for the 42V start-stop applications. To this end, the USABC had contracted with two developers, Maxwell Technologies and NESSCAP, to develop ultracapacitors for the 42-volt start-stop architecture. The Maxwell contract ended in 2006 (see the 2006 annual report), while the Nesscap contract ended in August 2007. The primary barriers addressed by Nesscap are the relatively low energy density and high cost of the systems. Highlights of the FY 2007 activities are presented below.

NESSCAP is developing ultracapacitors for 42V start-stop applications by improving fundamentals. The tasks include materials and electrode formulation, production verification, and module design. In 2007, NESSCAP focused on producing a lower cost 3500F, 2.7V cell while improving the electrode formulation to improve performance.

High Energy Battery R&D

The PHEV activity is just underway following a solicitation from the USABC that was issued in April of 2007. The technical requirements for the PHEV battery system which the developers will work towards are shown in Table II-3.

Table II-3. Goals for Plug-In Hybrid Electric Vehicle Batteries

Characteristics at EOL (End of Life)		**High Power/Energy Ratio Battery**	**High Energy/Power Ratio Battery**
Reference Equivalent Electric Range	miles	**10**	**40**
Peak Pulse Discharge Power (2 sec/10 sec)	kW	**50/45**	**46/38**
Peak Regen Pulse Power (10 sec)	kW	**30**	**25**
Available Energy for CD (Charge Depleting) Mode, 10 kW Rate	kWh	**3.4**	**11.6**
Available Energy in CS (Charge Sustaining) Mode	kWh	**0.5**	**0.3**
CD Life / Discharge Throughput	Cycles/ MWh	**5,000 / 17**	**5,000 / 58**
CS HEV Cycle Life, 50 Wh Profile	Cycles	**300,000**	**300,000**
Calendar Life, 35°C	year	**15**	**15**
Maximum System Weight	kg	**60**	**120**
Maximum System Volume	Liter	**40**	**80**
System Recharge Rate at 30°C	kW	**1.4 (120V/15A)**	**1.4 (120V/15A)**
Unassisted Operating & Charging Temperature	°C	**-30 to +52**	**-30 to +52**
Survival Temperature Range	°C	**-46 to +66**	**-46 to +66**
Maximum System Production Price @ 100k units/yr	$	**$1,700**	**$3,400**

In April 2007, USABC issued a solicitation for PHEV development contracts to address critical barriers to the commercialization of PHEVs, specifically battery cost and battery life. Five projects were selected for negotiation of awards of up to $17.2 million from DOE. Combined with cost-share from the USABC, these projects will allow up to $38 million in battery research and development. DOE funding is subject to negotiation of final contract terms and Congressional appropriations. Projects are expected to begin in 2007 and continue through 2009. USABC will negotiate final contract terms with five lithium ion battery developers. Companies selected for negotiation of awards are:

- **3M of St. Paul, MN** was selected for an award of up to $1.14 million from DOE (total DOE/industry cost share: $2.28 million) over two years to screen nickel/manganese/ cobalt (NMC) cathode materials through building and testing of small-sized cells;
- **A123Systems of Watertown, MA** was selected for an award of up to $6.25 million from DOE (total DOE/industry cost share: $12.5 million) over three years to develop batteries based on nanophase iron-phosphate chemistry for 10- and 40-mile range PHEVs;
- **Compact Power Inc. of Troy, MI** was selected for an award of up to $4.45 million from DOE (total DOE/industry cost share: $12.7 million) over three years to develop batteries for 10-mile range PHEVs using high energy and high power Manganese-spinel;
- **EnerDel, Inc. of Indianapolis, IN** was selected for an award of up to $1.25 million from DOE (total DOE/industry cost share: $2.5 million) over two years to develop cells for 10- and 40-mile range PHEVs using nano-phase lithium titanate coupled with a high voltage Nickel-Manganese cathode material;
- **Johnson Controls – Saft Advanced Power Solutions of Milwaukee, WI** was selected for an award of up to $4.1 million from DOE (total DOE/industry cost-share: $8.2 million) over two years to develop batteries using a nickelate/layered chemistry for 10- and 40-mile range PHEVs.

Thermal Management and Simulation

The National Renewable Energy Laboratory (NREL) is engaged in research and development to support the Energy Storage Program at the Office of Vehicle Technology in the Department of Energy. These activities range from supporting the Technology Development Program through battery thermal characterization/modeling and energy storage system simulations/analysis; the Applied Research (ATD) Program by developing thermal models to address abuse of Li-Ion batteries; and the Focused Long-Term Research (BATT) program by investigating improved Li-Ion battery electrode materials. The first two topics, those supporting technology development and applied research are reported here. The activities supporting BATT are reported in chapter 4 of this report.

Battery Thermal Analysis and Characterization

Proper thermal control is critical to achieving life, performance, and safety goals for advanced batteries for vehicle applications. Poor thermal control can lead to reduced battery performance and thus increased cost, reduced cycle and calendar life and increased chance of abuse conditions. The battery development related activity is aimed at addressing issues related to battery thermal control and improving the thermal performance of energy storage devices through thermal characterization, testing, modeling, analysis, and control strategies. The following sections provide overviews of the accomplishments in this area.

***Input to JCS Battery Pack Thermal Design* -** The objective of this effort was to measure the thermal characteristics of two generations of 6 Ah Li-ion cells (VL6P). The two generations use different carbons and were tested in NREL's advanced calorimeter (described below) to determine their heat generation rate and efficiency under various loads. The Gen 1 cell was tested at 0°C and 30°C. The Gen 2 cell was tested at -30°C, -15°C, -5°C, 0°C, 5°C, and 30°C. There were negligible differences in heat generation and efficiency between the two cells at 0°C and 30°C. A 5C discharge at 30°C and -30°C resulted in efficiencies of 98% and 79% respectively. Figure II-1 shows the heat generation of the Gen II cell as a function of temperature and discharge current. As expected, the heat generation increased as the temperature decreased. The Gen II cells' temperature performance was tested by charging and discharging at the target temperature, and the 1C discharge capacity of the cells at -30°C is ~50% of the discharge capacity at 30°C.

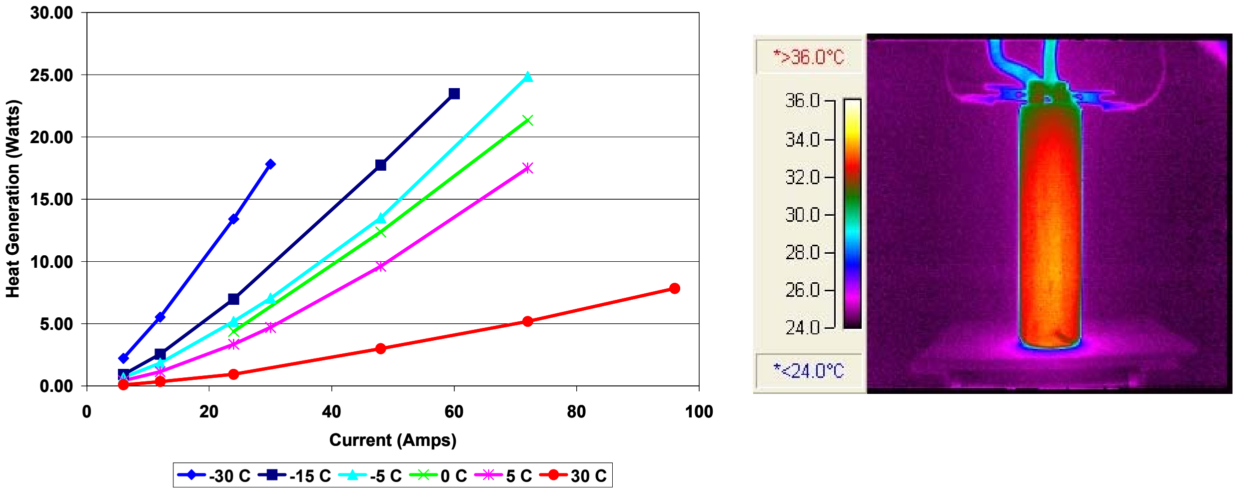

Figure II-1. Heat generation rate of JCS Gen II cells at various temperatures and currents (left), Thermal image of Gen II Cell at the end of 72 A constant current discharge (right).

Infrared thermal images of the cells were obtained while they underwent a 72A discharge from 100% to 0% SOC. Following the discharge, preferential heating was noted at the negative terminal for both generations of cell, however, no areas of thermal concern or hot spots were found. These results were shared with JCS and will be used for thermal design of battery packs.

***Thermal Characterization of CPI Cells* -** In support of the CPI/LG Chem program with the USABC, this group obtained thermal characteristics of their prototype 5 Ah lithium polymer cells (Gen 4.2) cells, developed for power-assist HEV applications. The heat generation rate and efficiency of the cells were measured at temperatures of -30°C, -15°C, 0°C, 30°C and 45°C, Figure II-2.

The efficiency of the cell during constant current discharge at 30°C was 97.6% at the 1C rate and 86.7% at the 20C rate. Efficiency measured for a scaled power profile derived from the US06 driving cycle for a midsize HEV, corresponding to an aggressive use of the battery, was 95.7%. Both the US06 profile and a geometric cycle, consisting of pulse charging and discharging at around 50% SOC, generated less heat than full constant current discharge tests at comparable RMS currents. Additional tests confirmed that the end-of-discharge portion (near 0% SOC) of the constant current discharge tests produces more heat than the middle portion (near 50% SOC), dominating the heat generation.

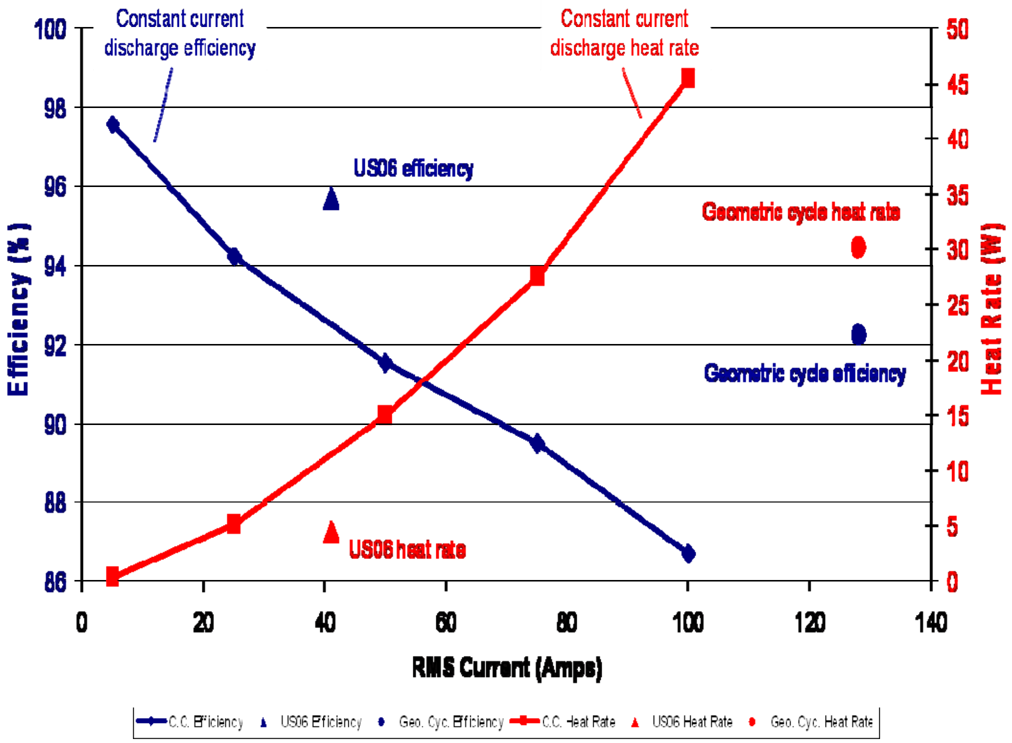

Figure II-2. CPI Gen 4.2 (5 Ah) cell's heat generation rate and efficiency for various profiles at 30°C.

The heat capacity of the cells was also measured and infrared thermal imaging was obtained, Figure II-3. Thermal imaging during aggressive cycling showed a maximum temperature difference across the cell exterior of ~5°C. The electrochemically active region of the cell exterior was even more uniform, generally within 2°C. Slightly elevated temperatures were observed at the positive terminal, perhaps due to the low electronic conductivity and smaller heat capacity of the of the aluminum foil at the positive electrode. There were no hot spots or areas of thermal concern. These results were shared with CPI/LG Chem to design modules with improved thermal performance for better in-vehicle battery pack thermal management.

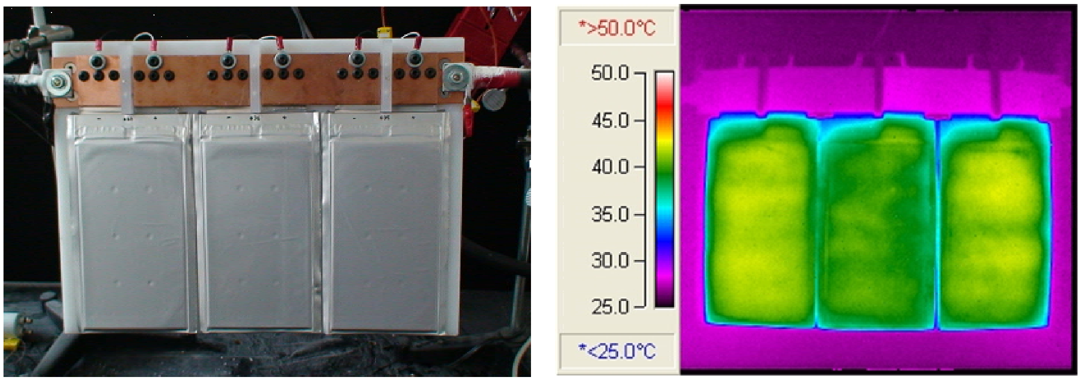

Figure II-3. Images of three CPI cells connected in series (left); Infrared thermal image of the cells at the end of 20C discharge, the thermal performance of the center cell is representative of most of cells in a module.

Thermal Evaluation of Saft 42V Liquid-Cooled Module - The Saft VL20P liquid-cooled 42V module was assessed, its thermal performance was evaluated and a data set for thermal model validation and battery model development was developed. The module consists of twelve 20 Ah cells. Saft, with input from NREL between 2003 and 2006, selected liquid cooling because of anticipated aggressive power profiles for the 42V HEV. A series of thermal studies were conducted to evaluate the thermal impacts of various coolant types, flow rates, insulations and power loads. The vehicle power load profiles for the 42V module were developed using both vehicle simulation and dynamometer data.

The module showed excellent thermal performance. The average cell temperature rise was less than 5°C for typical 42V mild hybrid applications such as that employed in the Saturn Vue Green Line Hybrid. In more aggressive profiles using maximum current limits, the average cell temperature rise was less than 10°C, still reasonable. Additionally, the temperature uniformity (cell-cell variations) was better than 2°C. Flow studies showed that the 0.5 gallons per minute glycol/water flow rate may be higher than needed. The temperature from various drive cycles fell between the (modified) USABC 50Wh profile and NREL 75A charge neutral cycles. A charge neutral 250A-40A (discharge-charge) cycle provided an upper limit for aggressive cycling, Figure II-4. Insulating the module, simulating placement of the module in a confined space in a vehicle, caused less than a 2°C rise in average temperature. Even in this worst case, the increase in temperature was less than 3°C. Although air cooling would have been sufficient under most driving loads, liquid cooling provides the option of placing the module in most locations in a car, particularly in sealed areas.

Fabricating a Large Calorimeter for Thermal Testing of PHEV Modules - Currently, NREL has a calorimeter that measures heat generation from small "air-cooled" HEV modules and cells. This team has recently completed design and fabrication of a larger calorimeter to test larger modules

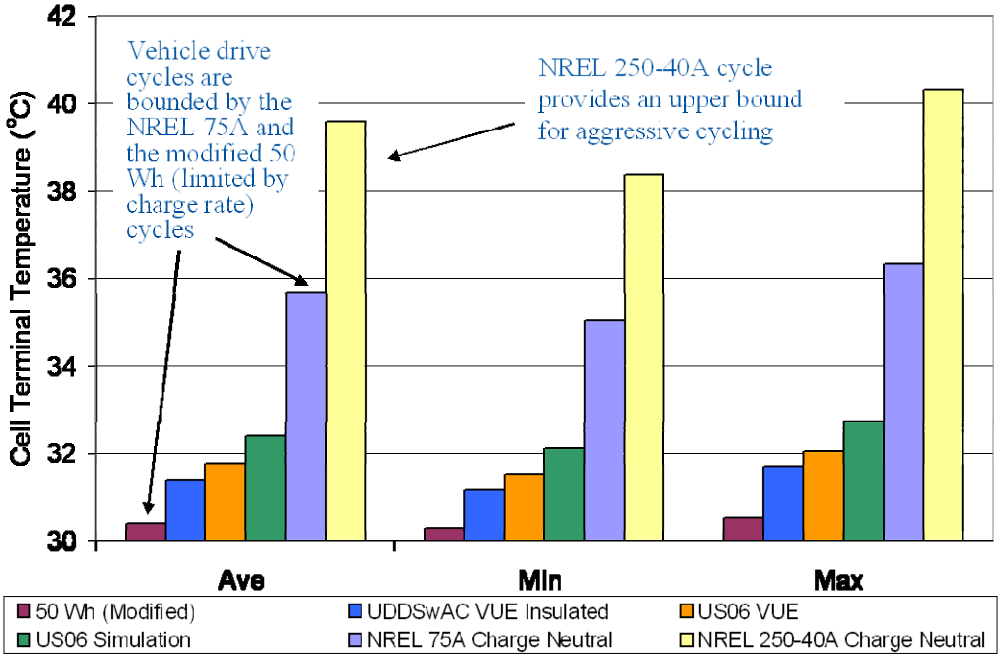

Figure II-4. Comparison of cell terminal temperatures for several drive cycles with ambient and coolant temperatures at 30°C.

that are expected to become available for PHEV applications and that are liquid cooled, Figure II-5. The new calorimeter is cable of measuring modules 60 cm x 40 cm x 40 cm and heat rates of 1 kW, (almost 7 times larger and 100 times the sensitivity of the existing calorimeter).

During FY07, most of the components of the calorimeter were fabricated: test chamber, refrigeration system, isothermal bath surrounding test chamber and external chamber. Testing of USABC batteries with this calorimeter will commence in mid FY08.

Figure II-5. Internal enclosure of test chamber with heat flux sensors being placed in the external enclosure.

***Evaluation of Phase-Change Material for Thermal Management of HEV Batteries* -** Battery thermal management using phase-change materials (PCM) has several possible benefits, such as passively buffering against high temperatures and smoothing temperature imbalances. NREL has developed both a system level and a component level model for evaluating PCM thermal management, and initiated testing on a prototype module provided by AllCell Technologies LLC (AllCell®). The prototype module consists of commercial 18650 (1.5 Ah cobalt oxide/graphite) cells surrounded by a graphite matrix impregnated with a “wax” that melts at ~ 52°C-55°C. As part of the study, tests were conducted on the cells to measure electrical and thermal performance (thermal imaging, heat generation, and efficiency). Researchers instrumented a prototype module with current, voltage, and 20 distributed temperature sensors, and experimental results were used to validate the analytical model, Figure II-6, which can be used to compare the PCM/graphite method to other approaches and to explore potential design improvements.

Analysis indicates that the PCM/graphite matrix can effectively limit the peak temperature reached during short periods, Figure II-7. However, the PCM by itself is not a sufficient cooling method as, in the absence of active cooling; continuous heat generation would fully melt the PCM following which the battery temperature would continue to rise. While the active cooling system must still be designed to handle the highest *continuous* thermal load, the benefits of the PCM include: reducing the size of the active cooling system (from having to handle the peak *intermittent* thermal load), less need to limit power output in high temperature conditions, and/or potentially reduced exposure to momentary or localized high cell temperatures. Modeling the PCM matrix design indicated that the high thermal conductivity could improve temperature uniformity and limit thermal runaway propagation by quickly distributing the generated heat. Continued evaluation in FY08 will further confirm the above findings and investigate the benefits and drawbacks of the PCM design under cold and variable temperature conditions.

***Quantified Design Parameter Impacts on System Performance* -** The purpose of this study was to identify approaches that engineers should consider when they design a battery thermal management system for vehicle applications. One important design parameter is the choice of coolant. The simplicity of an air cooling system is an advantage over a liquid cooling system. The disadvantage of air cooling, in addition to lower heat transfer coefficient, is that the small heat capacity of air makes it difficult to maintain temperature uniformity inside a cell or between cells.

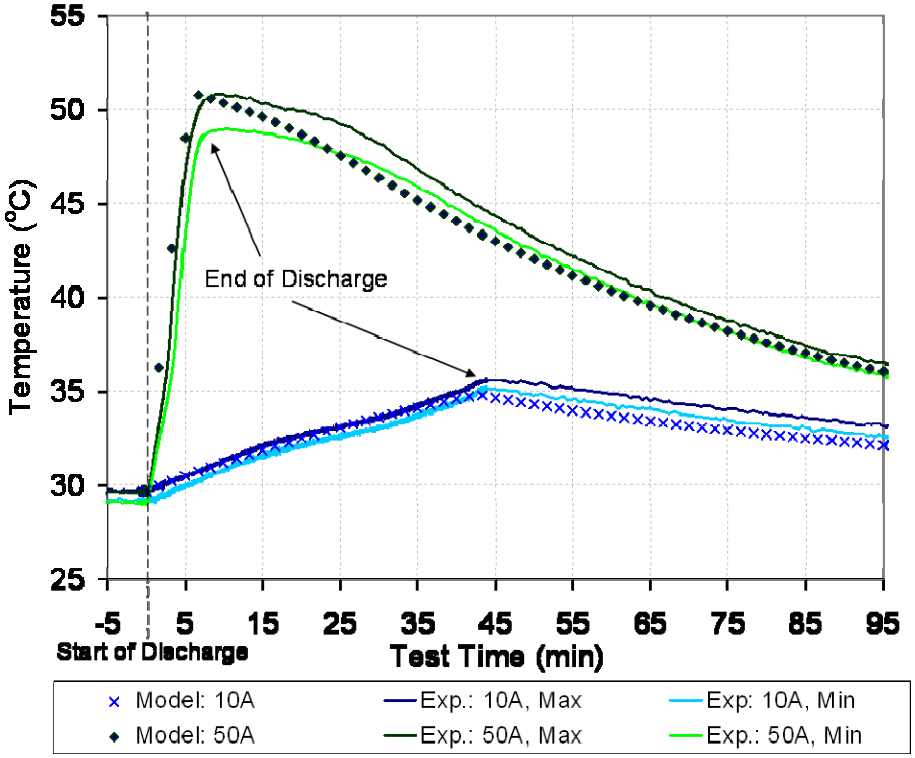

Figure II-6. Validation of thermal model with experiment measurements at different constant discharge rates.

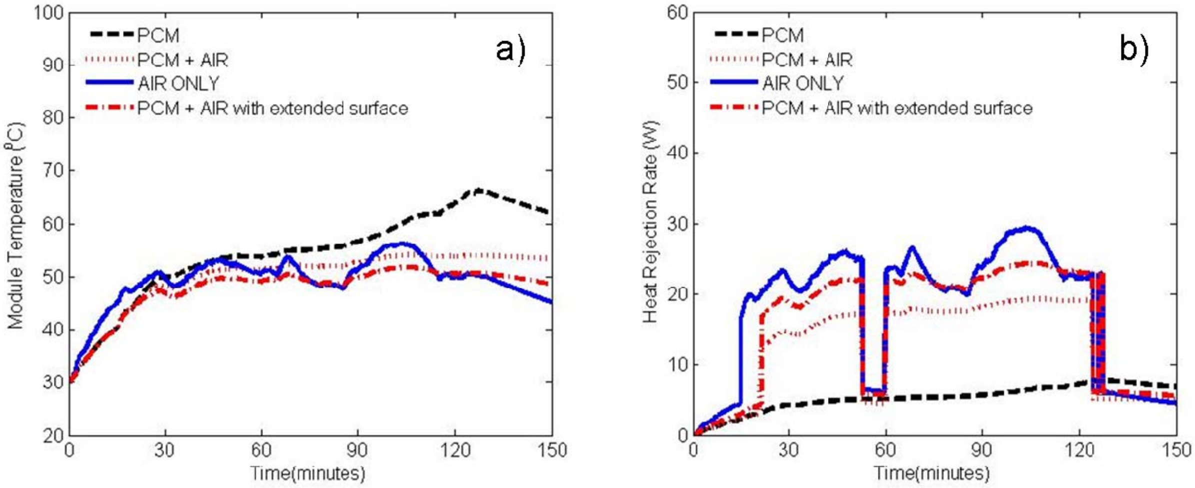

Figure II-7. Performance comparisons of (a) battery temperature variations and (b) heat rejection rates for different thermal management methods over a ‘real-world’ HEV driving.

Liquid cooling systems are more effective in heat transfer and take up less volume, but the added complexity and cost may outweigh the benefits.

The surface heat transfer coefficient, ***h***, and the blower power for air cooling are sensitive to the hydraulic diameter of the channel (D_h). On the other hand, ***h*** evaluated at cell surface is not as sensitive to the variation of D_h in a water/glycol jacket cooling system because of the added thermal resistances of jacket thicknesses, sample results are shown in Figure II-8. Results of computational fluid dynamics models imply that capturing the internal heat flow paths and thermal resistances inside a cell using a three-dimensional cell model are important for an improved prediction of cell/battery thermal behaviors.

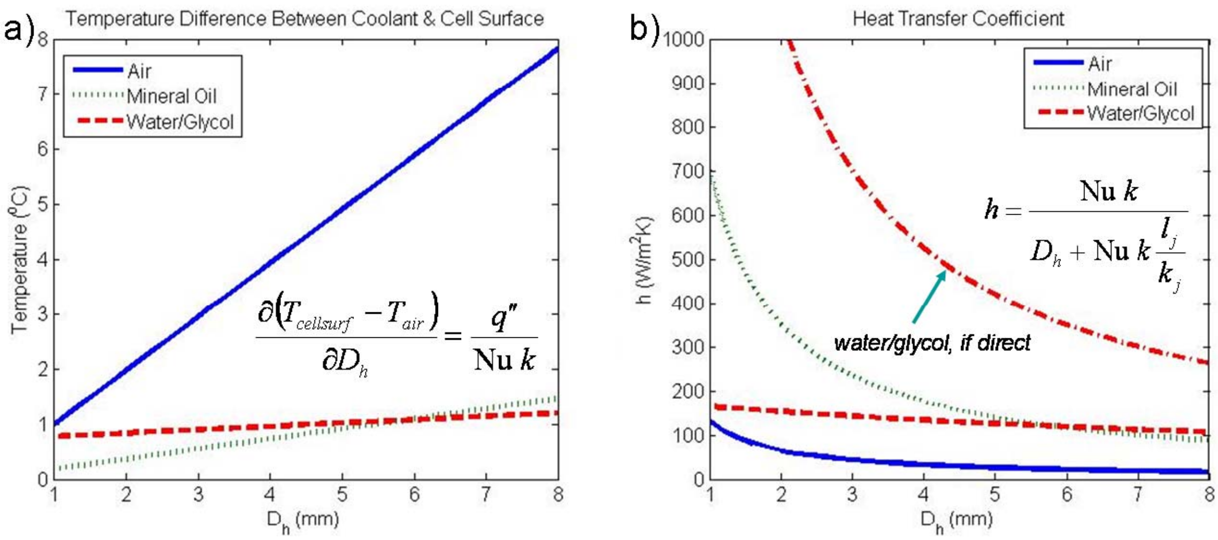

Figure II-8. Steady state laminar channel flow relations; (a) temperature difference between coolant and cooling surface, and (b) heat transfer coefficient at cooling surface to hydraulic diameter of channel.

***Development of a Three Dimensional (3D) Li-Ion Battery Performance Model* -** In high energy batteries for PHEVs or EVs, large-format cells are preferred due to the need for fewer electrical interconnects and reduced monitoring and balancing circuitry. However, the potential for temperature variation increases inside large-format cells than small cells. Researchers have initiated development of a 3D cell model to examine thermal-chemical-structural impacts on performance and life degradation of Li-ion cells. The goal of this modeling is to support thermal modeling of batteries both during normal and abusive conditions.

The model captures storing and releasing electrochemical energy through chemical reactions. It also considers temperature and chemical species transport to reaction sites which are important factors determining performance and life-reducing side reactions. Since the spatial distributions of temperature and electric potential inside a cell are affected by cell design, it is important to quantify the impacts of battery design variables on them. One of the difficulties is in resolving micro-scale layered electrodes while also modeling the much larger cell dimension scale. Researchers have proposed a multi-scale-multi-dimensional approach, and demonstrated the model's capability by applying it to a typical PHEV battery. Results indicate that there could be significant internal temperature imbalance and uneven use of materials under aggressive cycling and that these imbalances can be a strong function of cell size, Figure II-9.

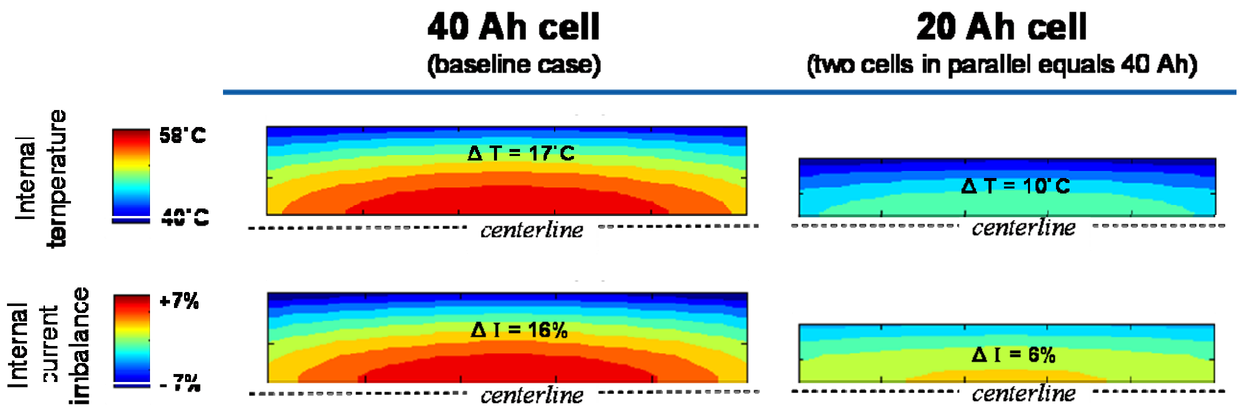

Figure II-9. Steady state internal temperature and current distributions in PHEV cylindrical cells under aggressive cycling. The 40Ah cell, with 17°C internal temperature imbalance and 16% current imbalance, may have a shorter life than the two 20Ah cells in parallel with a 10°C internal temperature imbalance and 6% current imbalance.

Simulation and Requirement Analysis

The activities in this area include developing models and tools for simulating batteries and then using them with vehicle simulation tools to define requirements of batteries and ultracapacitors or combinations thereof, in collaboration with DOE and USABC.

***Power-Assist HEVs with Smaller Energy Window Shows Considerable Fuel Savings* -** In support of the USABC, engineers studied the impact of available energy on fuel consumption of a minimum power-assist HEV. Researchers simulated vehicles with various battery capacities over several drive cycles and observed the trend between available energy and fuel economy. The sensitivity of the results to different degrees of vehicle hybridization and control strategies were also studied. In all cases, the fuel savings increase with available energy, but the returns diminish. The HEVs achieved considerable fuel savings with an energy window of ~50Wh, and captured most additional fuel savings from expansion out to 150Wh, Figure II-10.

To compare the simulations' results with real data, researchers also analyzed the energy window used by commercial HEVs on a number of test and drive cycles, Figure II-11. The vehicles examined included the Toyota Prius and the Camry, Ford Escape and Honda Accord hybrids. Analysis confirmed that even HEVs with large batteries used energy windows smaller than 200Wh on the standard test cycles. Based on the simulation and test data analysis, while fuel savings can be increased by expanding the energy window, the resulting savings need to be weighed against the expense of using larger batteries and/or the life implications of widening the battery's SOC limits. Conversely, the size and cost advantages of relaxing the energy storage requirement for an HEV should be weighed against both the anticipated fuel consumption and performance penalties. It should be noted that the performance impacts of smaller HEV energy windows (such as limiting acceleration assistance or idle-off air conditioning performance) was not considered for this study and could be factor in final selection of the energy window.

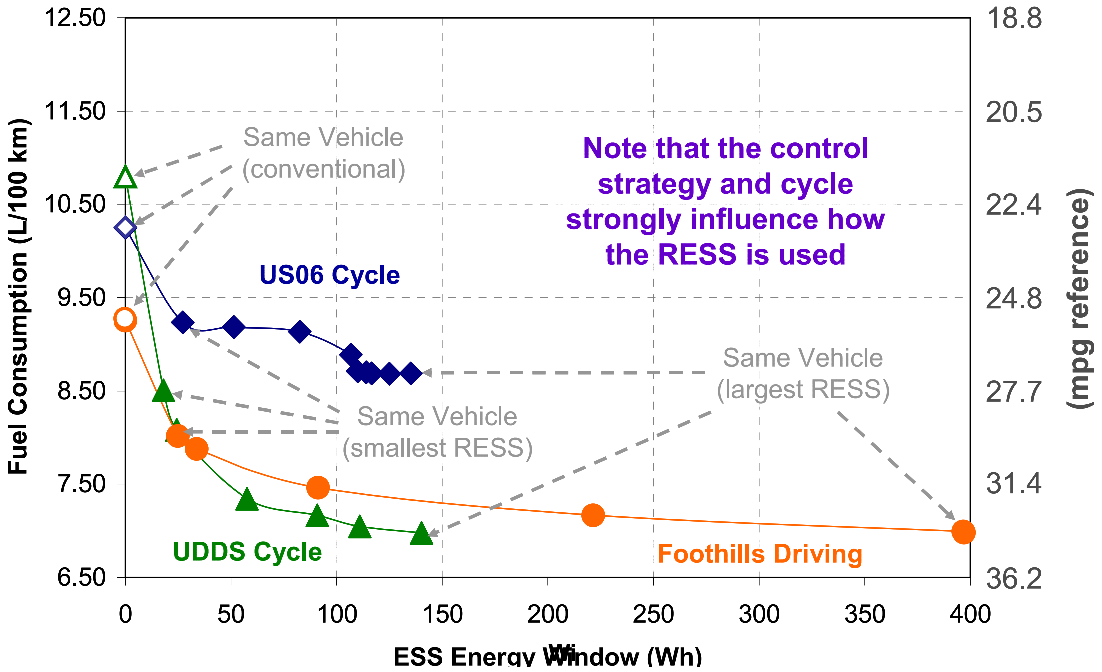

Figure II-10. Simulation results for different rechargeable energy storage system (RESS) vehicle cases over three different drive cycles.

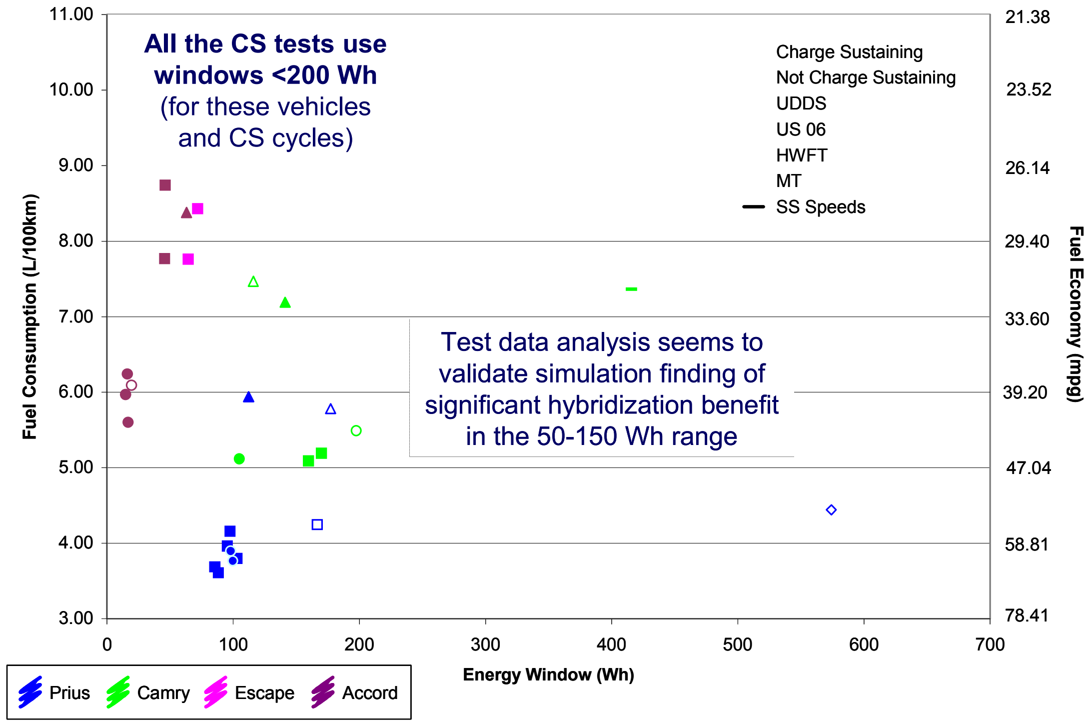

Figure II-11. Test data analysis for four commercial hybrids over several test cycles: the Urban Dynamometer Driving Schedule (UDDS), US06 profile, Highway Fuel Economy Test (HWFT), a mountain trace (MT) and steady- state (SS) speed testing. All charge-sustaining tests for these vehicles use energy windows smaller than 200 Wh.

Developed Thermal Runaway Abuse Models for Li-Ion Cells and Modules **-** The growing interest in Li-ion batteries for vehicle applications makes understanding abuse tolerance more urgent. In FY06, NREL developed 3D models to simulate thermal runaway in Li-ion cells by capturing chemical reactions, associated heat releases, and heat rejection from the cell exterior. In FY07, the model was further refined, and the 3D effect of chemical reactions and associated heat flow in abuse conditions such as internal short circuits, was demonstrated, Figure II-12. In addition, researchers developed a model that addresses cell-to-cell interaction and the propagation of thermal runaway in a module/pack. In a thermal runaway situation, the cells in a module act as heat sources thermally connected through various heat transfer paths. It was concluded that propagation of thermal runaway is determined by the competition between heat dissipation through the thermal network and localized heat generation.

Researchers explored how design features such as cell size; type of heat conduction medium; cell interconnects; and thermal contact between cells impact abuse tolerance. A design that reduces the concentrated heat delivery and improves the distributed heat transfer in a module is favorable for minimizing thermal runaway.

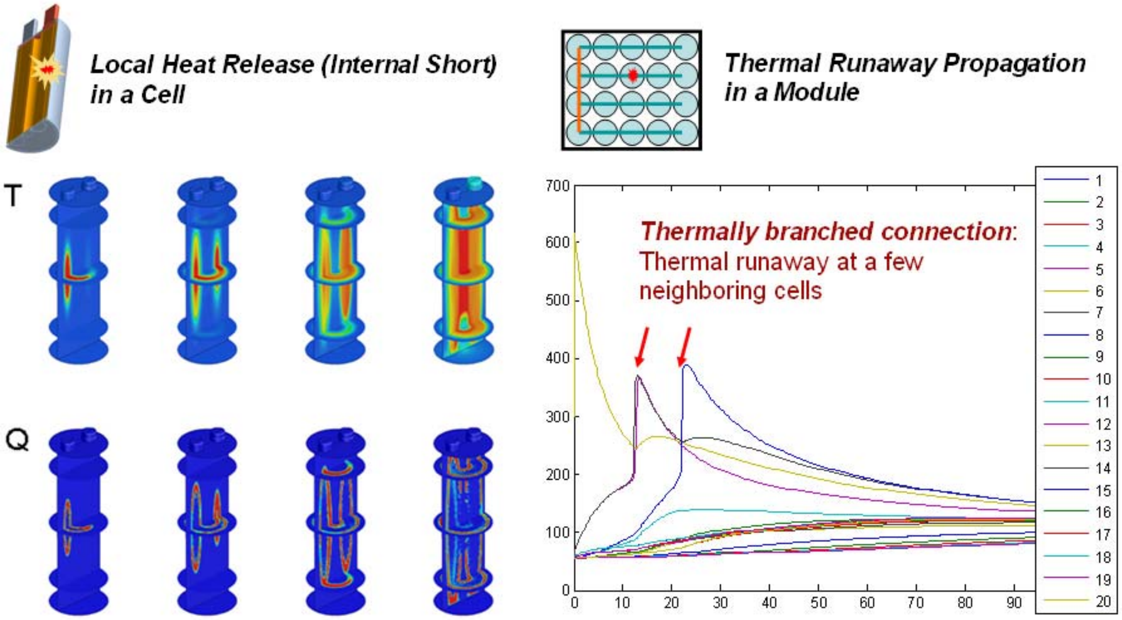

Figure II-12. Results of chemical-thermal modeling of lithium-ion battery thermal runaway: cell-internal abuse reaction propagation during internal short circuit event (left), thermal runaway propagation through a module after the red-marked cell goes into thermal runaway (right).

***Energy Storage Requirements for PHEVs* -** NREL supported DOE and USABC in defining the energy storage requirements for PHEVs. The analysis process included defining vehicle platforms, vehicle performance targets, the all electric range (AER) operating strategy (all electric or blended), and the SOC window. Based on the analysis, USABC members recommended two batteries: one for a 10-mile AER (minimum PHEV battery) and one for a 40-mile AER (maximum PHEV battery). The requirements are published at http://www.uscar.org/guest/article_view.php?articles_id=97.

***Developed an Approach for PHEV Battery Performance, Life, and Cost Tradeoff Analysis* -** Battery models with vehicle system simulation are typically empirical equivalent circuit models based on test data. This type of model is ideal for fast simulations but provides limited or no connection to battery design parameters such as electrode materials and geometry, or the electrochemical characteristics of the cell. The goal of this task was to review models of battery performance, cost, and life and begin to interconnect the models to explore the impact of battery design parameters on a PHEV application. This includes characterizing the cell performance, vehicle system simulations, and estimating system cost and life. The optimal battery design would satisfy life goals while meeting performance constraints at a reasonable cost.

Previous study at NREL suggested that long-term PHEV incremental cost over a comparable ICE would be between $5K and $10K, of which most is battery cost. Battery cost is a function of the cell materials, manufacturing methods, cell design, and to a lesser degree, required life. Battery life is a function of the electrochemistry, usage pattern, and cell design. The cell design is often driven by performance requirements. These intertwined relationships can be explored using models and automated design of experiments tools. To achieve market penetration, the battery cost must be reduced. This project explores the PHEV battery design space to highlight potential design scenarios that provide cost reduction while maintaining fuel savings. Three battery performance models are being developed or are available for use in these analyses. The first is a State Variable Model: a reduced order model of the fundamental electrochemical equations. The key added value of the model is the information on cell internal design, internal concentration gradients and its fast run time which allows co-simulation with vehicle systems models. The other models are 1D and 3D full electrochemical models that, solved by the finite volume method, are too slow to connect to vehicle system simulation but do provide the ability to investigate a wide battery design parameter space and screen multiple PHEV battery candidates.

Models for battery cost and life were challenging to identify. In FY07, a simple model was developed for evaluation of the overall trade-off analysis, but in FY08 we intend to use a simplified version of the USABC cost model. For life modeling, a stress accumulation approach was considered and will be further developed and refined in FY08.

Industry and International Support

***Support to USABC Technical Team and FreedomCAR Battery Developers* -** NREL continued analysis of energy storage requirements for HEVs, ultracapacitor 42V start/stop HEVs, and PHEVs for the USABC Electrochemical Energy Storage Technical Team. The support included performing analyses and participation and discussion at various workgroups.

***Support to several IEA HEV Agreements Task Force Annex VII* -** Support was also provided to the International Energy Agency (IEA) HEV activities through and IEA Implementing Agreement for Annexes VII (Hybrid Electric Vehicles), Annex XII (Heavy Duty Hybrid Vehicles) and Annex XIII (Fuel Cell Vehicles). These activities foster international collaborations on energy storage and hybrid vehicle technologies.

***Battery Management System for Korean Research Firm* -** The Korea Automotive Technology Institute (KATECH) provided funding to NREL to develop a battery management system for a Li-ion polymer battery produced by Kokam Engineering Company of Korea for use in a neighborhood electric vehicle (NEV). The battery management system includes thermal and electrical components to maximize the electric range of the 100Ah, 72V battery pack. Engineers found the cause of the low EV range and proposed improved designs; designed, fabricated and instrumented the 18-cell pack with improved thermal management; developed a monitoring and balancing system in cooperation with American Electric Vehicles; assembled the complete system for bench top charge/discharge testing and debugging; installed the complete system in the vehicle for on-road testing; performed vehicle dynamometer testing and on the road testing while debugging the system; and delivered the system documentation to the client. KATECH has agreed to share the results of this work with DOE.

Future Directions

In support of the President’s Advanced Energy Initiative, work on higher energy applications such as commercially competitive, full-function PHEVs is expected to accelerate in 2008. Some of the developers who were not selected for initial PHEV development contracts will be asked to supply cells for independent testing.

In the thermal management area, thermal analysis of cells and modules of FreedomCAR battery developer systems will be performed, and the advanced calorimeter will be used for measuring heat generation from liquid-cooled modules. In the energy simulation area, work will continue to develop battery and ultracapacitor electrical models for vehicle simulators and to review requirements and targets for energy storage systems for hybrid electric vehicles. We will continue to further refine and add capability to the 3D abuse model of Li-ion cells and develop a model to study the propagation of thermal runaway from cell to cell in a module.

Existing model capabilities will be enhanced by validation with experimental data from other national laboratories, extending the models to address additional chemistries, incorporating a thermally coupled electrochemistry model into the 3D cell model. The models will be valuable tools for aiding developers to evaluate various cell and module designs in their pursuit of developing safe and abuse-resistant Li-ion batteries.

II.B Technology Assessment

Technology assessments are conducted in order to validate a developer’s technical claims through independent testing and to gauge the developer’s ability to deliver a full-scale, fully packaged battery. The tests are performed both at the developer’s facilities and at DOE national laboratories in order to familiarize the developer with vehicular requirements and USABC testing procedures. The companies also share in the cost of the testing.

II.C Benchmark Testing

Benchmark testing of emerging technologies is important for remaining abreast of the latest industry developments. VT, working through ANL and INL, regularly purchases advanced battery hardware (cells and modules) and independently tests these battery systems against the most applicable USABC technical targets. Some products that have been tested recently include:

- A123 – Li-ion (power tools)
- ENAX – Li-ion (pouch, HEV)
- GS Yuasa – Li-ion (HEV)
- Kokam – Li-ion (HEV + EV)
- Hitachi Vehicle Energy – Li-ion (HEV)
- JCS – 3.6V 10Ah (HEV), 10 mile PHEV
- Lithium Tech/Gaia – Li-ion (42V)
- NEC Lamillion – Li-ion (HEV)
- Shin-Kobe – Li-ion (HEV + EV)
- SK Corp – Li-ion (HEV)
- Thundersky – Li-ion (EV)
- Tianjin Lishen – Li-ion (EV)
- Panasonic Electric Vehicle Energy – Ni/MH pack (HEV)
- Panasonic/Matsushita EV95 Ni/MH modules (EV)
- Valence Tech – Li-ion (HEV)

II.D Small Business Innovative Research (SBIR)

The SBIR program was created by the Small Business Innovation Development Act of 1982 (P.L. 97-219) and has been reauthorized through September 30, 2008. The SBIR program was designed to stimulate technological innovation, strengthen the technological competitiveness of small businesses, and use small businesses to meet Federal research and development needs. Phase I awards of up to $100,000 each for ~9 months are used to explore the feasibility of innovative concepts. Phase II is the principal research or R&D effort, with awards up to $750,000 over a two-year period.

Over the past several years, SBIR/STTR contracts have provided valuable support to EV and HEV battery development efforts. Phase II contracts awarded in FY 2007 are listed below:

- ***Farasis Energy, Inc.,*** Novel, Redox-Stabilized Li-Ion Cell
- ***NEI Corporation,*** High Power Density Li-Ion with Good Low Performance
- ***TDA Research, Inc.,*** Low-Cost Porous Carbons for Ultracapacitors
- ***TIAX, LLC,*** Nano-Structured Carbon/Silicon Composite for High Energy, Long Cycle Life Li-Ion Batteries

One STTR Project was funded in 2007:

- ***Yardney Technical Products, Inc.,*** Inexpensive, Environmentally Benign Li-Ion Battery Cathode Materials for HEV and PHEV Applications (updated)

Phase I contracts awarded in FY 2007 are listed below:

- ***JME, Inc.,*** Improved Lower-cost Electrochemical Capacitor
- ***Lithium Technology Corporation,*** New Materials to Improve the Performance of Li-Ion Batteries in HEV and PHEV Applications
- ***SBE Inc.,*** High Energy Density, Low-Cost, High Temperature Capacitors for Hybrid Vehicles
- ***TechDrive, Inc.,*** Novel Polylithium Salts for Small and Full Size Rechargeable Batteries

Technology Development Publications

1. G.-H. Kim, A. Pesaran, and R. Spotniz. "A Three-Dimensional Thermal Abuse Model for Lithium-Ion Cells." *Journal of Power Sources*, Vol. 170, pp. 476-489, 2007.
2. G.-H. Kim and A. Pesaran. "Battery Thermal Management Design Modeling." *World Electric Vehicle Association (WEVA) Journal,* Vol. 1, pp. 126-133, 2007.
3. T. Markel and A. Simpson, "Cost-Benefit Analysis of Plug-In Hybrid Electric Vehicle Technology," *World Electric Vehicle Association (WEVA) Journal,* Vol. 1, pp. 053-063, 2007.
4. G.-H. Kim and A. Pesaran. "Battery Thermal Management Design Modeling." *22nd International Electric Vehicle Symposium*. Yokohoma, Japan, October 2006.
5. A. Simpson and T. Markel, "Cost-Benefit Analysis of Plug-In Hybrid Electric Vehicle Technology," *22nd International Electric Vehicle Symposium,* Yokohoma, Japan, October 2006.
6. A. Pesaran, "Battery Choices and Potential Requirements for Plug-In Hybrids,"
   Presented at the Plug-in Hybrid Electric Truck Workshop Hybrid Truck Users Forum, Los Angeles, California, February 2007.
7. A. Pesaran and T. Markel, "Battery Requirements and Cost-Benefit Analysis for Plug-In Hybrid Vehicles," Proceedings of the *24th International Battery Seminar and Exhibit*, Fort Lauderdale, Florida, March 2007.
8. T. Markel and A. Pesaran, "PHEV Energy Storage and Drive Cycle Impacts," Presented at *Advanced Automotive Battery Conference*, Long Beach, California, May 2007.
9. G.-H. Kim and A. Pesaran. "Analysis of Heat Dissipation in Li-Ion Cells & Modules for Modeling of Thermal Runaway." *The 3rd International Symposium on Large Lithium Ion Battery Technology and Application* (LLIBTA/AABC2007), Long Beach, California, May 2007.
10. A. Pesaran and J. Gonder "*Factors & Conditions for Widespread Use of Ultracapacitors in Automotive Applications*," Proceeding of *Advanced Capacitor Summit*, San Diego, California, July 2007.
11. G.-H. Kim, K. Smith, A. Pesaran and R. Spotnitz, "Analysis of Thermal Behavior of Li-Ion Batteries using Thermal Abuse Reaction Model," *212th ECS Meeting*, Washington DC, October 2007.
12. G.-H. Kim and K. Smith, "Multi-Dimensional Electrochemical-Thermal Coupled Model of Large Format Cylindrical Lithium Ion Cells," *212th ECS Meeting*, Washington DC, October 2007.
13. G.-H. Kim, J. Gonder, J. Lustbader and A. Pesaran "Evaluation of HEV Battery Thermal Management with Phase-Change Materials," paper to be presented at the *23rd Electric Vehicle Symposium,* Anaheim, CA, December 2007.

III. APPLIED BATTERY RESEARCH

III.A Introduction

The applied battery research program is being conducted in support of the FreedomCAR and Fuel Partnership, which is targeting more fuel-efficient light duty vehicles that can reduce U.S. dependence on foreign petroleum, without sacrificing performance. There is an emphasis on developing and improving critical component technologies; and energy storage technologies are one of these critical components. Energy storage devices enhance the efficiency of the prime power source in HEVs by leveling the load, and they capture braking energy to produce more fuel efficient and cleaner vehicles. In addition, in PHEVs, they provide the primary power source for a number of "all electric" miles, after which they again operate in HEV mode. Better energy storage systems are needed to help expand the commercial markets for HEVs and to help make PHEVs commercially viable. The energy storage requirements for various vehicles are presented in Section II.

This program focuses on assisting developers of high-power Li-ion batteries to overcome key barriers to the commercialization of this promising technology for use in light-duty HEV applications (and beginning in 2008, high-energy Li-ion batteries for use in PHEVs). The key barriers associated with HEV batteries, and likely PHEV batteries, are:

- 15-year calendar life,
- Operation between -30°C and +52°C,
- Selling price of \$20/kW for HEVs and \$500/kWh of available energy for PHEVs (short term) and,
- Adequate abuse tolerance for use in light-duty vehicles.

This applied battery research program, the ATD program, was initiated to understand the factors that limit calendar life, abuse tolerance, and performance over the desired temperature range, so that improvements can be made in these areas. Also, it addresses the cost barrier at the cell level through the identification and development of lower-cost and more-stable cell materials and components.

The program seeks to advance the development of more optimal cell chemistries through the identification and development of cell materials that are more chemically, structurally, electrochemically, and thermally stable in the cell environment, as well as possessing a cost advantage over current materials. Conventional high-energy Li-ion batteries, of the type used in consumer electronics, employ sophisticated and relatively expensive electronic controls that limit their exposure to abusive conditions. This program focuses on both understanding and enhancing the inherent abuse tolerance of the cell chemistry, which will help reduce the level of sophistication of the electronic control system and thereby realize cost savings.

This year the program focused on the four cell-level areas listed below, each addressing one of the key barriers:

- Understand life-limiting mechanisms and enhance life,
- Understand and enhance low-temperature performance,

- Understand and enhance inherent abuse tolerance, and
- Realize lower cell-level costs via lower cost materials, components, and technologies.

Development of cells employing a Gen3 chemistry, employing a $Li_{1+x}Ni_{1/3}Mn_{1/3}Co_{1/3}O_2$ (called NMC or 1/3) layered cathode material and a synthetic graphite anode (MCMB 10-28), has been focused on understanding and solving a number of issues at the cell and material level. General specifications of this chemistry are shown in Table III-1. In 2007, the program expanded its investigation into the fundamental limitations associated with low T performance by investigating non-carbonate based electrolytes, and into the characteristics of the solid electrolyte interphase (SEI) and how it is impacted by formation conditions. In addition, work into robust nano-phase coatings that enhance cathode life was initiated.

Table III-1. General specifications for Gen3 cells.

Positive Electrode	8 wt % PVDF binder 8 wt % carbon black 84 wt % $Li_{1.05}(Ni_{1/3}Co_{1/3}Mn_{1/3})_{0.95}O_2$
Negative Electrode	8 wt % PVDF binder 92 wt % MCMB 10-28
Electrolyte	1.2 M $LiPF_6$ in EC:EMC (3:7) as baseline, or with 2% $LiBF_2C_2O_4$ as an electrolyte additive.
Separator	25µm PE

Five DOE national laboratories collaborate in the program. Argonne National Laboratory (ANL) provides coordination of the program activities for DOE. The other four participating DOE laboratories are Brookhaven National Laboratory (BNL), Idaho National Laboratory (INL), Lawrence Berkeley National Laboratory (LBNL), and Sandia National Laboratories (SNL). As part of this program, ANL researchers maintain close communications (and in some cases collaborations) with a large number of international material supply companies, through which they gain access to the latest advanced electrode and electrolyte materials for evaluation.

The following subsections provide technical highlights and progress on the Applied Battery Research program for FY 2007. The information provided is representative only and detailed information is available in the publications sited at the end of this section.

III.B Understand Life-Limiting Mechanisms and Enhance Life

Objectives

- Provide guidance to battery developers and other researchers regarding aging protocols and new tests, analyses, and modeling methodologies related to calendar and cycle life
- Understand the impact of various formation protocols on cell life and performance
  - Gain an understanding of the underlying mechanisms that govern the formation, characteristics, and impact on performance of passivation films on the positive and negative electrodes, and
  - Quantify conditions that promote favorable SEI layer formation, as well as conditions that lead to poor SEI layers
- Develop and apply novel diagnostics techniques that will help elucidate the causes of capacity and power fade

- Investigate degradation processes and their relationship to fundamental and engineering-based material properties
- Validate Technology Life Verification Test (TLVT) methodologies as described in the TLVT manual

Approach

- Conduct electrochemical studies on Gen3 chemistry cells to examine the role of each electrode in the aging process
- Use standard test protocols to characterize the aging characteristics of the Gen3 cells
- Apply microscopy, spectroscopy, and diffraction techniques, such as scanning electron microscopy (SEM), X-ray photoelectron spectroscopy (XPS), and X-ray diffraction (XRD), to understand the impact of electrode microstructure on cell life and performance.
- Apply statistical design of experiments (DOEx) approach to investigate the most significant formation cycle parameters (and their interactions).
  - Correlate the morphology and composition of electrode surface films with formation cycle protocols to determine the role of the passivation films on cell performance and life
- Perform validation tests on the TLVT methodology and use the results to improve and update the TLVT manual.
- Develop new diagnostic techniques to distinguish bulk and surface processes to monitor the degradation processes, to determine the effects of electrode material structural, the interfacial phenomena, etc. on the cell capacity and power fading and abuse tolerance

Accomplishments/Findings

- Secured cells with Gen3 cell chemistry from E1-Moli, Enerdel, Toyota Central Laboratory (TCL), and Nippon Chemical, and are engaged with manufacturers in determining causes of early- life soft shorts
- Adopted a new test fixture for testing TCL cells, which allows testing of cells without welding current/voltage leads to cell terminals
- Found that cell impedance drops significantly following formation cycles, which appear to change the surface energy of the electrodes, leading to better wetting
- Binder free graphite electrodes were developed and successfully used to study SEI layers
- The dominant graphite-SEI species are lithium alkyl carbonates ($ROCO_2Li$) and lithium alkoxides (ROLi)
- An observed difference between cell behavior with $LiPF_6$ and LiTFSI salts appears to be caused by greater instability of the $LiPF_6$ solutions
- Ar sputtering has been used to create surface defects in graphite electrodes, which in turn leads to a thicker SEI compared to non-sputtered graphite electrodes
- The $LiF_2BC_2O_4$ electrolyte-additive reduces cell impedance rise and capacity fade, i.e., the additive has a beneficial effect on cell-aging performance
- The SEI coverage was greater on graphite samples cycled in $LiF_2BC_2O_4$ electrolyte than in the $LiPF_6$ electrolyte
- No evidence was found for particle isolation in fresh Gen-3 electrodes or in electrodes taken from formed cells

- A new *in-situ* soft XAS technique has been developed to monitor the oxidation states of cathode materials at both surface and bulk simultaneously during heating.
- On cycle-life aging of Gen3 pouch cells, both positive and negative electrodes contribute to impedance rise.

Future Studies

- Complete further diagnostic tests to determine the nature of passivation films after formation cycling, changes in these films on aging, and the overall mechanisms responsible for performance degradation in cells with the Gen3.
- Identify products of formation processes on electrodes using mass and vibrational spectroscopy
- Investigate effect of additives (VC, LiF, and $LiF_2BC_2O_4$) on formation and interfacial impedance.
- Applying the Energy Dispersive XRD (EDX) techniques to develop three-dimensional structural mapping for various types of commercial Li-ion cells
- Begin investigating impact of water on Li-ion cell performance
- Test TLVT methodology on additional chemistries

III.B.1 Introduction

This subsection provides highlights and progress on work to understand the life-limiting mechanisms in high-power Li-ion cell chemistries and to relate that information to developing more stable and lower cost cell chemistries. Since the beginning of this program, it has been studying the aging characteristics of different cell materials and chemistries. New diagnostics on the Gen3 electrodes have begun using binder and carbon free electrodes and laboratory made pouch cells (~100mAh). A new investigation into the impact of formation on cell performance and life has begun, and researchers are currently working with manufacturers to understand the issues that have led to early Gen3 cell failure. Finally, the TLVT team has completed its initial testing to validate the TLVT methodology. Table III-2 summarizes how the five DOE laboratories contribute to the work.

Table III-2. Summary of how DOE laboratories contribute to the "Life Enhancement" focus are.

	ANL	BNL	INL	LBNL	SNL
SEI/Formation Study, DOEx, Diagnostics	X		X	X	
Gen 3 Cell Build Status	X				
TLVT Validation Testing and Data Analysis	X		X	X	X
Aging & Thermal Characteristics of Cathode Materials		X			
Cell Transport and Electrochemical Modeling	X				

III.B.2 SEI/Formation Study, DOEx, and Diagnostics

Formation Cycling, Statistical DOEx (Gering[6]) - The formation process is a very important step in producing stable cells that will exhibit good power and energy characteristics and long life. Formation cycling is the initial cycling, under a controlled set of conditions, conducted on a Li-ion cell before it is given to the end-user. Formation cycling goals include: (a) limit capacity fade and impedance rise, (b) ensure that identical cells perform similarly when subjected to similar test conditions, and (c) ensure the presence of "desirable" passivation films on the electrode active materials. These passivation films are known to protect active materials from further reactions with the electrolyte; the nature of these films affects both initial and long-term cell performance, including calendar life and safety characteristics.

The objective of this study is to gain an understanding of the mechanisms that govern the formation cycling process. The team intends to quantify conditions that promote favorable SEI formation, as well as conditions that lead to poor formation and subsequent poor cell performance. The statistical DOEx involves a systematic evaluation of the most significant formation parameters and their interactions. The parameters considered are temperature (T), upper cutoff voltage (UCV), charge and discharge cycling rate (C_{ch}, C_{dis}), open circuit rest periods (t_{ocv}), and the net number of complete formation cycles per cell (n_{cyc}). The relative effect of parameters on SEI formation and cell performance was assumed to be: $T > UCV > C_{ch} > C_{dis} > t_{OCV} > n_{cyc.}$ To accommodate both the large overall matrix and a finite number of test channels, the study was broken into three stages, where each stage has one or more distinct set of test parameters in sub-matrices. A statistical fractional factorial approach was used in setting up the matrix.

The formation experiments are conducted using 2032-type coin cells containing an MCMB 10-28 graphite negative electrode, $Li_{1.05}(Ni_{1/3}Co_{1/3}Mn_{1/3})_{0.95}O_2$ positive electrode, EC-EMC (3:7 by wt.) + 1.2M $LiPF_6$ electrolyte and Celgard 2325 separator. Immediately following formation cycling, the cells are characterized by: (a) electrochemical impedance spectroscopy (EIS) measurements at 80% SOC (~3.9V), (b) C/1 and C/24 capacity measurements, and (c) self-discharge tests, in which cells charged to 4.0V are left at OCV for two days. The cells are then cycle-life aged at 50°C using a continuous cycling profile at a $C_1/1$ rate around 80% SOC. Periodic characterization provides information on the degradation of cell performance.

It should be noted that the formation experiments and data described in this section are for one battery chemistry. Because SEI attributes and performance are dependent on battery chemistry, care should be taken when drawing inferences between this study and other chemistries.

Stages 1 and 2 have been completed, covering 20 unique formation conditions on 120 button cells. Statistical analyses have been performed on the datasets. The optimum combination of the four lesser formation parameters is: $C_{ch} = C/24$, $C_{dis} = C/24$, $t_{OCV} = 4$, and $n_{cyc} = 3$. The analyses also confirmed the need to execute Stage 3 to provide a complete data population for final statistical analyses, allowing the team to model all main effects and desired first-order interactions simultaneously. Four additional formation conditions were necessary to quantify the exact role of UCV as it relates to other formation parameters.

---

[6] Most projects in the ATD program involve multiple researchers, often at multiple national laboratories. The lead contributor to each section is provided following each section name. Additional contributors to each task are provided in Appendix A.

Stage 3 testing has begun, involving 11 formation conditions and 66 cells. Following Stage 3 experiments, final statistical analyses will be performed for all three stages using response variable expressions (RVE) and graphical analyses. Results from RVE analyses should allow interpolation and extrapolation to formation conditions not directly studied, including the feasibility of an abbreviated formation cycle to satisfy a minimum time requirement.

Impedance Changes during Formation Cycling (McLarnon) **-** Impedance measurements were carried out during initial cycling/formation experiments on Gen-2 anodes and cathodes using a three-electrode configuration. The cell (Figure III-1) employed a graphite anode, lithium metal counter electrode, and lithium reference electrode. For cathode experiments, the graphite anode was replaced with a cathode electrode. The polypropylene separator was soaked with an excess of electrolyte so that the experiments were carried out in a flooded condition.

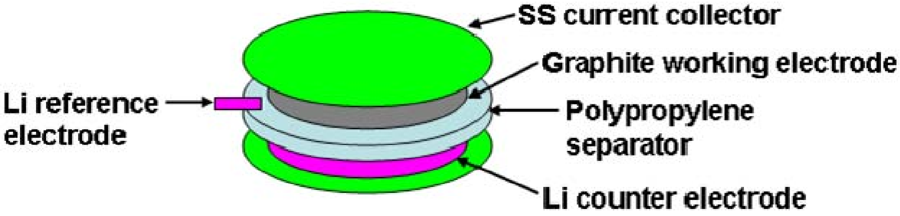

Figure III-1. Three-electrode cell configuration for formation experiments.

Three-electrode impedance experiments were carried out on the graphite working electrode before and after cyclic voltammetry experiments. Results are shown in Figure III-2 for two different electrolytes, the Gen-2 electrolyte (EC/EMC-$LiPF_6$) and a control electrolyte (EC/EMC-LiTFSI).

Prior to the formation cycle the impedance of the anode was unacceptably high for both electrolytes. Following the formation cycle, the impedance with $LiPF_6$ fell to an acceptable range and a large lithium de-intercalation peak was observed during the cycle. The impedance for LiTFSI remained high as seen in Figure III-2(b), and no de-intercalation peak was observed during cycling unless the electrode potential reached -0.1 V. In such a case, the de-intercalation peak was observed and the interfacial impedance fell to values similar to $LiPF_6$ after cycling. Similar behavior was observed with cathodes for which the impedance before charging and discharging was >200 Ω -cm^2 for both salt solutions. After a charge-discharge cycle the impedance with $LiPF_6$ diminished to <20 Ω -cm^2. With LiTFSI several cycles were required for the interfacial impedance to diminish. Note that a similar result has been described in the BATT program and is reported in Ch 4.

The following conclusions can be drawn:

- The formation cycles appear to cause a change in the surface energy of the electrodes, which leads to better wetting of the electrode particles. The change in surface energy appears to be caused by the formation of products that cover the electrode surfaces.

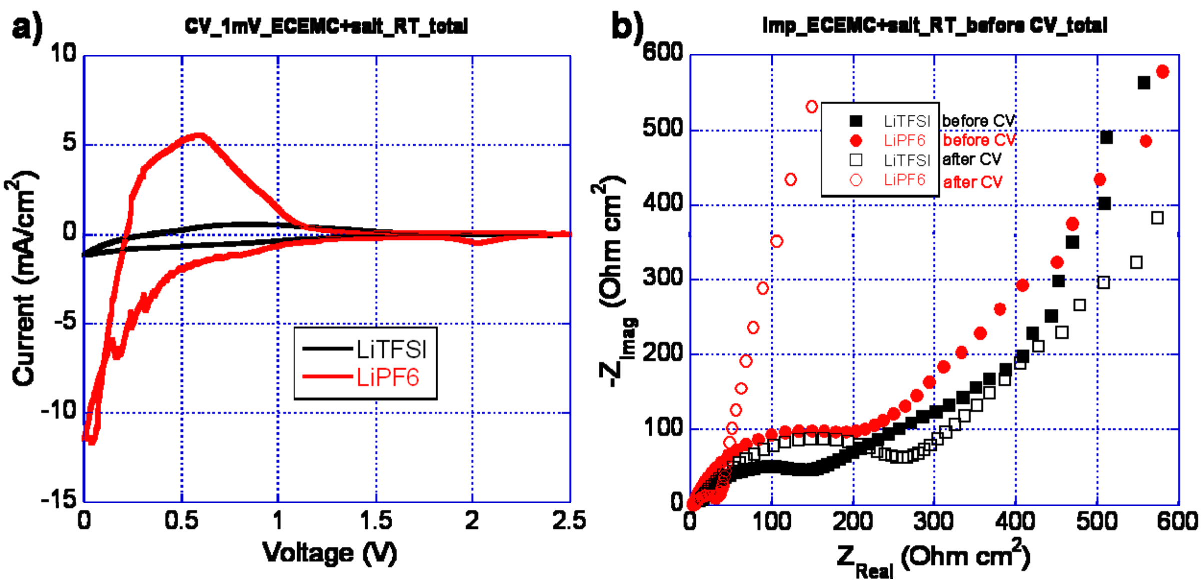

Figure III-2. Cyclic voltammetry (a) and impedance (b) of Gen-2 anodes versus a lithium reference electrode in 3-electrode configuration for EC/EMC-LiX (1.2M), where X=PF_6 or TFSI.

- The difference between cell behavior with $LiPF_6$ and LiTFSI appears to be caused by the greater instability of the $LiPF_6$ solutions. The water content of the electrolyte solutions was 30 ppm for LiTFSI and 0 ppm for $LiPF_6$, but potentiometric titration indicated that all water had converted to HF. HF is capable of initiating homogeneous reactions that could account for the peak at 2.0 volts for $LiPF_6$ in Figure III-2(a), possibly a result of CO_2 formation.

***Study of Graphitic Anodes' Contribution to Capacity Fade (McLarnon)* -** It has been previously shown that the Mag-10 graphite anodes suffered surface structural damage upon prolonged cycling in ATD Gen-2 cells. This deleterious structural effect is intensified at high charging rates and elevated temperatures, both of which may cause greater lithium concentration variation within a graphite particle. This is evidenced in the Raman spectra of graphite anodes by the increased prominence of the disorder or D-band with respect to the graphite or G-band. The effect has been observed in Mag-10 and KS-15 graphite and appears to occur in all graphitic carbons.

The effect of the surface structural damage in graphite on the degradation mode of the Li-ion cell was investigated. The structural disorder in graphite was artificially recreated by using argon-ion sputtering. Raman microscopy, SEM, and Brunauer Emmett Teller (BET) measurements confirmed that similar surface degradation was reproduced.

The surface structural damage of the graphitic anode does not significantly affect the reversible charge capacity of the Mag-10 graphite. However, these artificially modified Mag-10 anodes showed double the irreversible charge capacity during the first formation cycle, compared to fresh un-altered anodes (Figure III-3a). The sputtering process increased edge sites and catalytic activity on the graphite surface, but did not cause particle breakdown or exfoliation. Impedance spectra (Figure III-3b) of un-sputtered and 120 s sputtered Mag-10 anodes after the three formation cycles show very similar impedance behavior. A slight increase in the diameter of the semi-circle indicates that the interfacial resistance is greater for the sputtered electrode.

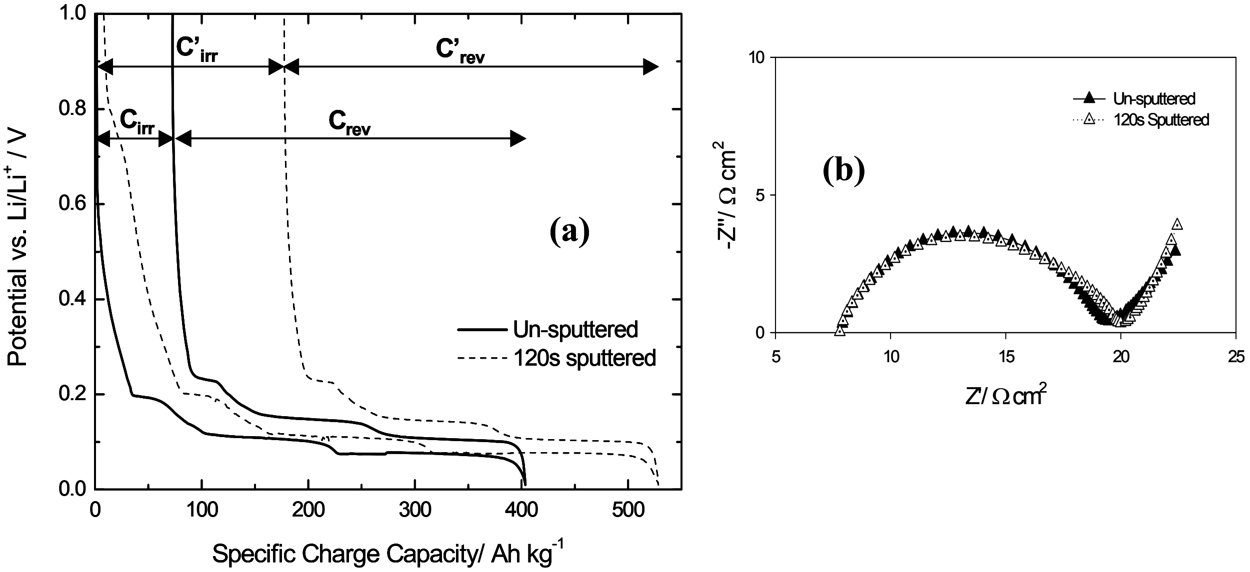

Figure III-3. (a) First galvanostatic charge-discharge curves of un-sputtered (__) and 120s sputtered (--) Mag-10 graphite in 1.0 M $LiPF_6$, EC:DMC 1:1 w/w at C/25. (b) Impedance spectra, measured at 0.05 V vs. Li/Li+, of cycled un-sputtered (__) and 120s sputtered (--) Mag-10 anodes.

The composition of the SEI layer on electrochemically cycled un-sputtered and 120 s sputtered Gen-2 anodes were studied *ex-situ* with Fourier transform infrared spectroscopy (FTIR) in the reflectance mode, Figure III-4. A number of comparable bands were seen for both the un-sputtered and 120-s sputtered samples; however, the band intensities for the sputtered anode were somewhat more intense, suggesting a thicker SEI layer.

Graphite crystalline lattice fragmentation at the surface caused by Ar-ion sputtering or long-term cycling exposes more surface active sites to the electrolyte, which reacts to reform the SEI. The structural disorder induced during a long-term cycling consumes a portion of the cyclable lithium and is responsible for the slow and continuous SEI layer reformation. This prolonged process results in the shift of lithium inventory, and consequently, the loss of reversible capacity in aged Li-ion cells.

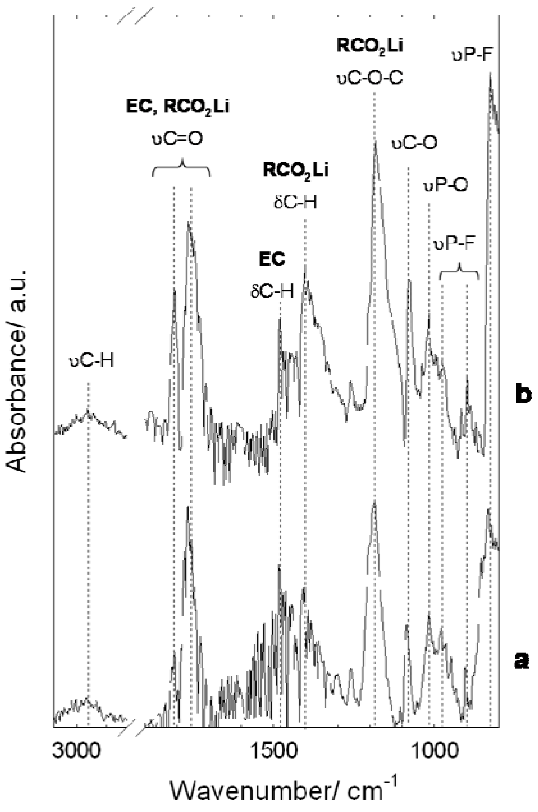

Figure III-4. FTIR spectra of cycled (a) un-sputtered and (b) 120s sputtered Mag-10 electrodes, washed in DMC.

Investigating the SEI Using Binder-Free Graphite Electrodes (Abraham) **-** Binder-free (BF) electrodes simplify interpretation of SEI data. Previously, several SEI studies have been conducted on highly oriented pyrolytic graphite

(HOPG) electrodes. However, HOPG electrodes have a large basal-to-edge-plane surface-area ratio. Because the SEI formed on graphite edge planes (the sites of lithium intercalation) is important from a practical perspective, the studies on HOPG electrodes are of limited value.

In this work, the SEI formed on BF graphite electrodes fabricated on Cu foil by electrophoretic deposition (EPD); shown in Figure III-5, were examined and characterized. The BF graphite electrodes were cycled in cells containing electrolytes with two different salts: $LiPF_6$ and lithium difluoro(oxalate)borate ($LiF_2BC_2O_4$). $LiPF_6$ is the baseline electrolyte salt for the ATD cells, whereas $LiF_2BC_2O_4$ is attracting attention as an alternative to $LiPF_6$, and is being used as an electrolyte additive in the Gen3 cells. Cell assembly, galvanostatic cycling, and cell disassembly were conducted in an Ar-atmosphere glove box (<1 ppm H_2O, <5 ppm O_2) to prevent any influence of air on SEI formation. FTIR and XPS studies were conducted to examine the SEI layer formed on the BF graphite electrodes in these electrolytes.

The data from these experiments indicated that:

- The dominant graphite-SEI species in both electrolytes are lithium alkyl carbonates ($ROCO_2Li$) and lithium alkoxides (ROLi).
- Li_2CO_3 was conspicuously absent, which suggests that the presence of this compound in the graphite SEI can be avoided by careful operation and handling of cells.
- Trigonal borate oligomers are most likely present in the SEI of graphite samples cycled in $LiF_2BC_2O_4$ electrolyte, while lithium fluorophosphates are present on graphite samples cycled in $LiPF_6$ electrolyte.
- The SEI layer coverage was greater on graphite samples cycled in $LiF_2BC_2O_4$ electrolyte than in the $LiPF_6$ electrolyte.

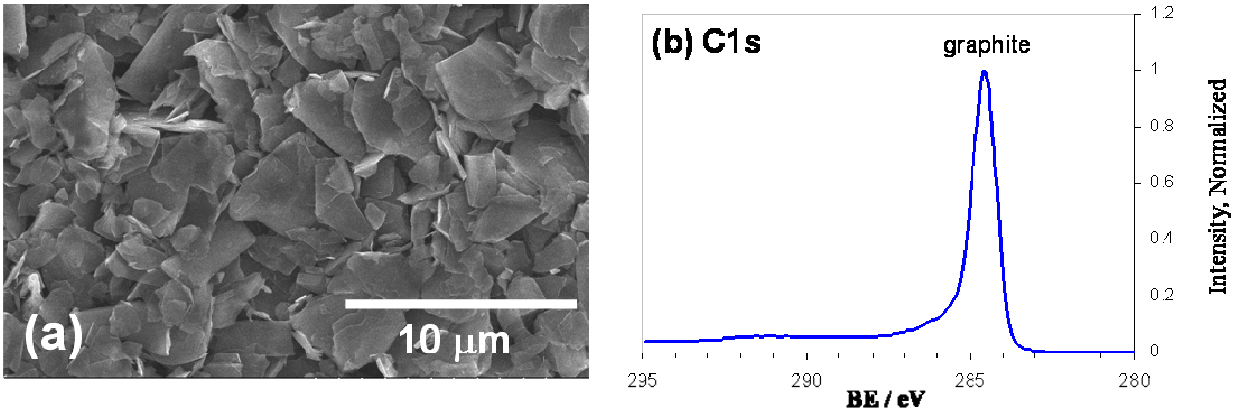

Figure III-5. Representative (a) SEM image and (b) XPS data, from fresh BF-graphite electrode

III.B.3 Gen3 Cell Build Status, Testing, & Diagnostics

Securing Cells with Gen 3 Cell Chemistry (Henriksen) - Efforts to acquire high-quality cells containing the Gen 3 cell chemistry continued. Cells were obtained from several suppliers, including E-One Moli, Enerland, Toyota Central Laboratory (TCL), and Nippon Chemical. In the cases of the first three companies, ANL supplied the Gen 3 anode and cathode materials, as well as the detailed design specifications. In the case of Nippon Chemical, ANL supplied the design specifications and Nippon Chemical provided the electrode materials, which included their own

NMC cathode material. The design specifications for the electrodes appear in the following tables. The electrodes in the Enerland pouch cells have somewhat lower loadings and they substituted Super P carbon black in the positive electrode for the ANL specified TB5500 carbon black conductive additive. The negative electrodes incorporate a small amount of carbon fiber (VGCF). Also, different PVDF binders were used in the fabrication of electrodes from the various suppliers.

The Enerland pouch cells were fabricated and shipped to ANL in the dry state (without electrolyte). They incorporated a side pouch for use in filling the cells with electrolyte, which was performed by ANL. The cells were then formed and sealed.

Table III-3. Enerland Pouch Cell Electrodes - As Built Specifications

	Positive Electrode	**Negative Electrode**
Composition	84% Seimi L-333	90% MCMB 10-28
	8% Super P carbon black	2% VGCF
	8% PVDF binder (KF7208)	8% PVDF binder (KF1100)
Active Loading Density	10.3 mg/cm^2	6.6 mg/cm^2
Coating Thickness	51 μm	51 μm
Foil Thickness	20 μm Al	18 μm Cu

Table III-4. Toyota Central Laboratory—As-Built Electrode Specifications

	Positive Electrode	**Negative Electrode**
Composition	84% Seimi L-333	92% MCMB 10-28
	8%TB5500 carbon black	8% PVDF binder (KF9130)
	8% PVDF binder (KF1120)	
Active Loading Density	13.0 mg/cm^2	8.0 mg/cm^2
Coating Thickness	60.8 μm	64.2 μm
Porosity	33%	34%

Table III-5. Nippon Chemical—Electrode Specifications

	target	**this time**
Positive Electrode		
active material	L-333 84%	L-333 84%
binder	PVDF 8%	PVDF 8%
carbon	TB5500 8%	Super-P 8%
Active Loading: (mg/cm^2)	13.0	13.5-14.0
Coating Thickness (μm)	60.8	60.0-65.0
Negative Electrode		
active material	MCMB 84%	MCMB 84%
binder	PVDF 8%	PVDF 8%
Active Loading (mg/cm^2)	7.97	8.0-8.5
Coating Thickness (μm)	64.2	60.0-65.0

In all cases the cells employed the same type of electrolyte: 1.2 M $LiPF_6$ in EC:EMC (3:7) and the majority of each cell build employed the $LiF_2BC_2O_4$ electrolyte additive at the 2 % by weight level in the electrolyte. A small number of cells (baseline cells) employed this electrolyte without the additive.

Testing of Gen3 Pouch Cells (Bloom) - 400mAh Gen3 pouch cells are being tested using the same test conditions as the Gen2 cells. The test matrix and cell distribution of baseline and additive cells are given in Table III-6.

Before testing started, the cells were characterized in terms of C/1 and C/25 capacities, HPPC-L and EIS. The characterization tests are carried out at 25°C. The tests are halted every 28 days and the cells are re-characterized to gauge performance loss.

Table III-6. Test matrix and cell distribution for Gen3 cells. The numbers in parentheses are baseline cells.

Condition	Cell count
25°C cycle life	5
45°C cycle life	4
45°C calendar life	5 (2)
55°C calendar life	5 (2)

Sixteen weeks of testing have been completed. The average ASI values of the cells containing the additive are plotted in Figure III-6 along with the best-fit curves for the Gen2 baseline cells. It can be seen that the initial Gen3 ASI values are less than those of the Gen2 cells. As the cells age at temperature, the ASI values increase. The ASI values from the Gen3 cycle life tests at 25 and 45ºC are below the corresponding values from the Gen2 cell tests. The cells in the calendar life experiment display different behavior. Between 0 and 8 weeks, the Gen3 ASI values at 45 and 55ºC are lower than the corresponding values from Gen2. At 12 weeks, the Gen3 impedance is above those from Gen2. Initial ASI values for the baseline cells were higher than those with the additive, and they increased more rapidly with calendar age.

There exists some concern about using pouch cells of this type for long-term accelerated aging tests. The TCL and Nippon Chemical cells are 18650 cells. Accelerated aging data from these cells will be compared to the data obtained on the Enerland pouch cells.

Diagnostic Tests on Cells with Gen3 Electrodes (Abraham) - Electrochemical cycling and aging data on cells with Gen3 electrodes were obtained using 2032-type coin cells (1.6 cm^2 electrodes), pouch cells (25 cm^2 electrodes) and larger cells (32 cm^2 electrodes) that incorporated a Li-Sn reference electrode (RE). Consistent capacity and impedance data were observed for all cell configurations.

Representative impedance data from pouch-cell aging tests are shown in Figure III-7. It is evident that cell impedance increases on aging. An unexpected feature of these data is the change in high-frequency arc width, which was also observed in coin cell and pouch cell data. This high-frequency impedance arc showed the following characteristics: (a) arc width increased with cell age, and increases with temperature, slow at 30°C and relatively rapidly at 55°C, (b) the arc

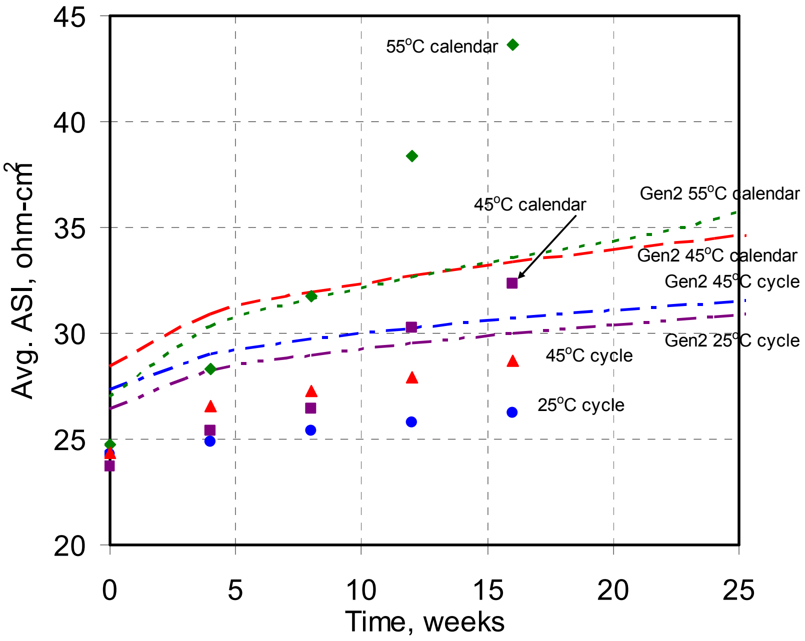

Figure III-6. Average ASI vs. time comparing the values obtained from the Gen3 additive pouch cells with those from Gen2 baseline cells. The curves represent the best-fit to Gen2 data and the points are the Gen3 data under the same conditions.

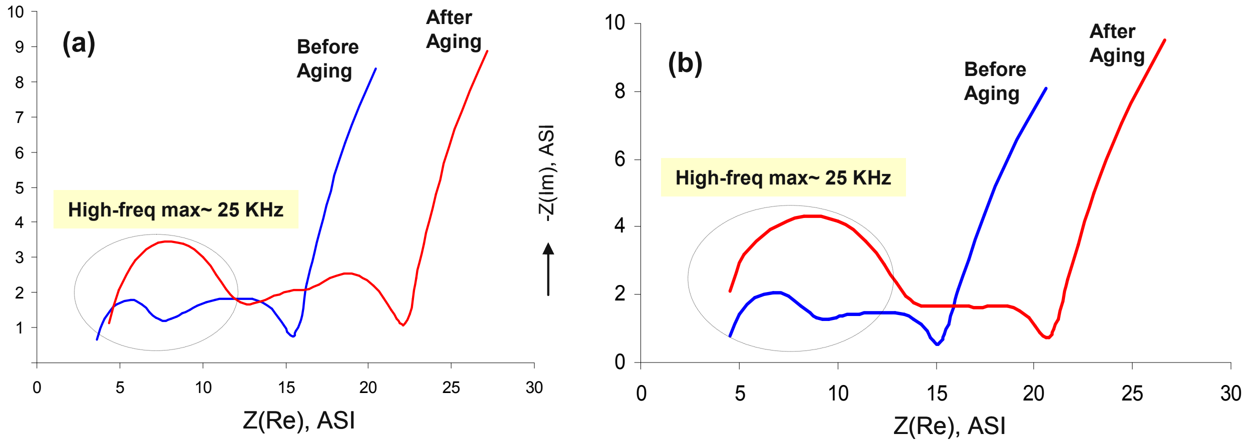

Figure III-7. EIS data from a Gen3 electrode pouch cell that contained the following electrolytes: (a) Gen2 and (b) Gen2 + 3 wt% $LiF_2BC_2O_4$. The data were acquired at 3.72V, 30°C, and between 100kHz-10mHz. The cells were aged at 55°C.

has a characteristic frequency of ~25 KHz, unchanged on aging, (c) the arc is not affected by the EIS measurement temperature and cell voltage, (d) the arc was also observed in cells containing various electrolyte additives.

The aging data collected from the RE cells shed light on electrode contributions to full cell impedance rise; representative data are shown in Figure III-8. All these cells showed significant changes to the high-frequency arc, especially during the early weeks of aging; and these changes could be traced to the positive electrode. Because the high-frequency regime of the EIS data suggests electron transfer problems, it is concluded that the impedance rise in this regime was a

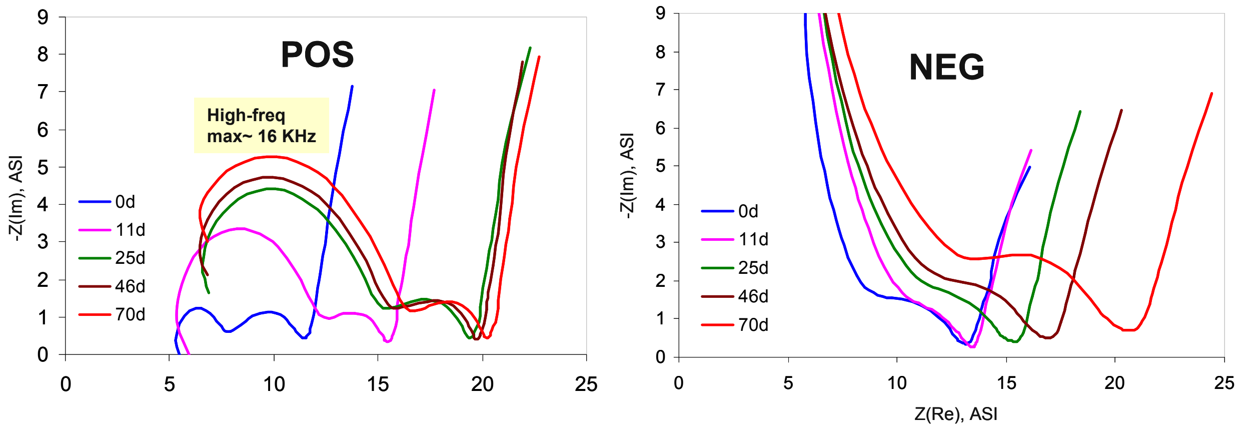

Figure III-8. Positive and negative electrode impedance data from a Gen3 cell that contained Gen2 + 3 wt% $LiF_2BC_2O_4$ electrolyte. The cell was aged at 4V and 55°C. The data were acquired at 3.72V, 30°C, and in the 100 kHz-10mHz frequency range. Note the increase in high-frequency arch width on aging for the positive electrode.

"positive electrode artifact" arising from one or more of the following sources: (a) oxide-oxide contact problems arising from inappropriate material synthesis, (b) oxide-carbon contact problems arising from a non-optimized electrode coating, or (c) composite coating-current collector contact problems arising from inadequate calendaring.

EIS measurements on cells containing positive electrodes from other suppliers did not show the high-frequency impedance arc, which verified the "positive electrode artifact" hypothesis. Moreover, because these "alternative" electrodes contained oxide particles synthesized by the same manufacturer, we can rule out problems resulting from oxide-oxide contact. More discussion on the positive electrode high-frequency arc is provided in the electrochemical modeling section below.

***Electrochemical Modeling (Dees)* -** The emphasis of the electrochemical modeling effort has focused on determining the source of the high frequency impedance described above. The methodology for the model is described in detail in the literature[7], and a short description is given in Section III.C.4. The model simulates the cell phenomena with the EIS version being used to associate the active material/electrolyte interfacial phenomena to the electrode's impedance. This is generally accomplished by fitting the EIS electrochemical model simulations to the electrode impedance results, relying heavily on separate independent experiments and diagnostic studies, as well as experience with other electrodes. The high frequency range of the impedance arc and the fact that most oxide based electrode's impedance curves do not exhibit the same behavior, suggested that the arc was likely caused by an electronic contact resistance. In the electrochemical model, the electronic contact resistance is associated with the contact between the oxide active material and the conductive carbon additive. Although not specifically included in the model, another possible source of the high frequency impedance is a high contact resistance at the electrode/current collector interface.

---

[7] D. Dees, E. Gunen, D. Abraham, A. Jansen, and J. Prakash, *J. Electrochem. Soc.,* **152** (7) (2005) A1409. D. Abraham, S. Kawauchi, and D. Dees, "Modeling the Impedance Versus Voltage Characteristics of $LiNi_{0.8}Co_{0.15}Al_{0.05}O_2$," Electrochim. *Acta*, In Press.

While being critical for proper electrode operation, the electronic conductivity (i.e. overall conductivity and particle-to-particle contact resistance) is difficult to determine because of the coating thickness, particle sizes, composite structure, and the presence of the current collector, especially when the electrode is flooded with electrolyte during operation. As an initial step, the resistance of a number of fresh electrodes was determined using a standard four probe measurement (i.e. 100µm probe diameter, 1 mm apart, and linearly arranged) on the face of the composite coating. Fifteen oxide active material composite electrode samples were examined such that about half of the electrodes were known to exhibit the high frequency impedance. In general the electrode coatings gave two types of resistance values. The electrodes that exhibited the high frequency circular impedance arc had a resistance of 0.1Ω or greater (0.1-4.3Ω). The normally operating electrode's resistance was much less than 0.1Ω (0.001-0.008Ω).

In order to interpret the resistance measurements, a model was developed using an effective electrode conductivity and a volume averaged form of ohms law. In the modeling studies, a high contact resistance was added at the electrode/current collector interface in combination with a very poor effective electrode conductivity to obtain resistance values on the order of tenths of ohms. The theoretical studies indicate that the four probe technique cannot be used to accurately determine the conductivity of electrode laminates. Also, having a low resistance value (<<0.1Ω) does not guarantee a good performing electrode or even a good electronically conducting electrode. However, a high resistance value (≥0.1Ω) is indicative of an electrode with poor electronically conducting properties.

***XRD Studies of Cathode Particle Isolation (McLarnon)* -** Particle isolation was previously shown to be a significant source of power fading in aged and cycled Gen-2 cathodes, with some isolation detected even in fresh electrodes (Figure III-9). Fresh and formatted Gen-3 electrodes were subjected to similar investigations, which involve rapid potentiostatic charging or discharging in flooded-electrolyte cells, followed by removal, washing, and examination by

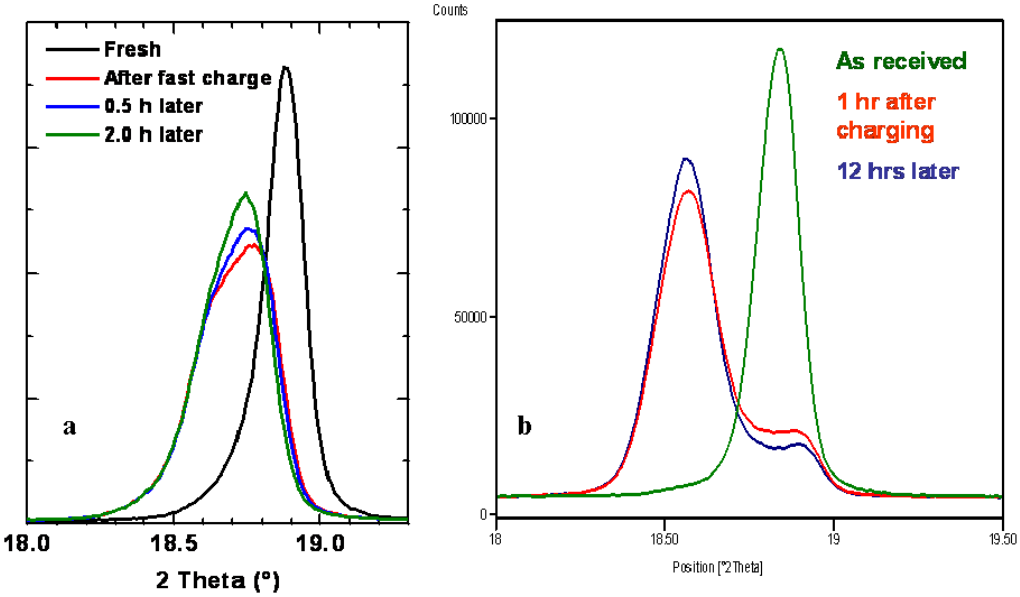

Figure III-9. 003 XRD peak showing particle isolation in a) fresh and b) aged Gen-2 cathodes.

ex-situ XRD as soon as possible after the pulse is applied and at intervals thereafter to search for the presence of particles in different states of charge and to follow the relaxation, if any, to a uniform state of charge.

No evidence was found for particle isolation in the fresh Gen-3 electrodes or in electrodes taken from formatted cells (Figure III-10).

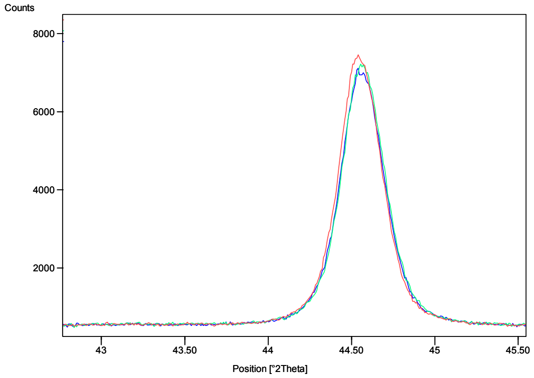

Figure III-10. 003 XRD peak showing no particle isolation in formatted Gen-3 cathodes.

EDX and SEM Studies of Cathode Particles (McLarnon) - Fresh, cycled, and aged Gen-3 cathodes were examined by SEM and EDX to search for degradation similar to that found in Gen-2 electrodes. The fresh electrodes were very uniform and showed no evidence of carbonate formation or delamination. Similarly, an electrode that had been aged at 3.72V and 55°C for 100 days, with a cell impedance rise ~ 40-45%, showed no structural changes or deviations from the initial ratios of the transition metals (Figure III-11).

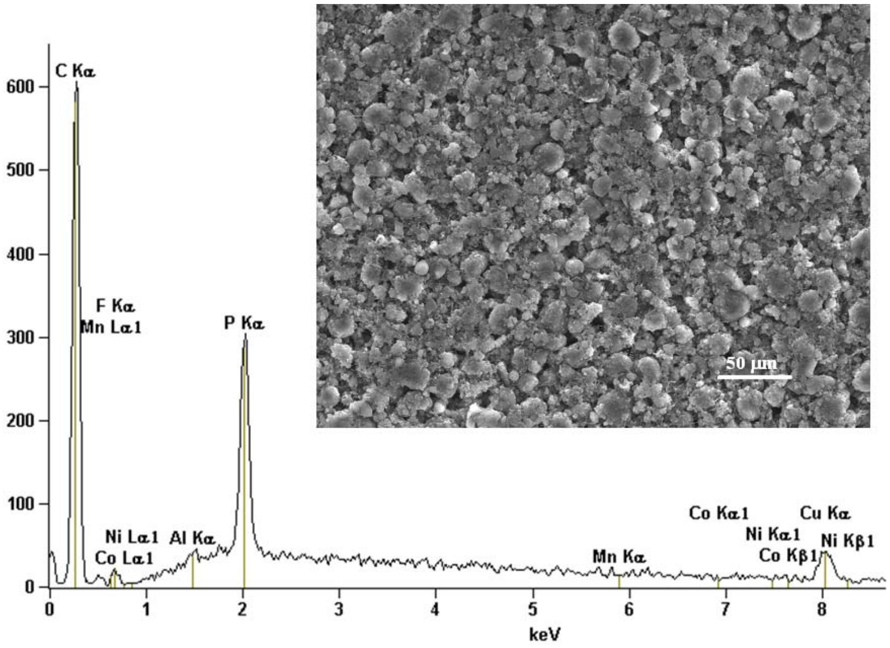

Figure III-11. SEM/EDX of aged Gen-3 anode (DAP10).

A fresh Gen-3 cathode was cycled 20 times at C/25 in 1M $LiPF_6$ in PC with taper charging at 4.1 V for five hours at the end of each charge step. This electrode maintained good performance and appeared normal after cycling except for the presence of a number of previously unobserved features (Figure III-12) that gave strong EDX responses for aluminum and chlorine. These may have been created by attack on the current collector, although the origin of chlorine is unexplained.

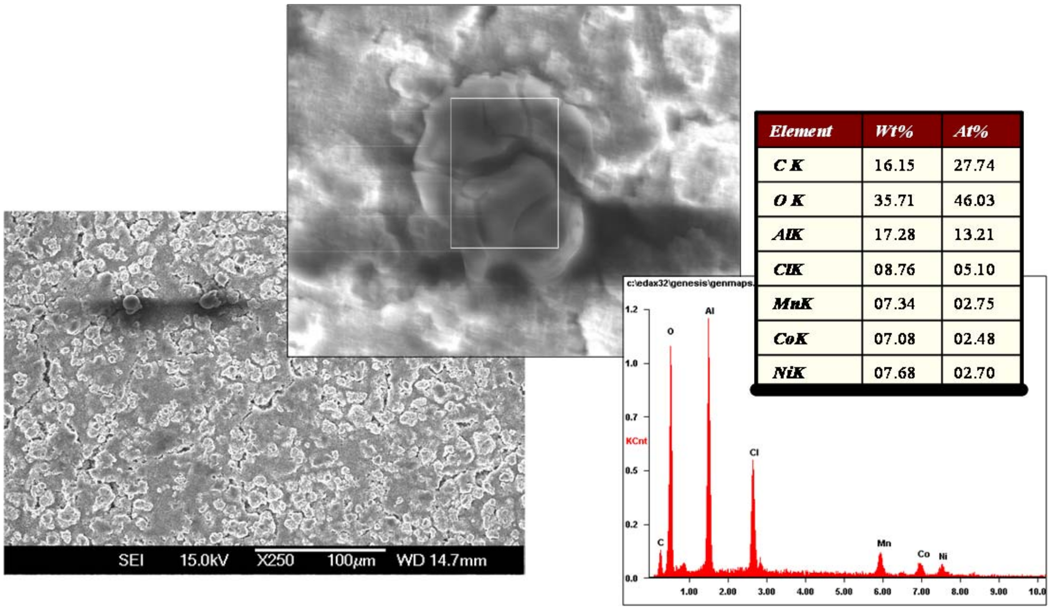

Element	*Wt%*	*At%*
C K	16.15	27.74
O K	35.71	46.03
AlK	17.28	13.21
ClK	08.76	05.10
MnK	07.34	02.75
CoK	07.08	02.48
NiK	07.68	02.70

Figure III-12. SEM/EDX of Gen-3 cathode after 20 cycles.

The general conclusions from the various characterization and aging studies on Gen3 cells are as follows:

- The fresh positive electrodes were very uniform and showed no evidence of carbonate formation or delamination. Examination of positive electrodes from short-term (< 1 month) aging showed no oxide structure changes or deviations from the initial ratios of the transition metals.
- On cycle-life aging, both positive and negative electrodes contribute to impedance rise, when the cell contains only the Gen2 electrolyte. The positive electrode impedance rise probably results from the blocking of the oxide edge planes by organo-phosphate and flurophosphate surface films. The negative electrode impedance rise probably results from a thickening of the SEI layer, which impedes Li-ion transport into and out of the graphite.
- The $LiF_2BC_2O_4$ electrolyte-additive reduces cell impedance rise and capacity fade, i.e., the additive has a beneficial effect on cell-aging performance.
- In cells containing the $LiF_2BC_2O_4$ electrolyte additive, the negative electrode is the main contributor to cell impedance rise; and the additive appears to inhibit positive electrode impedance rise. Further diagnostic tests are underway to determine the nature of passivation films after formation cycling, changes in these films on aging, and the overall mechanisms responsible for performance degradation in cells with this chemistry.

III.B.4 TLVT Validation and Testing

The Technology Life Validation Test (TLVT) and it is being developed to assess (in as little as two years) the life of batteries expected to live as long as 15 years. In FY 2007, this team completed testing of 42, 7Ah, high-power cells; developed a model that fits the data; and completed development of software that supports the model. Below is a brief synopsis of that effort beginning with the testing of the cells and resulting data, the model development, and the results of applying the software to analysis of the data.

***Introduction to TLVT Cell Testing (Battaglia)* -** Of the 42 cells being evaluated, 36 were tested under calendar-life conditions, with the remainder under cycle-life conditions. The testing was originally scheduled to last six months but continued for 12 months for cells that showed little impedance rise. Calendar-life testing consists of resting at an open circuit voltage (OCV) (which corresponds to a specific state of charge (SOC)) and test temperature with a daily taper charge back to the designated SOC. Aging is interrupted every 31.5 days for the minimum pulse power characterization (MPPC) test. The MPPC is performed at both the test and reference (30°C) temperatures, which allows for temperature compensation. At the beginning of testing and specified reference performance tests (RPT) thereafter, an L-HPPC test was also performed to determine available power loss. The results of the cell cycle-life tests were too inconclusive and are omitted here to save space.

***Calendar Life Testing (Christophersen)* -** Figure III-13 shows the average temperature-compensated discharge resistance growth from the MPPC test at SOC_{MAX} for each temperature group (closed symbols). SOC_{MAX} was defined by the manufacturer as 3.7 V and corresponds to a depth of discharge (DoD) of 38% between the voltage limits of 2.7 and 4.0 V when cycled at a rate of C/1 at beginning of life. The 30°C cell group only consists of three cells calendar-life aged at SOC_{MAX}. Each of the other groups consists of nine cells, three-each calendar-life aged at SOC_{MAX}+10% capacity, SOC_{MAX}, and SOC_{MAX}-10% capacity, respectively.

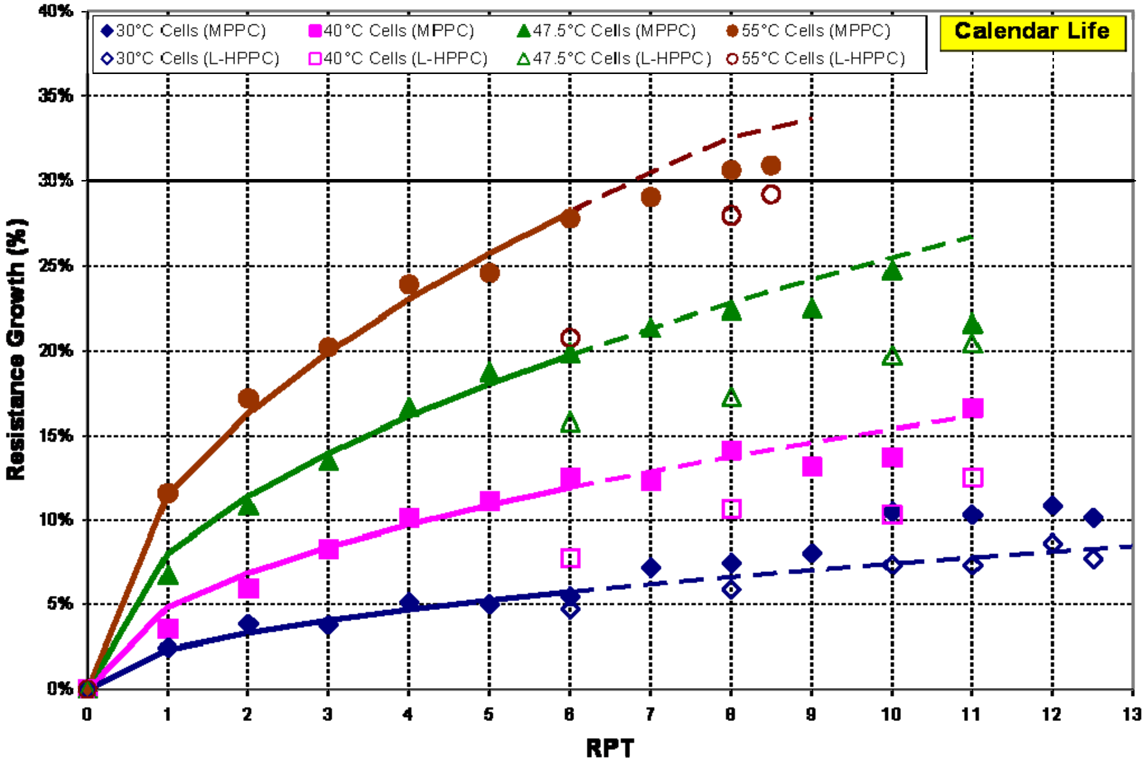

Figure III-13. Average, temperature-compensated, discharge resistance growth of all groups of cells calendar-life tested at SOCMAX and four different temperatures.

The effect of SOC is inconclusive, but appears small (as discussed below), so all nine cells were included in the average. These data show that temperature is an effective stress factor leading to a 30% impedance growth in seven months for the most extreme condition. The interpolated discharge resistance growth from the L-HPPC test at SOC_{MAX} is also shown (open symbols). The L-HPPC test consistently yields lower resistance growth than the corresponding MPPC. This indicates that life estimations based on the MPPC test should be more conservative than those based on the L-HPPC.

Figure III-14 shows the average temperature-compensated discharge resistance growth from the MPPC test at SOC_{MAX} for each group tested at 55°C. Since the standard deviations within the core group tend to overlap each other (SOC_{MAX}+10%, SOC_{MAX}, and SOC_{MAX}-10%), aging was also performed at two different conditions using six spare cells (three each at SOC_{MAX}+20% and SOC_{MIN}) to help better determine the effect of SOC. SOC_{MIN} was chosen to be 3.5 V and corresponds to approximately 76% DOD when cycled between 2.7 and 4.0 at C/1 at beginning of life. As shown, the cells aged at SOC_{MAX}+20% show a resistance growth rate similar to the core cells, but at SOC_{MIN}, the growth rate is significantly smaller. This suggests that SOC is be another stress factor for these cells as the voltage is increased from 3.5 and 3.7 V and 38% change in SOC, but has marginal effect as the voltage is changed slightly above or below 3.7 V.

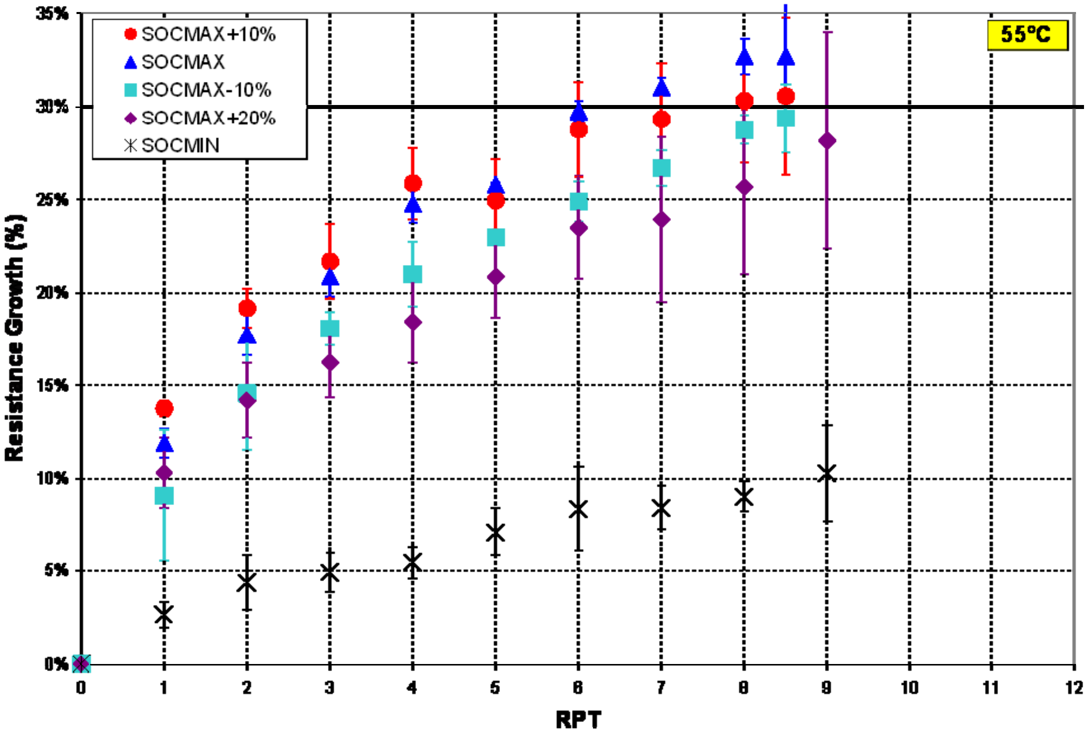

Figure III-14. Average, temperature-compensated discharge resistance growth for groups of cells calendar-life tested at 55°C.

***Introduction to Modeling (Battaglia, Thomas, Bloom)* -** The TLVT process used to design a core-life test matrix requires both a life model and an error model. The life model, expressed in the form of a deterministic *degradation model*, reflects the average (typical) cell degradation over time as a function of various stress factors. The *error model* reflects the cell-to-cell variability in observed degradation about the average. Degradation and error models were developed based on the resistance data obtained from the calendar life test of the 7-Ah, high-power cells.

***Degradation Model* -** The degradation model can be empirical, chemistry/physics-based, or some combination of both. In the case of the 7-Ah Li-ion cells used, the relative resistance data appeared to follow Arrhenius-like (thermally activated) kinetics given by: $Y = 1 + \exp\left\{\beta_0 + \beta_1 \cdot \frac{1}{T}\right\} \cdot t^{\rho}$, where Y is the relative resistance, T is the absolute temperature, and t is time. The log transformation reduces to $\log(Y-1) = \beta_0 + \beta_1 \cdot \frac{1}{T} + \rho \cdot \log(t)$.

The estimated time exponent ($\hat{\rho} = .52$) was statistically indistinguishable from ½. The remaining parameters were re-estimated resulting in $\hat{\beta}_0 = 18.11$ and $\hat{\beta}_1 = -6236$. A graphic of the fitted model and experimental data (as produced by the developed TLVT data analysis software) is displayed in Figure III-15.

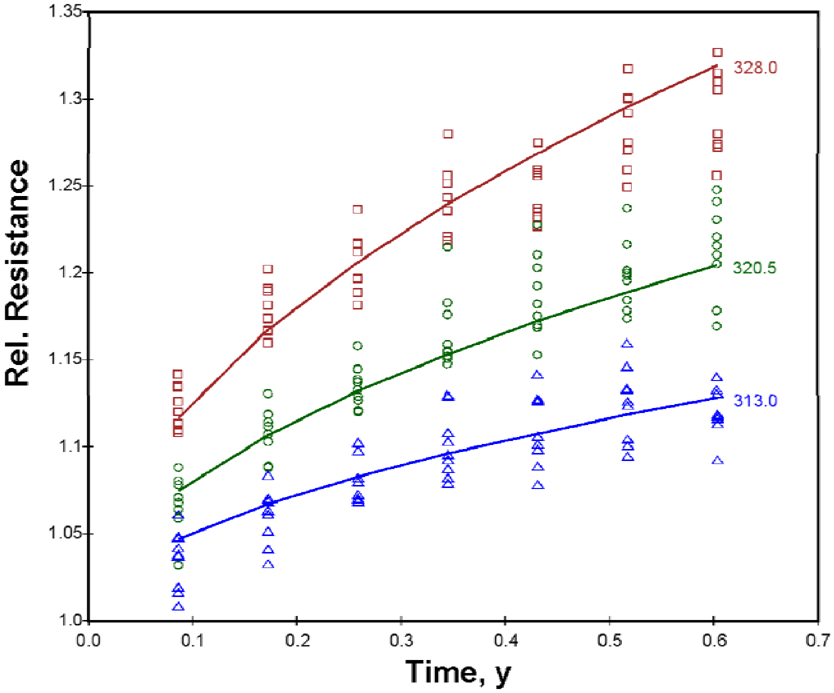

Figure III-15. Degradation model of calendar-life data. Temperature (K) is shown next to the curves.

***Error Model* -** The following derivation was used in developing an *error model*. Denote the observed relative resistance of the i^{th} cell aged at temperature T for time t by $Y_i(T;t)$ and the fitted model by $\hat{Y}(T;t) = 1 + \exp\left\{\hat{\beta}_0 + \hat{\beta}_1 \cdot \frac{1}{T}\right\} \cdot t^{1/2}$. $\gamma_i(T;t)$ is defined as the difference between the observed value of resistance rise and the fitted value of the resistance rise. An error model that accounts for differences between the observed relative resistance and the fitted degradation model is given by:

$$\gamma_i(T;t) = Y_i(T;t) - \hat{Y}(T;t) = \delta_i \cdot \left(\hat{Y}(T;t) - 1\right) + \pi_i(t).$$

Here δ_i represents a random cell-specific proportional effect (i^{th} cell) and $\pi_i(t)$ represents the effects of measurement error on $Y_i(X;t) = \frac{R_{true}(i,t) + \varepsilon_i(t)}{R_{true}(i,0) + \varepsilon_i(0)}$,

where $R_{true}(i,t)$ is the unknown (but true) value of the resistance of the i^{th} cell at time t, and $\varepsilon_i(t)$ is the specific unknown error associated with that measurement. Thus, $\pi_i(t) = \frac{R_{true}(i,t) + \varepsilon_i(t)}{R_{true}(i,0) + \varepsilon_i(0)} - \frac{R_{true}(i,t)}{R_{true}(i,0)}$. If we assume that the measurement errors are independent with variance σ_ε^2, then the variance of $\pi_i(t)$ is approximately $2 \cdot \sigma_\varepsilon^2$. Furthermore, if we denote the variance of δ_i by σ_δ^2, then

$$Var(Y_i(X;t)) = Var(\gamma_i(X;t)) \approx \sigma_\delta^2 \cdot \left(\hat{Y}(X;t) - 1\right)^2 + 2 \cdot \sigma_\varepsilon^2.$$

Thus, the variability of the cells is expected to increase as the expected level of degradation increases. Figure III-16 (produced by the software) shows the results of applying the error model to the experimental data. The high level of scatter about the robust regression line is consistent with the statistical variation of the variance based on sparse data. The estimated error model parameters are $\hat{\sigma}_\delta^2 = 1.6\text{x}10^{-3}$ and $\hat{\sigma}_\varepsilon^2 = 2.4\text{x}10^{-4}$, respectively.

***Monte Carlo Simulations (Bloom, Thomas)* -** The degradation and error models are used as the basis for conducting Monte Carlo simulations to assess uncertainty. In addition, candidate experiments (specified by test duration, RPT frequency, experimental conditions, level of measurement error, and number of cells per condition) can be examined for viability as a core matrix. For each hypothetical experiment, a large number of independent simulation trials are performed. For each trial, a set of simulated experimental data are generated. Using each set of simulated data, model parameters and average cell life are estimated. The set of simulations provides a distribution of estimated average cell life. Figure III-17 illustrates the uncertainty in cell life (for the 7Ah cells) obtained by using the software.

From these simulations, the average cell life is estimated to be 11 years and the 95% lower and upper confidence limits for cell life are 9.7 and 13.3 years, respectively.

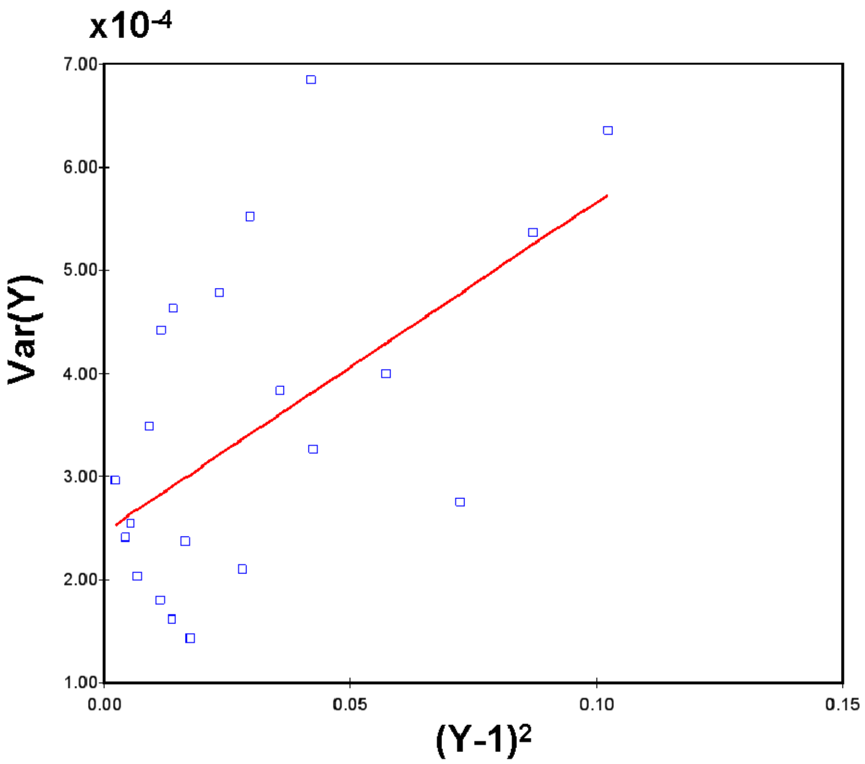

Figure III-16. Error model fit. The variance of the data at a given temperature and time is plotted versus the square of the resistance rise as predicted by the model at the same temperature and time. The line is a linear fit of the data whose slope is σ_δ^2 and whose intercept is $2\sigma_\varepsilon^2$.

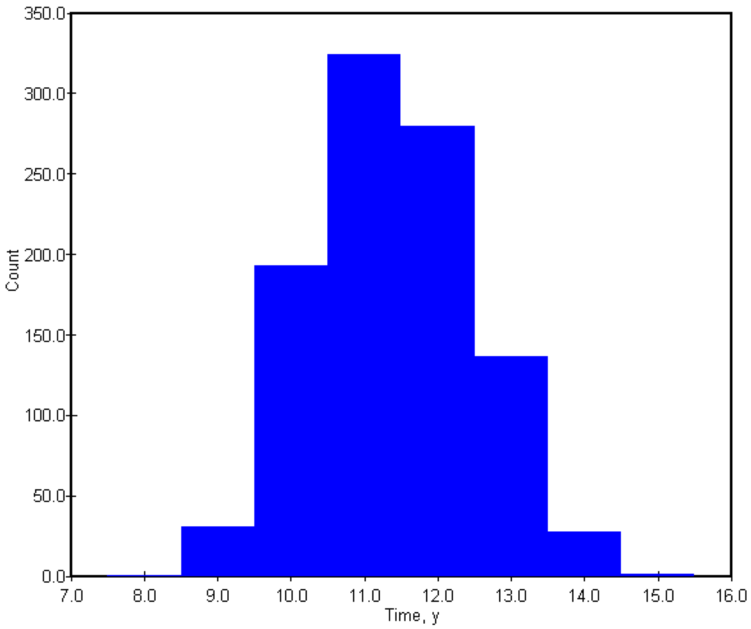

Figure III-17. Distribution of estimated average cell life obtained via the Monte Carlo simulations contained in the software package.

Data Analysis Software **-** The mathematics, described in the previous sections, has been implemented in a computer program. The program features an interface which guides the user through the data analyses and modeling. The program assumes a life model equation is provided and that it can be linearized. Estimation of model parameters (e.g., β_0, β_1, and ρ) was accomplished by using a *robust linear regression* procedure[8] that is nearly insensitive to anomalous data.

III.B.5 Aging & Thermal Characteristics of Cathode Materials

Simultaneous Surface/Bulk Monitoring (Yang) **-** The BNL team has developed an *in-situ* soft XAS technique, which allows the monitoring of oxidation states of the cathode materials at both surface and bulk simultaneously during heating. Using this new technique on a Gen3 cathode at 100% SOC, the oxidation state of nickel at the surface probed by the partial electron yield (PEY) is quite different than in the bulk probed by the fluorescence (FY) modes during heating. As shown in Figure III-18 for the Ni L-edge spectra, the reduction of Ni^{4+} ions to Ni^{3+} at the surface was clearly observed indicating that the surface of the electrode is decomposed at much lower temperature than the bulk. In contrast, no such effects were observed at Co and Mn L-edges.

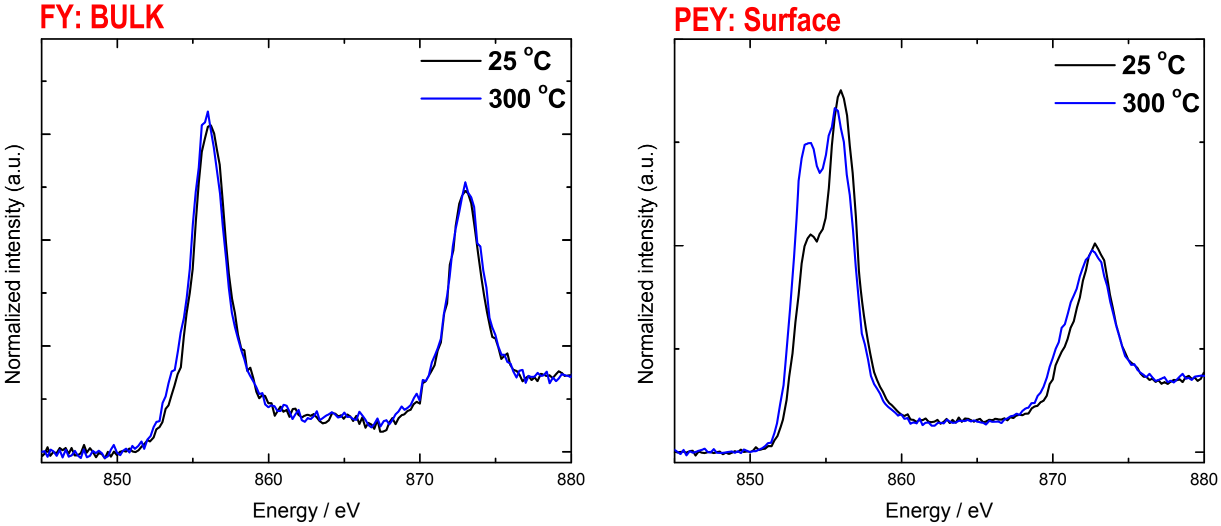

Figure III-18. Ni L-edge XAS for $Li_{1-x}Co_{1/3}Ni_{1/3}Mn_{1/3}O_2$ cathode at 100% SOC in bulk and at surface.

Cathode Material Thermal Instabilities (Yang) **-** Using the time resolved XRD technique developed at BNL, this group has discovered that the thermal decomposition of nickel based cathode materials is accelerated by electrolyte and that a Ni_2O_3 intermediate structure is a good indicator for the poor thermal stability of the cathode, which is responsible to the thermal run away of the cell. It was found that for the uncoated $Li_{0.33}Ni_{1-x}Co_xO_2$ (100% SOC) material heated with electrolyte, thermal decomposition occurred ~240°C and the formation of Ni_2O_3 was observed. At the end of heating at 450°C, the formation of NiO was clearly observed. In contrast, when the same sample was heated without electrolyte, the thermal decomposition occurred at much higher temperature. Neither the Ni_2O_3 phase nor the NiO phase was observed.

If this model of electrolyte accelerated thermal decomposition is valid, a surface coating which partially isolates the cathode from the electrolyte will improve the thermal stability. The results

---

[8] P.W. Holland and R. E. Welsch, “Robust Regression Using Iteratively Reweighted Least-Squares,” Communications in Statistics: Theory and Methods, A6, 1977, pp. 813-827.

shown in Figure III-19 provide strong support for this interpretation. It can be seen that the thermal decomposition indicated by the formations of Ni_2O_3 at about 240°C and NiO at about 450°C observed for the uncoated sample are both suppressed in the MgO coated sample.

***Mn Spinel Thermal Stability (Yang)* -** In collaborating with LG Chemical in Korea (through a CRADA), BNL has performed *in-situ* time-resolved X-ray diffraction (TRXRD) studies on the fresh, cycled, and stored LG pouch cells using $LiMn_2O_4$ based cathode to correlate the structural changes of the cathode and the performance deterioration due to cycling and storage. The phase separation of cubic II from cubic-I was observed at a 4C rate for both cycled and high temperature stored cells, indicating performance deterioration, especially at high rate cycling. However, as shown in Figure III-20, the phase separation of cycled cells is much more severe than the stored cells, although the capacity fading of them are almost the same. These results indicate that the capacity fading due to cycling is originated from the bulk structure damages during cycling, while that due to high temperature storage is related more closely to the surface problem.

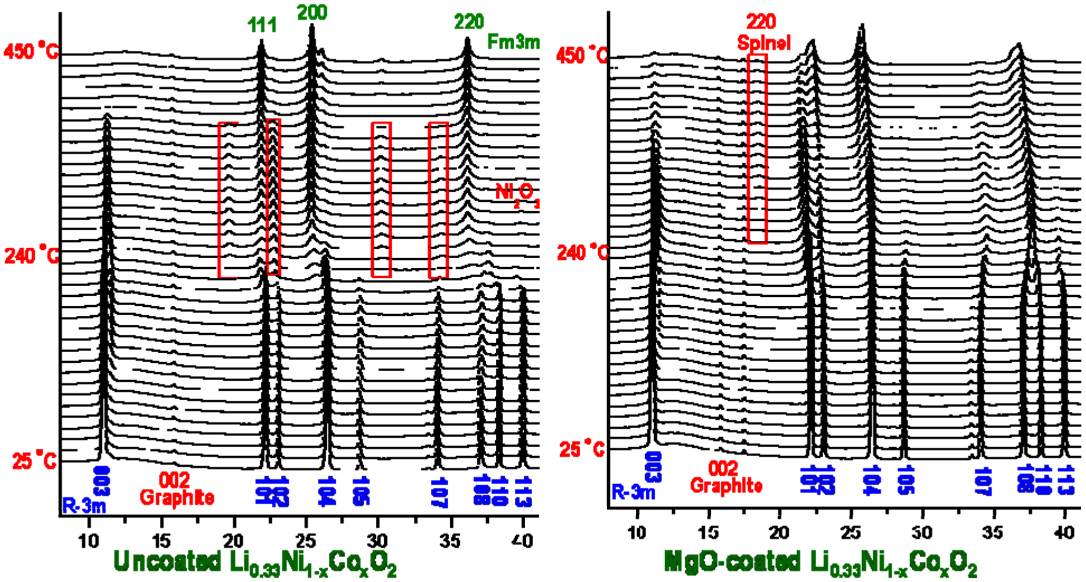

Figure III-19. Time resolved *in-situ* XRD spectra of uncoated and MgO coated fully charged $Li_{0.33}Ni_{1-x}Co_xO_2$ cathodes during heating.

Many collaborators have contributed to the results in this section, such as Dr. D. Abraham, Dr. K. Amine, Dr J. Liu, Dr. Kang, Dr. Thackeray and other scientists at ANL, Prof. Yoshio at Saga University in Japan, Dr. Chen at ITRI in Taiwan, and Prof. H. Li, X. Huang, and L. Chen in China.

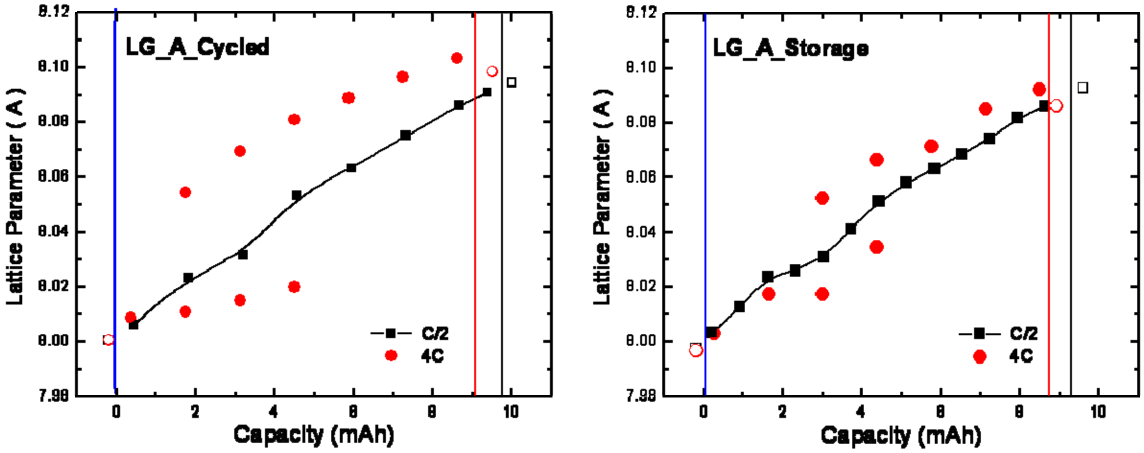

Figure III-20. Lattice parameters calculated from the Time resolved XRD data.

III.C Understand and Enhance Low-Temperature Performance

Objectives

- Thoroughly characterize the Gen3 cell chemistry at low temperatures, including the power loss during high-current pulse discharge and possible Li plating during charging.
- Understand factors that limit low-temperature performance and identify approaches to enhance that performance.
- Develop models of low-temperature electrolyte and cell behavior.

Approach

- Use *in-situ* and *ex-situ* diagnostics, including EIS, FTIR, XRD and modeling to aid in identifying sources of the problem.
- Investigate new electrolytes and salts, and anodes with varying surface areas, and understand their role in modifying low temperature performance.
- Identify methods for enhancing low-temperature performance and evaluate them.
- Use electrochemical microcalorimetry to quantify any lithium deposition on the graphite in Li-ion cells at low temperatures.

Accomplishments/Findings

- Higher surface area carbons decrease both low and room temperature impedance, but do not address the issue of the large ratio of low temperature to room temperature impedance.
- Various current HPPC tests established that impedance response at low temperature is dominated by Butler-Volmer kinetics and not diffusion.
- Early results of three ketone-based solvents showed outstanding rate capability at room temperature and a performance at -30°C that was similar to Gen2 electrolyte.
- Preliminary nuclear magnetic resonance (NMR) studies demonstrated a transition in solvent-salt coordination near 0°C.
- Initial calculations and experiments indicate that Li transport in graphite is relatively poor at low temperature, but appear good enough to prevent lithium plating.

- Using electrochemical microcalorimetry, no lithium plating was observed in Gen3 button cells at temperatures down to 0°C, which agrees with low-temperature cycling studies conducted last year.
- The capability to characterize and optimize mixed-salt (binary) systems was added to the Advanced Electrolyte Model (AEM) in 2007.
- The AEM was used to investigate mono-fluoroethylene carbonates (mFEC) and their effect on electrolyte properties.

Future Studies

- Understand and modify interface, investigate additives (vinyl ethylene carbonate (VEC), vinylene carbonate (VC), vinyl propionate (VP), *etc.*).
- Continue to investigate new electrolytes, including
  - Oxide-free electrolytes
  - Carbonate-free solvents
  - Mixed-salt systems and fluorinated carbonate electrolytes (FEC:EC:EMC)
  - Supporting electrolytes
    - $(Bu)_4NPF_6$, $(Bu)_4PPF_6$, $(Et)_4NPF_6$, $(CH_3)_4NPF_6$, NH_4PF_6
    - Cs_2CO_3 *(cesium doesn't intercalate into graphite)*
- Perform *in-situ* XRD on Gen3 and $LiFePO_4$ cathode materials at low temperatures.
- Employ "solid solvate detection" as a standard screening option.
- Complete assembly of negative electrodes which will produce higher positive-to-negative capacity ratios than the Gen3 technology.
  - Studies conducted with these cells should firmly establish the technique's sensitivity to quantifying lithium plating at low temperatures.
  - If needed, larger area cells could be used to improve the technique's sensitivity to lithium plating.
  - Currently using button cells (Area = 1.6 cm^2).
- Design new experiments that will confirm root causes of diminished cell performance at low temperatures.
- Continue to explore the possibility of Li plating at low temperature using micro-calorimetry.

III.C.1 Introduction

This subsection provides highlights and progress on understanding the factors that limit low-temperature performance of high-power Li-ion cells and identifying methods to enhance that performance via cell material and component changes. The limitations include possible Li plating on the negative electrode during charging and a major loss of discharge power ≤-10°C. The latter cannot be explained by the conductivity of the electrolyte. Efforts this year involved further studies to thoroughly characterize these limitations in the Gen3 chemistry, evaluating alternative electrolyte salts and solvents, and developing low-temperature electrolyte and cell transport models. Table III-7 provides a summary of how the participating DOE laboratories contribute to this focus area.

Table III-7. Summary of how the DOE laboratories and the Army Research Laboratory contribute to the "Low-Temperature Performance" focus area.

	ANL	BNL	INL	LBNL	SNL
Low-Temperature Performance Characterization	X				
Low-Temperature Electrolyte Modeling			X		
Low-Temperature Cell Performance Modeling	X				

III.C.2 Low-Temperature Performance Characterization

Anodes with Varying Surface Areas (Jansen) **-** Previous efforts have shown that the poor low temperature performance of Li-ion cells is not significantly affected by the active material, electrolyte viscosity and molarity, or presence of binder. The issue at low temperature is essentially the ratio of low temperature to room temperature impedance. With this ratio too small, one is forced to oversize the system to ensure that sufficient power is available at low temperature. Thus the search here is for materials that will reduce the ratio of low temperature to room temperature impedance.

One area that was explored in this year's effort is the effect of surface area. Three graphite materials from ConocoPhillips were used that are well suited for surface area studies. The nominal particle sizes (D50) are 5, 8, and 15μm. They each underwent a similar processing history, which resulted in nearly identical morphology. Cells were made with electrode areas of 32 cm² with a Gen3 electrode from Enerland as the positive and 1.2 M $LiPF_6$ in EC:EMC (3:7 by wt) as the electrolyte. Capacity utilization and HPPC tests were performed between 30 and -30°C.

ConocoPhillips' graphites performed well and had an impedance response very similar to the Gen3 graphite (MCMB-10). A closer examination was made of the impedance at -30°C and is shown in Figure III-21. The impedance does decrease as the surface area is increased; doubling the surface area from 1 to 2 m²/g resulted in a 15% decrease in ASI. Unfortunately, the impedance at -30°C is still ~25 times higher than the room temperature value of 20 to 30Ωcm². Higher surface area will not by itself solve the low temperature problem. It does improve the low temperature performance by providing more surface area for the electrochemical reactions to take place, but the power robbing mechanism still dominates – just over a larger surface. High surface area particles

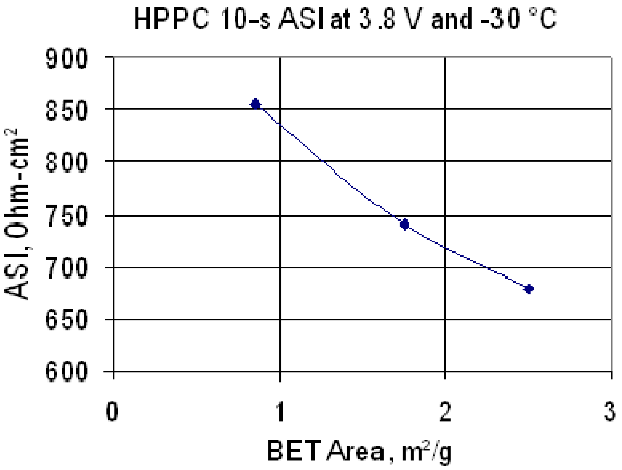

Figure III-21. HPPC ASI of three ConocoPhillips' graphites with varying surface area at -30°C.

could play a small role in solving the problem, provided they do not cause abuse tolerance concerns at higher temperature or excessive irreversible capacity loss during SEI formation.

***Butler-Volmer Kinetics (Jansen)* -** The influence of pulse current level on impedance values during the HPPC test was investigated for the Gen2 system. The Gen2 system was used because it is well characterized and has the best low temperature performance of the systems investigated by the ATD program to date. At least five HPPC tests were performed at each temperature (30, 0, -10, -20, and -30°C) at discharge pulses that ranged from 19 to 0.025 mA/cm². Current level ranges were decreased as the temperature decreased. None of the charge or discharge pulses exceeded the voltage window of 2.9 to 4.3 V.

Interesting results were obtained from this study, which are summarized in Figure III-22. The most surprising observation was the dramatic influence that current level had on impedance at temperatures below -10°C, especially at -30°C. The impedance dropped from 680Ω-cm² at near equilibrium conditions (very low current) to 300Ω -cm² at 2.5 mA/cm², which is a high current level for this temperature. In addition, the current-overpotential response was nearly symmetric, *i.e.,* charge and discharge resistance rise at low temperature can be considered identical. This large decrease in impedance is not due to I²R heating because of the large thermal mass (2.5 kg) of the stainless fixture and the planar electrode configuration. A decreasing resistance with increasing current may seem counter-intuitive, but this phenomenon is fully explained by Butler-Volmer kinetics. Limiting currents were not observed in these studies, which is further proof that diffusion effects are not responsible for the low temperature power loss. Impedance response at low temperature is dominated by Butler-Volmer kinetics and not diffusion.

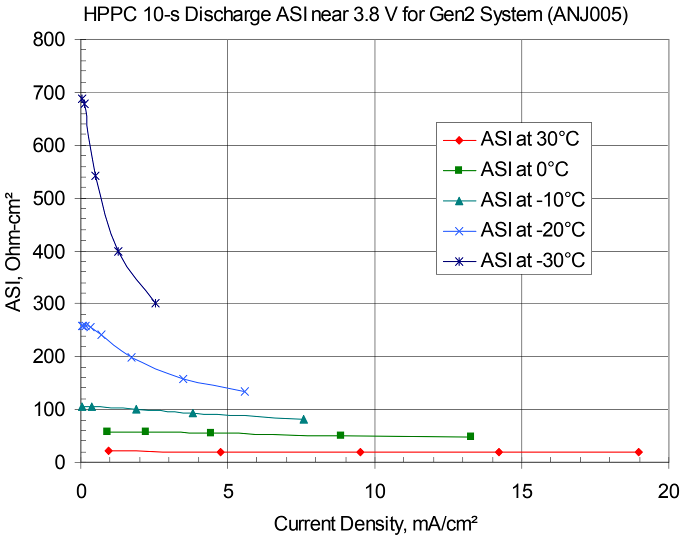

Figure III-22. ASI as a function of pulse current level for the Gen2 system with temperature as a parameter.

***Carbonate-Free Solvents (Vaughey)* -** Efforts were initiated this year to explore novel carbonate-free solvent systems in 2032-sized coin cells. Many non-traditional solvents are inappropriate in Li-ion batteries because they are readily oxidized or reduced at the positive or negative electrodes, respectively. To help alleviate the concern over oxidation at the negative electrode, the titanium spinel $Li_4Ti_5O_{12}$ was used because it cycles at 1.55 V above Li. A variety of cyclic and linear solvents was evaluated – alone, combined, with additives, and with various salts.

The solvents studied are generally classified as: sulfide containing, nitrogen containing, sulfone groups, esters, and ketones. Evaluations were based on salt solubility, electrochemical stability, and probability of side reactions. In general, sulfide-based solvents tended to have lower salt solubility and nitrogen-containing solvents tended to be unstable on charging (3.8-4.1V) or in the case of some di-nitrogen solvents they polymerized or gelled on addition of salt. Ketones in general have high partial negative charge compared to other organic solvents, but most ketone solvents failed on addition of $LiPF_6$. Ketones are susceptible to attack by Lewis acids (LA) to form a stable acyllium ion and a radical. Substitution of a non-LA salt, e.g. Lithium bis(oxolato)borate (LiBOB) or $Li_2B_{12}F_{12}$, eliminated this failure pathway and allowed for a wider variety of solvents to be evaluated. Early results of three ketones showed outstanding rate capability at room temperature and a performance at -30°C that was similar to Gen2 electrolyte. These results will be explored further in larger cell formats.

Various spectroscopic techniques (including NMR) and theoretical studies have indicated that the typical coordination of Li in the electrolyte solution is tetrahedral. In solid form (single crystals), the lithium has been found to be 6-coordinate (except with EC). In an attempt to understand the solvent from the lithium's point of view, variable temperature ^7Li NMR studies were performed on the electrolytes. These preliminary NMR studies demonstrated a transition in solvent-salt coordination near 0°C. Solvents were identified with minimal change in solvent sphere, but these solvents did not significantly lower the resistance at low temperature.

III.C.3 Low Temperature Electrolyte Modeling

The advanced electrolyte model (AEM) was utilized to characterize and optimize candidate electrolyte systems with emphasis on low-temperature performance. Targets achieved in FY 2007 include: determination of Li ion desolvation time and energy, modeling binary salt systems, modeling fluorinated solvent systems, and developing infrastructure for applying the AEM to cell-level transport modeling (e.g., double layer (DL) regions).

***Kinetic and Energy Costs of Lithium Desolvation (Gering)* -** The AEM can now estimate the thermodynamic and kinetic requirements for lithium desolvation, an important aspect of interfacial transport in Li-ion batteries. This capability is made possible due the AEM's treatment of ion solvation, allowing computation of quantities such as the thermodynamic solvation numbers for lithium and the anion, net and ligand-wise binding energy between solvent and lithium, and the net and ligand-wise desolvation times per lithium ion. The approach is self-consistent, based on fundamental theoretical principles, and produces predicted values that are in good agreement with those of published literature. An example is given in Figure III-23, wherein the predicted net desolvation time and energy are shown for the Gen2 electrolyte (3EC:7EMC + $LiPF_6$).

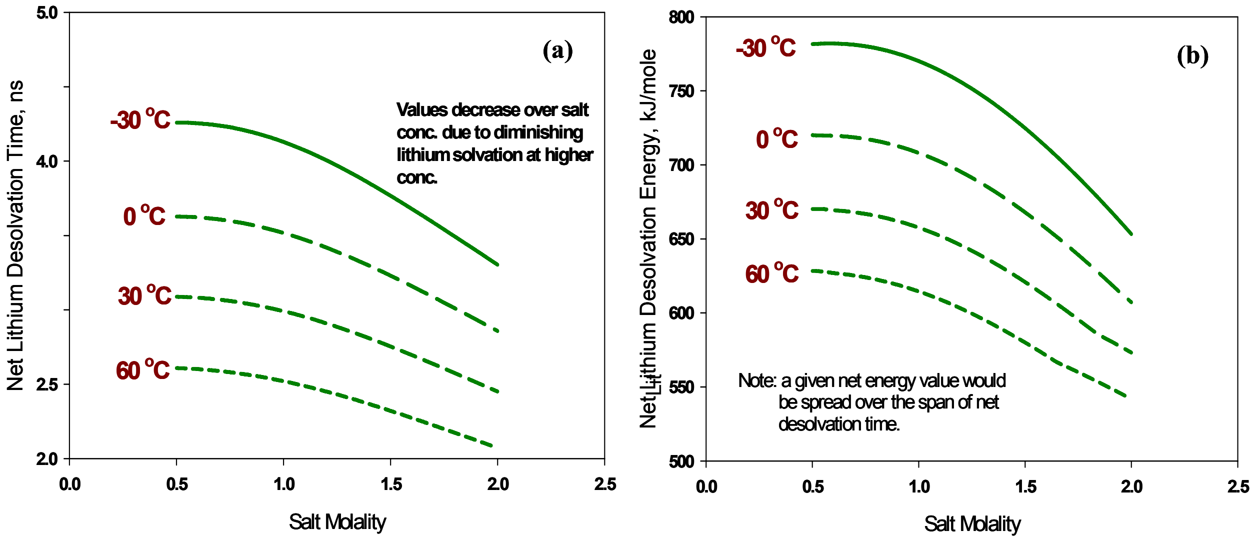

Figure III-23. Net requirements for (a) lithium desolvation time, and (b) lithium desolvation energy, as determined from kinetic and thermodynamic analyses via the AEM.

An Arrhenius analysis of a lumped parameter for lithium desolvation indicates that the activation energy tied to step-wise lithium desolvation is on average between 25-35 kJ/mole, which is roughly one-third to one-half the activation barrier published by other investigators for charge transfer resistance in Li-ion cells. Although AEM values serve as an important baseline, the local cell environment (e.g., SEI, DL regions) will doubtless complicate the desolvation process, increasing the net time and energy price tags.

***Mixed Salt Systems* -** The capability to characterize and optimize mixed-salt (binary) systems was added to the AEM in 2007. Benefits in transport properties and SEI formation can be realized by using mixed salt electrolytes, just as mixed solvents are necessary for contemporary electrolyte systems. The approach is based on molar averaging of molecular-scale quantities. This new capability opens up a new frontier in electrolyte development and screening. For example, taking six of the more common salts in the AEM library, pair combinations produce an additional 15 salt combinations that can be investigated for ATD applications. An example of AEM output is given in Figure III-24.

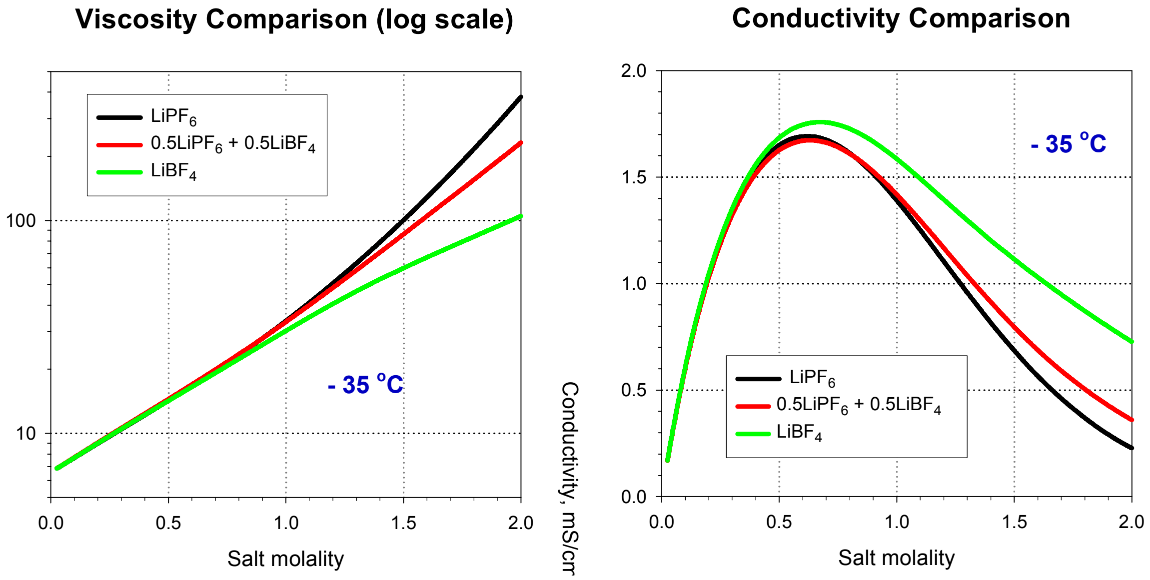

Figure III-24. Comparison of AEM results for viscosity and conductivity of single and mixed-salt electrolytes having gamma-butyrolactone as the solvent.

***Electrolytes with Fluorinated Solvents* -** AEM simulations were used to investigate the effects of the additive mono-fluoroethylene carbonate (mFEC) on electrolyte properties. Results indicate that mFEC provides advantages in lowered solvent interactions with lithium, which is important regarding the (potentially problematic) lithium desolvation step of lithium transport through interfacial regions; hence, mFEC should reduce desolvation contributions to charge transfer resistance. However, mFEC doesn't appear to provide improvements in bulk transport properties (viscosity, conductivity, etc.). The table below summarizes an AEM comparison of mFEC vs. EC regarding solvation related properties, and shows the advantage of using mFEC.

System	Lithium Solvation Number	Solvent-Lithium Binding Energy (kJ/mole)	Activation Energy for lithium desolvation (kJ/mole)
EC + 1 M $LiPF_6$	3.90	477.5	30.0
mFEC + 1 M $LiPF_6$	3.43	426.0	24.5

***Key Issues in Transport Modeling* -** In FY 2007, the AEM was modified to perform transport calculations, using its capability of predicting electrolyte behavior in the dynamic cell environment. A new capability was developed wherein the performance of Dynamic Charged Interfacial Regions (DCIR) or "double-layers" can be assessed. This capability makes use of the accurate property predictions of the AEM, which in this case must cover cases of non-electroneutrality and concentration polarization. This is aimed at understanding multiple issues of battery performance. One feature of the DCIR model is that it accounts for thermodynamic and kinetic requirements of lithium desolvation, an important aspect of interfacial transport in Li-ion batteries that is linked to charge transfer resistance. The DCIR model covers all regions in Li-ion batteries that are in contact with electrolyte, and is in final development and validation.

Early results indicate that local electrolyte properties change in the battery environment under pulse conditions, due to the reallocation of electrolyte species and solvent. This reallocation can cause regions of reduced conductivity which might become limiting at low temperature operation or at high pulse rates. The AEM is being developed to provide accurate model electrolyte properties without the need for simplifying assumptions such as property averaging and local electroneutrality. Such oversimplifications can obscure the root causes of performance limitations tied to the electrolyte.

III.C.4 Low Temperature Cell Performance Modeling

Lithium Plating (Dees) **-** The emphasis of the low temperature electrochemical cell modeling effort this year was on lithium plating on graphitic anodes during charging. A combined modeling and experimental effort is being conducted to fully quantify lithium transport in the graphitic active material as a function of temperature. Galvanostatic Intermittent Titration Technique (GITT) studies were conducted on the Gen3 negative electrode from room temperature to -30°C. Further, the GITT electrochemical model was modified and utilized to simulate the lithium diffusion in the Gen3 negative electrode. Alternative modeling approaches were examined to efficiently track the lithium diffusion in the active material, including phase transitions. Finally, electrochemical microcalorimetry was explored as an alternative technique to quantify the actual lithium deposition rate on the graphite in Li-ion cells at low temperatures.

The GITT studies were conducted on Gen3 graphitic negative electrode pouch cells with a reference electrode and a lithium counter electrode. Low current level 10 minute pulses followed by a rest period were applied to the cell over the negative electrode's full SOC range. An electrochemical model developed to simulate Li-ion cell phenomena was utilized to interpret the GITT results.

The general methodology for the electrochemical model follows the work of Professor Newman at Berkeley and has been described in previous reports. While all the detailed interfacial phenomena were not needed for the GITT version of the electrochemical model, the EIS and HPPC versions include Li diffusion, migration, and reaction in the SEI. The GITT version, originally developed to examine Li transport in the oxide active material of the Gen2 positive electrode, was modified this year to include the phase change phenomena occurring in the graphitic active material.

The open circuit voltage curve (i.e. electrode voltage vs. SOC) for the graphitic active material is made up of a series of steps where each step corresponds to a change of phase with the highest lithium loading being the LiC_6 phase, or stage. The flat portions of the curve are considered two phase regions and in the steep portions of the curve single phase diffusion of Li is occurring. Typical room temperature GITT results from the single and two phase regions are given in Figure III-25. The most notable difference between the results is that the two phase region is much slower to relax than the single phase region. The slow relaxation time made it necessary to account for the two phase reaction in the electrochemical model in that region. The GITT electrochemical model simulation for each case is also shown for comparison. The single phase region GITT results were useful for determining the lithium diffusion coefficient for that phase with the electrochemical model and the two phase GITT results provided the phase change reaction rates.

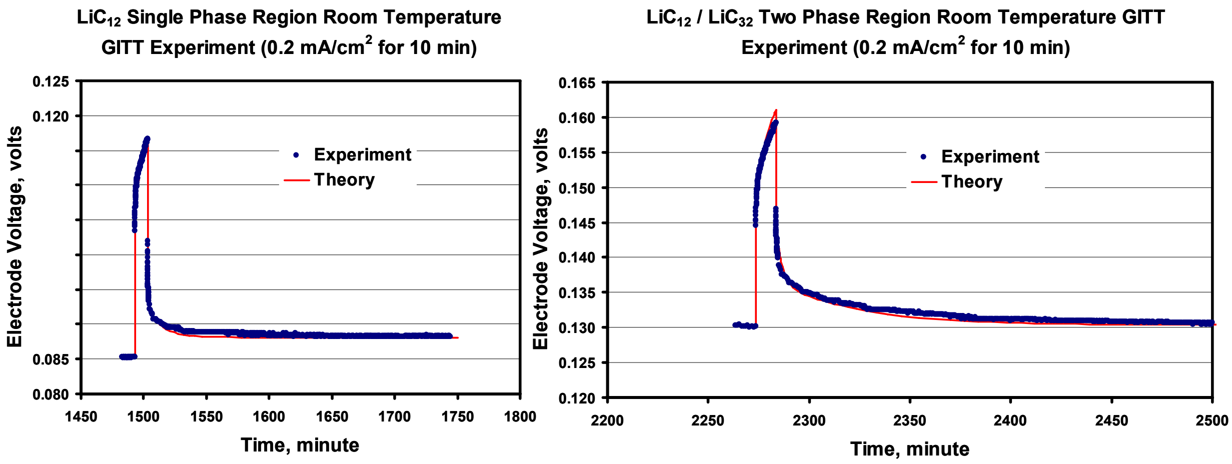

LiC_{12} Single Phase Region Room Temperature GITT Experiment (0.2 mA/cm^2 for 10 min)

LiC_{12} / LiC_{32} Two Phase Region Room Temperature GITT Experiment (0.2 mA/cm^2 for 10 min)

Figure III-25. Comparison of typical Gen3 negative electrode GITT experimental results for lithium diffusion in the graphitic active material single and two phase regions to electrochemical model simulations.

The Li diffusion coefficient for the graphitic active material is considerably lower than those measured for the oxide positive active materials (10^{-13} for Gen3 graphite vs. 10^{-10} – 10^{-11} cm^2/s for Gen2 & 3 oxides at room temperature), but some of that difference is offset by the graphite's higher surface area (0.4 vs. 2 m^2/g for Gen3 materials). Also, the diffusion coefficient for the Li diffusion through the graphite is a relatively strong function of temperature (activation energy ~8 Kcal/mole). These two factors combine to create relatively poor transport conditions for the Li into the graphite at low temperatures. However, initial calculations indicate that the Li transport rates are good enough to prevent lithium plating. This conclusion could change as improvements in the low temperature interfacial impedance are made.

Electrochemical microcalorimetry was explored as a technique to quantify the lithium deposition rate on the graphite in Li-ion cells at low temperatures. Oxidation of even small amounts of metallic lithium on the surface of the graphite during plating should be easily detected from the cell's heat signature. No lithium plating was observed in Gen3 button cells at temperatures down to 0°C, which agrees with low-temperature cycling studies conducted last year at Argonne. However, these studies firmly established the technique's sensitivity and utility to quantifying lithium plating at low temperatures. Future studies will be focus on lower temperatures and using cells with higher negative-to-positive capacity ratios. The possibility of improving the technique's sensitivity using larger cells (i.e. higher area) may also be examined if needed.

III.D Understand and Enhance Abuse Tolerance

Objectives

- Understand cell component roles in the abuse characteristics of high-power Li-ion cells.
- Identify and develop more stable cell components that enhance the inherent abuse tolerance of Li-Ion cells.
- Validate inherent abuse tolerance enhancements at the cell level and quantify them.

Approach

- Use accelerated rate calorimetry (ARC) and differential scanning calorimetry (DSC) to identify the role of each cell component on the thermal characteristics of the Gen3 and other cell chemistries.
- Identify methods to enhance overcharge and thermal abuse tolerance and evaluate them in 18650 cells.
- Fabricate 18650 cells with the most promising cell components and additives to validate and quantify respective enhancements using ARC and thermal block tests.
- Study overcharge abuse of different chemistries in 18650 cells.
- Assess the role of alternative separators on the abuse tolerance characteristics of cells with a given cell chemistry.

Accomplishments/Findings

- Carbon-based anodes were found to be capable of generating sufficient heat to cause cell failure. Thus abuse tolerance improvements should involve both anode and cathode materials.
- Lower surface area carbons were found to generate less heat under thermal ramp tests, supporting the theory that breakdown and re-formation of the carbon SEI is a significant source of heat in cells that employ high surface area carbonaceous anodes.
- VEC and LiBoB additives that form more stable SEI layer leads an increase in the onset temperature of the SEI breakdown and a reduction of the overall accumulated heat.
- Anodes that do not form an SEI, such as LTO, were shown to generate much less heat during thermal ramp abuse tests.
- A new overcharge redox-shuttle was shown to provide reliable overcharge protection at ~4.3V vs. Li, and to improve the capacity retention of Li-ion batteries during normal operation condition.
- ARC thermal runaway measurements have shown reduced thermal runaway energies for electrolytes using the EC:PC:DMC (1:1:3) solvent compared to EC:EMC (3:7) with $LiPF_6$ salt. The effect of the EC:PC:DMC was greatest for the least reactive oxide cathodes.
- Initial ARC measurements were made on cells with stabilizing additive 3% $LiC_2O_4BF_2$ that showed reduction in thermal runaway heating rates compared to standard electrolyte.
- Demonstrated that hydrogen generation is a precursor indicator for overcharge failure.
- Demonstrated improved abuse tolerance in 18650 cell configuration.
    - Improved cathode material using stabilized cathode chemistry.
    - Electrolyte composition and additives can reduce peak reactions.

Future Studies

- Investigate mitigation techniques associated with carbon-anode thermal response
- Further characterize of the abuse tolerance of LTO and other alternate anode materials
- Further characterize and investigate the longevity and stability of the PFPTFBB overcharge shuttle.
- Further develop the *in-situ* soft XAS technique for thermal stability studies. Apply the techniques to different type of cathodes such as Gen3, spinel, and $LiFePO_4$.

III.D.1 Introduction

This subsection provides highlights and progress on understanding the factors that limit the inherent abuse tolerance of high-power Li-ion cell chemistries and using this knowledge to identify alternative materials and cell components that enhance their abuse tolerance. The cell chemistries used in conventional Li-ion cells are thermodynamically unstable. During the initial charge/discharge cycle, passivation films are formed on the active surfaces of the electrodes which stabilize the system. Detailed studies have been performed on the individual components of the Gen3 cell and the cell chemistry has been thoroughly studied in terms of its thermal and overcharge abuse characteristics. Two new efforts in 2007 were to characterize and understand the role that carbon-based anodes play in thermal runaway of Li-ion cells, and to begin investigating overcharge shuttles that might play a role in enhancing the abuse tolerance of higher energy cells to overcharge. Table III-8 provides a summary of how the DOE laboratories contribute to this focus area.

Table III-8. Summary of how the DOE laboratories contribute to the “Abuse Tolerance” focus area.

	ANL	BNL	INL	LBNL	SNL
Thermal Abuse Studies	X				X
Overcharge Tests with Advanced Materials	X				X

III.D.2 Thermal Abuse

III.D.2.1 Component-Level Studies

***Anode Contribution to Abuse Tolerance (Amine)* -** A new research area in 2007 was the contribution of carbon-based anodes to thermal runaway in Li-ion cells. Early in the year, a fully charged commercial Li-ion cell containing $LiFePO_4$ and graphite was exposed to an external heat source. The cell generated a significant amount of heat and exploded at 400°C. Olivine is noted for its structural integrity and ability to withstand high heats at high states of charge with no thermal runaway. Further investigation indicated that graphite was the major cause of heat release. Therefore, there was a need to understand the mechanism by which graphite is responsible for such a dramatic heat release from a Li-ion cell.

For this purpose, graphite was investigated by DSC to quantify the heat associated with the decomposition of the SEI layer. Figure III-26 shows the DSC curve of a lithiated MCMB graphite between room temperature and 400°C. As can be seen in this figure, the temperature of the breakdown of the SEI layer occurred slightly below 100°C, after which a significant amount of heat was released. It is believed that this is due to the continuous breakdown and formation of the SEI on the graphite surface up to 170°C. The amount of accumulated heat generated at temperature lower than 170°C is enough (507 J/g) to trigger a thermal runaway inside a cell regardless of the cathode, especially in large batteries with a large number of cells. This result demonstrates that the safety of Li-ion cells should be addressed through both cathode and anode materials.

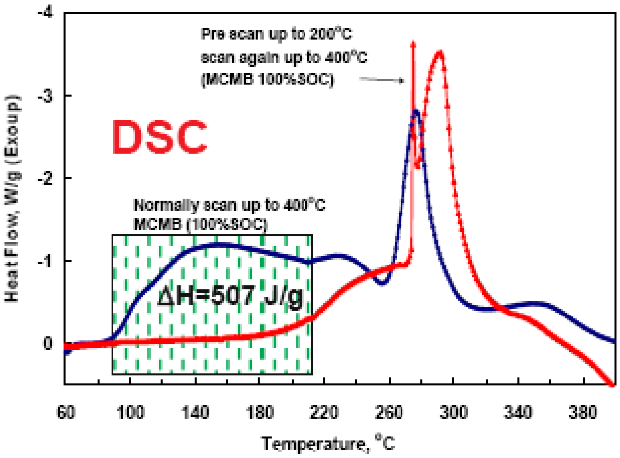

Figure III-26. DSC curves of lithiated graphite before (blue) and after (red) SEI decomposition

If the above theory of anode heat generation is correct, then a carbon with a lower surface area should generate less heat. Figure III-27 shows a comparison of the accumulated heat generated from two types of graphite anodes. The heat from MAG graphite, which has 5.2 m^2/g surface area, was twice that of the MCMB graphite, with 2.2 m^2/g, approximately half the surface area. Therefore lower surface area carbon could result in lower heat caused by the continuous breakdown and formation of the passivation film, and could result in a safer Li-ion battery.

Since the onset temperature of the breakdown of the SEI is dependent on the stability of the SEI itself, selecting electrolyte additives that form stable SEIs at the carbon anode can raise the onset temperature higher and perhaps reduce the accumulated heat. Figure III-28 shows the DSC curve of pristine graphite with a standard electrolyte compared to that of graphite anodes with 1% LiBOB and 1%VEC were added to the electrolyte, respectively. It is clear from the figure that the use of additives that form more stable SEI layers has led to the increase in the onset temperature of the SEI breakdown and the reduction of the overall accumulated heat below 170°C.

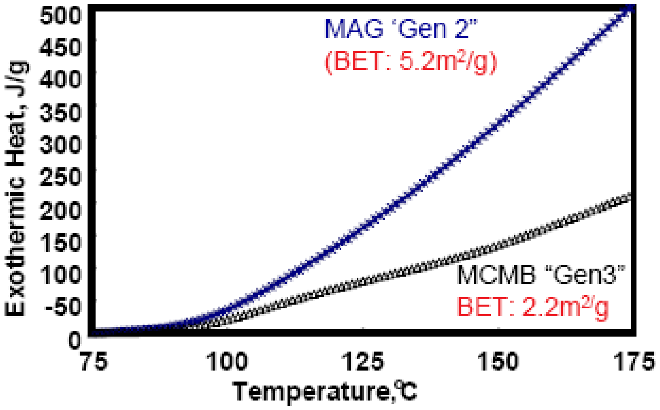

Figure III-27. Accumulated heat curves of two lithiated graphites with different surface areas

ANL also investigated the possible use of alternative anodes. In this context, spinel titanate (LTO), which operates at 1.5 V vs. Li metal, which will not form the SEI film associated with the graphite anode (the reduction of the organic species occurs below 1 V) was investigated. In addition, the issue of lithium plating in Li-ion cells may be resolved because of the high potential of the $Ti^{4+/3+}$ redox couple vs. Li metal. Moreover, unlike graphite, no volume change is expected during the insertion of lithium atoms. Fully lithiated LTO results in the formation of a stable rock-salt type $Li_7Ti_5O_{12}$ material with a zero-strain. Therefore, it was hoped that LTO can provide an electrode system with better safety characteristics than graphite.

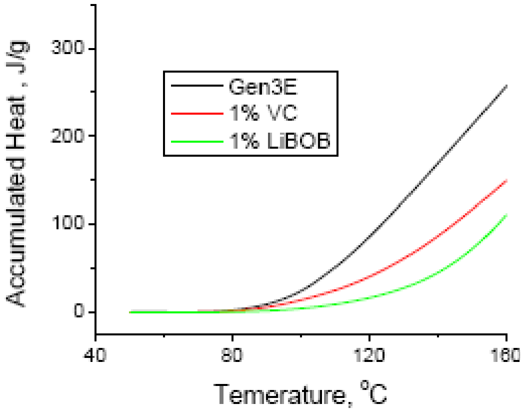

Figure III-28. Effect of electrolyte additives on the heat generated from lithiated graphite.

Figure III-29 shows the isothermal micro-calorimetry (IMC) curves of both $Li_4Ti_5O_{12}$ and MCMB graphite anodes.

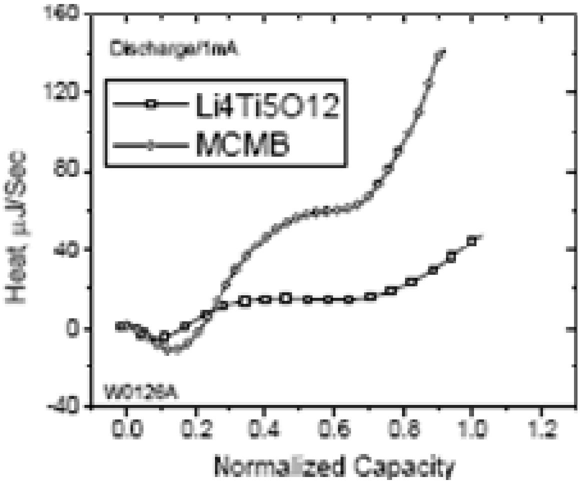

Figure III-29. Comparison of the heat measured by isothermal microcalorimetry during the lithiation process of graphite and $Li_4Ti_5O_{12}$.

Lithiated $Li_4Ti_5O_{12}$ generated much lower heat during the two-phase reaction when compared to the lithiated graphite during which several staging steps with different entropy changes occur leading to significant internal self heat, an order of magnitude higher than that of $Li_4Ti_5O_{12}$. ARC data in Figure III-30 show that the reaction that accompanies the thermal abuse of titanate is much less vigorous than that of graphite.

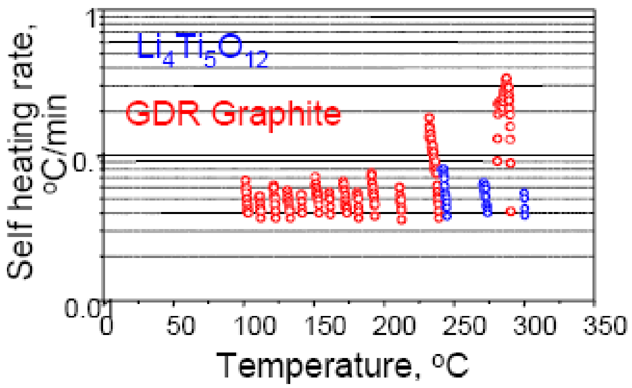

Figure III-30. ARC results of lithiated graphite and lithiated $Li_4Ti_5O_{12}$.

Separator Evaluations (Roth) **-** Separator integrity is critical to the abuse tolerance of Li-ion cells. Loss of separator integrity can lead to internal shorts which can result in immediate and rapid disassembly of the cell with resulting gas release and fire. Separator shutdown of one cell in series connected strings can result in high voltages across that cell that can cause failure of that cell's separator. To characterize them, the shutdown properties of separators soaked in electrolyte were measured using AC impedance as well as measurement of DC voltage breakdown as a function of temperature. The shutdown properties of several commercial separators were compared and their properties in full cells under abuse conditions were also evaluated.

The shutdown property and high temperature integrity of separators from Celgard, Entek, and Tonen are shown in Figure III-31.

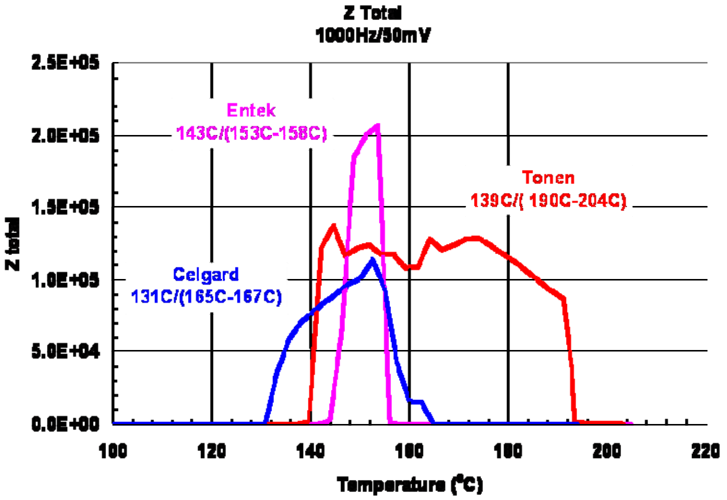

Figure III-31. Separator impedances over temperature range showing shutdown and loss of integrity (Celgard, Entek, and Tonen separators).

Next the separators were tested with an applied voltage of 20V to test their high voltage integrity, results are shown in Figure III-32. As shown, the Tonen separator displays impressive stability, well past 180ºC which is much higher than it's shutdown.

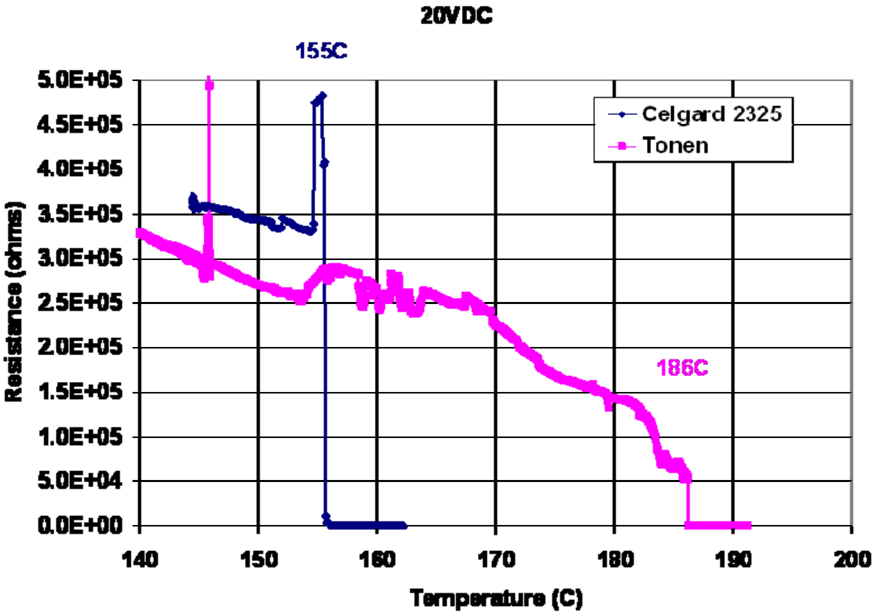

Figure III-32. Separator failure above shutdown with applied 20V.

Figure III-33 shows what may happen when a separator loses high temperature melt integrity, with the cell moving into thermal runaway shortly thereafter.

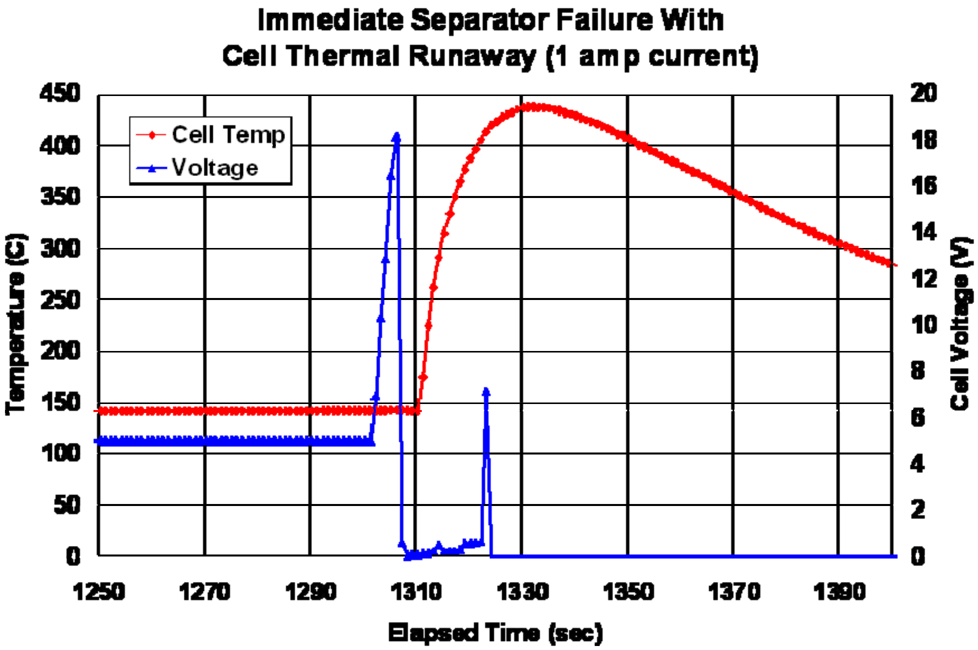

Figure III-33. Immediate 20V Breakdown with Cell Thermal Runaway.

III.D.2.2 Cell-Level Studies (Roth) - The goal of this work is to demonstrate improved abuse tolerance in Li-ion cells based on new electrode materials and additives. Significantly improved abuse tolerance in 18650-size cells (constructed at SNL) was demonstrated using stabilized cathodes with different solvent/salt components. New materials evaluated have included stabilized cathodes, anodes, electrolytes and electrolyte additives. The thermal properties of these materials have been characterized and used to determine the effect on full cell abuse response including heat generation, gas generation, and flammability. Accelerating Rate Calorimetry (ARC) and thermal ramp tests have been used. The major cell materials evaluated were:

- ***Cathode materials***: $LiCoO_2$, $LiNi_{0.85}Co_{0.15}O_2$ (Gen1), $LiNi_{0.8}Co_{0.15}Al_{0.05}O_2$ (Gen2); $LiNi_{1/3}Co_{1/3}Mn_{1/3}O_2$; $Li_{1.1}(Ni_{1/3}Co_{1/3}Mn_{1/3})_{0.9}O_2$ (Gen3), $LiMn_2O_4$ (Spinel), $LiFePO_4$
- ***Anode materials***: MCMB (Gen1 and 3), MAG10 (Gen2), GDR (Gen2)
- ***Electrolytes/salts***: EC:EMC (3:7) 1.2M $LiPF_6$, EC:PC:DMC (1:1:3) 1.2M $LiPF_6$, LiBOB, LiBETI

***ARC Study* -** 18650 cells with nominal capacities between 950 mAh and 1200 mAh were built using these chemistries for subsequent abuse measurements. ARC measurements allowed comparison of the heat generation enthalpies and reaction kinetics as well as the gas evolution profiles. Measurements were performed on full cells and also on cell electrodes removed from fully charged cells and resealed in 18650 cans. These measurements have allowed determination of the relative contributions of the anode and cathode to the full cell heat and gas generation. 1200mAh $LiCoO_2$ –based cells (one of the most common cathode oxides used in the commercial market) were constructed at SNL to provide a baseline for comparison. The main observations from these studies are:

- Cobaltate baseline cells had the lowest thermal runaway onset temperature, highest heating rate and greatest reaction enthalpy compared to the other cathode oxide cells. A steady improvement in thermal response was observed for cathodes with decreasing oxygen generation at high-temperature, from $LiNi_{0.8}Co_{0.15}Al_{0.05}O_2$ (Gen2), to $Li_{1.1}(Ni_{1/3}Co_{1/3}Mn_{1/3})_{0.9}O_2$ (Gen3) to $LiMn_2O_4$. The oxygen loss is a function of the degree of lithiation and is given by:

$$Li_yMO_2 \rightarrow (1+y)Li_{\frac{y}{1+y}}M_{\frac{1}{1+y}}O + \frac{1-y}{2}O_2$$

- ARC thermal runaway measurements (Figure III-34) have shown reduced thermal runaway energies for electrolytes using the EC:PC:DMC (1:1:3) solvent compared to EC:EMC (3:7) with $LiPF_6$ salt.
- The effect of the EC:PC:DMC electrolyte was greatest for the least reactive oxide cathodes. Figure III-35 and Figure III-36 show that the reduced heating rate (compared to EC:EMC electrolyte) was significant for the Gen3 cathode but much less for Gen2. Almost no effect was seen for the most reactive $LiCoO_2$.
- Initial ARC measurements were made on cells with stabilizing additive 3% $LiC_2O_4BF_2$ that showed reduction in thermal runaway heating rates compared to standard electrolyte.

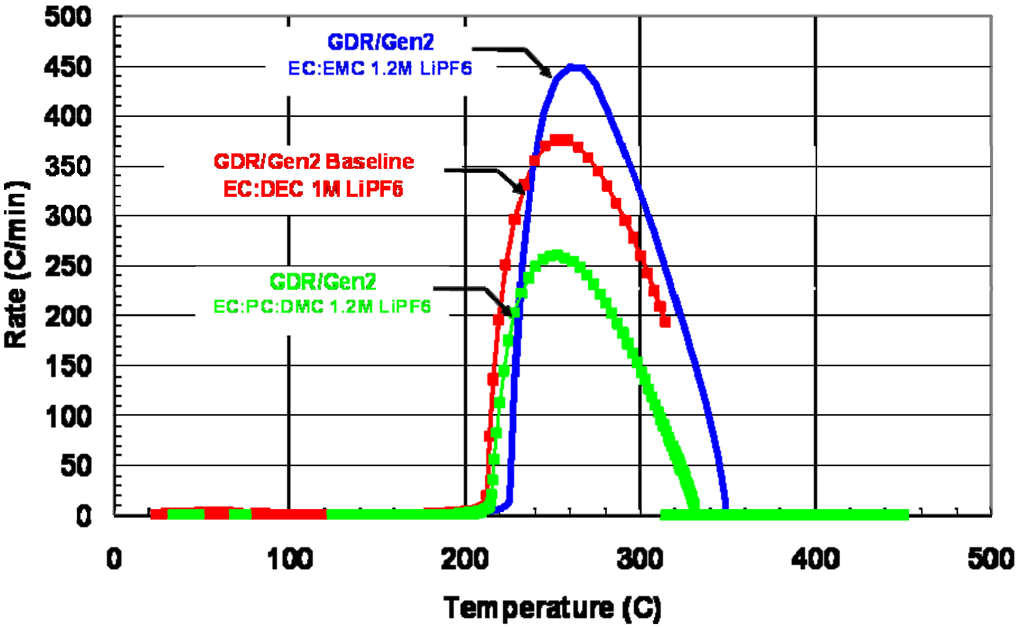

Figure III-34. ARC thermal runaway profiles showing improved thermal response with EC:PC:DMC based electrolytes.

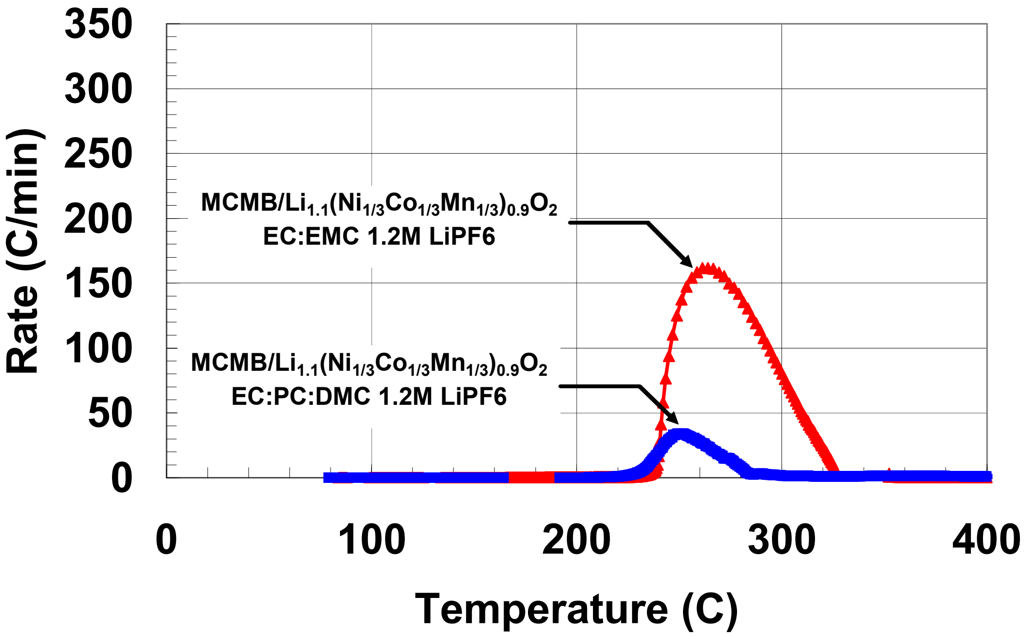

Figure III-35. ARC profile showing significant reduction in heating rate for the less reactive Gen3 cathode material with EC:PC:DMC.

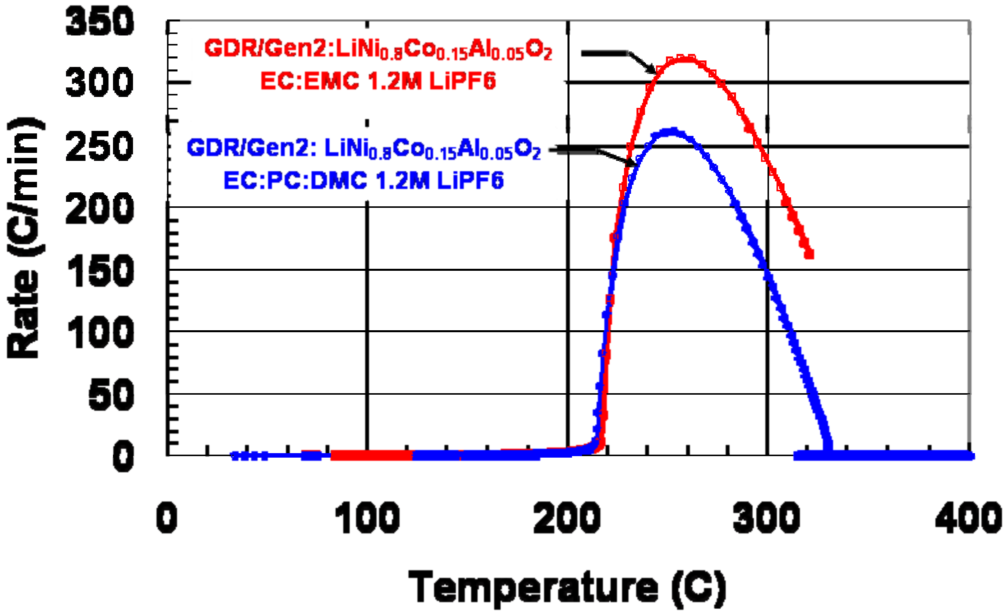

Figure III-36. ARC profile showing less effect of EC:PC:DMC with the more reactive Gen2 oxide cathode.

***Thermal Ramp Response/Flammability* -** The thermal abuse response of these cells and the flammability of the vented gases were measured using a thermal block apparatus developed at SNL. This allows determination of the onset of cell heat generation and also records the flammability of the vented gases in the presence of an external ignition source. Cells were ramped in open air at a rate of 6°C/min until thermal runaway. Comparative measurements of the layered oxides, $LiMn_2O_4$ spinel and $LiFePO_4$ cells were made under identical conditions.

- $LiFePO_4$ cells showed heat generation onset near 220°C followed by a low-rate thermal runaway at 240°C (Figure III-37). The heating rate was the lowest measured for any cell chemistry and was likely due to the lack of oxygen release from the cathode. The runaway resulted from the anode reaction with the electrolyte after the protective SEI was fully decomposed. The onset temperature was similar to $LiMn_2O_4$ which is also anode dominated in this temperature range. ARC data was also obtained which showed higher runaway temperatures for the cathode oxides with reduced oxygen release.

- All of the cells undergoing thermal ramp also showed flammability of the vent gases. Internal gas generation from electrolyte decomposition aerosolizes the flammable electrolyte and results in flame. The addition of flame retardants has not yet resulted in a non-flammable electrolyte under these conditions.

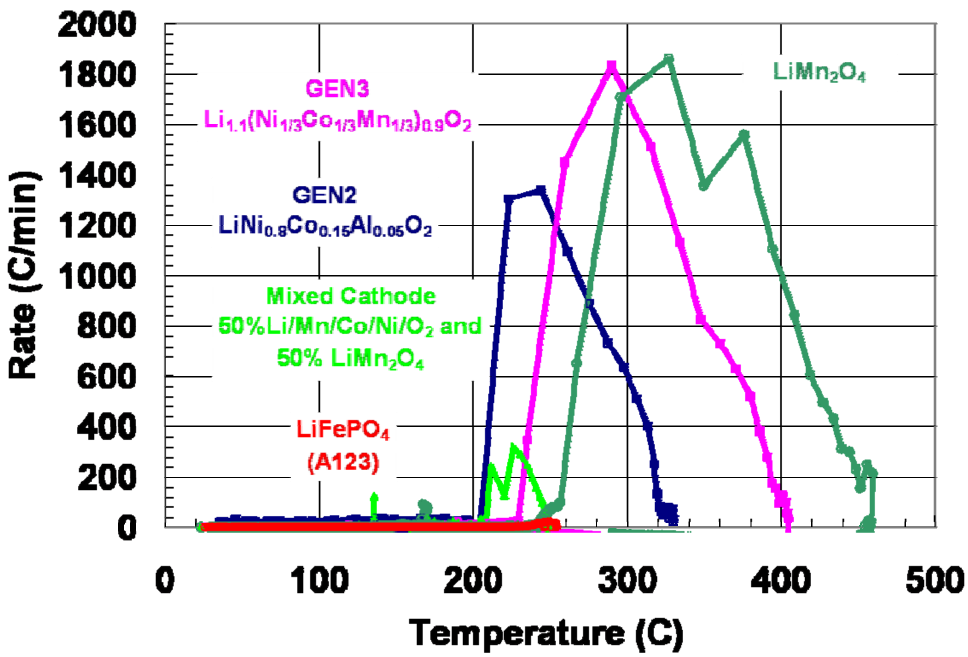

Figure III-37. Thermal ramp profiles showing high rate runaway for oxygen generating cathodes and low rate runaway for $LiFePO_4$ cathode.

III.D.3 Overcharge Abuse

III.D.3.1 Component-Level Studies

Overcharge Shuttles (Amine) – Due to life and safety issues of Li-ion cells, the cells must be charged to a specific upper cutoff voltage, but not beyond. Overcharge generally occurs when a current is forced into the cell above the cutoff voltage. This can lead to the chemical and electrochemical reactions of battery components, gas release, rapid temperature increase, and can also trigger self-accelerating reactions and even explosion. Redox shuttle additives have long been pursued as a protection against overcharge. The redox shuttle molecule (S) has a redox potential, at which it can be oxidized on the positive electrode and form a radical cation ($S^{\bullet+}$).

$$S \rightarrow S^{\bullet+} + e^- \tag{1}$$

The radical cation then travels to the negative electrode through the electrolyte and is reduced.

$$S^{\bullet+} + e^- \rightarrow S \tag{2}$$

The redox shuttle molecule then diffuses back to the positive electrode for the next cycle. During normal operation, the redox potential of the shuttle is not reached and it remains inactive. When the cell is overcharged, the potential of the positive electrode increases and the redox cycle is activated. The net reaction is to shuttle the charge forced by the external circuit through the cell without further forcing intercalation/deintercalation of lithium in the electrodes. Another advantage is that it contributes to maintaining cell balance in a battery pack.

Figure III-38 shows cyclic voltammograms of 0.05M 2-(pentafluorophenyl)-tetrafluoro-1,3,2-benzodioxaborole (PFPTFBB) and 1.2 M $LiPF_6$ in EC/ EMC (3:7, by weight). Both the counter and reference electrodes were lithium foils, and the working electrode was a platinum disk (Φ = 1 mm). As seen, PFPTFBB has a reversible redox reaction of ~4.43 V vs. Li^+/Li, which is high enough to provide overcharge protection for most currently used positive electrode materials. The diffusion coefficient is estimated to be 1.4×10^{-6} cm^2/s.

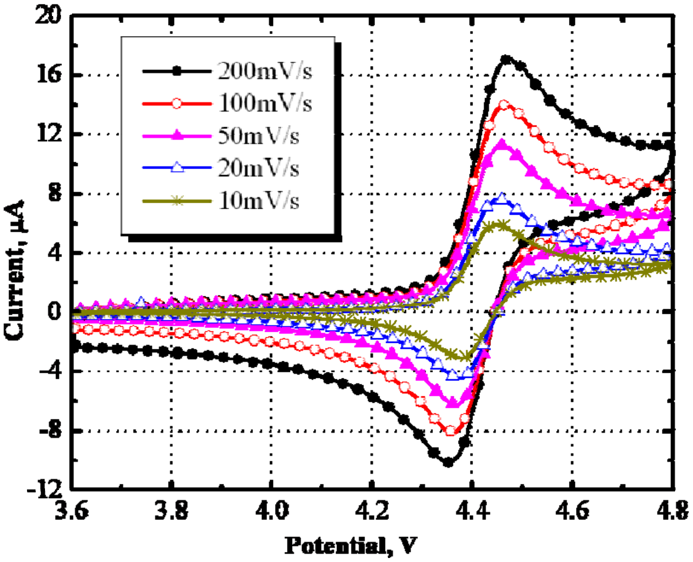

Figure III-38. Cyclic voltammograms of 0.05 M PFPTFBB and 1.2 M $LiPF_6$ in EC/EMC (3:7, by weight) using a Pt/Li/Li three-electrode cell.

Figure III-39 shows the charge/discharge capacity of a graphite/Gen2 cell containing 5 wt% PFPTFBB in 1.2 M $LiPF_6$ in EC/PC/DMC (1:1:3, by weight). The overcharge protection provided by PFPTFBB was effective and reversible for over 170 cycles of 100% overcharge. Figure III-39 also shows the cell completely lost its capacity after 125 cycles. However, the redox shuttle remained active for another 50 cycles at 55°C. Figure III-40 shows that the addition of PFPTFBB also improves the capacity retention of Li-ion cells during normal operation.

As a summary, PFPTFBB can be a stable redox shuttle for overcharge protection of state-of-the-art 4 V class Li-ion batteries. The addition of the novel additive can also improve the capacity retention of Li-ion batteries during normal operation condition.

***Cell Level Overcharge Abuse (Roth)* -** The goal of this work is to determine the effects of overcharge and thermal decomposition leading to cell thermal runaway. Overcharge studies have been performed using a custom apparatus at SNL designed to allow quantitative measurements of the heat generation of the cells during overcharge and simultaneous real-time gas monitoring. High-rate overcharge can lead to thermal runaway. This group has also shown that, for extended overcharges at low rates, thermal runaway does not automatically occur for cells based on Gen2 and Gen3 materials as long as the cell temperature remains below the separator melt temperature (135°C). Overcharge failure was seen to be a thermal reaction resulting often from failure of the separator leading to internal shorts. In addition, overcharge leads to cell venting of gases that can reach explosive levels in the presence of oxygen (air). Measurements of a Gen2 cell with an open vent allowed determination of the gases during the overcharge process.

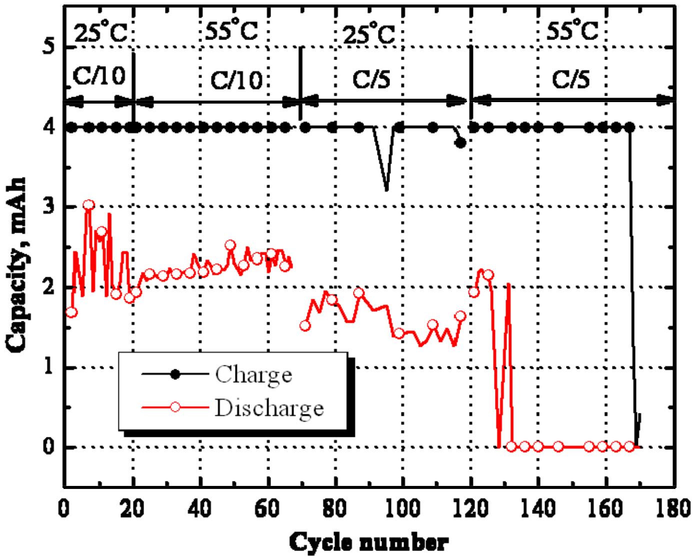

Figure III-39. Charge and discharge capacity of a graphite/Gen2 cell during an overcharge test. The electrolyte used contained 5 wt% PFPTFBB.

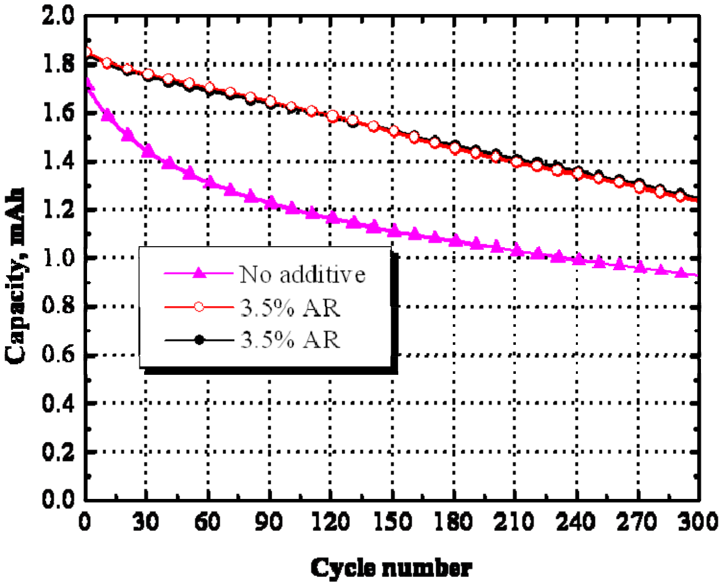

Figure III-40. Capacity retention at 55ºC of MCMB/Gen3 cells showing the positive impact of PFPTFBB (shown as AR in the labels).

Some of the more prominent observations from this work are that heat generation is fairly closely correlated to cell voltage as shown in Figure III-41. Also, hydrogen generation is observed at onset of heat generation as shown in Figure III-42. Finally, carbon dioxide and carbon monoxide are observed one minute after hydrogen signal.

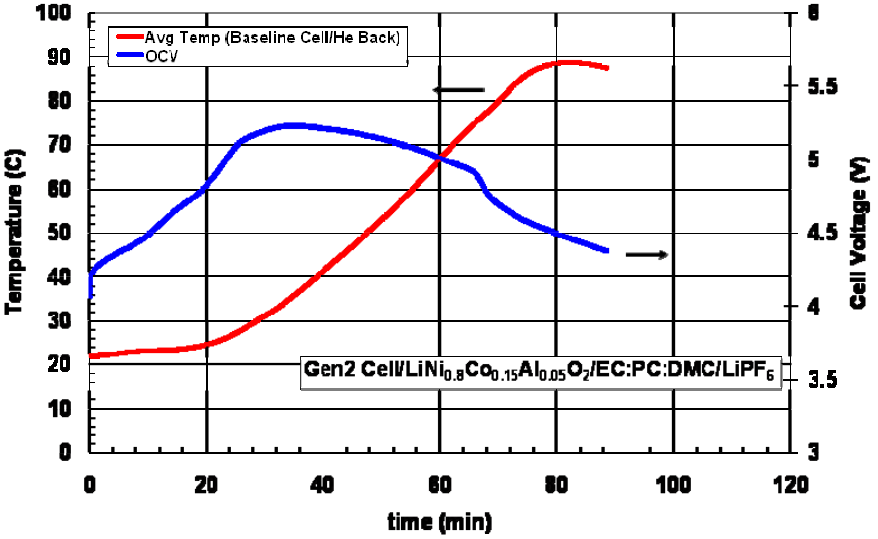

Figure III-41. Overcharge profile showing temperature and voltage correlation starting at 100% SOC.

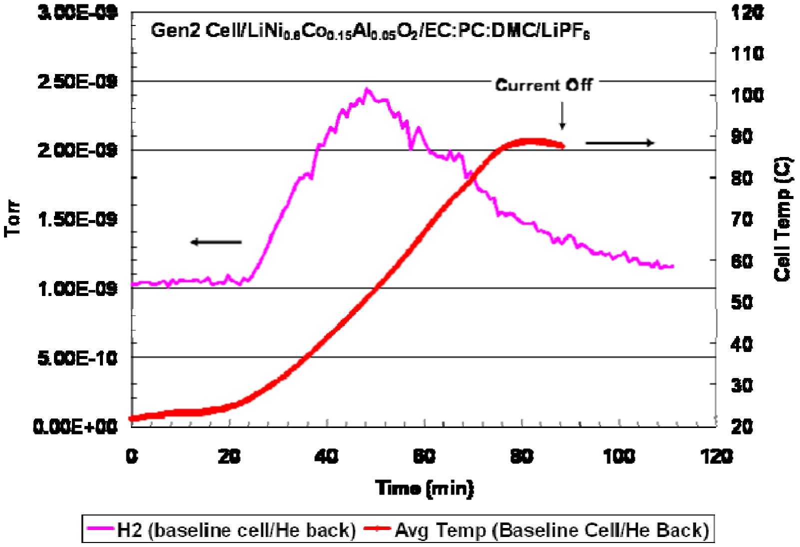

Figure III-42. Overcharge profile showing heat and hydrogen generation starting at 100% SOC.

- Protection from failure during overcharge can be achieved by bypassing the overcharge current so that the cell active material is not being overcharged, using e.g., an overcharge shuttle. An overcharge shuttle from Air Products and Chemicals, Inc. based on $Li_2B_{12}F_9H_3$ has been tested. The voltage, temperature and heat output response of a Gen2 cell using 0.4M $Li_2B_{12}F_9H_3$ and 0.1M $LiPF_6$ in EC/DEC (3:7).

- Overcharge activation limited cell voltage to less than 4.5V. Figure III-43 compares the voltage profile with a standard cell which eventually reached separator shutdown and failure. Increase heat output results from activation of the shuttle but remains fairly constant during overcharge, shown in Figure III-44.

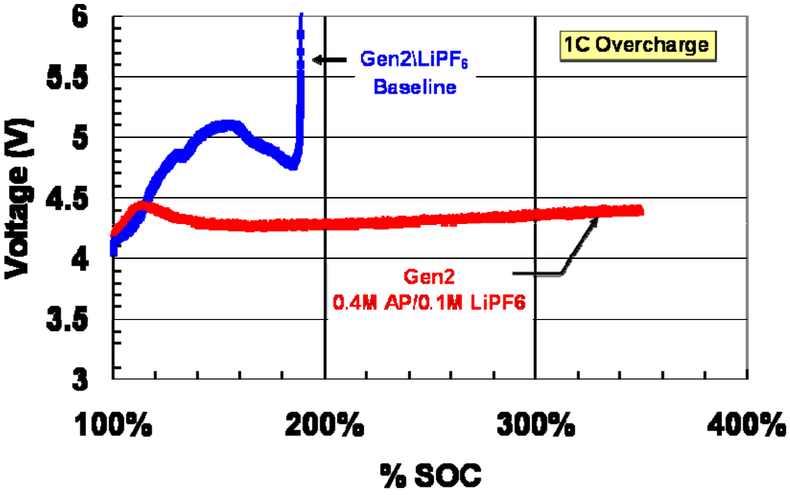

Figure III-43. Overcharge profile showing voltage for cells with and without Air Products overcharge shuttle salt.

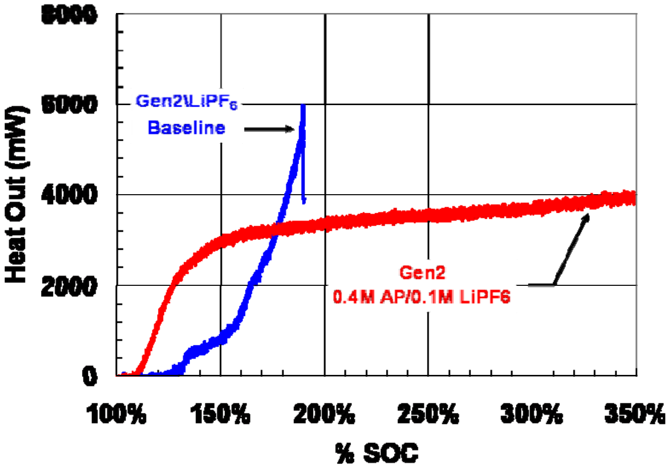

Figure III-44. Overcharge profile showing heat generation for cells with and without Air Products overcharge shuttle salt.

III.E Cell-Level Cost Reduction

Objectives

- Identify and secure advanced low-cost cell materials from material suppliers and evaluate samples for high-power HEV applications and report most promising materials to the USABC-sponsored industrial battery developers.
- Investigate methods to improve the performance and stability of existing anode and cathode materials.
- Develop lower-cost high-power cell materials/chemistries and conduct evaluations to establish their viability.

Approach

- Secure samples of the most advanced materials from material suppliers worldwide.
- Refine rapid screening test protocols to assess the suitability of novel materials. Employ protocols to evaluate material capabilities, provide feedback to the material suppliers.
- Produce cells from the most promising materials and conduct preliminary evaluations on their performance, life, and safety characteristics, using sealed prismatic cells.
- Prepare electrodes with nano-phase coatings and characterize their capacity, power, and stability.

Accomplishments/Findings

- AlF_3-coated $LiNi_{1/3}Co_{1/3}Mn_{1/3}O_2$ and Gen2 electrodes show better cycling stability and rate capability compared with non-coated materials at high cut-off voltage of 4.5-4.6V.

Future Studies

- Coat 5 kg of $LiNi_{1/3}Co_{1/3}Mn_{1/3}O_2$ and ship the material for pouch and possibly 18650 cell builds to quantify this technology for HEV and possibly for high energy/high voltage PHEV applications.
- Continue to monitor material and cell development in Asian and European markets.

III.E.1 Introduction

Since the beginning of this program, researchers have been searching for lower cost cell materials and components that possess enhanced stability. These cell materials include: electrode active materials, conductive additives for the positive electrode, electrode binders, electrolyte salts, electrolyte solvents, and electrolyte additives. Where it makes sense to do so, a limited amount of internal R&D is performed to develop more stable materials (primarily in terms of electrolyte components and positive electrode materials). Recently, ANL has been investigating a relatively new AlF_3 coating that appears to stabilize the cathode active material leading to enhanced high temperature stability, better power, and enhanced abuse tolerance. Table III-9 provides a summary of how the DOE laboratories contribute to this focus area.

Table III- 9. Summary of how the DOE laboratories contribute to the "Cost Reduction" focus area.

	ANL	BNL	INL	LBNL	SNL
High Voltage Cathodes and Advanced Cathode Coatings	X				
Develop Electrode and Electrolyte Materials	X				
Advanced Materials from Asia	X				

III.E.2 High Voltage Cathodes and Advanced Cathode Coatings

***AlF_3-coatings (Amine)* -** It has been found that the main cause of the impedance rise in aged the Gen2 ($Li[Ni_{0.80}Co_{0.15}Al_{0.05}]O_2$/Graphite) cell was the increase in the interfacial impedance of the cathode caused by the surface reduction of the oxide cathode to NiO and the byproduct of the oxidation of the solvent. One way to prevent these types of reactions is to coat the cathode with uniform nano-layer of AlF_3. Since AlF_3 is a very stable material and is not oxidized during cell cycling, it will inhibit reactivity between the charged cathode and the electrolyte at the interface. In this study, the role of AlF_3 coating on Gen2 cells' performance and safety was investigated.

To prepare AlF_3-coated Gen2 material, ammonium fluoride and aluminum nitrate nonahydrate were dissolved in separate containers of distilled water. After the $Li[Ni_{0.80}Co_{0.15}Al_{0.05}]O_2$ powder was immersed into the aluminum nitrate nonahydrate solution, the ammonium fluoride solution was added. The amount of AlF_3 in the solution was 0.25 mol % of the active powders. The solution containing the active material was constantly stirred at 80°C for several hours, accompanied by a slow evaporation of solvent. The $Li[Ni_{0.80}Co_{0.15}Al_{0.05}]O_2$ powders were heated at 400°C for 5 hours under nitrogen. Figure III-45 shows TEM images of the AlF_3-coated Gen2 material, with a 10nm AlF_3 layer coated homogeneously on the surface of the active material.

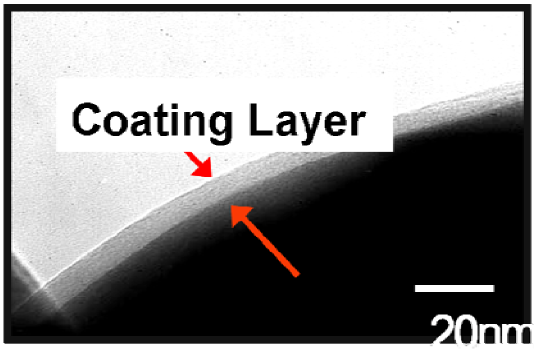

Figure III-45. Bright- field TEM images of AlF_3-coated $Li[Ni_{0.8}Co_{0.15}Al_{0.05}]O_2$.

Figure III-46 (left) shows the discharge voltage versus capacity profiles of Li/pristine and AlF_3-coated $Li[Ni_{0.80}Co_{0.15}Al_{0.05}]O_2$ (Gen2) cells at various C-rate between 3.0 and 4.3 V. The cells were charged galvanostatically at 36 mA/g (0.2 C-rate) before each discharge test and then discharged at different rates. The coated Gen2 material showed enhanced discharge rate compared to the pristine material. Figure III-46 (right) shows the discharge capacity vs. cycle number of pristine and AlF_3 coated Gen2 charged to 4.3 V. The AlF_3 coated material shows much better capacity retention when compared to the pristine material.

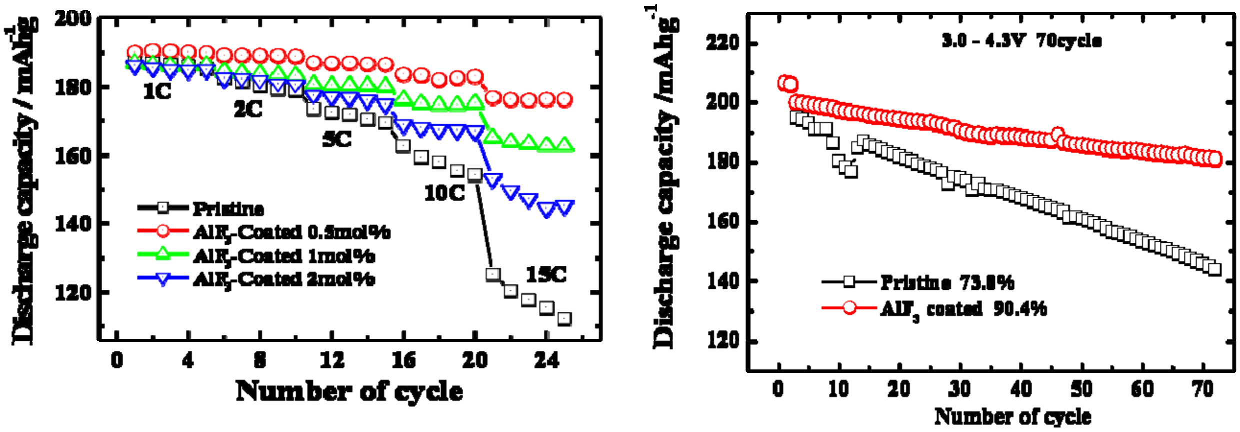

Figure III-46. Comparison of pristine and AlF_3 coated Gen2 material: rate capability (left), cycling stability (right).

To further investigate the cycling performance, an MCMB carbon electrode was employed as the anode. 50mAh laminated-type Li-ion cells in an Al pouch were assembled. The cells using pristine and AlF_3-coated active material were charged and discharged for 600 cycles at 1 C-rate between 3.0 and 4.2 V (Figure III-47). The C/pristine cell showed a gradual capacity fading with cycling with a capacity retention of 85% after 400 cycles. On the other hand, the AlF_3-coated cathode cell retained 95% capacity after 600 cycles.

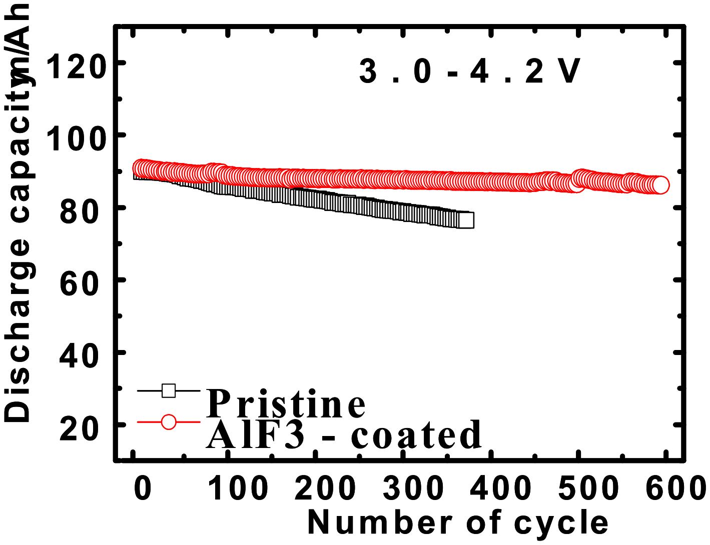

Figure III-47. Continuous charge-discharge curves of C/pristine Gen2 and C/AlF_3-coated Gen2 cell.

The thermal stability of cathode materials, especially at the delithiated state, is of great interest because of their impact on battery safety. Figure III-48 represents the DSC data of the Li/pristine and AlF_3-coated Gen2 cells charged to 4.3 V versus Li. For the pristine Gen2 electrode, the exothermic peak temperature was about 190^{o}C. However, the AlF_3-coated Gen2 electrode showed the exothermal peak shifted to higher temperature (240^{o}C) and significantly reduced generated heat. These results show that the AlF_3-coated cathode has better thermal stability than pristine one. The thin AlF_3 coating layer prevents the direct contact of the active cathode material with the liquid electrolyte, which could greatly reduce the decomposition of active material and the oxidation of the electrolyte.

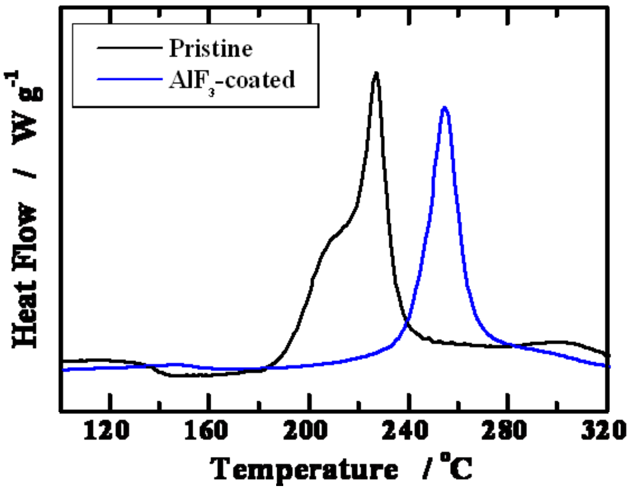

Figure III-48. DSC profiles of pristine Gen2 and AlF$_3$-coated Gen2 cell charged to 4.3 V.

III.E.3 Advanced Materials from Asia

Materials Summary (Amine) - Each year members of the ATD and BATT programs travel to Japan and Korea to collect the latest information on advanced material and technologies for batteries. The purpose of the trip is to visit with management and research personnel at material companies to seek a better understanding of the status of their lithium battery technologies. Another reason of the trip is to request samples of state-of-the-art materials for use in high-performance rechargeable batteries. These materials are of critical importance to the program's efforts to develop advanced batteries for transportation applications such as HEVs and PHEVs. The battery manufacturer and component suppliers visited in 2007 were SK-Japan, Toda, Nippon Chemical, Mitsui Mining & Ship Building, Ishihara, Hitachi chemical, Kyoritsu, and GS-Yuasa. This section summarizes the information obtained in each of the areas covered during this trip.

Carbon Anode - Hitachi Chemical dominates the carbon anode market, holding 50% of the market share. Much of this is accounted for in their MAG (Massive Activated Graphite) line of anodes. While this material is good for high power, it is expensive and has poor abuse tolerance. In order to enhance the life and safety of their carbon, Hitachi is developing a technique to modify the surface of a graphite or soft carbon core to an amorphous state. This allows for less SEI formation, more surface stability with the electrolyte, and less Li-deposition. Two types of carbons are being produced; SMG-A for high energy, and SMG-N for high power and low cost. These new carbons show low irreversible capacity loss (less than 6%) and high capacity (approaching 360 mAh/g on the 1st discharge). Hitachi is also developing soft carbon with crystallinity between graphite and hard carbon. The power of the soft carbon is similar to that of hard carbon at room temperature, but with much lower resistance at -30°C.

LTO Anode - There is currently significant interest in the titanate anode due to its higher potential *vs.* Li which promises improved safety compared to carbon. Two of the companies visited, Isihara Sangyo and Kyoritsu, are involved with LTO development. Isihara has been producing two grades of the material for watch batteries, one a nanomaterial with low tap density and the other an agglomerate on the order of 20µm that has a much higher tap density. The materials' retained

~80% capacity at 50C rate. Kyoritsu has adapted their barium titanate process to make high crystallinity LTO. The company has three grades with particle sizes ranging from 5µm to 160 nm, with a target price of ~$13/kg. The current price is ~$28/kg.

***Mn-Spinel Cathode* -** One company visited, Toda, is involved in the development of $LiMn_2O_4$ cells. One grade, tested at ANL, consists of 5 µm particles with a capacity of 100 mAh/g. Data at ANL shows that this material has a low ASI (~20 Ωcm^2 during a 40C pulse discharge) and is suitable for HEV applications. Toda is developing a stabilized $LiMn_2O_4$ cathode delivering 140mAh/g. This cathode may be suitable for PHEVs.

***NMC Cathode* -** Nippon chemical is producing four different mixed transition metal layered cathode materials. These include Ni:Mn:Co ratios of 1:1:1 (the well-known NMC material), 8:1:1, 6:2:1, and 7:2:2. The materials have a narrow particle size distribution ranging from 5 µm to 15 µm. Tests at ANL show that the NMC material has a low ASI. The 8:1:1 has a capacity of 190 mAh/g and reasonable cycle life. However, it is not clear if the abuse tolerance is compromised because of the high Ni content in this material.

***$LiFePO_4$ Cathode* -** There is significant interest in the $LiFePO_4$ material in Japan given the recent developments driven by A123Systems. Companies who were visited and who are working on this material include Nippon, Toda, Mitsui, and Sumitomo. Nippon Chemical's material is geared toward the high energy, high tap density market and hence their particle sizes are ~3.5 µm. Sumitomo is pursuing $LiFePO_4$ synthesis via a hydrothermal process. Particle sizes ranged from 1 to 400 nm primary particles agglomerated into secondary particles of 3.5 to 20 µm. The large particle size appeared to severely limit the rate capability of the material. On the other hand Toda chemical has particles in the 200 nm range with tap density of 1.9 g/cc. Efforts were focused on material with and without a carbon coating. Rate performance was reasonable. Probably the best $LiFePO_4$ was from Mitsui Mining and Ship Building. Their material had ~100 nm primary particles with a carbon coating. Rate capability was excellent with 65% capacity at 20 C. The company projects that they can increase production to 3000 mega tons/year by 2011. However, performance of the olivine materials in Japan was inferior to that synthesized by A123Systems. One reason could be the smaller particle size of the A123 materials (<40 nm).

***Flame Retardant* -** A meeting was held with Bridgestone at Nippon Chemical. These two companies have agreed to commercialize the phoslyte additive for improving lithium battery safety. Bridgestone has given an exclusive license to Nippon Chemical for scale up and commercialization. Bridgestone reports that they have also developed a new non-flammable electrolyte that will be announced in the near future. Nippon Chemical is developing new ionic liquid system for high energy batteries.

***Battery Companies*: -** Meetings were held with two battery companies, GS-Yuasa and SK Japan. **GS-Yuasa** is concentrating on the NMC/graphite system and working on a NEDO project to assess this system's ability to satisfy HEV applications. In addition, the company has a NiMH chemistry delivering 1800 W/kg using a pasted electrode design. The company has chosen the $LiNi_{0.55}Mn_{0.3}Co_{0.15}O_2$/hard carbon system for HEV applications based on capacity and power retention after calendar life tests. The system delivers 4.12 kW/kg for a 10 s pulse. Accelerated testing at 50°C for 300 days shows that the loss in capacity was 6% while power fade was 3%. The company is also working on room temperature ionic liquids (RTIL) based on N-methyl-N-propyl piperidinium. While typical RTIL's react with the graphite anode, mixing the IL with conventional electrolyte results in a stable passive layer and better cell performance. Results suggest that up to 4% RTIL is needed to eliminate flammability. However, the power capability of the new electrolyte is worse than the liquid systems.

SK is a Korean company pursuing the development of spinel-based system for HEVs. The company reports a power of 2.2 kW/kg and energy of 60Wh/kg on a module level. SK has converted a Toyota Prius with their battery and show that their module has the same energy as the NiMH cells, but only half the weight, more power, and results in 4% greater fuel economy. While calendar life remains an issue with the spinel chemistry, the company has made consistent improvements. At present, they report that 15 year life is possible at 35°C, but is a problem at 40°C. The company also has a module for PHEV applications.

Applied Research Publications

1. A.N. Jansen, D.W. Dees, D.P. Abraham, K. Amine, G.L. Henriksen, Low-Temperature Study of Lithium-Ion Cells using a LiSn Micro-Reference Electrode JPS 174 (2007) 373.
2. D. Abraham, J. Heaton, S.-H. Kang, D. Dees, and A. Jansen, Investigating the Low-Temperature Impedance Increase of Lithium-Ion Cells, *JECS*, In Press.
3. D. Abraham, J. Knuth, D.W. Dees, I. Bloom, J.P. Christophersen, Performance degradation of high-power lithium-ion cells-Electrochemistry of harvested electrodes, JPS 170 (2007) 465.
4. D. Abraham, S. Kawauchi, and D. Dees, Modeling the Impedance Versus Voltage Characteristics of $LiNi_{0.8}Co_{0.15}Al_{0.05}O_2$, *Electrochim. Acta*, In Press.
5. D. Abraham, J.R. Heaton, S.-H. Kang, D.W. Dees, A.N. Jansen, Investigating the Low-Temperature Impedance Increase of Lithium-Ion Cells, JECS 155 A41 (2008)..
6. D. Dees, A. Jansen, D.P. Abraham, Theoretical Examination of Reference Electrodes for Lithium-Ion Cells, JPS 174 (2007) 1001..
7. D. Zeng, J. Cabana, J. Bréger, W. –S. Yoon and C. P. Grey, Cation Ordering in $Li[Ni_xMn_xCo_{(1-2x)}]O_2$ Layered Materials; An NMR, Pair Distribution Function and X-ray Absorption Spectroscopy Study, *Chemistry of Materials*, accepted.
8. I. Belharouak, W. Lu, D. Vissers, and K. Amine, Safety Characteristics of the $Li_4Ti_5O_{12}/LiMn_2O_4$ Li-Ion Battery, Mater. Res. Soc. Proc. 972, 339-344 (2007)
9. J. Liu, Z. Chen, S. Busking, and K. Amine, Lithium Difluoro(oxalato)borate as a Functional Additive for Lithium-Ion Batteries, Electrochem. Commun., 9: 475-479 (2007).
10. J. Liu, Z. Chen, S. Busking, I. Belharouak, and K. Amine, Improved Graphite/ $Li_{1.1}[Ni_{1/3}Co_{1/3}Mn_{1/3}]_{0.9}O_2$ Li-Ion cells Containing Additives ; JPS, in press, (2007).
11. K. Lee, S. Myung, K. Amine, Y. Sun, Structural and Electrochemical Properties of Layered $Li[Ni_{1-2x}Co_xMn_x]O_2$ ($x = 0.1 - 0.3$) Positive Electrode Materials for Li-Ion Batteries, JECS, 154, A971 (2007).
12. K. Y. Chung, W. –S. Yoon, H. S. Lee, J. McBreen, X.–Q. Yang, S. H. Oh, W. H. Ryu, J. L. Lee, W. I. Cho, and B. W. Cho, *In Situ* XRD Studies of the Structural Changes of ZrO_2 Coated $LiCoO_2$ during Cycling and Their Effects on Capacity Retention in Lithium Batteries, *JPS*, 163 (2006) 185.
13. K. Y. Chung, W. –S. Yoon, J. McBreen, X. –Q. Yang, S. H. Oh, H. C. Shin, W. I. Cho, and B. W. Cho, Structural Studies on the Effects of ZrO_2 Coating on $LiCoO_2$ during Cycling using In Situ X-ray Diffraction Technique, *JECS*, 153, (2006) A2152.
14. K. Y. Chung, W. –S. Yoon, J. McBreen, X. –Q. Yang, S. H. Oh, H. C. Shin, W. I. Cho, and B. W. Cho, In Situ X-Ray Diffraction Studies on the Mechanism of Capacity Retention Improvement by Coating at the Surface of $LiCoO_2$*, JPS*, accepted.
15. S.-H. Kang, D.P. Abraham, A. Xiao, B.L. Lucht, JPS (2007), doi:10.1016/j.jpowsour.2007.08.112, Investigating the solid electrolyte interphase using binder-free graphite electrodes.
16. S.H. Park, S.-W. Oh, S.H. Kang, I. Belharouak, K. Amine, and Y.-K. Sun, Comparative study of different crystallographic structure of $LiNi_{0.5}Mn_{1.5}O_{4-\delta}$ cathodes with wide operation voltage (2.0–5.0 V), Electrochimica Acta, 52, 7226 (2007)
17. S.-H. Kang, D.P. Abraham, Preparation and Examination of Binder- and Carbon-Free Electrodes used in Lithium-Ion Cells, JPS 174 (2007) 1229..
18. S.-U. Woo, C.S. Yoon, K. Amine, I. Belharouak, and Y.-K. Sun, Significant Improvement of Electrochemical Performance of AlF_3-coated $Li[Ni_{0.8}Co_{0.1}Mn_{0.1}]O_2$ Cathode Materials, JECS, 154, A1005 (2007)
19. S-B. Ma, K.–W. Nam, W.–S. Yoon, X.–Q. Yang, K.-B. Kim A Novel Concept of Hybrid Capacitor Based on Manganese Oxide Materials, *Electrochemistry Communications*, accepted.
20. W. Lu, I. Belharouak, J. Liu, and K. Amine, Electrochemical and Thermal Investigation of $Li_{4/3}Ti_{5/3}O_4$ Spinel, JECS, 154, A114 (2007).
21. W. Lu, I. Belharouak, S.H. Park, Y.K. Sun, K. Amine, Isothermal calorimetry investigation of $Li_{1+x}Mn_{2-y}Al_zO_4$ spinel, Electrochimica Acta, 52, 5837 (2007).

22. W. Lu, Z. Chen, H. Joachin, J. Prakash, J. Liu, and K. Amine, Thermal and Electrochemical Characterization of MCMB/$LiNi_{1/3}Mn_{1/3}Co_{1/3}O_2$ Using LiBOB as an Electrolyte Additive, JPS 163: 1074 (2007).
23. W. –S. Yoon, K. Y. Chung, J. McBreen, D. A. Fischer, and X. –Q. Yang, Changes in Electronic Structure of the Electrochemically Li-ion Deintercalated $LiNiO_2$ System Investigated by Soft X-ray Absorption Spectroscopy, *JPS*, 163 (2006) 234.
24. W. –S. Yoon, K. Y. Chung, J. McBreen, D. A. Fischer, and X. –Q. Yang, Electronic Structural Changes of the Electrochemically Li-ion Deintercalated $LiNi_{0.8}Co_{0.15}Al_{0.05}O_2$ Cathode Material Investigated by X-ray Absorption Spectroscopy, *JPS*, accepted.
25. W. –S. Yoon, K. Y. Chung, J. McBreen, D. Wang, X. Huang, L. Chen, and X. –Q. Yang, Electronic Structural Changes of the Electrochemically Delithiated $LiFe_{0.5}Co_{0.5}PO_4$ Cathode Material studied by X-ray Absorption Spectroscopy, *JPS*, accepted.
26. W.–S. Yoon, K. Y. Chung, K.–W. Nam, and K.-B. Kim "Characterization of $LiMn_2O_4$ - Coated $LiCoO_2$ Film Electrode Prepared by Electrostatic Spray Deposition" JPS, Vol. 163 (2006) 207.
27. W.–S. Yoon, K. Y. Chung, M. Balasubramanian, J. Hanson, J. McBreen, and X. –Q. Yang "Time Resolved XRD Study on the Thermal Decomposition of Nickel-Based Layered Cathode Materials for Li-ion Batteries" JPS, Vol. 163 (2006) 219.
28. Y.-K. Sun, S.-W. Cho, S-.W. Lee, C. S. Yoon, and K. Amine, Improvement of High Voltage Cycling Performance of AlF_3-coated $Li[Ni_{1/3}Co_{1/3}Mn_{1/3}]O_2$ Cathode Materials for Lithium Secondary Batteries, JECS, 154, A168 (2007).
29. Z. Chen and K. Amine, Degradation Pathway of 2,5-Diterbutyl-1,4-dimethoxybenzene at High Potential, Electrochimica Acta, 53: 453 (2007).
30. Z. Chen and K. Amine, High Rate Pulse Overcharge Protection for HEV Applications Using Redox Shuttles, to be submitted to Electrochem. Commun., (2007).
31. Z. Chen, and K. Amine, Bifunctional Electrolyte Additive for Lithium-Ion Batteries, Electrochem. Commun., 9: 703 (2007).
32. Z. Chen, J. Liu, and K. Amine, Lithium Difluoro(oxalato)borate as New Salt for Lithium-Ion Batteries, Electrochem. Solid-State Lett., 10: A45 (2007).
33. Z. Chen, Q. Wang, and K. Amine, Understanding the Stability of Aromatic Redox Shuttles for Overcharge Protection of Lithium-Ion Cells, JECS 153: A2215 (2006).

Patents

34. K. Amine, Z. Chen, and Q. Wang, Novel Redox Shuttles for Overcharge Protection of Lithium-Ion Batteries, U.S. Pat. App. No. US20060199080A1.
35. Z. Chen and K. Amine, Lithium-Ion Batteries with Intrinsic Pulse Overcharge Protection, U.S. Pat. App. No. US20070178370A1.
36. K. L. Gering and D. R. Haefner, Thermal Management Systems and Methods, Pat. Num. 7,147,071 B2.

Invited presentations

37. W.–S. Yoon, K. Y. Chung, X.–Q. Yang, and J. McBreen "X-ray Absorption Spectroscopic Study on the Cathode Material for Li rechargeable batteries during Electrochemical Cycling," Invited, Presented at the 210th Meeting of the Electrochem. Society, October 29 to November 3rd, 2006, Cancun, Mexico.
38. W.–S. Yoon, K.–W. Nam, J. Hanson, H. S. Lee, J. McBreen, and X.–Q. Yang "Application of Synchrotron-Based X-Ray Techniques to Study Electrode Materials for Lithium Rechargeable Batteries" Invited talk in Samsung Advanced Institute of Technology in Yongin, Korea, July 2, 2007.
39. W. –S. Yoon, K. –W. Nam, J. Hanson, H. S. Lee, J. McBreen, and X. –Q. Yang "Investigation of Electrode Materials for Lithium Rechargeable Batteries using Various Synchrotron X-Ray Techniques" Invited talk in SK Corporation in Daejeon, Korea, July 3, 2007.
40. X. Q. Yang, W. S. Yoon, K. Y. Chung, H. S. Lee, J. McBreen, K. Y. Chung, W. I. Cho, Karim Zaghib, X. Huangd, L. Chen, and J-M. Chen, "Structural Changes and Thermal Stability of the Intercalation

Compounds as Cathode Materials Studied by Synchrotron based X-ray Techniques," Invited, Presented at the 210th Meeting of the Electrochem. Society, October 29 to November 3rd, 2006, Cancun, Mexico.

41. X. Q. Yang, W. S. Yoon, K. Y. Chung, H. S. Lee, J. McBreen, K. Y. Chung, W. I. Cho, Karim Zaghib, X. Huangd, L. Chen, and J-M. Chen, "Structural Changes of New Cathode Materials Relating to the Thermal Stability and Low Temperature Performance Studied by Synchrotron based X-ray Techniques," Invited, Presented at Lithium Mobile Power 2006, December 4 , 2006, Miami Beach FL.
42. X. Q. Yang, W. S. Yoon, K. Y. Chung, H. S. Lee, J. McBreen, K. Y. Chung, W. I. Cho, Karim Zaghib, X. Huangd, L. Chen, and J-M. Chen, "Structural Changes of New Cathode Materials for Lithium Batteries Studied by Synchrotron Based X-ray Diffraction and Absorption Spectroscopes," Invited, Presented at The Energy Materials Forum, April 16-18, 2007, Taichung, Taiwan.

IV. FOCUSED LONG-TERM RESEARCH

The Focused Long-Term Research Program, also called the Batteries for Advanced Transportation Technologies (BATT) program, is supported by the DOE's Vehicle Technologies program (DOE-VT) to research and analyze new materials for high-performance, next generation, rechargeable batteries for use in HEVs and EVs.

Background and Program Context

The BATT Program addresses the fundamental problems of chemical and mechanical instabilities that have impeded the development of EV, HEV, and PHEV batteries with acceptable costs, performance, lifetimes, and safety. The aim is to identify and better understand cell and material performance and lifetime limitations before initiating battery scale-up and development. Emphasis is placed on the synthesis of components into cells with determination of failure modes, while continuing with materials synthesis and evaluation, advanced diagnostics, and improved model development. The selected battery chemistries are monitored continuously with timely substitution of more promising components. This is done with advice from within the BATT Program and from outside experts, including consultation with automotive companies and DOE. Also factored into the BATT Program direction is the monitoring of world-wide battery R&D activities. The Program not only supports research that leads to incremental improvements to existing materials, but also into high-risk "leap-frog" technologies that might have a tremendous impact in the marketplace.

A key event during FY 2007 was a discussion meeting of all the BATT PIs along with DOE Program Managers. The PIs were arranged into panels and a panel chair was chosen to lead a discussion on BATT's efforts and possible future activities in a given area. The purpose of the meeting was to provide the latest status of the various tasks and to identify promising new areas of research. This highly effective meeting not only helped set the overall program focus and priorities for FY 2008, but also guided the development of detailed research plans by the researchers.

Based on this feedback, the structure of the BATT effort is being modified to incorporate theme-based research in addition to exploratory research. In this new structure some members of the BATT Program will contribute to broad themes while other PIs continue the synthesis and characterization of new anodes, cathodes, and electrolytes for use in the next-generation Li-ion chemistries. Three themes were identified: (i) improving energy and life of PHEV batteries, (ii) studying the impact of nano-materials on battery behavior with emphasis on phosphate cathodes and alloy and intermetallic anodes, and (iii) understanding interfacial processes with emphasis on characterizing the SEI and on reactions in composite cathodes at potential greater than 4.3V.

The three themes were identified to ensure that BATT will have the maximum impact on addressing the pressing issues that prevent PHEVs from reaching the marketplace, namely battery cost and cycle/calendar life. One method to decrease the cost is to increase the energy of each cell, thus decreasing the number of cells needed, consequently decreasing cost. BATT will pursue two avenues to achieve this goal, first by engineering existing materials to improve their energy density, and second, by developing new materials that have more energy per mass. While the engineering approach is expected to yield results in the short-term, the materials research is expected to lead to a larger impact in the long-term. PHEV batteries also are expected to be subjected to 5000 deep-discharge cycles over a 15-year period. The ability of Li-ion cells to be cycled under these circumstances is presently unknown. BATT will address this by studying two fundamental issues that limit life of batteries, first, on the formation of the SEI and its stability throughout life, and second, on the processes that occur in cathodes at potential above 4.3 V.

The work is administered by the Lawrence Berkeley National Laboratory (LBNL), with principal researchers from LBNL and four additional laboratories plus twelve universities (see Appendix A). The program, and this document, is organized into the following areas (the new themed based areas will be used in the 2008 report, following a full year of effort on them):

IV.A New Cathode Systems, Performance and Limitations
    IV.A.1 $LiFePO_4$ Systems
    IV.A.2 Mn Spinel and Spinel Composite Systems
    IV.A.3 Nickelate Systems
IV.B New Anode Materials
IV.C Novel Electrolytes and their Characterization,
IV.D Li-Ion Modeling, Diagnostics, and Cell Analysis

Brief descriptions of each research area follow.

- The ***$LiFePO_4$ System*** is a moderate energy, low (material) cost, and abuse tolerant material. This task includes studies of capacity and power fade, lower cost synthesis methods, and the impact of processing steps on performance. Finally, researchers are performing theoretical and experimental investigations on the impact of carbon coatings on performance.

- The ***Mn Spinel Systems*** system with a liquid-electrolyte provides good high-rate capability and improved abuse tolerance over nickelates. This task aims to understand the failure and degradation modes using various material doping, cell cycling, empirical and *ab-initio* calculations, and advanced diagnostics.

- The ***Nickelate Systems*** includes the $LiNi_{1/3}Mn_{1/3}Co_{1/3}O_2$ (called NMC) cathode material that, with a carbon-coated graphite anode, is a high-energy cell that also promises good power. This task aims to understand the failure and degradation modes in the 123 and other nickelate systems using cell builds, cell cycling, advanced diagnostics, and modeling.

- The ***New Anode Materials*** task aims to find improved composite negative electrodes containing one (or more) metal components within a graphite matrix, for example C/Sn and C/Sb systems, and nano-composite alloys. Some researchers are also beginning to investigate carbons that might replace MCMB, which may be commercially unavailable shortly.

- The ***Novel Electrolyte Materials*** task involves investigating the limitations of polymers, ionic liquids, and single-ion conducting gels which promise low cost and abuse tolerant batteries. Post-test analyses and spectroscopic and microscopic techniques are used to investigate morphology, structure, and compositional changes of electrode materials.

- The ***Modeling and Diagnostics, and Cell Analysis*** tasks involve the use of advanced diagnostics techniques, such as FTIR, to investigate interfacial properties in Li-ion batteries by studying the SEI and its change with cycling. It also involves studying the changes in electrode structure using X-ray absorption fine structure (XAFS), XRD, NMR and other techniques. Several modeling approaches are used to understand cell and fundamental material properties, including *ab-initio* calculations, macroscopic cell calculations, and finite element simulations. Finally, standard cell making and testing techniques are developed and applied to provide a common evaluation process for new materials.

This chapter summarizes the research activities of this program in FY 2007. The website for the BATT Program is found at http://berc.lbl.gov/BATT/BATT.html.

IV.A New Cathode Materials

The overall objective of these tasks is to evaluate advanced cathode materials for Li-ion batteries. Current materials suffer a number of shortcomings, including expensive raw materials or processing, poor calendar life in some cases, and relatively poor response to abuse conditions. This program is investigating three baseline chemistries, (including variations on each) $LiFePO_4$, $LiMn_2O_4$, $LiNi_{1/3}Mn_{1/3}Co_{1/3}O_2$, and several more exploratory systems including composite cathodes, that offer improvements over $LiCoO_2$. The baseline systems serve as a standard against which the more exploratory systems are compared.

IV.A.1 $LiFePO_4$ and other Phosphate Systems: Performance and Limitations

Objectives

The primary objective of the metal-phosphate research is to understand and overcome the inherently poor conductivity of these materials to permit cell developers to take advantage of their relatively low cost and good abuse tolerance characteristics. Other objectives are to understand the impact of particle size and morphology on performance, and to investigate new lower cost processing routes. Researchers also aim to improve power and life through novel electrode structures and nano-sized conductive additives.

Approach

To address the inherently low conductivity of this material, different experimental and modeling strategies are being explored. Experimental efforts include the use of different conductive additives such as the use of conductive binders, nano-sized carbon fibers, and conductive coatings to better understand the additives' role in high-rate performance and degradation mechanisms. The purpose of the electrochemically-active polymers research is to replace electrochemically inactive cathode components such as binders and conductive carbons with electroactive materials that will contribute to the cell's energy storage capacity. Modeling efforts are attempting to develop a more realistic electrode-morphology model including the impact of porosity on electrode performance.

To understand the phase transition between $LiFePO_4$ and $FePO_4$, researchers are growing the crystals using hydrothermal synthesis, studying the chemical delithiation process, and characterizing the particles themselves.

In situ XAS is used to study the electronic and local structure of transition metal ions in electrode materials. The absorption peak features of the transition metal K-edge XAS provide important structural information such as oxidation state of chemical species, specific ion site symmetry, and covalent bond strength. *In situ* XAS studies are reported on the $LiFe_{1-y}M_yPO_4$ cathode materials, which show promise for higher energy density batteries for PHEVs.

Accomplishments

***Novel Cathode Materials and Electroactive Polymers (Goodenough)* -** Recently, this group prepared a series of silicates as cathode materials, specifically Li_2MSiO_4 (M = Fe, Mn, Ni, Co), $Li_2Fe_{0.5}Mn_{0.5}SiO_4$ and $Li_2Mn_{0.9}Mg_{0.1}SiO_4$. However, no better performance was obtained as compared with the corresponding phosphates.

Therefore, focused has been placed on $LiFePO_4$ composite cathodes with electrochemically-active polymers. The purpose is to replace electrochemically inactive cathode components such as binders and conductive carbons with electroactive materials that will contribute to the cell's energy storage capacity. Carbon-coated $LiFePO_4$/polymer composite cathodes with polypyrrole (PPy), polyaniline (PAn) and polytriphenylamine (PTPA) were fabricated and their electrochemical performances investigated. Different methods were used to make these composite cathodes, i.e., direct mixing of $LiFePO_4$ with polymer, simultaneous polymerization of polymer with $LiFePO_4$ in the precursor solution, and an electrodeposition route.

With the electrodeposition route, the composite film is *in situ* deposited on a stainless steel mesh in a suspension containing the active oxide particles, which is directly used as the cathode. This method is successful for fabricating C-$LiFePO_4$/PPy films with an enhanced capacity and excellent rate capability, Figure IV-1.

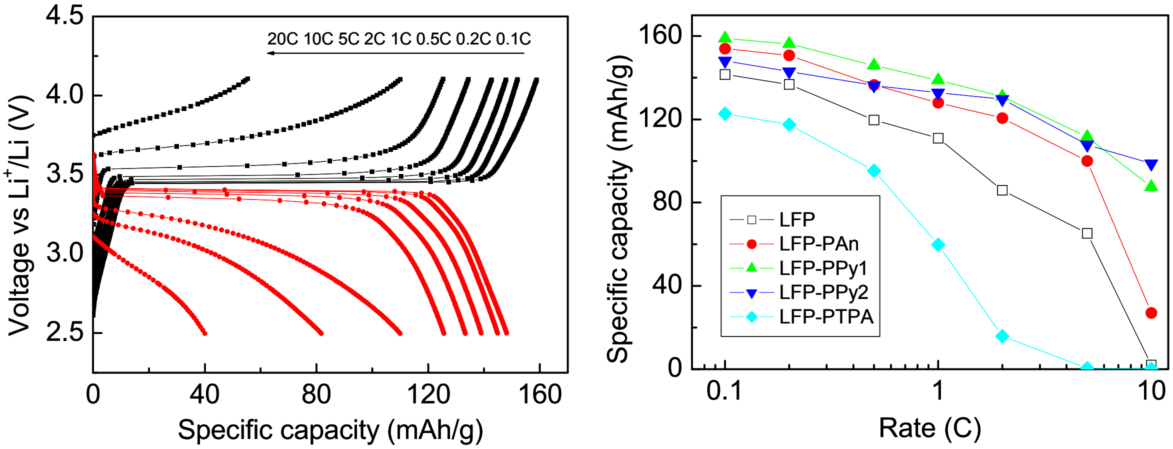

Figure IV-1. Rate capability of C-$LiFePO_4$/PPy prepared with simultaneous chemical polymerization (left). Rate capabilities for C-LFP/polymer composite cathodes (right). LFP-PPy1 was obtained by electrodeposition; LFP-PPy was prepared with chemical polymerization (right).

However, the electrodeposition method is not available for $LiFePO_4$ composites with PAn or PTPA, or with PPy and some layered oxides like $LiNi_{2/3}Mn_{1/3}O_2$. Although the effects of solvent, electrolyte, monomer concentration, and cyclic voltammetry parameters were carefully investigated, the oxide particles could not be incorporated into the polymer matrices.

With the direct mixing method, C-$LiFePO_4$/PPy, PAn and PTPA cathodes were prepared. PPy was polymerized from a pyrrole monomer with sodium ptoluenesulfonate dopant and $(NH_4)_2S_2O_8$ as oxidizer in deionized water. PAn was synthesized from aniline with $(NH_4)_2S_2O_8$ as oxidizer in water. PTPA was also obtained via chemical polymerization with triphenylamine as monomer and $FeCl_3$ as oxidizer in $CHCl_3$ solution. No improvement in capacity or rate capability was observed. Instead, composite materials were prepared with simultaneous polymerization of monomer with $LiFePO_4$ in the precursor solution. $LiFePO_4$ were well coated by the polymer. Figure IV-2 shows the capacity and cyclability of a C-$LiFePO_4$/PAn cathode with added C/PTFE. Compared with the conventional C-$LiFePO_4$/C/PTFE cathode, the capacity is enhanced at 0.1–5C. The cycle stability is good even at 5C. Preliminary results show that the capacity with 5C charging can reach 80% of theoretical capacity.

Recently, this work further focused on the chemically-polymerized C-$LiFePO_4$/PPy and PAn composite cathodes and investigated the effect of the polymer content on the capacity and rate capability. The C-$LiFePO_4$/polymer composites with different PPy or PAn contents were fabricated and tested. The composite with ~7 wt% polymer exhibits the best rate capability, shown in Figure IV-1 (left). The cell was charged and discharged from 0.1C to 20C. Even at 10C, the electrode could be charged up to 110mAh/g, almost 70% of its theoretical capacity. Note that the cell can be simultaneously charged and discharged at a high current density, a procedure that leads to a large collapse in the capacity for most Li-ion batteries.

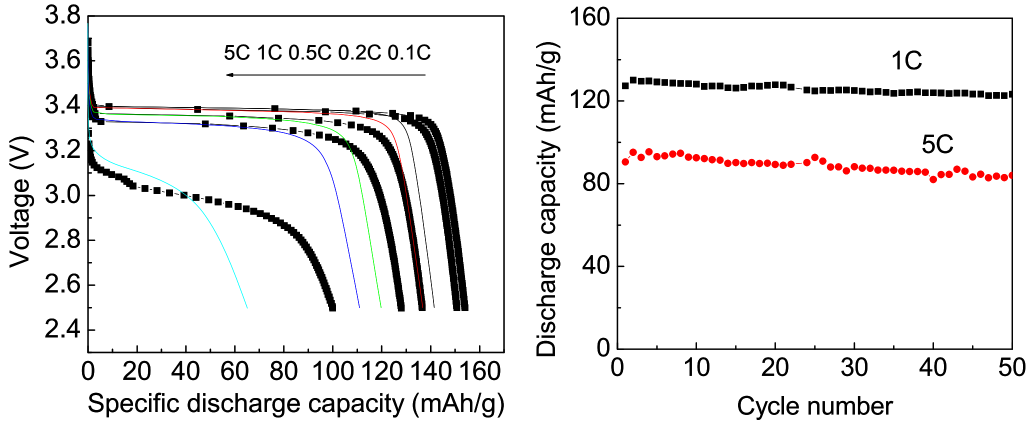

Figure IV-2. Rate capability of C-$LiFePO_4$/PAn. The light curves are for C-$LiFePO_4$ without PAn (left). Discharge capacity vs. cycle number for C-$LiFePO_4$/PAn at 1C and 5C (right).

The rate capabilities of several composite cathodes are compared in Figure IV-1 (left). All the cells were charged at 0.1C but discharged at 0.1–10C. The electrodeposited C-$LiFePO_4$/PPy, and chemically-synthesized C-$LiFePO_4$/PPy and PAn composites show an excellent rate capability. Their specific capacities are significantly enhanced, especially at high current densities, as compared with the conventional C-$LiFePO_4$/PTFE cathode. The electrodeposited C-LFP/PPy shows the best rate capability. For the chemically-synthesized LFP/PPy, the capacities at low rates are almost the same as those of C-LFP/C/PTFE, but the capacities at high rates are enhanced remarkably. The rate capability of C-LFP/PAn is between those of the two different LFP/PPy composites. However, no improvement in either capacity or rate capability was observed in a C-LFP/PTPA composite cathode.

***$LiFePO_4$-$FePO_4$ Phase Transition (Richardson)* -** This effort is a continued investigation into the nature of the $LiFePO_4$ to $FePO_4$ phase transition using hydrothermal crystals to visualize the distribution of phases and the effects of the sizeable mismatch in lattice parameters between the stoichiometric end members. Li is extracted in a narrow transition that progresses in the direction of the *a*-axis, consuming $LiFePO_4$ and leaving behind $FePO_4$. While crystals with a small *b*-axis dimension (200 nm) are rapidly and completely delithiated by an excess of bromine in acetonitrile, delithiation of 10 μm-thick crystals ceased after a ~1μm thick layer of $FePO_4$ has been formed (10% conversion) because the moving transition zone passed across the crystal face before it could penetrate deeper into the crystal. Even when exposed to the more powerful oxidizing agent, NO_2BF_4, no further delithiation occurs because access to the underlying $LiFePO_4$ is blocked. The latter reagent removes 30% of the Li from fresh crystals, however, and induces severe cracking in both phases due to the large expansion in the direction of the *c*-axis, accompanied by contraction in the *a* direction (Figure IV-3). The greater penetration depth for delithiation by NO_2BF_4 suggests that movement of Li in the transition zone is limited by electron conduction as well as ion mobility. This is consistent with the conclusions of Ceder and co-workers, who emphasize the strong coupling between ion mobility and local electronic structure.

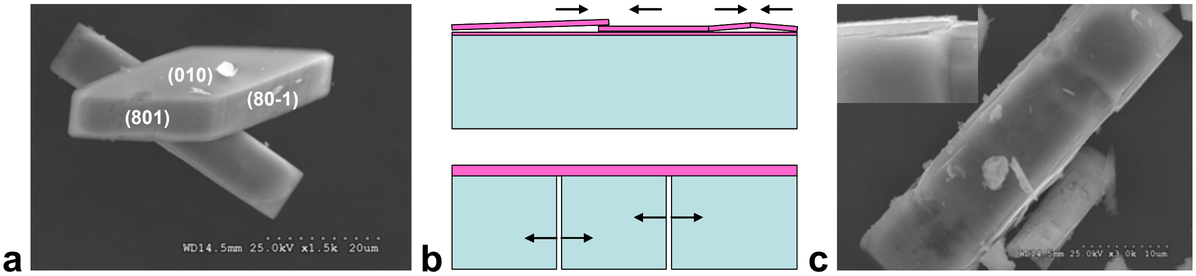

Figure IV-3. a) Fresh hydrothermal crystals measuring 15 μm x 10 μm x 40 μm; b) brittle fracture modes for an expanding surface layer strongly bonded to a rigid substrate; c) brittle fracture in partially delithiated crystal.

***Li_xFePO_4 Solid Solutions Intermediate Line Phases (Richardson)* -** The formation of single phase Li_xFePO_4 solid solutions at elevated temperature, subsequent demixing on cooling, and aging behavior at room temperature were monitored on samples with various crystal sizes and/or Li content. For the entire Li range, only two intermediate phases, $Li_{0.60}FePO_4$ and $Li_{0.34}FePO_4$, persist in the cooled crystals. Their presence and metastability at room temperature depend on the global Li content of the sample and the size of the *ac* cross section in the crystals. A room temperature phase diagram (Figure IV-4) for cooled Li_xFePO_4 solid solution crystals with dimensions 4μm x 2μm x 0.2μm was constructed based on Rietveld refinement of XRD patterns. In the low and high Li content regions, two-phase mixtures of $Li_{0.34}FePO_4$/$FePO_4$ and $Li_{0.60}FePO_4$/$LiFePO_4$, respectively, are observed.

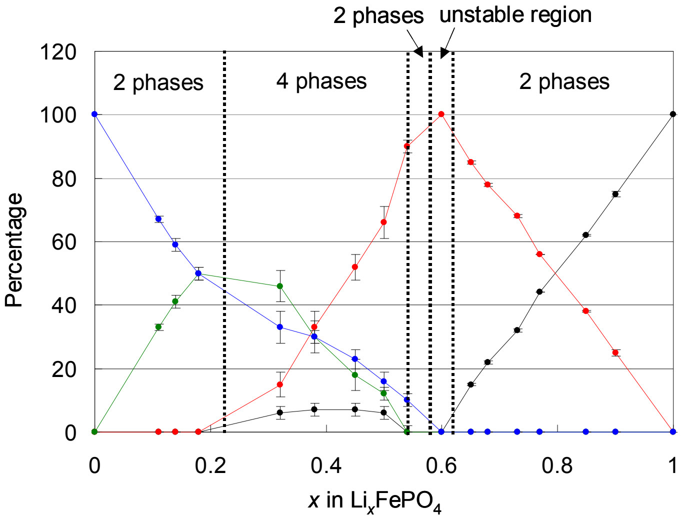

Figure IV-4. Room temperature phase diagram of Li_xFePO_4 crystals after cooling from a solid-solution state. (●) $LiFePO_4$ (●) $Li_{0.60}FePO_4$ (●) $Li_{0.34}FePO_4$ (●) $FePO_4$

Efforts to prepare a pure sample of $Li_{0.60}FePO_4$, which forms as a transient intermediate during the conversion of two-phase mixtures to single phase solid solutions on heating and precipitates during cooling, were not successful. It disproportionated into the end members during the cooling process, until amounts of one or the other end member sufficient to form a 10 nm layer in the *ac* plane had accumulated. When enough $FePO_4$ is formed, $Li_{0.34}FePO_4$ begins to appear, presumably between $Li_{0.60}FePO_4$ and $FePO_4$ to minimize the strain energy at the *ac* phase boundary. The chemical and electrochemical Li extraction/insertion processes in cooled crystals containing these intermediates differ from those observed in the freshly-prepared crystals.

Intermediate phase electrodes were prepared by casting a slurry mixture of carbon black, PVdF, and $Li_{0.68}FePO_4$ crystals (that had been heated to form a single-phase solid solution and then cooled) onto aluminum foil. These crystals contained 80% $Li_{0.60}FePO_4$ (an intermediate line phase) and 20% $LiFePO_4$. The intermediate phase was found to be stable during the mixing and casting process, and did not disproportionate when wetted with the electrolyte. It did, however, begin to slowly disproportionate if the freshly cast electrode was dried above 120ºC. Electrodes large enough for XRD measurements were cut and mounted in a beaker cell in the glovebox.

Because of the high $Li_{0.68}FePO_4$ electrode resistance, which results from the large, uncoated crystals, experiments were carried out under potentiostatic conditions. The applied potential was 4.2 V during charging and 2.5 V during discharging. After the desired amount of Li was extracted or inserted, the electrode was removed from the cell and washed free of electrolyte. Figure IV-5 compares the diffraction patterns of the electrode at various stages of charge and discharge. During the initial stages of charging (Figure IV-5a), $LiFePO_4$ was consumed, and a new line phase which had not been seen in thermal studies, $Li_{0.10}FePO_4$, began to appear when the total amount of Li in the electrode approached 0.60. Upon further charging, the $Li_{0.60}FePO_4$ intermediate phase was converted to $Li_{0.10}FePO_4$, and another intermediate phase, $Li_{0.34}FePO_4$, formed in the electrode. Near the end of charge, $Li_{0.10}FePO_4$ was converted to $FePO_4$. Significant amounts of $Li_{0.60}FePO_4$ and $Li_{0.34}FePO_4$ remained even when no more Li could be extracted.

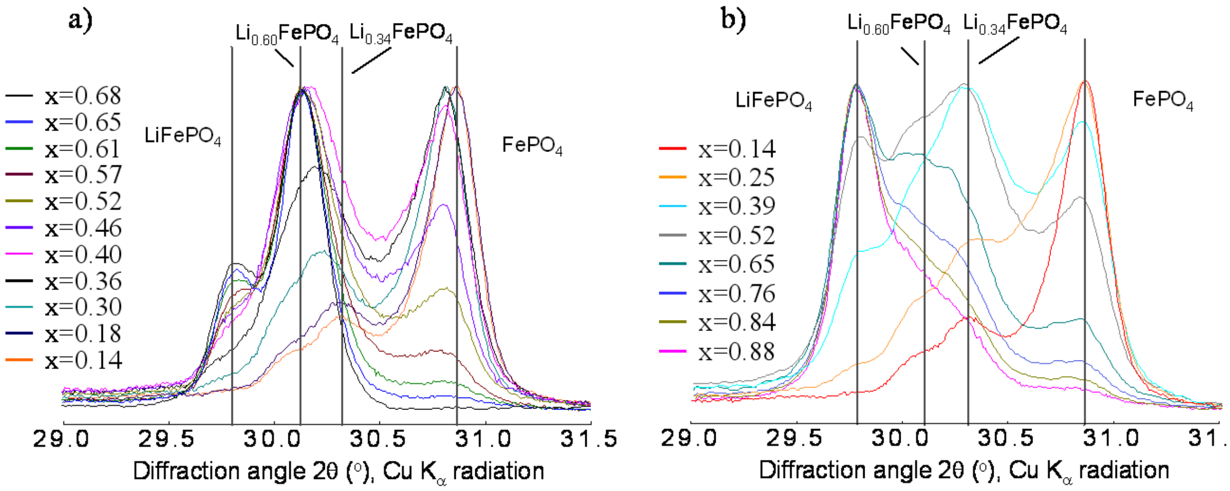

Figure IV-5. *Ex situ* XRD patterns of a $Li_{0.68}FePO_4$ solid solution electrode at various stages of electrochemical extraction and insertion of lithium. a) charging at 4.2 V; b) discharging at 2.5 V.

The electrode was then discharged in the same manner, XRD profiles are shown in Figure IV-5b. As Li was inserted into the electrode, the amounts of both $LiFePO_4$ and $Li_{0.6}FePO_4$ increased, and $Li_{0.34}FePO_4$ began to appear. $Li_{0.10}FePO_4$ was not detected during discharge. The relative amount of each phase in the electrode varied depending on the discharge state, and was very similar to that found in cooled solid solution samples with the same global lithium content. The gradual conversion of one phase to another indicated that the line phases participated as intermediates in the transformation of $FePO_4$ to $LiFePO_4$. In contrast, $Li_{0.10}FePO_4$ was the only intermediate phase observed during charging of pure $LiFePO_4$.

***Electrode Modeling and Optimization (Wheeler)* -** To understand the factors that limit the performance of relatively highly loaded porous electrodes, this group is exploring the role of electronic and liquid phase resistances. Thicker electrodes increase energy density and to a lesser degree power density, which are both important for PHEVs. In addition, they can contribute to unit cost savings. Recent work involved designing new experiments for measuring electronic and liquid-phase resistances in porous cathodes, and improving the porous electrode model to better match a range of experimental observations.

This work is of a general nature, not limited to one particular active material, and should permit a more quantitative understanding of issues such as transport that largely determine porous electrode performance. These tools will allow better understanding of the properties and structure to aid in developing improved electrode morphologies to increase energy density without decreasing power density of cells.

The current porous battery model provides insight into the effect of calendaring (porosity) on the electrochemical performance of the battery. In Figure IV-6 are model and experimental discharge curves for two different porosities. Porosity strongly affects the liquid-phase mass-transport as well as electronic resistances in porous cathodes. The model suggests that in order to maintain power density for cells with relatively high loading, it is important to optimize the porosity, a variable that is not normally considered important for thin cells.

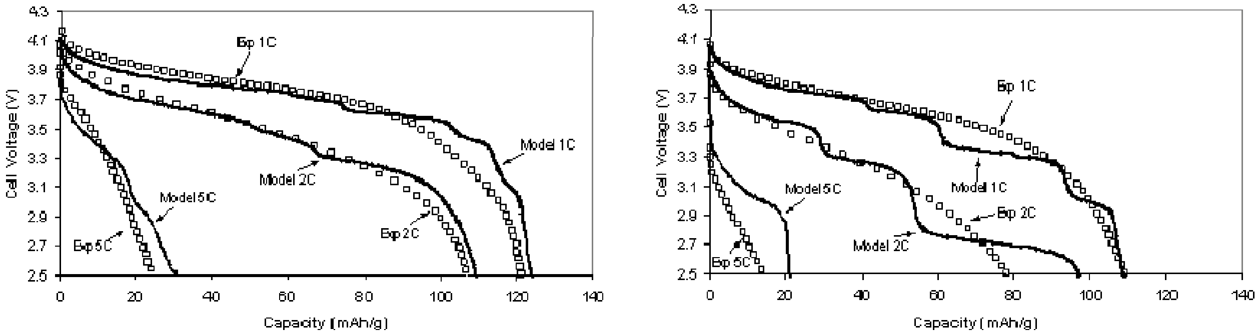

Figure IV-6. Model and experimental discharge comparisons for two porosities, left has a loading of 1.62mA/cm^2 with porosity=0.43, right has a loading of 1.53mA/cm^2 with porosity=0.71.

Other work shows that the ionic and electronic transport in the porous cathode is significantly below that predicted by the Bruggeman relation that is often used in macroscopic battery models. In order to correctly model and optimize cells it is important to know transport properties accurately. For instance, for porous cathodes with $LiFePO_4$, the liquid-phase transport appears to be a factor of 10-20 below that predicted by the Bruggeman relation as determined by modeling and experimentation. Similarly, the electronic conductivity is many times lower than what would be expected from intrinsic material conductivities.

$LiMPO_4$/C Nanotube Co-Synthesis (M=Fe, Mn, Co, Ni) (Doeff) **-** This project is exploring ways to produce high rate metal phosphate cathode materials by co-synthesizing them with conductive carbon components such as nanotubes or nanofibers. This bypasses cost and fabrication issues associated with mixing nanotubes or fibers into electrode slurries. In 2007, it was found that synthesis via combustion methods led to $LiMPO_4$ composites containing nanotubes or fibers in a convenient one-step process.

For example, a nanotube in a $LiFePO_4$/C composite (4.15% C) synthesized *via* a combustion route is shown in Figure IV-7.

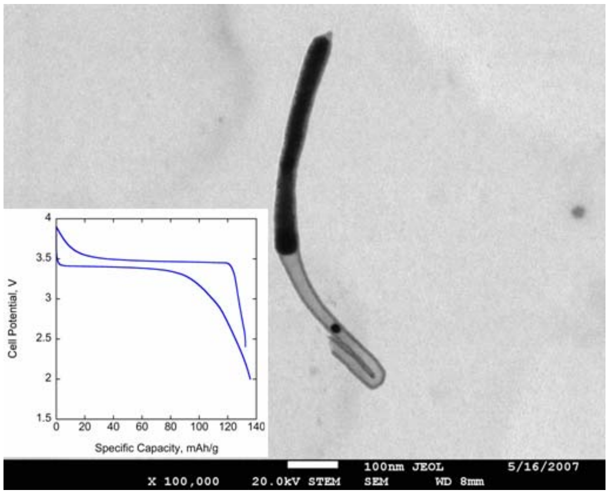

Figure IV-7. Carbon nanotube in $LiFePO_4$ sample and first cycle in Li cell.

Under other synthesis conditions, nanofibers with amorphous carbon are produced. Products processed with urea or citric acid have high (but variable, depending upon conditions) carbon contents, but those made with glycine alone as the fuel source are nearly carbon-free. Addition of pyromellitic acid prior to combustion can be used to increase carbon content and control structure. $LiMPO_4$ products, where M = Mn, Ni or Co, have also been synthesized *via* combustion.

Mixed $LiFe_{1-y}M_yPO_4$ Materials (Yoon/Yang) - *In situ* XAS using hard X-ray (>1000 eV) beamlines has been developed to study the electronic and local structure of transition metal ions in electrode materials for Li batteries. *In situ* XAS studies were carried out on the $LiFe_{1-y}M_yPO_4$ cathode materials, which show promise for higher energy density batteries for PHEVs. Figure IV-8 shows that for the undoped $LiFePO_4$, the charge compensation during lithium de-intercalation was achieved by oxidizing the Fe^{2+} to Fe^{3+} and only one plateau was observed in the charge curve. When 50% of Fe was replaced by Co, two plateaus were observed in the charge curve. The XAS spectra show that the lower plateau about 3.6 V corresponds to the Fe^{2+} to Fe^{3+} oxidation, while the higher plateau at about 5.0 V corresponds to the oxidation of Co^{2+} to Co^{3+}.

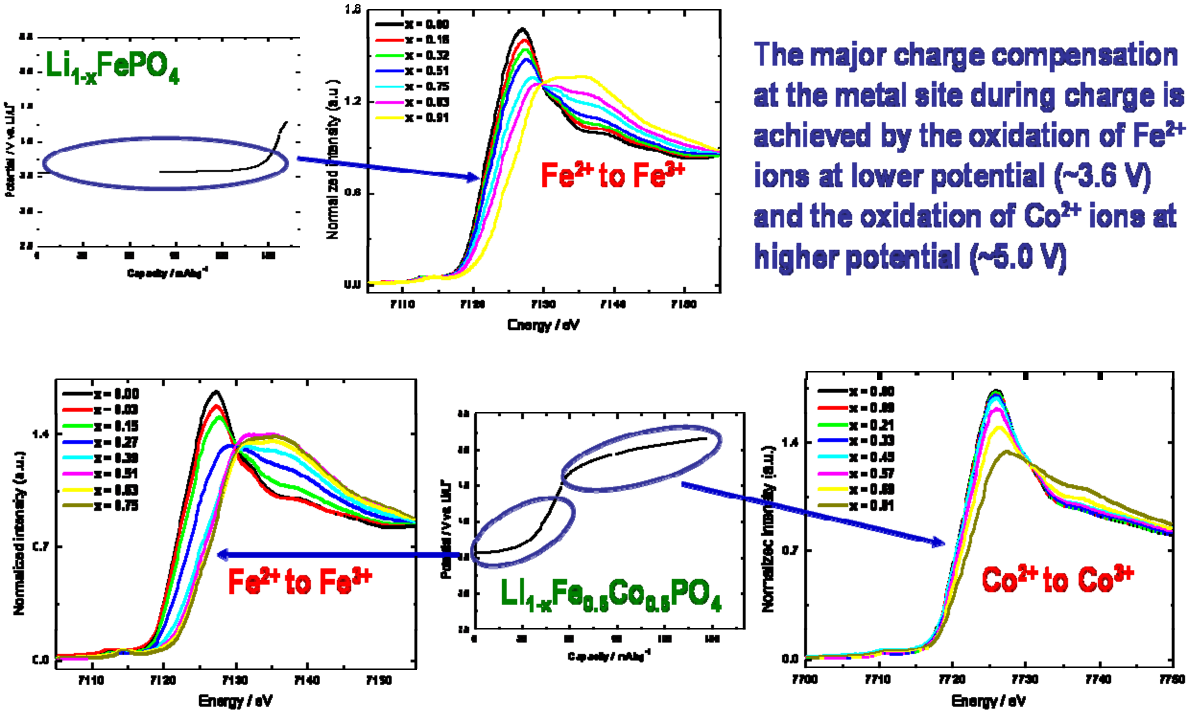

Figure IV-8. *In situ* Fe K-edge XAS for $Li_{1-x}FePO_4$ and Fe and Co K-edge for $Li_{1-x}Fe_{0.5}Co_{0.5}PO_4$ during charge.

IV.A.2 Spinel and Composite Systems: Performance and Limitations

Objectives

The objectives of this work are to develop low-cost spinel manganese oxide compositions that offer excellent capacity retention, high rate, low irreversible capacity loss, and good storage characteristics at elevated temperatures. Another objective is to understand the causes of capacity and power fade in current materials, including spinels, to permit an extension of their operating range to higher voltages and thus higher energies.

Approach

The approach to improving Mn-spinel performance includes developing a firm scientific understanding of the factors that control or influence its electrochemical performance and utilize that knowledge to design and develop improved Mn-spinel compositions. In this regard, cationic and anionic substitutions are tested, and characterization and electrochemical evaluation of the materials in cells are performed. In addition, materials and cells are tested using standard test procedures, and are being compared to commercially available spinel materials. A related approach involves the evaluation of spinel/layered electrode composite materials in which the layered material leads to both increased energy and life when the electrode is subjected to a high voltage formation charge.

A second approach is to continue the search for, develop, and characterize low-cost Mn oxide-based cathodes. The major focus remains on high-voltage, high-capacity electrodes with two-component integrated structures, *e.g.,* ‘layered-layered’ $xLi_2M'O_3\bullet(1-x)LiMO_2$ and ‘layered-spinel’ $xLi_2M'O_3\bullet(1-x)LiM_2O_4$ electrodes in which M′ is predominantly Mn and M is selected mainly from Mn, Ni and Co. These electrodes are evaluated in full cells against various anode materials including the intermetallic systems described in the anode project in Section IV.B.

A first principals investigation into the thermodynamics of acid attack reactions, in layered and spinel materials, is being carried out to help understand the fundamental mechanisms associated with cathode dissolution, capacity and power fade.

Finally, one group is investigated the thermal stability and Mn dissolution characteristics of various Mn spinel materials as a function of temperature and state of charge using new standardized test procedures.

Accomplishments

***Improved Capacity Retention in Mn Spinel Cathodes (Manthiram)* -** Previous work by this group has shown that optimized spinel compositions such as $LiMn_{1.8}Li_{0.1}Ni_{0.1}O_{3.8}F_{0.2}$ exhibit improved electrochemical performances with both metallic Li and graphite anodes compared to conventional $LiMn_2O_4$ cathodes. The improved cyclability at ambient and elevated temperatures is due to reduced Mn dissolution. A way to further reduce Mn dissolution is to trap trace amounts of protons present in the electrolyte within another material in the initial stage of the charge-discharge process. This group has shown[9] that layered oxides such as $Li_{1-x}CoO_2$, $Li_{1-x}Mn_{0.5}Ni_{0.5}O_2$, and $Li_{1-x}Mn_{1/3}Ni_{1/3}Co_{1/3}O_2$ incorporate protons into the lattice at deep chemical delithiation with an oxidizer NO_2BF_4 in acetonitrile medium while layered $Li_{1-x}NiO_2$,

---

[9] J. Choi, E. Alvarez, T.A. Arunkumar, and A. Manthiram, *Electrochem. Solid-State Lett.* **9**, A241 (2006).

orthorhombic $Li_{1-x}MnO_2$, spinel $Li_{1-x}Mn_2O_4$, and olivine $LiFePO_4$ do not. As certain layered oxide cathodes at low Li contents could act as an effective proton scavenger, this group has added a small amount of $LiCoO_2$ to $LiMn_{1.8}Li_{0.1}Ni_{0.1}O_{3.8}F_{0.2}$ and charged the cathode to high voltages (4.7 V) in the first cycle to capture trace amounts of protons.

Figure IV-9 shows the cycling performances of Li-ion cells fabricated with spinel $LiMn_2O_4$, a mixture of $LiMn_2O_4$ and $LiCoO_2$ (70:30), spinel $LiMn_{1.8}Li_{0.1}Ni_{0.1}O_{3.8}F_{0.2}$, and a mixture of $LiMn_{1.8}Li_{0.1}Ni_{0.1}O_{3.8}F_{0.2}$ and $LiCoO_2$ (70:30) cathodes, all with graphite anodes at 60°C at C/5 rate. (Experiments reveal that the 70/30 wt % ratio exhibits the best combination of cyclability and power.) The $LiMn_{1.8}Li_{0.1}Ni_{0.1}O_{3.8}F_{0.2}$ cathodes both with and without $LiCoO_2$ exhibit better performance than the $LiMn_2O_4$ cathode alone due to a suppression of Mn dissolution. Interestingly, with the spinel + layered oxide mixtures, charged to 4.7 V in the first cycle and holding it for 2 hours, exhibits a further improvement in capacity retention compared to charging up to 4.3 V. The spinel cathode shows similar capacity retention irrespective of the first charge voltage (4.3 or 4.7 V).

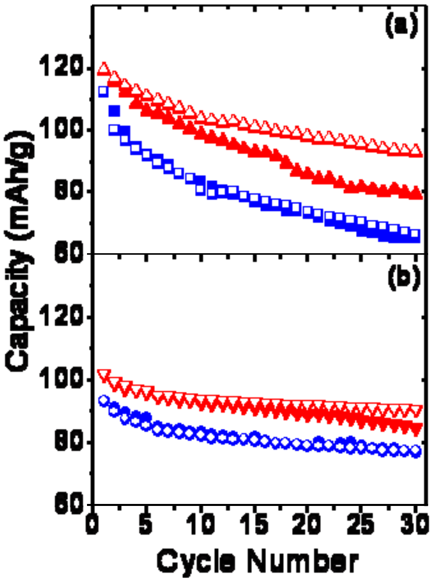

Figure IV-9. Cycling performance of Li-ion cells fabricated with graphite anode. (a) (■) $LiMn_2O_4$ between 3.5 and 4.3 V, (□) $LiMn_2O_4$ between 3.5 and 4.3 V after charging up to 4.7 V during first charge, (▲) 70 wt% $LiMn_2O_4$ + 30 wt% $LiCoO_2$ between 3.5 and 4.3 V, and (△) 70 wt% $LiMn_2O_4$ + 30 wt% $LiCoO_2$ between 3.5 and 4.3 V after charging up to 4.7 V during first charge, (b) (●) $LiMn_{1.8}Li_{0.1}Ni_{0.1}O_{3.8}F_{0.2}$ between 3.5 and 4.3 V, (○) $LiMn_{1.8}Li_{0.1}Ni_{0.1}O_{3.8}F_{0.2}$ between 3.5 and 4.3 V after charging up to 4.7 V during first charge, (▼) 70 wt% $LiMn_{1.8}Li_{0.1}Ni_{0.1}O_{3.8}F_{0.2}$ + 30 wt% $LiCoO_2$ between 3.5 and 4.3 V, and (▽) 70 wt% $LiMn_{1.8}Li_{0.1}Ni_{0.1}O_{3.8}F_{0.2}$ + 30 wt% $LiCoO_2$ between 3.5 and 4.3 V after charging up to 4.7 V during first charge. The first cycle discharge capacities are not included as they vary with first cycle charge voltage of 4.3 or 4.7 V.

This group has also investigated $LiMn_{1.8}Li_{0.1}Ni_{0.1}O_{3.8}F_{0.2}$ + $LiNi_{1/3}Mn_{1/3}Co_{1/3}O_2$ and $LiMn_{1.8}Li_{0.1}Ni_{0.1}O_{3.8}F_{0.2}$ + $LiNi_{1/2}Mn_{1/2}O_2$ cathodes in Li-ion cells with a graphite anode. Cyclability data at 60°C reveals that charging up to 4.7 V in the first cycle and holding it for two hours leads to an improvement in capacity retention similar to that found with the $LiCoO_2$. Evaluation of Mn dissolution in coin cells after storing for 7 days reveals that it is suppressed by initial charging of the spinel + layered oxide mixtures to 4.7 V via a trapping of protons within the oxide lattice. Thus, the addition of a layered oxide into spinel cathodes with an initial deep charging helps to reduce the capacity fade compared to spinel alone cathodes.

Figure IV-10 shows that the rate capability of the spinel is not sacrificed by $LiCoO_2$. The experiments were carried out by charging the cells up to 4.7 V at C/20 rate in the first cycle, holding for 2 h, discharging to 3.5 V at C/10 rate in the first cycle, charging at C/10 in the second cycle, and then discharging at rates of C/10 to 4C to assess the rate capability. Evaluation of the capacity values after storing at 60°C for 7 days at various DODs reveals that the initial charging to 4.7 V with a layered oxide leads to improved storage properties.

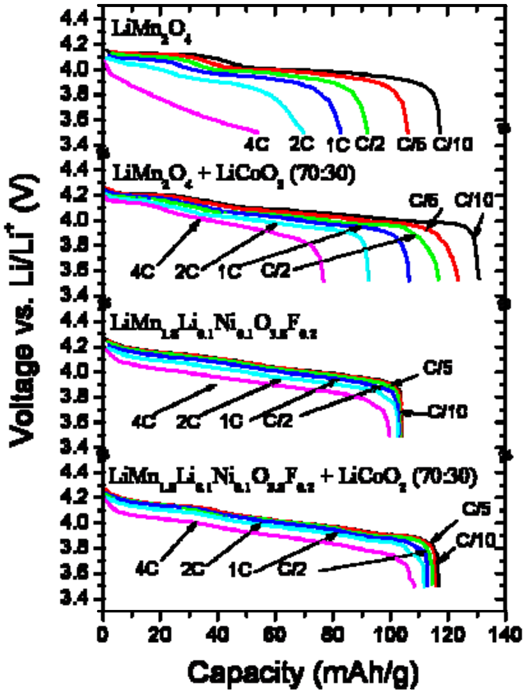

Figure IV-10. Comparison of the discharge profiles at various C rates of coin cells with metallic Li anode, illustrating the rate capabilities of $LiMn_2O_2$, 70 wt% $LiMn_2O_4$ + 30 wt% $LiCoO_2$, $LiMn_{1.8}Li_{0.1}Ni_{0.1}O_{3.8}F_{0.2}$, and 70 wt% $LiMn_{1.8}Li_{0.1}Ni_{0.1}O_{3.8}F_{0.2}$ + 30 wt% $LiCoO_2$.

***Thermal Analysis of Mn Spinel Materials (Battaglia)* -** Samples of Toda's $LiMn_{1.85}Li_{0.15}O_4$ and Dr. Manthiram's $LiMn_{1.85}Li_{0.075}Ni_{0.04}Cu_{0.035}O_4$ (referred to as BATT) were prepared for thermal gravimetric analysis (TGA). All samples were pressed into aluminum screens. The samples to be delithiated were done in a Swagelok cell, after which they were washed with DMC and dried over night at 120°C in a vacuum chamber. Results are shown in Figure IV-11.

These two materials behave very similarly under thermal stress. The lithiated materials show an initial weight loss at ~660°C, followed by a second at ~900°C. It appears that the weight losses are attributed to oxygen release and that the first loss is associated with transition of the Mn average valence from Mn[~+3.66] to Mn[~+4.3] and the second loss to the Mn average valence going to Mn[~+3]. The delithiated materials also behave similarly to each other and to the lithiated

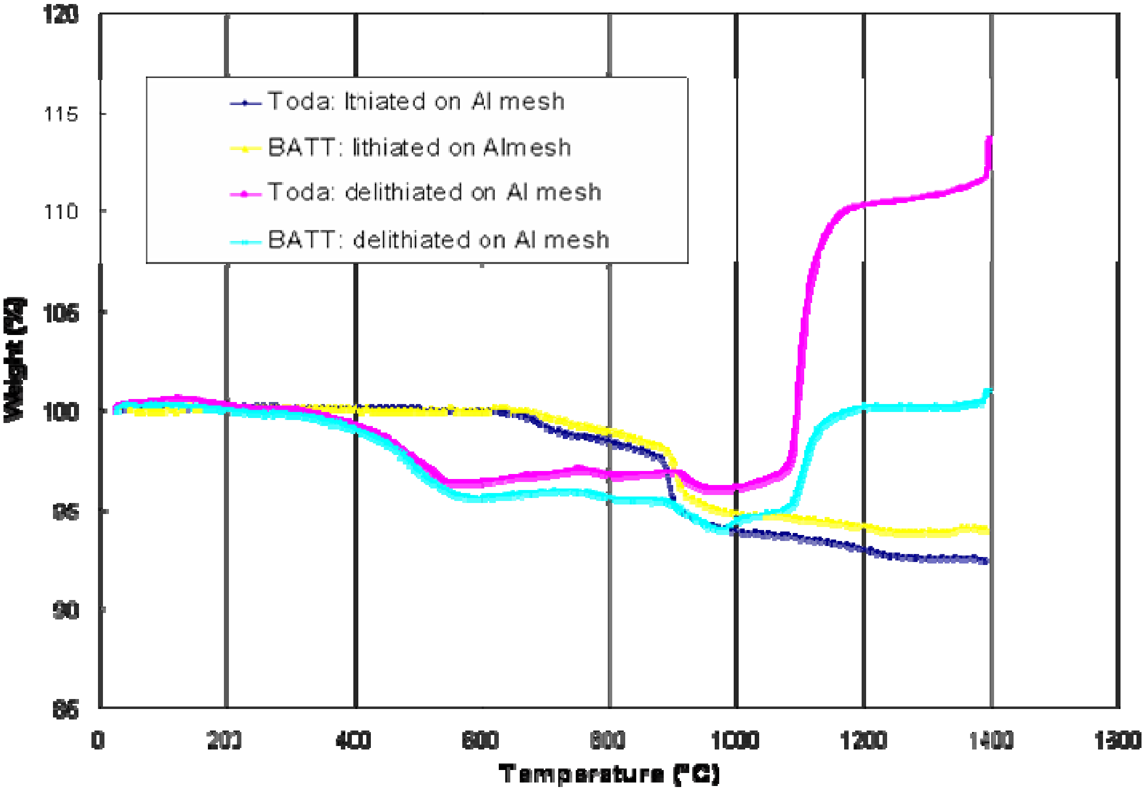

Figure IV-11. TGA of two Mn-spinel cathodes powders with and without lithium.

materials. The first transition starts at 300°C and ends 450°C, immediately followed by the second transition that ends at 530°C. Based on the literature, these reactions are expected to occur at lower temperatures in the presence of electrolyte.

Comparison on Mn Dissolution Rates (Battaglia) **-** The effect of electrolyte conditions on the dissolution of Mn from a Li-doped Mn-spinel from Toda was investigated. Battery grade solvents of EC and DEC were combined to make 120 g of 1:1 w/w EC:DEC solution. 25 grams of the solvent was added to one vessel. In another vessel, enough $LiPF_6$ was combined with solvent to make 50 g of 1M $LiPF_6$ at room temperature. This quantity was stored in two separate vessels in equal amounts. In one was added 200 ppm water. In a fourth vessel, enough LiTFSI was added to the solvent to make 25 g of 1 M LiTFSI solution. In each of the four vessels was added 5 g of Toda's spinel. The samples were placed in a 55°C chamber that rotated at one revolution per 4 seconds, reducing liquid phase diffusion limitations. The chamber was kept in a glove box to limit the intrusion of water. Two ml samples were removed from each vessel at 1 week, 4 weeks, and 9 weeks. In the two vessels without $LiPF_6$, there was no measurable Mn found in solution using ICP-OES. After 1 week, in the two samples containing $LiPF_6$, there was ~50 ppm soluble Mn found in one and 80 ppm soluble Mn found in the sample containing the additional H_2O. Both samples displayed a monotonic increase with time over the 9-week period.

Next, the Toda and BATT fully lithiated materials were tested for Mn dissolution in 1M $LiPF_6$, EC:DEC (1:1) using the same apparatus and test conditions as above. Figure IV-12 shows that the samples dissolve Mn at roughly the same rate.

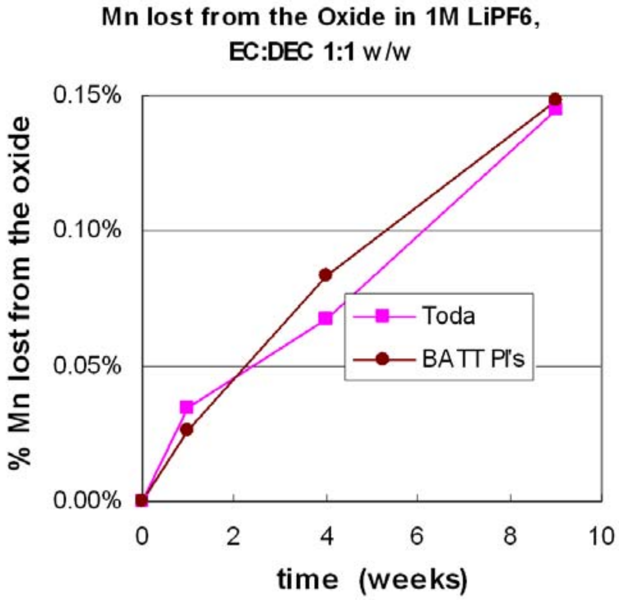

Figure IV-12. Toda and BATT Mn-spinel sample Mn dissolution. The amount of Mn found in solution was measured over time using ICP-OES. The amount of Mn found in the electrolyte was used to calculate the amount of Mn that was lost from the oxide.

Thermodynamics of Acid-attack Reactions (Thackeray) **-** The thermodynamics of acid-attack reactions involving cathode materials is being analyzed using first principles calculations. This is treating dissolution reactions and proton-for-Li ion-exchange reactions for Li_xCoO_2 and spinel $Li_xMn_2O_4$. Despite improvement achieved by protective coatings to shield cathodes from acid-promoted dissolution from water in the electrolyte, a better fundamental understanding of the reactions in acid could assist battery developers. Although dissolution *rates* in acid cannot presently be predicted from first principles, *free energies* for acid-promoted reactions of cathode materials can be calculated with reasonable accuracy. Free energies of the reactant and product species can be ascertained from a combination of measured properties (particularly for aqueous species) and first principles calculations (particularly for solid phases). Calculations of the reaction free energies for the dissolution and protonation reactions of Li_xCoO_2 in aqueous acid are presented in Figure IV-13.

Work by Gupta and Manthiram provide evidence for the disproportionation reaction, in which the role of F^- ions derived from the $LiPF_6$ electrolyte salt is ignored for simplicity:

$$2x\ H^+(aq) + Li_xCoO_2 \rightarrow (1-x/2)\ CoO_2 + x\ H_2O(aq) + x/2\ Co^{2+}(aq) + x\ Li^+(aq) \qquad (1)$$

Recent measurements by Aurbach et al. have detected Co_3O_4 in $LiCoO_2$ electrodes immersed in a $LiPF_6$/EC-DMC electrolyte solution that suggest an alternative disproportionation reaction:

$$4\ Li_xCoO_2 + 4x\ H^+ \rightarrow (4-3x)\ CoO_2 + x\ Co_3O_4 + 4x\ Li^+ + 2x\ H_2O \qquad (2)$$

The two-step sequence of reaction (2) followed by the dissolution of Co_3O_4 in acid,

$$Co_3O_4 + 4\ H^+ \rightarrow CoO_2 + 2\ Co^{2+} + 2\ H_2O \qquad (3)$$

is equivalent to the direct disproportionation reaction (1). An alternative to dissolution is protonation, the simplest form of which is the reaction

$$x\,H^+ + Li_xCoO_2(s) \rightarrow xLi^+ + (1-x)\,CoO_2 + x\,HCoO_2; \qquad (4)$$

although the co-intercalation of Li and H to form $Li_xH_yCoO_2(s)$ is also a possibility. Figure IV-13 shows schematically the calculated reaction free energies, at x=1, pH=0, for reactions (1)-(4); the abscissa is arbitrarily chosen as the average oxidation state for Co in the least oxidized product phase. The largest driving force (absolute ΔG^0) is obtained for the dissolution reaction (1); the partial disproportionation reaction (2) and the protonation reaction (4) have lower driving force. Dissolution is favored over protonation by a constant free energy ratio, independent of x.

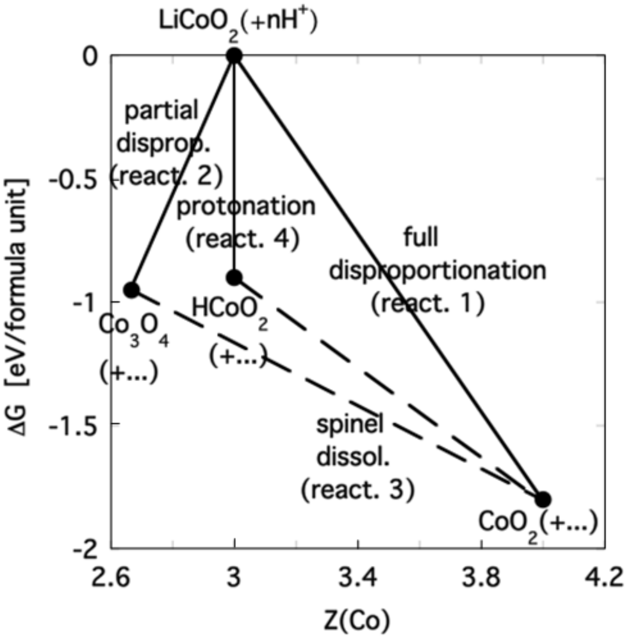

Figure IV-13. Schematic representation of the free energy magnitude (ΔG) for various reactions of $LiCoO_2$ with acid.

Protonation, although not necessarily benign, is less damaging than dissolution, so it is natural to focus engineering efforts on the latter. This provides no information regarding dissolution rates; however, it is reasonable to expect that lowered driving forces $|\Delta G^0|$ will lead to reduced dissolution rates. One approach to restrict dissolution $|\Delta G^0|$ is to modify the transition metal oxidation states and sublattice composition, *e.g.*, by the substitution of Li for Mn in $LiMn_2O_4$.

IV.A.3 Nickelate Systems: Performance and Limitations

Objectives

The primary objectives of the high energy portion of this work are to find lower-cost and higher-capacity cathodes, exceeding 200mAh/g, and for the high rate portion to find HEV compatible cathodes, both of which are based on environmentally benign materials.

Approach

One approach is to investigate layered $Li[NiMnCo]O_2$ electrodes with reduced Co content, and/or reduced Ni content, to reduce cost and improve abuse tolerance, respectively. Another is to investigate low temperature synthesis approaches to further lower cost. These materials are synthesized, and characterized both structurally and for thermal and chemical stability, and then electrochemically evaluated in a variety of cell configurations.

Magnetic sensing is being used to estimate Ni disorder in $LiNi_{0.5}Mn_{0.5}O_2$. Ni disorder has been shown to be associated with poor Li dynamics in this promising cathode material.

In situ X-ray spectroscopy, including XANES and XAS among other techniques, is used to investigate the structural properties of layered cathode materials as a function of Li excess, charge and discharge state, and temperature.

Li-rich layered transition metal oxides composite cathodes are being investigated to understand their structure, and the origin of their relative high capacity using XRD diagnostics.

NMR, TEM, *in situ* diffraction and pair distribution function (PDF) studies have been performed to investigate the structure, stability (including thermal decomposition reactions), and rate capabilities of layered lithium nickel manganates charged to high voltages in an attempt to use existing materials at higher voltages, thus enabling higher energy density storage. Finally, new electrode materials based on layered oxysulfides have been fabricated and tested for capacity and stability.

Accomplishments

Layered Mixed Metal Oxides (Whittingham) - This work continues to explore $Li[NiMnCo]O_2$ compounds with Mn content above that of Ni while maintaining a 10% Co level. The advantages include lower cost (due to the low Co content) and improved safety (lower Ni content). The maximum Mn content in the stoichiometric $LiMO_2$ cannot exceed 50% without the formation of a second phase, possibly spinel [Figure IV-14(a)]. Rietveld refinement shows that the Ni^{2+} - Li^{+} disorder is similar in $LiNi_{0.4}Mn_{0.5}Co_{0.1}O_2$ and $LiNi_{0.45}Mn_{0.45}Co_{0.1}O_2$. Part of the Mn is reduced to 3+ in $LiNi_{0.4}Mn_{0.5}Co_{0.1}O_2$ in order to balance the charge, but the concentration of Mn^{3+} ions is not high enough to induce a Jahn-Teller distortion. Thus the layered structure is maintained during charging and discharging. In the first cycle [Figure IV-14(b)] $LiNi_{0.4}Mn_{0.5}Co_{0.1}O_2$ delivers 218 and 181 mAh/g for charge and discharge, respectively, as high as $LiNi_{0.45}Mn_{0.45}Co_{0.1}O_2$. Thus, it appears that the Mn content can be increased to 50%.

Recently it has been found that the layered structure could be maintained at Mn concentrations above 50% by increasing the Li and Mn content simultaneously. A layered material with the composition $Li_{1.1}Ni_{0.28}Mn_{0.55}Co_{0.07}O_2$, was synthesized. Rietveld refinement of the XRD pattern for this material shows a single phase with a layered structure except for extra peaks which may indicate a superlattice ordering of the transition metal layers caused by the increasing amount of Li and Mn. Further studies including synchrotron XRD, NMR and electron diffraction will be done to clarify this issue. The charge and discharge capacities of $Li_{1.1}Ni_{0.28}Mn_{0.55}Co_{0.07}O_2$ in the first cycle are as high as 285 and 200 mAh/g, respectively. When the cut-off voltage is extended to 4.8 V, additional capacity (245 mAh/g for the initial discharge) is obtained, indicating that extra capacity becomes available at 4.6-4.8 V possibly by removal of Li_2O from the structure. An *in situ* XRD test is being performed in collaboration with BNL to observe the structural changes in this complex material.

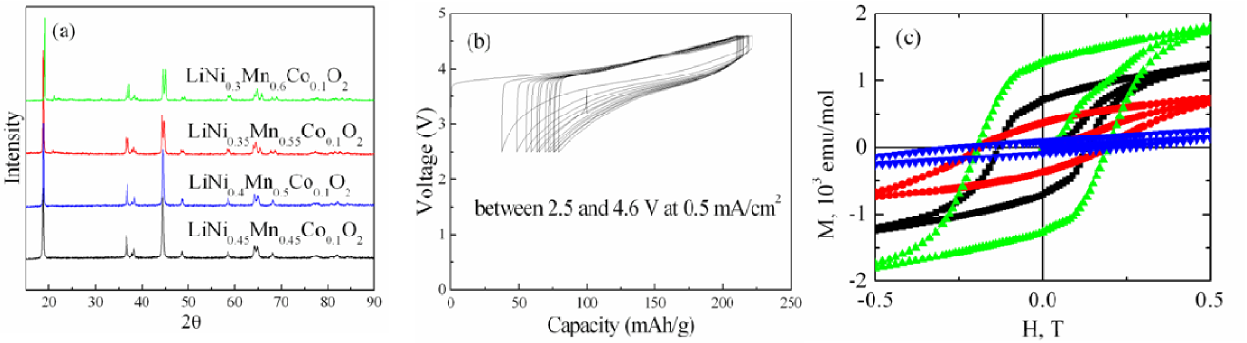

Figure IV-14. (a) XRD patterns of $Li[Ni_yMn_{0.9-y}Co_{0.1}]O_2$, $0.3 \leq y \leq 0.45$; (b) charge-discharge curves for $LiNi_{0.4}Mn_{0.5}Co_{0.1}O_2$ cycled between 2.5 and 4.6 V at 0.5 mA/cm^2; (c) magnetization curves of $NaNi_{0.5}Mn_{0.5}O_2$ (blue triangles), $LiNi_{0.5}Mn_{0.5}O_2$ ion-exchanged in: LiBr solution at 160-170°C (red circles); ion-exchanged at 280°C in molten salts (green triangles); and synthesized by high-temperature solid-state reaction (black squares).

Cobalt Lean Mixed Metal Oxides (Doeff) - The feasibility of substituting all or some of the Co with other metals in mixed metal oxides $Li[Ni, Co, Mn]O_2$ is under investigation. It was found that Al substitution of Co in the $Li[Ni_{1/3}Co_{1/3-y}Al_yMn_{1/3}]$ system raised the irreversible capacity, and lowered overall capacity. Better results were obtained for $Li[Ni_{0.4}Co_{0.2-y}Al_yMn_{0.4}]O_2$, where improved rate capability was observed for all substituted materials (Figure IV-15). Best results are found for y=0.05, which significantly outperforms all other materials at current densities above 0.5 mA/cm^2. Even at low rates, capacities between 4.3 and 2.0 V are barely affected by low-level Al substitution, although Co content is less than half of that in $Li[Ni_{1/3}Co_{1/3}Mn_{1/3}]O_2$.

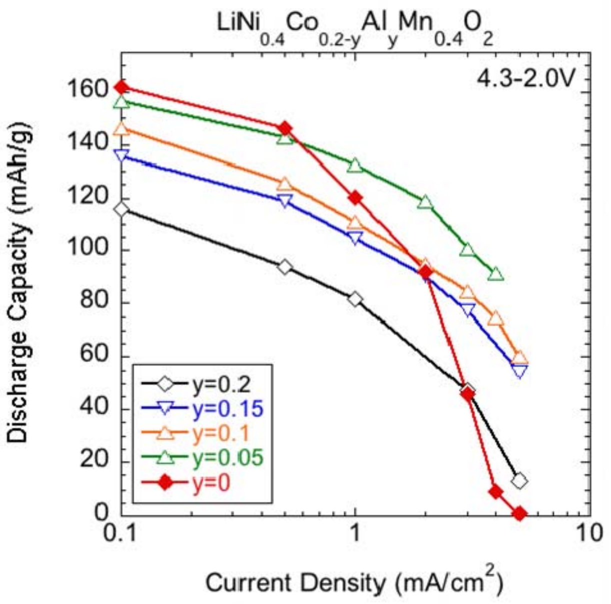

Figure IV-15. Rate behavior of $Li[Ni_{0.4}Co_{0.2-y}Al_yMn_{0.4}]O_2$ electrodes (y=0.05-0.2) in Li cells, 4.3-2.0V.

***In situ* X-Ray Spectroscopy of Layered Cathodes (Yoon/Yang) -** This project has been focusing on the $Li_{1+x}M_{1-x}O_2$ system which has complex atomic arrangements as the Li+ ions have a strong tendency to form a cation ordering with Mn^{4+} ions. This group has carried out Mn and Ni K-edge XAS for pristine $Li_{1+x}(Mn_{0.5}Ni_{0.5})_{1-x}O_2$ powders with varying excess Li content (x). Figure IV-16 shows normalized Mn and Ni K-edge XANES spectra of these powders as a function of excess Li (x). The Mn XANES spectrum does not exhibit any substantial changes indicating the oxidation state of Mn ions does not change with Li content. In contrast, the Ni edge continuously shifts to higher energy with increasing Li content. A comparison of these spectra with those of the Ni^{2+} and Ni^{3+} reference materials, indicates that the average oxidation state for Ni is ~2+ for the stoichiometric $LiMn_{0.5}Ni_{0.5}O_2$, and gradually increases to 3+ at x = 0.2, which was the highest excess Li content. Mn and Ni K-edge XAS results for pristine $Li_{1+x}(Mn_{0.5}Ni_{0.5})_{1-x}O_2$ powders suggest that Li_2MnO_3 or Li_2MnO_3-like phases are present, and the $Li_{1+x}(Mn_{0.5}Ni_{0.5})_{1-x}O_2$ compounds can be reformulated in a two-component composite notation as $2xLi_2Mn^{4+}O_3 \bullet (1-3x)Li(Ni^{2+}{}_{1-y}Ni^{3+}{}_{2y-1}Mn^{4+}{}_{1-y})O_2$ (y=(1-x)/[2(1-3x)]). Li_2MnO_3 or Li_2MnO_3-like domains are actively involved in the charge compensation process after first high voltage cycling, which provide this system an abnormally high capacity. So understanding the Li_2MnO_3 or Li_2MnO_3-like domains would be very helpful to designing high energy materials.

In addition, a new thermal *in situ* soft XAS technique is being developed, which will enable the monitoring of structural changes both at the surface and the bulk during thermal abuse conditions. Preliminary data suggest that the surface of the electrode is decomposed at much lower temperature than the bulk during the heating process.

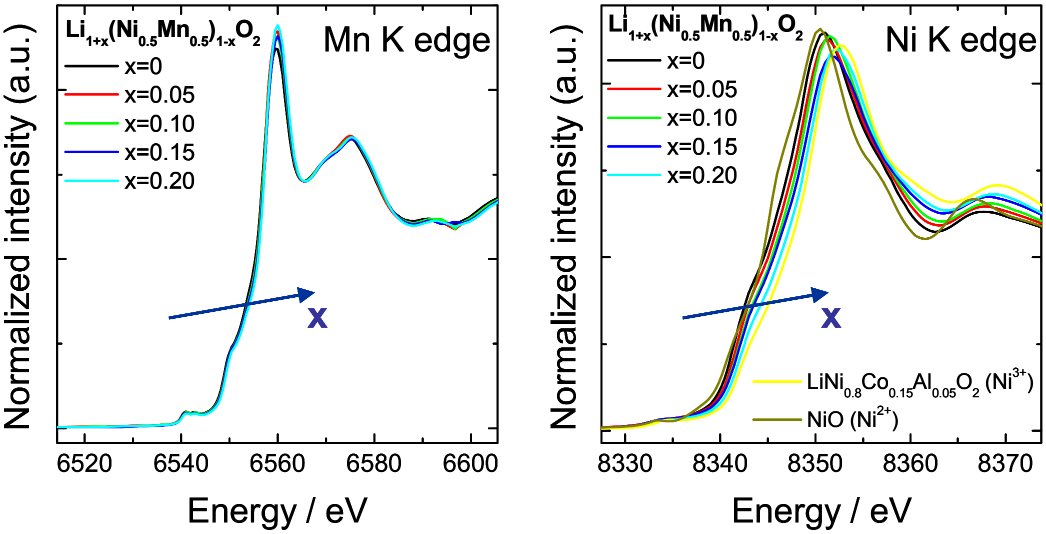

Figure IV-16. Normalized Mn and Ni K-edge XANES spectra of $Li_{1+x}(Mn_{0.5}Ni_{0.5})_{1-x}O_2$ powders as a function of x.

This group has also continued their investigation into the $Li_{1-x}Ni_{0.8}Co_{0.15}Al_{0.05}O_2$ (Gen 2) cathode. O K-edge XAS spectra of electrochemically delithiated Gen2 system are shown in Figure IV-17. The O K-edge XAS spectrum collected by the PEY mode (surface sensitive) plotted in Figure IV-17 (a) is dramatically different from that collected by the FY mode (bulk sensitive) shown in Figure IV-17 (b).

Pre-edge peaks below ~534 eV in these spectra correspond to the transition of an oxygen 1s electron to the hybridized state of the metal 3d and oxygen 2p orbitals, whereas the broad peaks above ~534 eV correspond to the transitions to hybridized states of oxygen 2p and metal 4sp orbitals. O K-edge XAS spectra collected by the FY mode show an intense absorption peak at ~528.5 eV which corresponds to a transition to the hybridized state of $Ni^{3+,4+}$ 3d – O 2p orbitals. In contrast, in the O K-edge XAS spectra collected by the PEY mode, an additional pre-edge peak at ~531.8 eV is observed, which corresponds to the hybridized state of Ni^{2+} 3d – O 2p orbitals. The observation of this transition indicates that a substantial amount of Ni ions at the surface of Gen 2 is in the form of Ni^{2+}. The reference spectrum of Li_2CO_3 is also plotted as a dashed line in Figure IV-17 (a). Another pre-edge peak at ~533.8 eV could be due to the existence of Li_2CO_3 on the surface. Li_2CO_3 is a common contaminant and gradually dissolves in the electrolyte during Li deintercalation. The peaks representing Li_2CO_3 disappear in the early stages of charging. As shown in Figure IV-17 (a), during the overcharge period when x is greater than 0.6, as the degree of electrochemical deintercalation increases (the x value increases), the integrated peak intensity at ~531.8 eV increases in the PEY mode, indicating the reduction of Ni^{3+} and Ni^{4+} ions to Ni^{2+} as a result of instability of the material at high charged states.

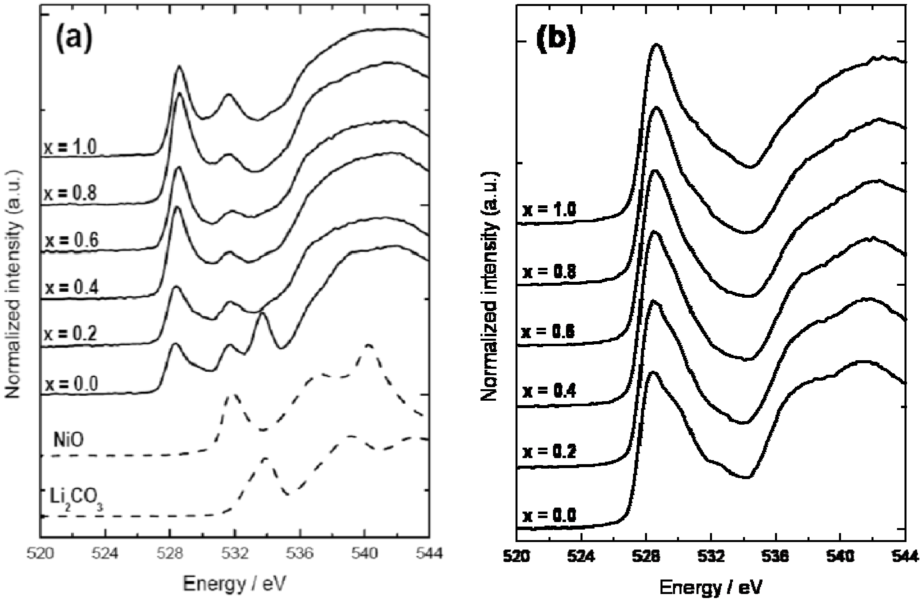

Figure IV-17. Normalized O K-edge XAS spectra of $Li_{1-x}Ni_{0.8}Co_{0.15}Al_{0.05}O_2$ electrode at different x values using (a) PEY method and (b) FY method.

Ni Disorder in $LiNi_{0.5}Mn_{0.5}O_2$ (Whittingham) **-** This task, in collaboration with Drs. Grey and Ceder, is focused on understanding Ni disorder in $LiNi_{0.5}Mn_{0.5}O_2$ synthesized by ion exchange from the sodium precursor. Magnetic properties were used to estimate Ni disorder obtained by various ion-exchange routes. The size of the magnetization loop increases with increasing Ni content in the Li layer[10]. It was found that ion exchange in molten salts is accompanied by diffusion of a significant amount of Ni from the transition metal to the Li layer. This confirms the Rietveld results indicating ~4% Ni in the Li layer of this compound. The amount of the interslab Ni is reduced by using softer ion-exchange routes [Figure IV-14 (c)], but the question still remains as to whether the nickel will migrate to a higher equilibrium value on cycling.

High Capacity Composite Cathodes (Thackeray) **-** Li-rich layered transition metal oxides containing tetravalent Mn ions can be formulated either in standard layered notation, $Li_{1+x}[Mn_{1-y}M_y]_{1-x}O_2$, or in two component notation, $xLi_2MnO_3\bullet(1-x)LiMO_2$, where M is typically Mn, Ni and/or Co. When small amounts of excess Li are used, the Li_2MnO_3-like features are sometimes difficult to discern in the XRD patterns, particularly when cobalt is present. This team has studied Li-rich $Li_{1+x}[Mn_{0.5}Ni_{0.5}]_{1-x}O_2$ (1/2, 1/2 system) and the $Li_{1+x}[Mn_{0.333}Ni_{0.333}Co_{0.333}]_{1-x}O_2$ (1/3 system) materials as a function of x to monitor changes in the Li_2MnO_3-like character of their structures. The complexity of the structurally integrated $xLi_2MnO_3\bullet(1-x)LiMO_2$ compounds manifests itself in pronounced differences in the peak intensities of the weak ordering reflections in the XRD patterns of the two compounds. In the (1/2, 1/2) material, the ordering peaks increase with x, consistent with an increasing Li_2MnO_3 content. In the 1/3 system, the ordering peaks are significantly weaker and remain essentially unaltered as x increases. The reason for this is attributed to the lower Mn content in the 1/3 structure and, consequently, to the difficulty of

---

[10] N.A. Chernova, M. Ma, J. Xiao, M.S. Whittingham, J. Breger, and C.P. Grey, "Layered $Li_xNi_yMn_yCo_{1-2y}O_2$ Cathodes for Lithium Ion Batteries: Understanding Local Structure via Magnetic Properties," *Chem. Mater.* **2007**, *19,* 4682-4693.

clustering the Li around the Mn ions to generate short range order in the $LiMn_6$ (or disordered $LiMn_{6-x}M_x$) hexagonal units, which are the building blocks of Li_2MnO_3.

In the (1/2, 1/2) system, increasing the Li content at the expense of the $Mn_{0.5}Ni_{0.5}$ content increases the average Ni oxidation state from 2+ (x=0) to 3+ (x=0.2). If the Li remains clustered to the tetravalent Mn ions as it is added to the flower arrangement of $LiMn_{0.5}Ni_{0.5}O_2$ (Figure IV-18a), then a picture of an integrated Li_2MnO_3-$LiNiO_2$ structure emerges, consistent with the XRD data, as depicted in Figure IV-18b for $x \approx 0.1$, in which twelve Li- ions have been added to the flower pattern at the expense of six Mn ions and six Ni ions. The ideal structure of Li_2MnO_3 is shown in Figure IV-18c for comparison.

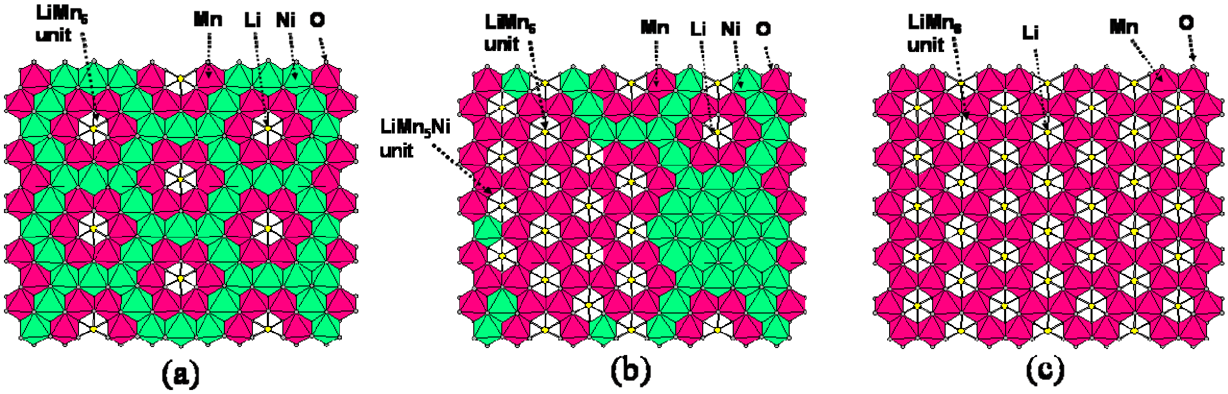

Figure IV-18. Schematic illustrations of the atomic arrangements in the transition metal (TM) layers of (a) $LiMn_{0.5}Ni_{0.5}O_2$, (b) $Li_{1+x}(Mn_{0.5}Ni_{0.5})_{1-x}O_2$ ($x \approx 0.1$) and (c) Li_2MnO_3.

***Cathode Decomposition (Ceder/Grey)* -** The decomposition of Li_xNiO_2 was found to be a two step process (Figure IV-19). The first step is a kinetically controlled exothermic conversion in which the layered structure transforms to the stable spinel structure. The second step is an endothermic decomposition of the spinel into a rock-salt phase, accompanied by the loss of oxygen. The heat generation for the overall reaction from the layered to the rocksalt structure is exothermic when $x < 0.5$ and endothermic when $x > 0.5$. From the calculated phase diagram a similar mechanism is expected for Li_xCoO_2, but the high migration barrier for Co may inhibit the layered to spinel transformation and lead to decomposition into $LiCoO_2$ and Co_3O_4. For the stable spinel $LiMn_2O_4$, high temperature is needed to provide enough thermodynamic driving force for its endothermic decomposition reaction. The fully charged λ-Mn_2O_4 transforms kinetically into the stable phase β-MnO_2, then decomposes at elevated temperature into the lower valent oxides, α-Mn_2O_3 and Mn_3O_4. The calculated decomposition heat for the three systems is in good agreement with experiments. Electrolyte can act as a sink for the oxygen released from the cathode. While oxygen release from the cathode is generally endothermic, its combustion with the electrolyte leads to a highly exothermic reaction.

***High Voltage Cathode Stability (Ceder/Grey)* -** NMR, TEM, *in situ* diffraction and pair distribution function (PDF) studies have been performed to investigate the stability of layered LiNiMn materials charged to high voltages. These studies have been coupled with gas chromatography/mass spectrometry experiments to monitor oxygen loss and electrolyte decomposition reactions. *In situ* diffraction experiments have been carried out to follow the synthesis of a series of layered materials in real time, to establish the optimum conditions required to synthesize specific cation ordering schemes. Work has focused on the Li-excess material $Li[Ni_{1/3}Mn_{5/9}Li_{1/9}]O_2$. One question that we are attempting to address stems from the work of Armstrong and coworkers.[11] They observed oxygen loss on charging the related material $Li[Li_{0.2}Ni_{0.4}Mn_{0.4}]O_2$ to high voltages and ascribed this, based on neutron diffraction refinements of the structure, to oxygen loss and migration of transition metal ions back into the structure to form a material with stoichiometry $(Li_{0.09}Ni_{0.019}[Mn_{0.73}Ni_{0.21}]O_2$.

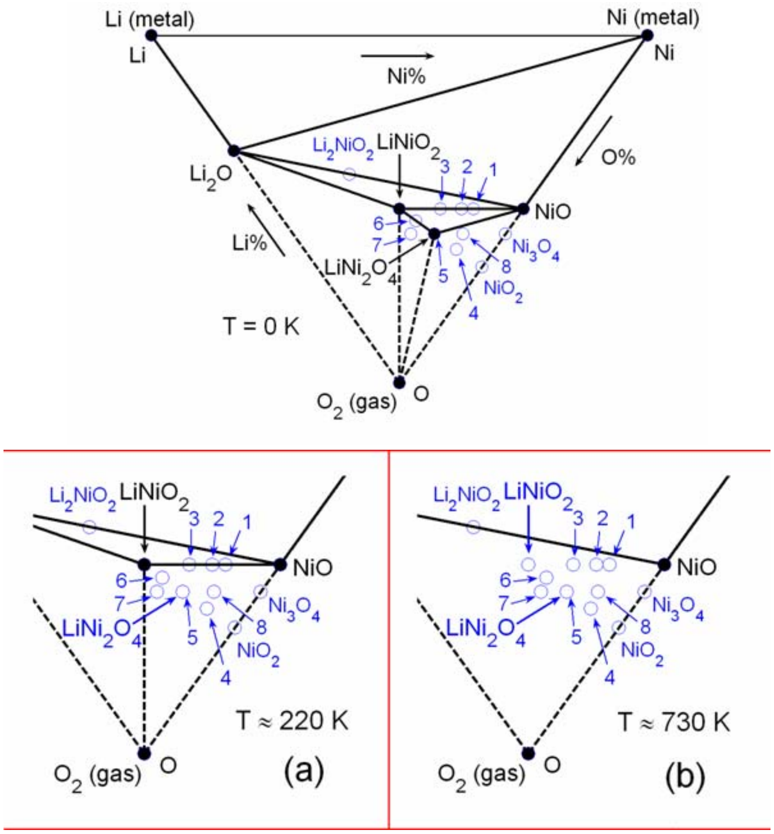

Figure IV-19. (a) Calculated ternary phase diagram for Li-Ni-O_2 at 0 K. Dashed lines indicate that triangles connecting O_2 depend on pressure. Filled (unfilled) circles indicate stable (unstable) compounds. Points labeled as 1, 2 and 3 represent rock-salt structures

NMR and diffraction studies have demonstrated that the structural changes that occur on the 1st charge are very sensitive to the voltage window. On charging to 5.2 V, almost all Li ions are removed from the structure, even though only 2/3 of these ions should be removed based on the Ni^{2+} content of this material. Although Li is originally present in both the predominantly transition metal and Li layers of the structure, the Li does not return to the transition metal layers on discharging. The superstructure due to the long-range ordering of Li and Ni/Mn largely disappears. On discharging, a stable capacity of 200 mAh/g is observed. In contrast, charging to 4.6V leads to a much lower capacity. Li ions are again removed from the Li-layers, but this structural process

---

[11] Armstrong, A.R.; Holzapfel, M.; Novak, P.; Johnson, C.S.; Kang, S.-H.; Thackeray, M.M.; Bruce, P.G.; J. Am. Chem. Soc.; 2006; 128(26); 8694-8698.

takes multiple cycles to achieve. Both transmission electron microscopy (TEM) and diffraction results indicate that the high voltage process is extremely complex. At least two phases are seen at the top of charge, along with some spinel regions. Many of the large, crystalline particles break into multiple domains. Attempts to detect and quantify oxygen gas evolution at high voltages by using pouch cells have not detected significant quantities of oxygen, in contrast to the work of Armstrong et al., although the O_2 amount was not quantified in this earlier study. It is possible that, at least in these cells, much of the additional capacity results from the electrolyte oxidation at high voltages (the oxygen coming from the electrode material), and the reduction of Ni^{4+}. Again in contrast to the work of Bruce et al, we find that the final structure is not "more layered" but rather contains additional metal ions in the Li layers. The presence of these ions may prevent Li re-intercalation into the transition metal layers. This is actually beneficial to the capacity because it limits the capacity to ~200 mAh/g and prevents Mn reduction to Mn^{3+}.

***Rate Capability of NMC Cathodes (Ceder/Grey)* -** A systematic study of the $Li[Ni_xMn_xCo_{(1-2x)}]O_2$ ($0.01 \leq x \leq 1/2$) series is underway to investigate the role that cation ordering, both in the layers and between the layers, plays in controlling rate performance and capacity retention. Recent work has focused on the materials synthesized using the mixed hydroxide method, where $0.01 \leq x \leq 1/3$, Ni/Mn/Co XANES results, performed in collaboration with BNL, verified the presence of Ni^{2+}, Mn^{4+} and Co^{3+} in the pristine samples. The local environment and short-range ordering were investigated by using a combination of ^6Li Magic Angle Spinning (MAS), NMR, and neutron PDF analysis, associated with c) calculations, and the local structure was compared with the electrochemical data. Several ^6Li NMR resonances were observed in the compounds with low Ni/Mn contents ($x \leq 0.10$) and were assigned to specific local arrangements for Li (Figure IV-20).

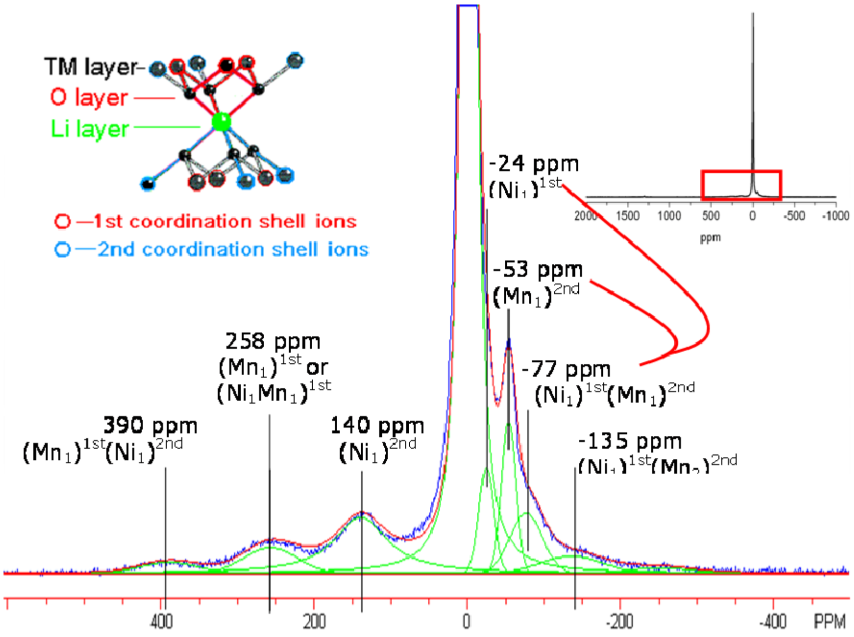

Figure IV-20. Enlargement of the 6Li MAS NMR spectrum of $Li[Ni_{\backslash 0.02}Mn_{0.02}Co_{0.96}]O_2$ (full spectrum shown in inset). Assignments of the resonances to different Li local environments, differing in the number of Ni and Mn ions in the 1st and 2nd cation coordination shell, are shown.

A detailed analysis of the ^{6}Li MAS NMR spectrum of ^{6}Li[$Ni_{0.02}Mn_{0.02}Co_{0.96}$]$O_2$, indicates the formation of "Ni^{2+}/Mn^{4+} clusters", rather than a random distribution of Ni and Mn in the transition metal layers. The oxidation state of Ni in this high Co content sample is found to be extremely sensitive to the Li/transition metal ratio of the starting reagents, and can be monitored by using both NMR and electron spin resonance (ESR). On increasing the Ni:Mn:Co ratio, the NMR spectra broaden and the Co-rich local environments diminish. Neutron diffraction data and PDF analysis of Li[$Ni_{1/3}Mn_{1/3}Co_{1/3}$]O_2 show a non-random distribution of Ni and Mn cations in the TM layers, with Ni closer to Mn in the first coordination shell (resembling the $\lfloor\sqrt{3}\times\sqrt{3}\rfloor$ R30º-type superlattice model) but a more random distribution of Co. The results suggest strong Ni^{2+}-Mn^{4+} ordering, the Co^{3+} breaking up this ordering and hindering long-range ordering. Analysis of the resonance due to $LiCoO_2$-like regions in the NMR spectrum show that the disappearance of this resonance, on increasing x, is correlated with the disappearance of the insulator-to-metal transition that occurs on extracting Li from Li_yCoO_2 at approx. y = 0.94. The Co^{3+}-Co^{4+} oxidation voltage appears to increase noticeably at this point, which is in agreement with first principles calculations which put the voltage of localized Co^{3+}/Co^{4+}above that of Ni^{2+}/Ni^{4+}.

***New Electrode Materials: Layered Oxysulfides (Ceder/Grey)* -** As part of the search for new electrodes this group has explored a series of new materials in collaboration with Dr. Clarke, University of Oxford. Oxysulfides represent an interesting class of materials because they often allow for rapid Li^+ mobility and good electronic properties. The layered oxysulfides $Sr_2MnO_2Cu_{2m-0.5}S_{m+1}$ (m = 1, 2, 3) (Figure IV-21)[12] consist of alternating perovskite-type Sr_2MnO_2 layers and copper sulfide layers which resemble fragments of the Cu_2S anti-fluorite structure, and consist of single, double, or triple layers of CuS_4 tetrahedra for the m = 1, 2, 3 materials respectively. Intergrowths of these structures are also possible, and a material with alternating single and double copper sulfide layers has also been prepared.

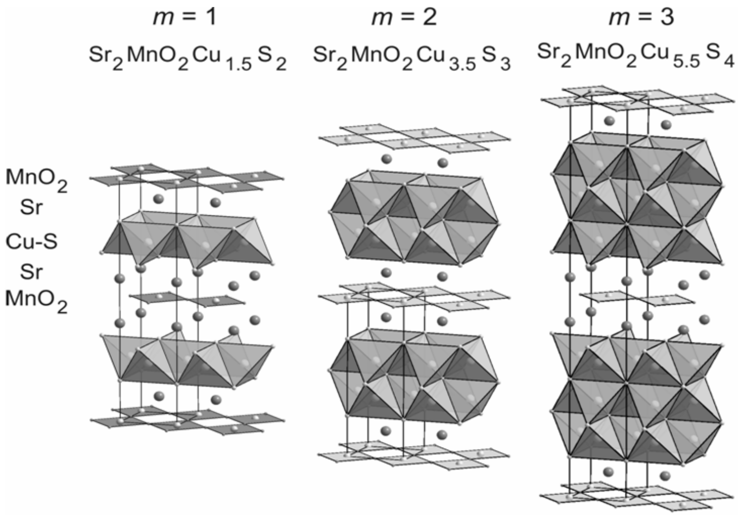

Figure IV-21. Structure of $Sr_2MnO_2Cu_{2m-0.5}S_{m+1}$ (m = 1, 2, 3).

---

[12] Gál, Z.; Rutt, O.; Smura, C.; Overton, T.; Barrier, N.; Clarke, S.; Hadermann, J *J. Am. Chem. Soc.* **2006**, 128, 8530.

Previous work had shown that these materials can be chemically lithiated using *n*-butyl-lithium,[13] with Li^+ replacing Cu^+ ions in the MS_4 tetrahedra, and extrusion of elemental copper. This is similar to the process that occurs on Li insertion in layered copper vanadates by Tarason and coworkers.[14] We have now demonstrated that this process can be achieved electrochemically. Figure IV-22 shows the 1st galvanostatic discharge for the *m* = 1, 2 and 3 samples, *vs*. Li. A long sloping plateau is seen between 1.8 and 1.3 V for all three samples. This plateau ends at a Li content, *x*, of approx. 1.5, 3.5, and 5.5 for the samples with *m* = 1, 2 and 3, respectively, corresponding to the initial Cu contents, suggesting that this plateau corresponds to complete Li-Cu exchange. ^7Li MAS NMR spectra of the *m* = 1, 2 and 3 samples following discharging to a voltage of 1.1 V are similar to those of samples prepared using *n*-BuLi, indicating that (a) Li is intercalated within the Cu_2S sheets and (b) the Li^+ mobility within the Cu_2S lines is extremely rapid, particularly for m > 2 (i.e., for the double Cu_2S slabs). Also, for the m = 3 compound (3 Cu_2S slabs) the Li-ions hop between the Li tetrahedral sites on a timescale shorter than 6×10^{-5} s.

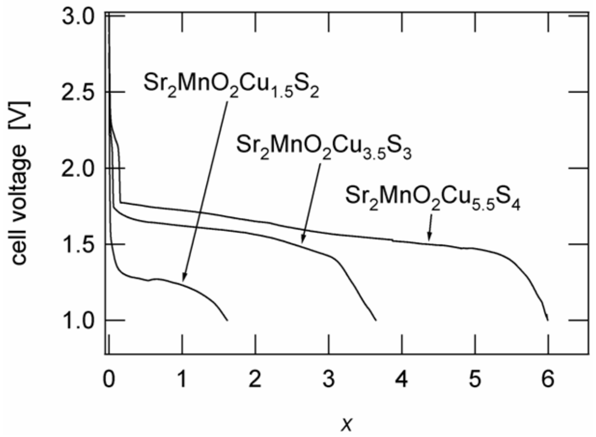

Figure IV-22. The first discharge of $Sr_2MnO_2Cu_{2m-0.5}S_{m+1}$ for m = 1, 2, 3, vs. a $Li|Li^+$ negative electrode, with a discharge rate of C/20 (i.e., all the Cu ions are replaced by Li within 20 hours). x denotes the number of Li ions inserted per formula unit.

The reversibility of the copper extrusion process was evaluated between 2.7 and 1.1 V (Figure IV-23). This voltage window corresponds to the Cu-Li exchange process and is associated with theoretical capacities of 95.4, 161.6, and 199.1 mAh/g (for *m* = 1, 2, and 3) for *x* = 1.5, 3.5, and 5.5, respectively. The electrochemical Cu-Li exchange is fairly reversible: the thinner the sulfide layers, the lower the capacity but the higher the capacity retention. The *m* = 1 material shows the largest drop in capacity between the 1st and 2nd cycles, but the smallest capacity fade in subsequent cycles. Unlike the other two compounds, this material does not contain vacant octahedral holes between the MS_4 tetrahedra; these are likely involved in ion transport, which may enhance the Cu-Li exchange in compounds with thicker sulfide layers. Cycling experiments for the *m* = 1/*m* = 2 intergrowth ($Sr_2MnO_2Cu_{2.5}S_{2.5}$) shows a reversible capacity of 100 mAh/g (Figure IV-23), apparently combining the higher capacity of the *m* = 2 phase with the higher

---

[13] Rutt, O.J.; Williams, G.R.; Clarke, S.J. *Chem Commun* **2006**, 2869.

[14] Morcrette, M.; Rozier P.; Dupont, L.; Mugnier, E.; Sannier, L.; Galy, J.; Tarascon, J.-M. *Nature Matls* **2003**, 2, 755.

reversibility of the *m* = 1 phase. Cu_2S was also tested: its initial capacity is much higher (theoretical: 336.8 mAh/g; observed: >225 mAh/g) but drops much more rapidly within the first few cycles. No attempt has been made at this point to optimize electrode construction, to improve reversibility. The results indicate that the stabilization of an electroactive structure with poor reversibility (antifluorite Cu_2S) by combining it with a rigid perovskite network yields a structure that can accommodate the structural changes that occur on Li/Cu exchange. These results suggest the possibility of designing related structures in which a compromise between stability and capacity are achieved, leading to wide variety of new electrode materials for possible use in Li-ion batteries.

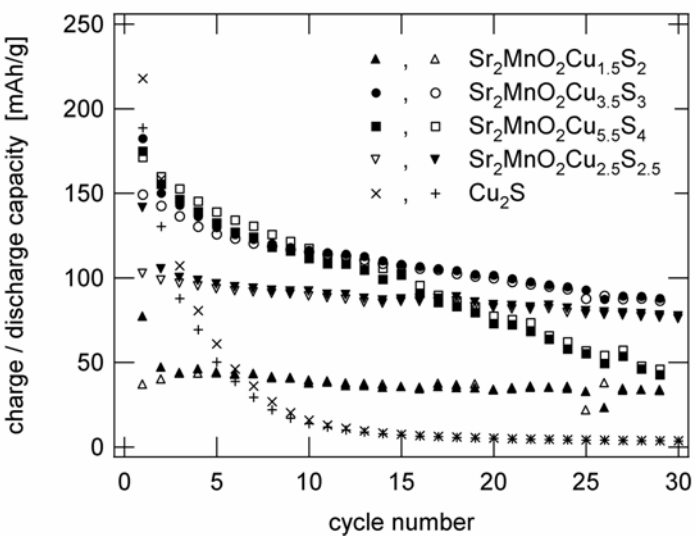

Figure IV-23. The charge and discharge capacities of $Sr_2MnO_2Cu_{2m-0.5}S_{m+1}$, m = 1-3, and Cu_2S as a function of cycle number, between 2.7 and 1.1 V. Full symbols: discharge; empty symbols: charge; crosses: Cu_2S.

Sample Future Plans in Cathode Materials

- Complete testing and report on the results of phase transition, rate, and stability studies of Li_xMnPO_4 cathode materials.
- Improve the particle size of olivine $LiMPO_4$, and evaluate other phosphate structures containing Fe and Mn and compare them with high temperature $LiFePO_4$.
- Determine feasibility of synthesizing electrochemically active nano- $LiMnPO_4$ and/or $Li(Mn,Fe)PO_4$ and other polyanionic compounds.
- Complete investigation of electrochemical co-deposition of polyaniline (PAn) and C-$LiFePO_4$. Prepare and test nanowires of PAn for chemical attachment to C-$LiFePO_4$.
- Extend the nanotube/$FePO_4$ work to include mixed metal systems, particularly M=Mn + Fe.

- Complete development of experiments for measuring transport properties in $FePO_4$, use these to obtain effective transport properties as a function of electrode composition and morphology.

- Conduct TGA experiments on Mn spinel cathodes in the presence of electrolyte.

- Determine the dependence of Mn dissolution on the degree of delithiation in Mn spinel cathodes.

- Compare the thermal stabilities of delithiated $Li_x[Ni_{0.4}Co_{0.2}Mn_{0.4}]O_2$ and $Li_x[Ni_{0.4}Co_{0.15}Al_{0.05}Mn_{0.4}]O_2$, and determine the origins of the observed rate improvement in the substituted materials.

- Investigate Li/Ni disorder in Li rich $LiNi_{0.5}Mn_{0.5}O_2$ materials.

- Perform additional NMR spectroscopy and theoretical studies to analyze the phenomena that influence the rate capability of the NMC cathode in more detail.

- Further optimize the technique for the C-LFP/polymer composite cathodes. In addition, prepare nano-scale $LiFePO_4$ and layered oxides $Li(Ni_{0.5+\delta}Mn_{0.5-\delta})O_2$ and $Li(Ni_{1/3}Mn_{1/3}Co_{1/3})O_2$ for the polymer-based composites and the influence of particle size will be investigated.

IV.B New Anode Materials

Objectives

The objectives of the work in this area include replacing graphite with an alternative inexpensive anode material that will be compatible, in particular, with low-cost manganese oxide cathodes. In addition, researchers are trying to improve the capacity and cycle life limitations of intermetallic and alloy based electrodes as well as the abuse tolerance of Li-ion cells.

Finally, one group is investigating the root causes (mechanisms) of dendrite formation and thus continue the search for high energy Li metal rechargeable batteries.

Approach

The first approach is to search for inexpensive intermetallic electrodes that provide 1) an electrochemical potential a few hundred mV above that of metallic Li, and 2) a capacity of at least 400 mAh/g (>1500 mAh/ml). This is focused predominantly on Sn-based systems that appear to have a good chance of success in practical cells. Focus is on new ternary and quaternary systems. Electrodes are evaluated in full cells against high capacity metal oxides. Studies of SEI layers that are formed on these materials are also reported.

Another approach being used to move Li alloys closer to usability is to use microwave plasma-assisted chemical vapor deposition (MPACVD) to synthesize electronically conductive thin films of graphitic carbon with uniformly distributed tin nano-particles.

A novel nano-sized MoO_3-based electrode material has been grown at high density by potentially economical hot-wire chemical vapor deposition. The resulting material has been fabricated into functioning electrodes using electrophoresis and demonstrates promising capacity and cycling. In addition, another team prepared oriented arrays of TiO_2 nanotubes on Ti metal substrate by using an electrochemical anodization technique to investigate their cycling and rate capabilities.

One project is investigating the electrochemical behavior of nanofiber manganese oxide in LiBOB electrolytes, to understand how that salt ameliorates the extensive first cycle capacity reactions.

Another high energy anode investigation involves Li-Mg cermats which show promise as high capacity materials and as a material that appears to inhibit Li dendrite growth.

Dendrite formation and growth is being monitored by electrochemical and optical methods as a function of electrolyte composition and applied potential. In an attempt to study the cause or causes of dendrite formation, the impact of pulse plating on dendrite formation is considered. Nucleation and growth of Li deposits will be characterized by electrochemical methods.

Accomplishments

Intermetallic Alloy Anodes (Thackeray) - This project is investigating intermetallic anode materials that have a strong structural relationship with their lithiated products. This group has shown that the late transition metals (Fe, Co, Ni, and Zn) have some solubility in Cu_6Sn_5. Following this, solubility limits in $Cu_{6-x}M_xSn_5$ materials were established, with a particular focus on Ni, Co, and Zn. It was determined that Ni_3Sn_2 and Co_3Sn_2 form solid solutions with Cu_6Sn_5 ($Cu_{2.4}Sn_2$) over a wide range of x because they both have NiAs-related structures, whereas Zn showed limited solubility ($x \approx 1$, i.e., Cu_5ZnSn_5) before stable Cu-Zn (brass) binary phases were formed.

These studies have continued with studies of their electrochemical properties as a function of composition and voltage window. Materials were prepared by high energy ball milling of the elements and by subsequent high temperature (>700 ºC) annealing, grinding and processing. The electrodes were evaluated in lithium cells over two voltage ranges, 2.0-0.2 V and 2.0-0.0 V; the results of the tests are shown in Figure IV-24.

In general, when the electrodes were cycled over the wider voltage range (2.0-0.0 V), a higher capacity (>400 mAh/g) but inferior cycling stability were obtained, consistent with this group's earlier studies of Cu_6Sn_5. By contrast, when the discharge was limited to 0.2 V, stable capacities of 200-250 mAh/g were achieved. An exception, however, was $CoCu_5Sn_5$ that provided a stable ~400 mAh/g (over limited cycling) when cycled between 2.0-0.0 V. Therefore, efforts are being focused on the Co-Cu-Sn system. *In situ* XRD and XPS experiments are in progress in collaboration with K. Edstrom (Uppsala University).

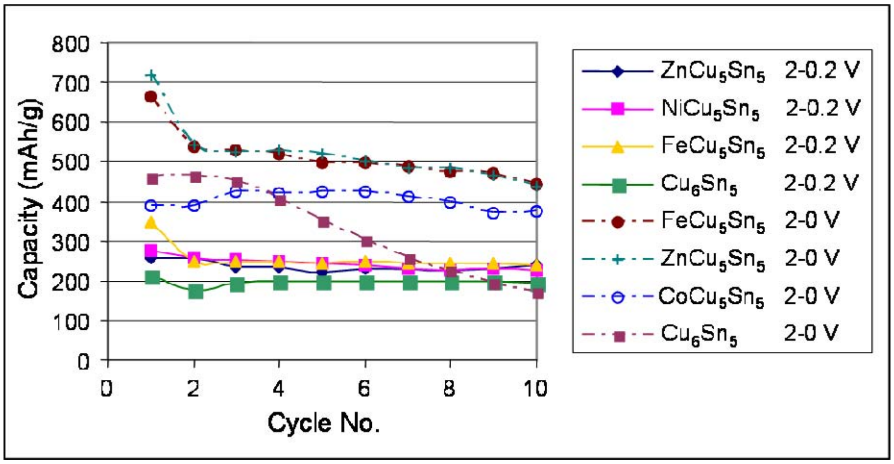

Figure IV-24. Capacity vs. cycle no. plots of various Li/Cu_5MSn_5 cells (M= Fe, Co, Ni, Zn).

***Nanosized Alloy Anode Materials (Thackeray)* -** Metals and intermetallic compounds expand significantly on reaction with Li. When used in electrodes in Li cells, this leads to mechanical pulverization, loss of electronic contact between particles, and poor cycling. The electrochemical performance of these materials should, in principle, be improved by using nanosized particles. With this in mind, this team has initiated efforts to evaluate the effect of particle size on the electrochemical performance of intermetallic electrode materials.

In collaboration with Primet Precision Materials (Ithaca, NY), this team is studying materials within the Co-Cu-Sn system such as CuSn, Cu_6Sn_6 and $CoCu_5Sn_5$ with primary particle sizes ranging from tens to hundreds of nanometers. The nano-materials are made by Primet's proprietary Nano-Scission™ process and are compared to samples produced at ANL by high-energy ball-milling that typically produce a particle size distribution in the 10-30µm range.

Primet prepared two CoSn samples, one with an average particle size of ~60 nm and the other, ~200 nm, and two Cu_6Sn_5 samples (~500nm and ~200nm) and one $CoCu_5Sn_5$ sample (~200 nm). Figure IV-25 (left) shows an SEM image of an Argonne ball-milled $CoCu_5Sn_5$ sample after down-sizing by the Primet process; it shows primary particles 50 nm or less in one dimension, and secondary particles 100 nm or more in size. The XRD pattern of this sample (not shown) indicates a crystalline product, i.e., $Co_xCu_{6-x}Sn_5$ (x=1), isostructural with Cu_6Sn_5; with significant peak broadening, which is consistent with the reduction in particle size.

Electrochemical experiments have demonstrated that ball-milled CoSn samples show the lowest capacity (~100 mAh/g) but stable cycling behavior, whereas the 60 nm samples display the highest capacity (~350 mAh/g) but that fades 150 mAh/g after 20 cycles. The poor cycle life of the 60 nm particles is attributed tentatively to their high surface area and therefore chemical reactivity with the electrolyte. The larger 200nm particles have displayed the best cycling stability thus far, delivering a steady 300 mAh/g for the first 12 cycles (Figure IV-25 (right)). Down-sized Cu_6Sn_5 and $Co_xCu_{6-x}Sn_5$ electrode particles have shown similar behavior to the parent ball-milled samples, with the cobalt-substituted materials delivering ~400 mAh/g; however, they exhibit significant capacity fade after 5-10 cycles.

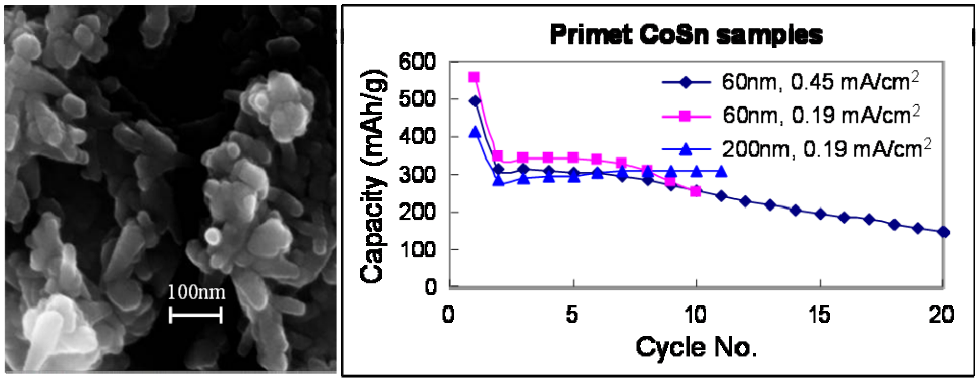

Figure IV-25. SEM image of $CoCu_5Sn_5$ particles (left), Cycling stability of 60nm and 200nm CoSn electrode particles (right).

***MoO_3 Nanoparticles for Li-Ion Electrodes (Dillon)* -** Crystalline molybdenum oxide (MoO_3) nanoparticles, made from non-toxic and inexpensive materials, were grown at high density by potentially economical hot-wire chemical vapor deposition (HWCVD), Figure IV-26. Furthermore, the particle size and morphology were tailored by varying the synthesis conditions i.e. reactor temperature and pressure, filament type and temperature, and gas composition. Then the nanoparticles were used to fabricate high surface area electrodes through electrophoresis deposition. The electrodes were tested in a half-cell configuration with a Li counter electrode. Crystalline α-phase MoO_3 nanoparticle negative electrodes exhibited a reversible capacity of 630 mAh/g with good rate capability, ~500 mAh/g, at 2C. The nanoparticle negative electrodes show no degradation in capacity after 150 deep cycles at C/2 rate with an average Li-extraction potential of ~1.5 V. Electrodes tested with micron-sized MoO_3 particles suffered capacity fade after several cycles under the same test conditions, Figure IV-27.

Theoretical calculations elucidated the Li-ion insertion process and revealed a novel mechanism confirming the nanoscale, high-rate, reversible capacity. Theory showed that the nanoparticle stability could be improved and a higher capacity realized by incorporating tungsten into the β-phase MoO_3 nanoparticles.

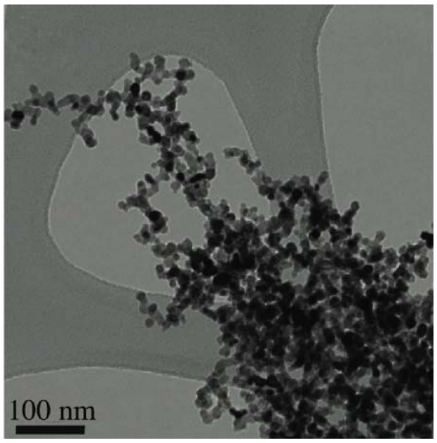

Figure IV-26. TEM image of MoO_3 HWCVD nanoparticles.

Preliminary proof of concept results showed that HWCVD $Mo_{1-y}W_yO_3$ particles containing ~35 at% W (percent of total number of atoms) resulted in a more stable material than β-phase MoO_3 nanoparticles. Additionally, theoretical results showed that $Mo_{1-y}Ti_yO_3$ nanoparticles had an increased charge/discharge potential of ~ 3.5 V. Proof of concept experiments showed that $Mo_{1-y}Ti_yO_3$ nanoparticles might be made with HWCVD.

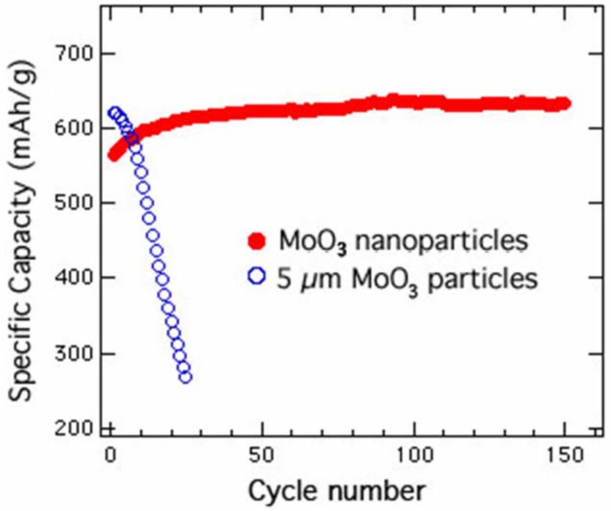

Figure IV-27. The cycling stability of the α-phase MoO_3 nanoparticle negative electrode compared to commercially available μm-sized MoO_3 particles cycled at C/2 rate.

This material can also be employed as the positive electrode, where α-phase MoO_3 nanoparticle electrodes have a capacity of 120 mAh/g at C/1 and exhibit minimal degradation after 1500 complete charge/discharge cycles. A positive electrode of β-phase MoO_3 nanoparticles had a higher initial capacity, ~ 225 mAh/g at C/1 rate, but exhibited capacity fade upon cycling. Both the α- and β-phases had a relatively flat charge/discharge potential of ~2.5 V.

TiO_2 Nanotubes Anodes (Frank) - Several researchers have developed ordered TiO_2 nanotube electrodes, including at NREL for solar thin film applications, and others have reported on their use as electrode materials for Li-ion batteries[15]. Recently, this team prepared oriented TiO_2 nanotubes (NT) on a Ti metal substrate by using an electrochemical anodization technique. The resulting NT arrays were several μm in length with wall thicknesses and intertube spacings of 8–10 nm and pore diameters of 30 nm. The as-deposited films were converted from an amorphous material to the TiO_2 anatase crystalline phase by annealing at moderate temperatures. Tests of the TiO_2 NT films as an anode material against Li in a half cell showed that (1) repeated Li insertions/extractions had no effect on the morphology of the NTs, indicating that the arrays are structurally robust; (2) the Li-storage capacity of the NT films was significantly larger than the theoretical capacity of the bulk material; and (3) the rate capability of NT films was >10 times larger than that of films consisting of ~300 nm TiO_2 particles, Figure IV-28. A cycling stability study of one electrode showed some capacity loss, which was tentatively attributed to the detachment of some NTs from the conducting substrate.

---

[15] G. Armstrong, A.R. Armstrong, J. Canales, and P. Bruce. Electrochemical and Solid-State Letters, 9, A139 (2006).

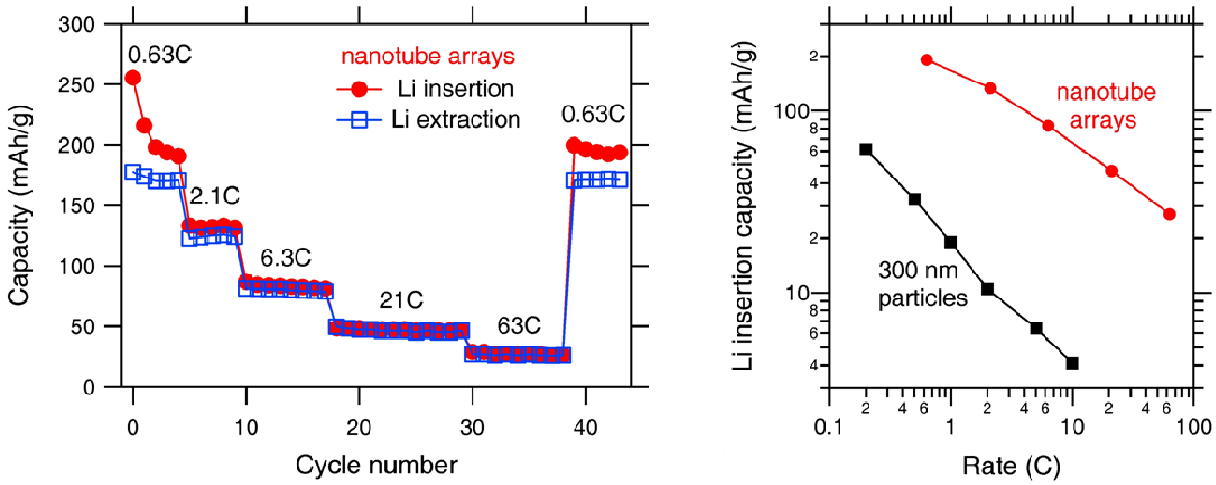

Figure IV-28. Rate capability of TiO_2 NT electrodes (left) and comparison with the rate capability of electrode composed of 300 nm particles (right). Data for 300 nm particle films was adapted from Maier et al, Adv. Mater. 19, 2087 (2007).

Nanofiber Manganese Oxide Anode Material (Whittingham) **-** This project is investigating the electrochemical behavior of nanofiber manganese oxide in LiBOB electrolytes, which ameliorates the extensive first cycle capacity reactions. Anhydrous LiBOB was prepared and dissolved in EC/DMC (1:1 volume) to give a ~0.7M saturated solution. It was mixed with 1M $LiPF_6$ in EC/DMC (1:1) in several ratios. The resulting electrochemical behavior of electrospun manganese nanofiber is shown in Figure IV-29. The first discharge capacity is ~700 mAh/g in all cases, which is within the theoretical maximum of 940 mAh/g. This contrasts with values of over 2000 mAh/g when only $LiPF_6$ was used as the electrolyte salt. Clearly LiBOB is forming a more effective SEI layer that may have eliminated the electrolyte decomposition.

The cycling behavior with various percentages of LiBOB, shown in Figure IV-29, is better than pure LiBOB. The extended cycling in the 10% solution is comparable to that in the LiBOB free electrolyte. The reversible capacities of the fibers show a decreasing trend with the increasing amount of LiBOB, which is likely due to the lower conductivity of LiBOB/EC/DMC electrolyte.

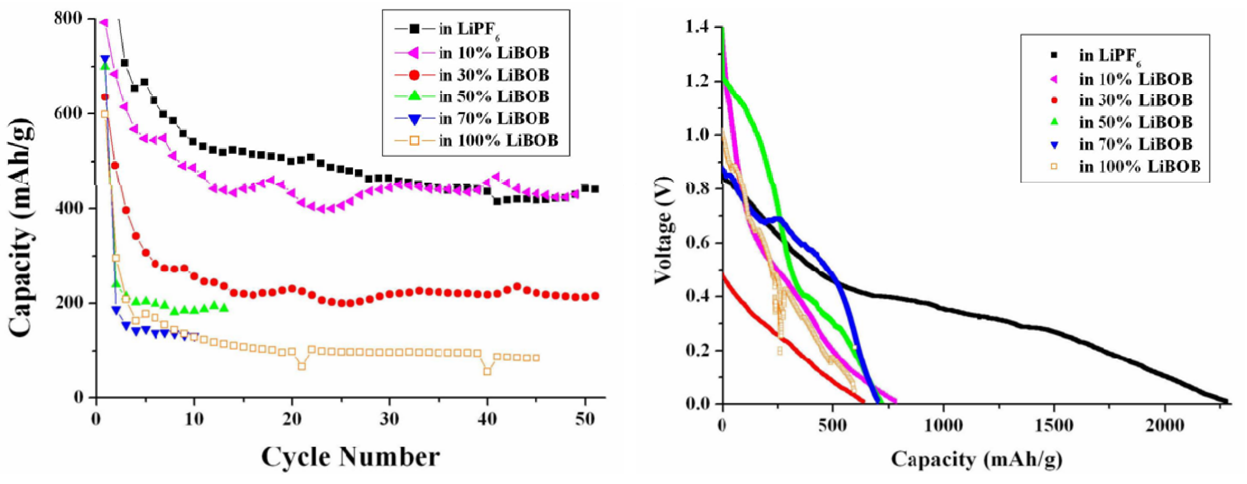

Figure IV-29. Electrochemical behavior of MnO nanofibers: (left) discharge capacities in LiBOB/$LiPF_6$ mixed electrolytes, and (right) first discharge capacity showing the elimination of the excess capacity by LiBOB.

***Li-Mg Alloy Anodes (Richardson)* -** Another high energy anode investigation involves Li-Mg cermats. These materials have shown promise as high capacity materials that also appear to inhibit Li dendrite growth. In 2007, $Li_{0.9}Mg_{0.1}$ foil was obtained from Chemetall Foote Corporation. Identical cells were constructed using high-rate Gen3 positive electrodes from the ATD program and either Li or $Li_{0.9}Mg_{0.1}$ foil as anode. Somewhat better capacity retention and substantially better rate performance (Figure IV-30) were observed for the alloy anode cell. Further experiments are under way to determine the origin of these effects.

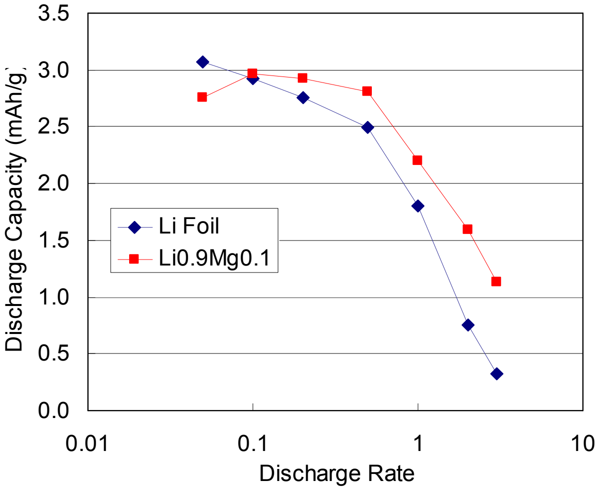

Figure IV-30. Discharge capacity vs. rate for $Li_{1.1}Mn_{0.3}Ni_{0.3}Co_{0.3}O_2$ cells with Li and $Li_{0.9}Mg_{0.1}$ anodes.

The metathesis technique for preparing cermet powders containing Li alloys and intermetallics was extended to the Li-Si system. Direct reaction of Si powder with Li_3N at 400°C produced $Li_{12}Si_7$ and a small amount of Si_3N_4, along with some unreacted Si. Adding Mg powder to the precursor mixture allowed for more rapid reaction and resulted in a product containing only $Li_{12}Si_7$ and Mg_3N_2.

***Thin Film and Nano-Composite Alloy Anodes (Kostecki)* -** The primary objective of this project was to evaluate carbon-tin nano-composite anodes synthesized by a direct *in situ* MPACVD from tin(IV) tert-butoxide precursor. Preliminary MPACVD experiments showed that the nano-composite Sn/C thin-films can be produced in a one-step synthesis on any type of substrate from the tin-based organic salt precursors without using stabilizers or reducing agents.

The qualitative analysis of the films shows a C/Sn mass ratio of ~2:1 i.e., very similar to tin(IV) tert-butoxide precursor. A typical Raman microscopy spectrum of C/Sn thin-films suggests that the C/Sn films consist mainly of nanocrystalline graphite. The SEM images show a continuous thin surface film of fairly uniform thickness ~5-7 µm. The morphology of the film is very porous. The film consists of large ~300-600 nm, featureless agglomerates, which are fused together into a micro- and nanoporous “lava rock”-like structure.

The TEM images show a remarkably uniform and fine dispersion of tin in the C/Sn composite. The particle size distribution is very narrow; the calculated average size of Sn particles (ca. 2.75 nm) is noticeably smaller than the average particle size estimated from the X-ray data. The microwave-assisted co-deposition of tin and carbon had evidently facilitated the nucleation and growth of small and uniform Sn particles in a nanocrystalline carbon matrix. The HRTEM image of the Sn/C agglomerate reveals 1-5 nm Sn particles embedded in partially graphitized, carbonaceous material. The presence of nanocrystalline tin particles was confirmed by their electron diffraction patterns. Interestingly, the carbon shows relatively large c.a. 10-15 nm well-organized graphene domains in the bulk of the agglomerate as well as in locations adjacent to the Sn particles. It also displays regions where shorter layers of irregular shape prevail, which are typical of carbon blacks.

The reversible electrochemical activity of the nano-structured Sn/C thin films is attributed mainly to Sn nanoparticles. The Sn/C electrodes display a relatively large reversible capacity of ~440 mAh/g, mainly associated with SEI formation on tin and graphite. The C/Sn composite electrodes display good rate capabilities (Figure IV-31). The electrodes also showed an outstanding cycling performance (500 cycles at 1C rate, Figure IV-31).

The improved electrochemical behavior of the Sn/C composite anode is mainly due to high porosity of the film, and fine dispersion of Sn nanoparticles, which are embedded in the 3D carbon matrix. The 3D composite design allows the accommodation of dimensional changes of Sn nanoparticles and the preservation of the structural and electronic integrity of the Sn/C electrode during cycling.

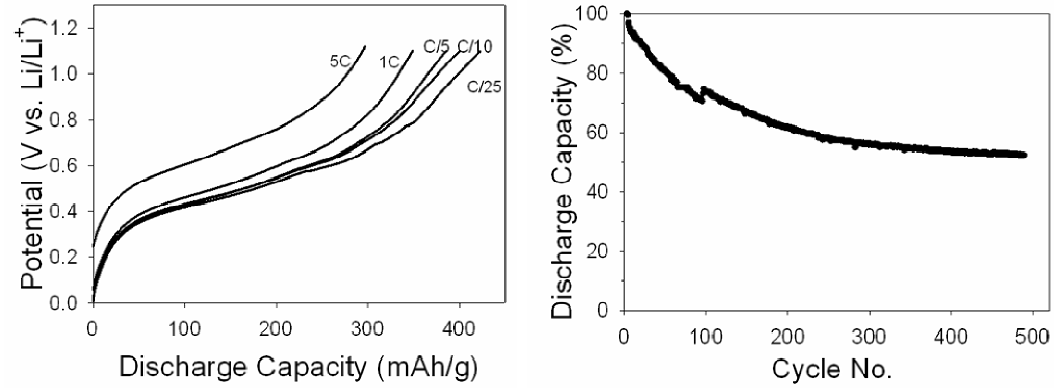

Figure IV-31. Rate (left) and cycling (right) performance of the C/Sn thin film nano-composite anode produced by MPVCVD on a Cu-foil. The electrode was charged at C/10 in the rate experiment, long-term cycling was performed at room temperature at the 1C rate.

***Sn-Thin Film Anode Diagnostics (Kostecki)* -** This effort focused on *ex situ* spectroscopic and microscopic studies of interfacial phenomena during early charge-discharge cycles of Sn anodes (in collaboration with S. Whittingham). The main goal of this effort was to monitor early stages of detrimental processes, which accompany formation of tin-lithium intermetallic compounds, which may be responsible for the loss of electrochemical performance. A 50 nm Sn layer was sputtered on a smooth Cu substrate. The electrode showed 905 mAh/g charge capacity during the first scan from 1.5 to 0.1 V at 0.1 mVs^{-1}. However, the first discharge scan produced a substantially smaller capacity (92.7 mAh/g), indicating severe degradation of the Sn thin-film anode. The subsequent CV cycles led to complete disintegration of the electrode. Cathodic peaks at 0.98, 0.65 and 0.37 V may be attributed to the reduction of impurities and/or formation of the SEI layer, early stages

(Li_xSn, x<1) of the Li-Sn alloying process, and formation of highly lithiated phases, *i.e.,* $Li_{2.33}Sn$, $Li_{4.4}Sn$, respectively.

Spectroscopic investigations of the Sn anodes were carried out *ex situ* in an airtight cell. Prior to measurements the electrodes were washed with DMC. The typical FTIR spectrum (Figure IV-32) displays a narrow peak at 3680 cm^{-1}, which originates from LiOH. FTIR bands at 853, 872 and 1028 cm^{-1} are assigned to fluorophosphate compounds Li_xPF_y and $Li_xPF_yO_z$, which come from the decomposition of $LiPF_6$. There is also clear evidence of organic compounds in the SEI layer. Three weak bands at 2845, 2913 and 2967 cm^{-1} belong to γ_{C-H} vibrations, the broad peak centered around 1585 cm^{-1} may be assigned to carboxylate species $-CO_2^-$, whereas the band at ~1098 cm^{-1} corresponds to γ_{C-O} vibration mode.

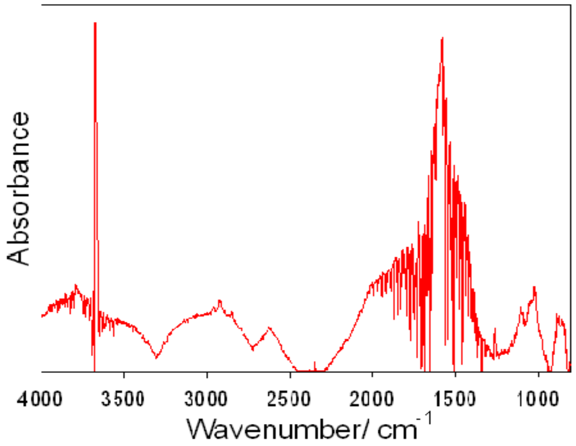

Figure IV-32. A typical FTIR microscopy spectrum of the SEI layer at the cycled thin-film Sn anode.

***Dendrite Formation (West)* -** This project is investigating the mechanism of dendrite formation during charging of a secondary Li metal battery. It was reported in 2006 that *ex situ* measurements of surface roughness are unreliable which highlighted the need to develop an *in situ* experiment. This team has used a microfluidic flow cell to view *in situ* Li dendrite growth. Copper is thermally evaporated onto a 75 mm by 25 mm glass slide and patterned to provide twenty 100 µm working electrodes spaced 100 µm apart. A 1/32" thick piece of rubber is machined with four 0.5 mm flow channels. Each slide contains eighty 0.05 mm^2 Cu working electrodes (WE). A 1 mm diameter Cu wire approximately 5 mm downstream from the last WE serves as the counter electrode (CE).

The microfluidic cell's advantages are: no concentration and ohmic effects; all substrates are initially the same; minimum electrolyte use (1-3 ml/h); and the ability to rapidly change electrolyte composition to study the effect of additives. A Carl Zeiss Stemi 2000-C stereo-microscope is used in conjunction with a PixeLINK A623-C camera to record dendrite growth. The "time to first observed dendrite" is used to quantify the electrolytes' effect on Li deposit morphology.
Figure IV-33 (left) shows a sample of pictures used to determine the time to first observed dendrite. After 45 seconds a small circular feature (pointed to by the arrow) begins to form. After 250 s, the feature is clearly dendritic.

Figure IV-33 (right) shows the effect of changing the PC:DMC solvent ratio on the time to the first dendrite. The figure shows that it takes longer for an observable dendrite to form as the DMC content increases.

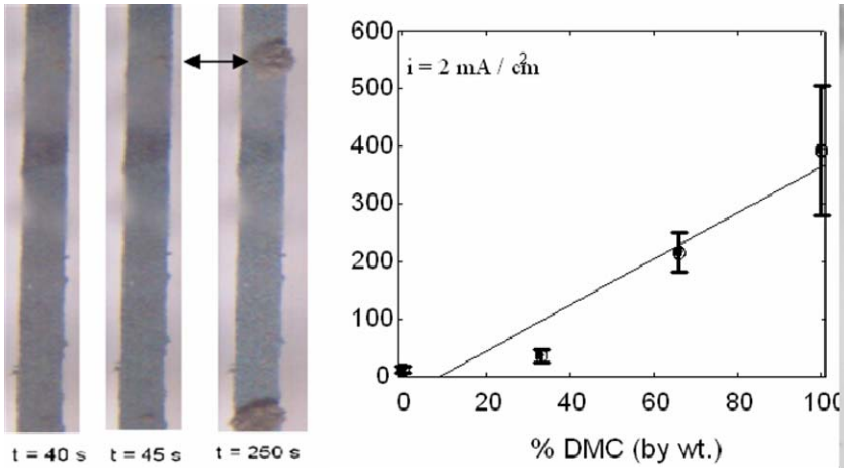

Figure IV-33. Method to detect a dendrite (left) and dendrite detection time vs. PC/DMC ratio (right).

Figure IV-34 shows the effect of current density. The electrolyte was 1.0 M $LiPF_6$ in PC:DMC (1:2) and each electrode is 100 µm wide with 100 µm spacing. Lithium was deposited at a rate of 0.1 mA/cm^2 on the first two electrodes and they are shown at charges of 0.2 and 1.0 C cm^{-2}. The first deposit was smooth but even at this low current density dendrites form if given enough time as shown on the second electrode. Lithium was deposited at 1.0 mA cm^{-2} on the third and fourth electrode. The third electrode was rougher than the second electrode even though they both are at a charge density of 1.0 C cm^{-2}. A large bush like dendrite was growing towards the center of the fourth electrode at 3 C cm^{-2}. Lithium was deposited on the bottom electrode at 20 mA cm^{-2}. Dendrites started growing nearly immediately and quickly spread to the neighboring electrode.

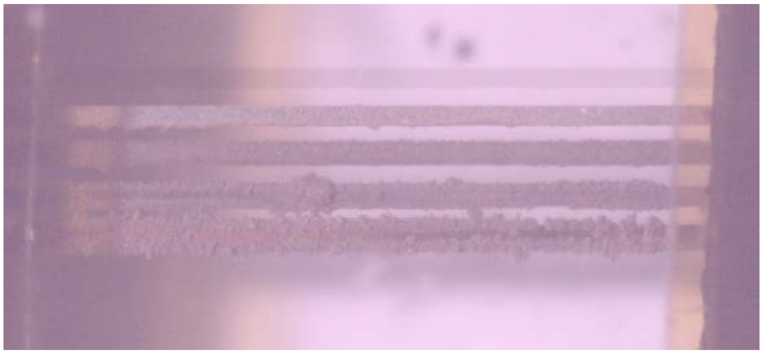

Figure IV-34. Effect of current and charge density.

Sample Future Plans in Anode Materials

- Study the effect of electrolyte salt on dendrite formation by using LiTFSI in PC:DMC as the electrolyte.

- Complete investigation into pulse plating parameters and the effects of promising additives, such as VC and triacetoxyvinylsilane, on dendrite formation.

- Begin studying dendrite growth in the Li/polymer system and SEI-effects in the graphite and/or alloy/liquid electrolyte systems.

- Test a modified LiBOB salt in the nanofiber manganese oxide anode system to determine if it will increase the conductivity, as well as to minimize the irreversible capacity after 1st discharge.

- Determine the electronic and crystallographic reasons why the Co-Cu-Sn system outperforms other substituted compounds.

- Synthesize larger quantities of HWCVD α-phase MoO_3 nanoparticles for further evaluation and to investigate the potential for economical scale-up for commercial application.

- Optimize a method for conventional fabrication of $\geq$100 μm thick electrodes. The resulting MoO_3 electrodes will be tested in a coin cell configuration as a negative electrode against a commercial $LiCoO_2$ positive electrode.

- Explore degradation mechanisms in MoO_3 nanoparticles, particularly perform *in situ* Raman studies of all of the anode materials to understand structural changes during cycling.

- Test the MoO_3 nanoparticle anode with a commercial cathode and employ doping or alloy formation to lower the charge/discharge potential (to increase the energy, or Wh/kg).

- Continue current efforts to improve the functionality of binders and current collectors to address capacity fade.

IV.C Novel Electrolytes and Their Characterization

Objectives

The objectives of this work include determining the chemical and electrochemical reactivity of Li ion electrolytes and ascertaining the impact of impurities such as water and additives such as LiF on the kinetics of the reactions and how this relates to calendar and cycle life of Li ion cells. In addition, researchers are investigating the feasibility of organic electrolytes for use with 5V electrodes and elucidate the roles of additives and impurities in their stability.

Researchers are also working to synthesize and characterize nanostructured dry polymer electrolytes with high conductivity and high shear modulus that can resist dendrite growth during cell cycling, to fabricate new ionic liquids (IL) that provide good conductivity and improved abuse tolerance.

A final objective is to gain a molecular level understanding of Li^+ transport mechanisms in ILs, SEI layers, and during Li intercalation into/from cathode from/into liquid electrolyte. Provide guidance for the design of novel electrolytes with improved lithium transport, reduced interfacial resistance and/or improved electrochemical stability allowing operation at higher voltages.

Approach

To understand the kinetics and influence of Li salts on cell performance, a variety of electrolytes have been prepared and tested in symmetrical lithium metal, Li-graphite, Li metal oxide-Li metal and Li metal oxide–graphite cells. LiTFSI salt is used as a control to allow comparison with $LiPF_6$ based electrolytes and to facilitate comparison with TFSI-based ionic liquid electrolytes.

Other groups have synthesized and characterized ionic liquid electrolytes with low-lattice-energy anions attached to a suitable plasticizer, scaffold or solvating matrix (*e.g.,* polyether oligomer). Salts are synthesized with recent focus on attachment of fluorosulfonate and fluorosulfonimide anions onto polyether oligomers to produce ionic melts (IM). Transport properties are measured using impedance spectroscopy combined with potentiostatic and galvanostatic DC polarization techniques. Half-cell and full-cell cycle testing and other diagnostics are performed on small (*e.g.,* Swagelok-style) cells.

Composite polymers (with a hard non-conducting part that inhibits dendrites and second highly conducting portion) are synthesized and characterized by AC impedance spectroscopy. Polymers are then tested for stability against Li electrodes in collaboration with other BATT PIs. Additional work is focused on gel polymer electrolytes with low polymer content to achieve comparable high-rate performance to liquid cells.

The simulation team is extending a set of the previously developed and validated many-body polarizable force fields (used in molecular dynamics (MD) simulations) to novel ILs, gel electrolytes and representative SEI components. Calculate free energy barrier for the Li^+ cation intercalation from electrolyte into the SEI layer components and a representative cathode material. Estimate electrochemical stability of model electrolytes using gas-phase quantum chemistry calculations.

Accomplishments

***Kinetic Characterization of Electrolyte Reactivity (Kerr)* -** A variety of electrolytes have been prepared and tested in symmetrical Li metal, Li-graphite, Li metal oxide-Li metal and Li metal oxide–graphite cells. LiTFSI salt is used as a control to allow comparison with $LiPF_6$ based electrolytes and to facilitate comparison with TFSI-based IL electrolytes. Initial results with EC/EMC solutions of LiTFSI and $LiPF_6$ show some startling results with respect to the dependence of the interfacial impedance at graphite electrodes. Figure IV-35 shows the charging and discharging of Gen 2 graphite anodes in EC/EMC-LiTFSI.

The initial charge is quite inefficient (~60%) but after five cycles the efficiency approaches 100%. The impedance **decreases** by an order of magnitude over the first five cycles to values that are more acceptable for Li ion batteries. Similar behavior has been observed with $LiPF_6$ based electrolytes. Measurement of the water content and the HF content in the case of PF_6 indicates that acid-base catalyzed chemistry of the electrolytes plays a critical role.

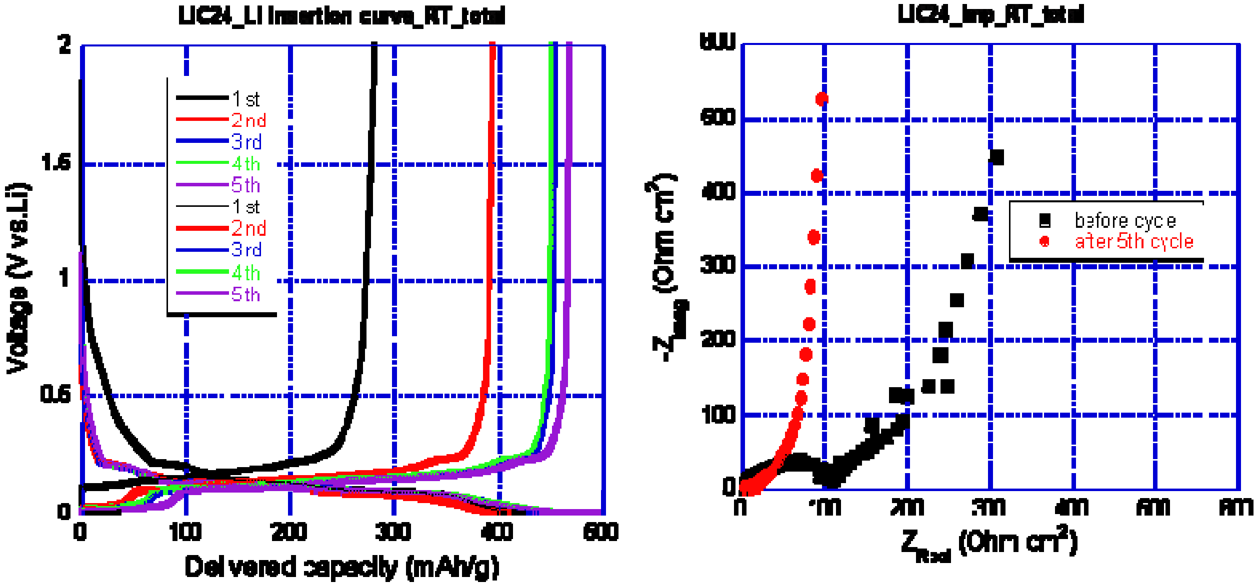

Figure IV-35. Voltage profile vs. Li reference of galvanostatic Li insertion/extraction (left) at 0.1mA at RT and Nyquist plot (right) for Li/EC/EMC(3/7 v/v) + 1.2M LiTFSI/Gen2 cell (Three electrode configuration- Li reference).

Similar measurements have been carried out at graphite anodes with pyrrolidinium TFSI ILs as the solvent. Strong evidence has been obtained for intercalation of the ILs into the graphite. The interfacial impedance is unacceptable for the IL–based electrolytes with graphite anodes. Work is proceeding on the interfacial behavior of the electrolytes with a variety of cathode materials.

A similar investigation has been carried out on Gen 2 and Gen 3 cathodes. As with the anodes, significant changes in the interfacial impedance at the cathode materials upon cycling have been observed. Prior to any electrochemical activity the interfacial impedance at the Gen 2 cathode is large, ~ 200 Ωcm^2 (Figure IV-36). Following cycling the interfacial impedance drops to lower levels, particularly at the end of charge (4.1V). The initial coulombic efficiency for the cathode is low (<70%) but climbs to 95% on cycling. The capacity fades slowly with cycling and the interfacial impedance of the cathode slowly grows.

The remarkable drop in impedance upon cycling occurs on cathodes and anodes, leading to the hypothesis that the cycling alters the interfacial properties such that the electrodes "wet" better, leading to more effective utilization of the electrodes. It seems plausible that side reactions produce changes in the surface or in the electrolyte close to the surface.

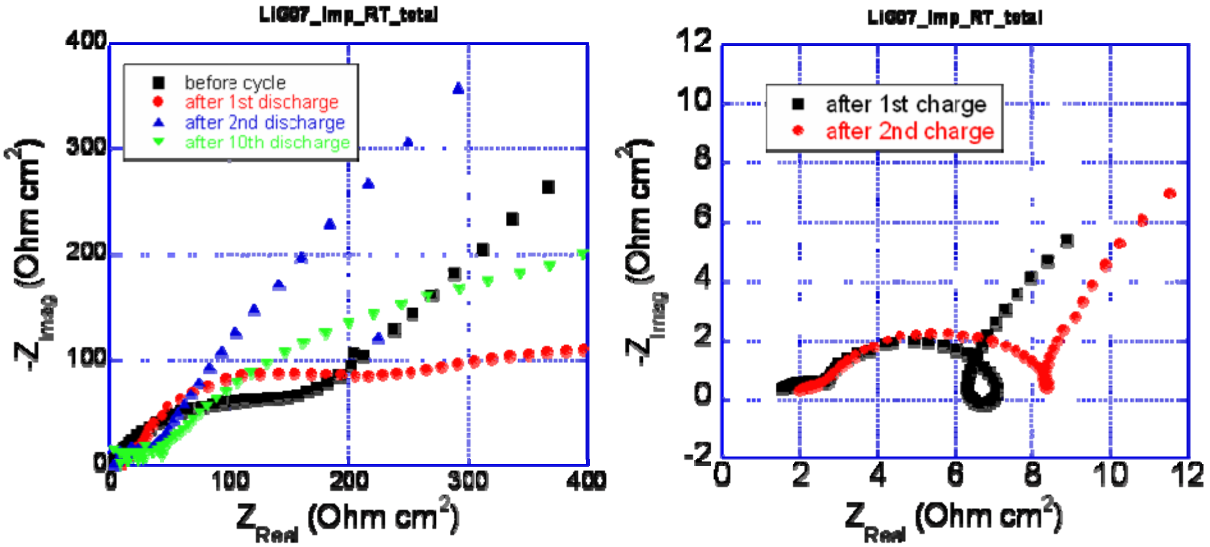

Figure IV-36. Nyquist plot of Li/EC/EMC + 1.2M LiTFSI/GEN2 cathode cell at room temperature. Working electrode: GEN2 cathode. Counter electrode: Li metal. Reference electrode: Li.

Feasibility of Organic Electrolytes with 5-Volt Stability (Kerr) - Methods of drying electrolyte components (EC/EMC) are under study to enable 5-Volt stability. Use of calcium hydride as a drying agent leads to transesterification and EC ring opening products which are detected by gas chromatography (GC). Even contact with Super activated Neutral Alumina is sufficient to initiate transesterification and ring-opening of EC and indicates how sensitive the carbonate solvents are to acids and bases. The next step is to avoid these complications in order to prepare completely dry electrolytes to test the 5-Volt stability limit.

During the formation studies described above it was noted that the moisture content had a distinct effect. For PF_6 electrolytes formation was rapid due to the formation of HF and other acidic species that catalyze the formation of surface active species. With TFSI based electrolytes several cycles on cathodes were necessary for “dry” (<20ppm H_2O) electrolytes before the impedance decreased whereas “wet” (>60ppm H_2O) electrolytes exhibited low impedance more rapidly but then exhibited increasing impedance on cycling or calendar life testing. This is consistent with the water promoting the formation of acidic species during cycling that catalyze reactions of the electrolyte components leading to surface active products on both anodes and cathodes. Thermal stability experiments show that electrolytes are stabilized by the presence of excess LiF in solution and by removal of moisture. Detailed measurements are under way to attempt to quantify these effects.

High Voltage Electrolytes (Yoon/Yang) - Several families of boron based compounds have been designed, synthesized, and characterized. The solubility of LiF in organic solvents can be increased by using these compounds as additives, which may then be used as high voltage electrolytes. Testing Li half cells using electrolytes containing boron based compounds showed better capacity retention than the reference cell using no additives when cycled at elevated temperatures or wider voltage ranges as shown in Figure IV-37.

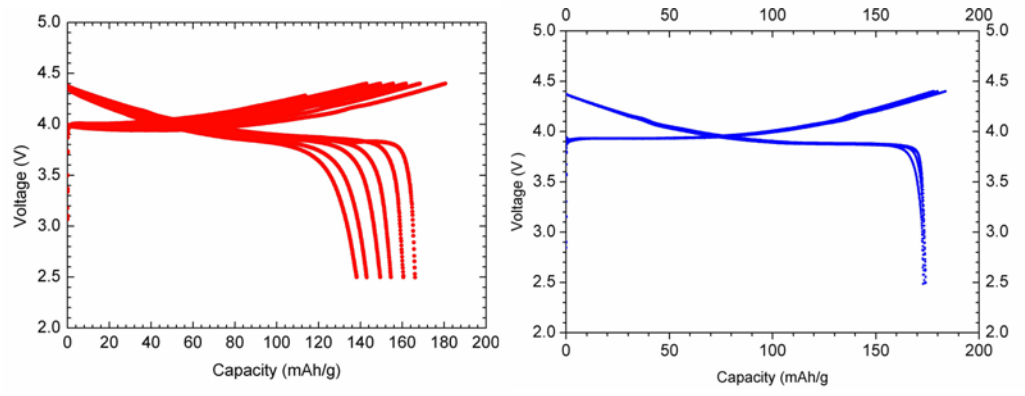

Electrolyte: 1.0 M LiBF$_4$, PC:DMC(1:1)

Electrolyte: 1.0 M THFPB, 0.2 M LiBF$_4$, PC:DMC(1:1)

Figure IV-37. The cyclability of a Li/LiCoO$_2$ half cell using LiBF$_4$ based electrolytes without or with boron-based additive. The boron based additive used here is [(CF3)2CHO]3B:THFPB.

***Nanostructured Polymer Electrolytes (Balsara)* -** This project is using composite polymer electrolytes comprised of an extremely hard (but non-conducting) polystyrene (PS) based portion (to block dendrite formation), interwoven with a conducing PEO based portion (to permit Li diffusion). Recently, this team electrically characterized mixtures of poly(styrene-*block*-ethylene oxide) (SEO) copolymers with LiTFSI salt. Electron micrographs of the composites studied are shown in Figure IV-38 where the dark channels are the conducting phase. The surprising result is that the conductivity of the block copolymer electrolytes *increases* with increasing molecular weight, Figure IV-39. This is in contrast to conventional polymer electrolytes where the conductivity decreases with molecular weight.

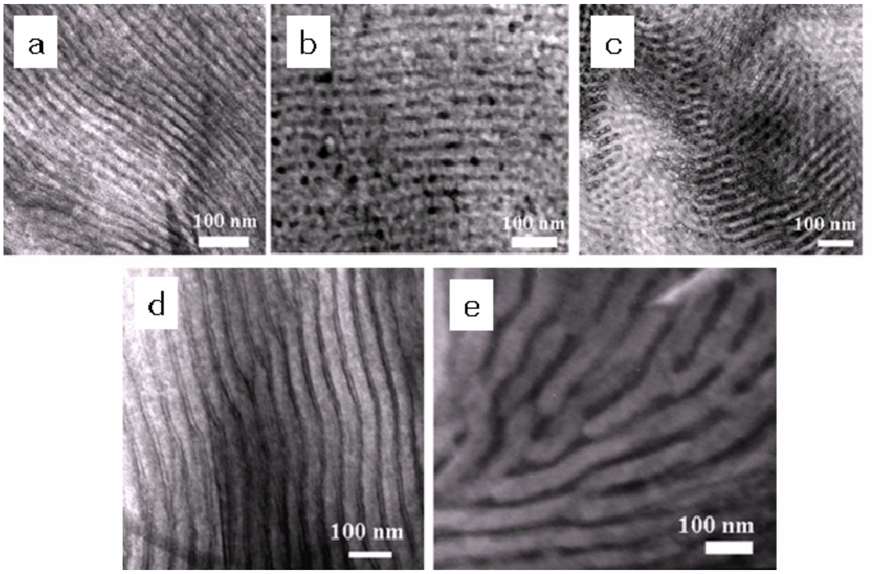

Figure IV-38. TEM of the pure SEO copolymers: a) SEO(16-16); b) SEO(36-25); c) SEO(40-31); d) SEO(40-54); e) SEO(74-98). The PEO phase is darkened by RuO$_4$ staining.

More extensive DC cycling tests of Li/PS-PEO/Li cells have been conducted and it has been found that the copolymers resist dendrite growth. Additional work on this important characteristic will continue following installation of a glovebox containing a Li-deposition chamber in early October 2007.

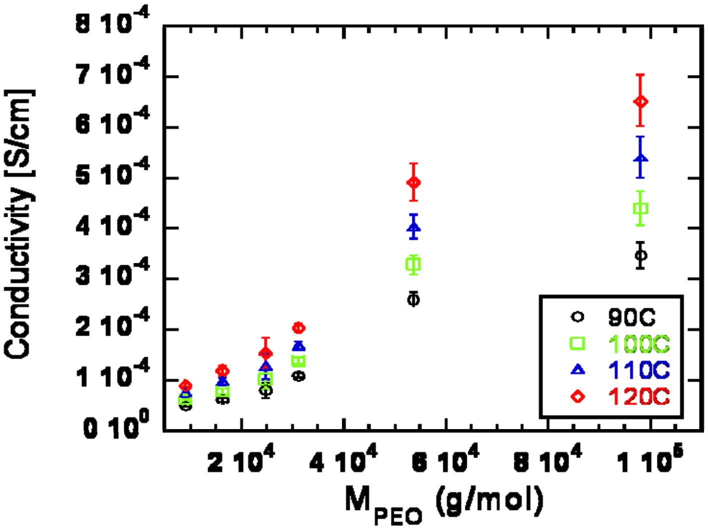

Figure IV-39. Ionic conductivity of SEO/LiTFSI mixtures with r = 0.02 versus MPEO. at selected temperatures.

New SEO copolymers are being synthesized to further investigate the range of physical and electrical properties available. One has an average molecular weight of 120,000 with a volume fraction of PEO equal to 0.54. A second is predicted to have a molecular weight of ~70,000 with volume fraction of PEO equal to 0.34. This latter polymer is expected to exhibit cylindrical microphase morphology. Further SEO copolymers are being synthesized with the same size PEO block, but varying PEO volume fraction (0.30 and 0.26) in order to study how block copolymer morphology affects conductivity.

Ionic conductivities have been measured as a function of salt concentration, temperature, copolymer composition and molecular weight. The work has focused on lamellar block copolymers with salt-free EO volume fractions ranging from 0.38 to 0.55, and molecular weights ranging from 25 kg/mol to 98 kg/mol. Ionic conductivities near 10^{-3} S/cm have been measured for both the 98 kg/mol and 58 kg/mol samples when *r*, the molar ratio of Li to ethylene oxide, is ~0.08. The stability of the polymer/Li interface was tested by cycling experiments using a DC current of 76µA/cm^2 through a 250µm thick copolymer electrolyte with *r*=0.02 (1/2 the estimated limiting current density). No evidence of deterioration of the Li/polymer interfaces was observed.

***Ionic Liquids (Doeff)* -** Work was directed towards determining if safer, high energy cells could be realized by using IL electrolytes. Methylpropylpyrrolidinium (P_{13}) bis(fluorosulfonyl)-imide (FSI) and bis(trifluoromethanesulfonyl)imide (TFSI) systems were compared to conventional electrolytes. Of the two IL systems, P_{13}FSI was superior to P_{13}TFSI, allowing room temperature operation at reasonable rates. Li/P_{13}FSI, LiTFSI/Li_xMnO_2 and $Li_xMn_{0.89}Ti_{0.11}O_2$ cells were cycled at room temperature. However, severe capacity fading was seen in Li_xMnO_2 cells. XRD and SEM/EDX analysis of the electrodes postmortem show that a Mn dissolution/ precipitation process takes place. This is stopped entirely by partial Ti substitution, resulting in excellent cycling behavior and retention of the original particle morphologies (Figure IV-40).

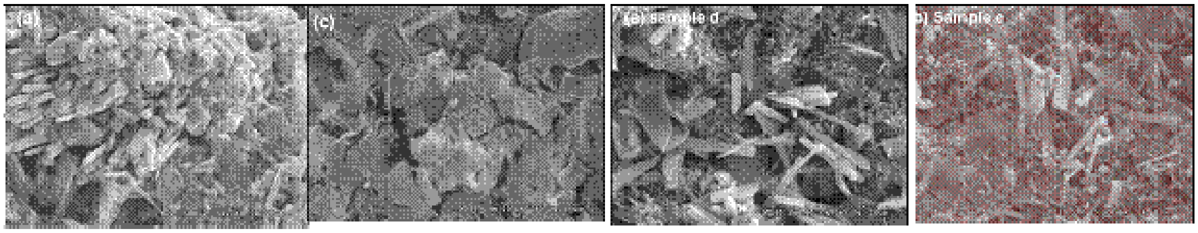

Figure IV-40. (left). Fresh Li_XMnO_2 electrode showing needle-like particle morphology of electroactive material and small particles of carbon and PVdF binder. (center left) Li_XMnO_2 electrode after 25 cycles in P13FSI-LiTFSI electrolyte, showing changes in particle morphologies, due to dissolution/precipitation of Mn. This caused capacity fading. (center right) Fresh $Li_xMn_{0.89}Ti_{0.11}O_2$ electrode. (right) $Li_xMn_{0.89}Ti_{0.11}O_2$ after 25 cycles in P_{13}FSI-LiTFSI. The particle morphology is retained and there is little capacity fading.

Li_xMnO_2 electrodes stored in P_{13}FSI/0.5M LiTFSI for several months do not show the same degradation as those cycled, indicating that the observed dissolution/ precipitation process in the latter is electrochemically induced. These results indicate that electrodes will need to be specially designed for use with ionic liquids to ensure good cycling. In addition, high interfacial impedances at the anode side, which lead to rate limitations, may be ameliorated by replacing lithium metal with alternatives such as $Li_4Ti_5O_{12}$.

***Ionic Melts for Li-ion Batteries (DesMarteau/Creager)* -** In the continuing search for more abuse tolerant electrolytes, research into ILs and single ion conducting (SIC) electrolytes has continued. Recently, charge-discharge testing of small-scale cells with IL electrolytes has been completed. Preliminary findings using the IM550 electrolyte ($CH_3O-(CH_2CH_2O)_{11.8}-CF_2CHFO-CF_2CF_2-SO_2N(Li)SO_2CF_3$) suggest that electrolyte transport into and out of the electrodes may be a limiting factor, which is consistent with other BATT projects. Work has also progressed on synthesis and characterization of new IL electrolytes, especially electrolytes of general structure $CH_3O-(CH_2CH_2O)_{15.3}-CH_2CH_2-$ Imidazolium$^+$(TFSI$^-$)-$CF_2CFHOCF_2CF_2SO_3(Li)$ (Imidazolium IL electrolyte) and $CH_3O-(CH_2CH_2O)_{11.8}-C_6H_4-R_f-SO_2N(Li)SO_2CF_3$, where R_f could be nothing (phenyl-linked IL electrolyte) or a $-CF_2CF_2OCF_2CF_2-$ linkage (extended-phenyl IL electrolyte).

Cell testing using IL electrolyte IM550 was conducted using Swage-style cells with Li and graphite anodes, $LiFePO_4$ (from Hydro-Quebec) and $LiCoO_2$ made in the lab. Cells having only the IM550 electrolyte have so far not charged well and consistently show quite small capacities on discharge, i.e. the cell voltage drops to nearly zero almost immediately when discharge current is passed. This is taken as evidence of poor electrolyte penetration into the electrode(s). Cells fabricated with IM550 electrolyte containing 40 wt % of EC:DEC (1:1) could be charged to 4.18 V (graphite anode, $LiCoO_2$ cathode) at a C/100 rate. Initial studies showed a precipitous drop in cell voltage when discharge was attempted at C/5, however more recent results show promising behavior at C/7 and C/8 discharge rate.

Promising results were recently obtained on cells for which the cathode formulation had been modified to include a partially fluorinated IL in the binder having the following structure: $X-CF_2O-(CF_2CF_2O)_p-(CF_2O)_q-CF_2-X$ where $p = 6$, $q = 1.5$ and

X = $-CH_2-(OCH_2CH_2)_n-O-CF_2CFHO-CF_2CF_2-SO_2N(Li)SO_2CF_3$, n = 0.5. Figure IV-41 shows representative results on a $Li_4Ti_5O_{12}$ / IM550 + 50 wt% PEGDME/$LiCoO_2$ cell. The cathode is: 86 wt% $LiCoO_2$, 5 wt% acetylene black; and 4 % LHB-108P + 5 wt% partially fluorinated IL as binder. Full capacity was achieved on cell formation at C/100, and the same full capacity was achieved on discharge at C/14 and C/10, and nearly full capacity was achieved at C/5. Experiments with otherwise identical cells for which the cathode formulation did not include any IL in the binder gave poor results; full capacity was never achieved during cell formation so charge-discharge experiments were not attempted on charged cells. It appears that the ionically-conducting partially fluorinated IL-binder raised the rates of ion transport within the electrode. Experiments using a non-fluorinated IL in the binder also failed, because the IL was soluble in the electrolyte which caused the electrodes to fall apart. The combination of the partially fluorinated polyether, which is insoluble in the electrolyte, and high ionic conductivity was essential to achieving good binding properties and low resistance. We plan to follow up on this promising finding via studies of electrodes with fluorosulfonimide-based perfluorinated ionomers of structure $(CF_2CF_2)_n-(CF_2CF-O-CF_2CF(CF_3)-OCF_2CF_2SO_2N(Li)SO_2CF_3)$ where n varies from ~2 to 8 as binder.

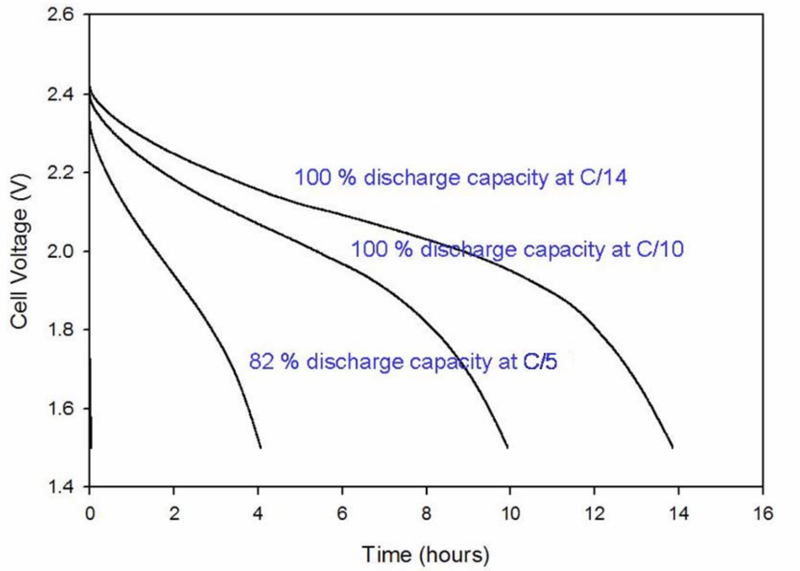

Figure IV-41. Discharge curves for cells of composition $Li_4Ti_5O_{12}$ / IM550 + 50 wt% PEGDME / $LiCoO_2$ composite cathode.

Progress was also made in testing the extended phenyl series of IL electrolytes. This series was conceived to have higher conductivity than the phenyl-linked IL electrolytes, due to the additional fluorocarbon character in the linker connecting the sulfonimide anion to the phenyl group. Figure IV-42 presents conductivity data for both the phenyl-linked series (filled triangles) and the extended-phenyl series (open triangles). Conductivity of the extended phenyl IL is comparable to, though not much higher than, that of the phenyl-linked series.

Progress was made on synthesis and characterization of new ILs containing both imidazolium and Li cations, and fluorosulfonate and/or fluorosulfonimide anions. Figure IV-43 presents structures and conductivity data. These electrolytes were targeted because they might offer a favorable combination of liquid character (hopefully low viscosity, promoted by the anticipated plasticizing character of the imidazolium/TFSI subunit), high ion content, and thus high conductivity. The particular structures shown in the figure were selected because they separate the polyether and imidazolium portions of the molecule from each other, and it doing so might help to lower viscosity and increase conductivity. Unfortunately, the data do not bear out this expectation. Conductivities are generally lower for these imidazolium ILs relative to our earlier generation polyether-based ionic melts, *e.g.,* sample "B" in Figure IV-43. Further work on these specific melts will therefore be suspended pending further developments.

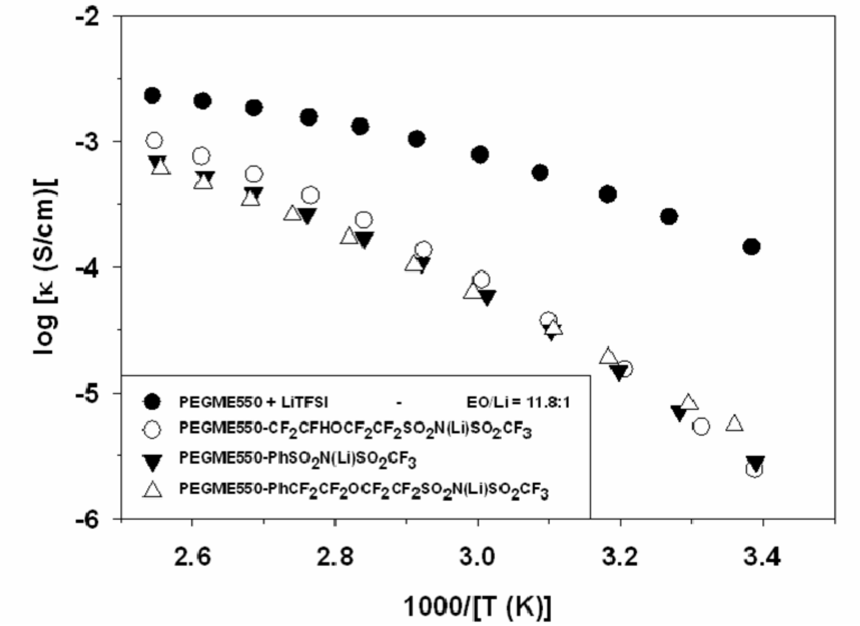

Figure IV-42. Arrhenius plots for 3 different PEGME550-based fluorosulfonimide ionic melts: a PFVE-based IL 550 (open circles), a phenyl-based (filled triangles) and an extended-phenyl-based (open triangles). Data for salt LiTFSI in PEGME550 solvent are included for comparison.

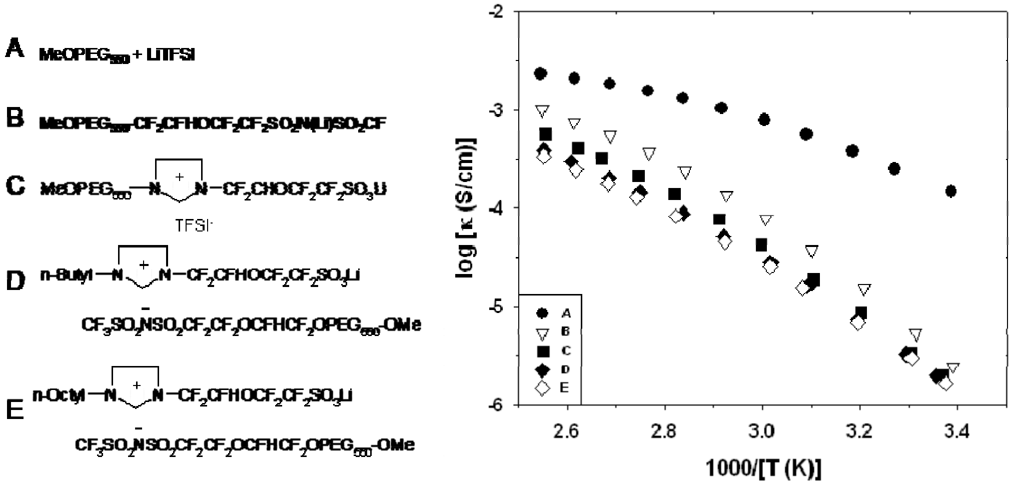

Figure IV-43. Structures and ionic conductivity data for a series of Li imidazolium fluorosulfonate and fluorosulfonimide IMs. Sample A is a binary salt (LiTFSI) dissolved in a polyether solvent; included for comparison.

It remains to be seen whether the partially fluorinated materials offer advantages as flame retardants. Experiments are in progress with other plasticizers, *e.g.,* small amounts of carbonate solvents, to see if they can offer a favorable combination of improved conductivity, especially at low temperature, and high Li transference. Calorimetry experiments are also in progress to assess reactivity of polyether ILs with active electrodes, and a voltammetry method has been developed and is being used to assess voltage stability limits at conventional electrodes.

***Molecular Dynamics of Electrolytes and Electrode/Electrolyte Interfaces (Smith/Borodin)* -** This work is simulating structure and transport properties of IL electrolytes. MD simulations of ILs have focused on two types of materials:

a. Pyrrolidinium and imidazolium-based ILs with bis(trifluoromethylsulfonyl)imide ($TFSI^-$) and bis(fluorosulfonyl)imide (FSI^-) anions doped with Li-salts;
b. ILs comprised of oligomer-attached-to-$TFSI^-/Li^+$. This electrolyte is attractive because it does not contain any solvent and is expected to prevent concentration polarization during battery operation.

Two generations of many-body polarizable force fields have been developed for ILs containing *N*-propyl-*N*-methyl-pyrrolidinium ($mppy^+$) and 1-ethyl-3-methyl-emidazolium ($emim^+$) cations, $TFSI^-$ and FSI^- anions. The first generation force fields for [mppy][TFSI] and for [mppy][TFSI] doped with LiTFSI adequately predicted ion transport and structure of ILs, see O. Borodin et. al., *J. Phys. Chem. B* **2006,** 16879, and Borodin, O.; Smith, G. D. *J. Phys. Chem. B* **2006**, 11481.)

Second generation force fields have improved transferability between ILs and organic solvents. Ion conductivity of [mppy][TFSI], [mppy][FSI],[emim][TFSI] and [emim][FSI] at room temperature predicted from MD simulations were found to be within 30% of experimental data (*J. Power Sources* **2006,** *160*, 1308.) Self-diffusion coefficients from MD simulations and pgf-NMR experiments are shown in Figure IV-44, showing that MD simulations reproduce experimental data very well. Further simulations have been performed on [mppy][FSI] and [emim][FSI] ILs and [emim][TFSI] + 1 M LiTFSI and [emim][FSI] + 1 M LiFSI. Comparison of ion self-diffusion coefficients of pure ILs is shown in Figure IV-45.

Notably, the FSI^- anion has a faster diffusion and lower activation energy for diffusion compared to $TFSI^-$ anions, while cation ($mppy^+$ and $emim^+$) self-diffusion coefficient is only insignificantly influenced by changing the anion from $TFSI^-$ to FSI^-. Similarly, simulations of ILs doped with Li-salts showed significant improvement of Li^+ transport and lower activation energy for diffusion for FSI-based ILs compared to TFSI-based ILs.

ILs comprised of an oligoether-attached-to-$TFSI^-/Li^+$ were also studied[16]. These ILs are attractive as they exhibit no concentration polarization during cell discharge. Conductivity of oligoether-$TFSI^-/Li^+$ is quite low ≈0.07 mS/cm at 333 K in both experiments and simulations. Two strategies for improving it have been examined: a) variation of the Li solvating group properties by replacing oligoether with the siloxane backbone with short three repeat unit oligoether side chains with TFSI- attached to the backbone, denoted as (MD_6EO_3TFSI)/Li and $TFSI^-$-(7 repeat unit siloxane denoted as MD_7)-$TFSI^-/2Li^+$ or by changing oligoether/Li^+ interaction; b) plasticizing the

---

[16] *J. Phys. Chem. B* **2006,** *110*, 24266.

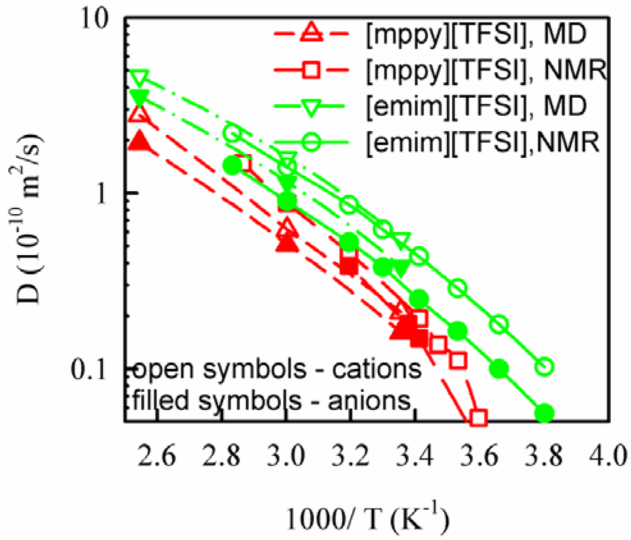

Figure IV-44. Comparison of the ion self-diffusion coefficients from MD simulations and previously published pgf-NMR experiments (J Phys Chem B 2005, 109, 22814; J Phys Chem B 2001, 105, 4603).

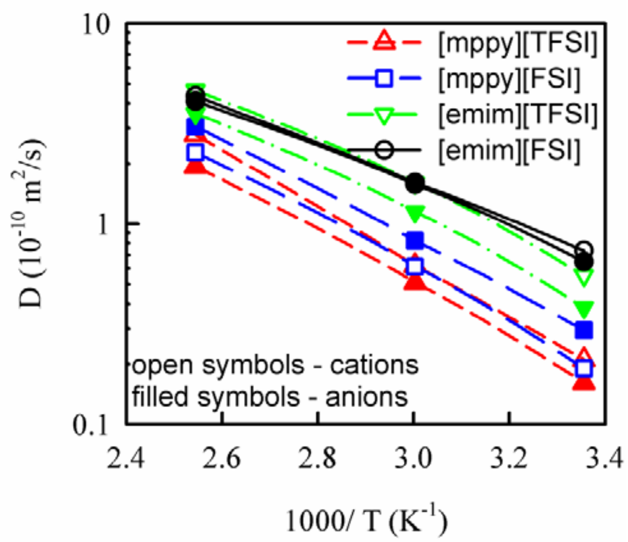

Figure IV-45. Ion self-diffusion coefficients predicted from MD simulations.

oligoether-$TFSI^-$/Li^+ with oligoether (M_w=530). The first strategy showed improvements (within a factor of 2-4) of conductivity at room temperature can be achieved. The second strategy leads to better improvements in conductivity at the expense of developing concentration polarization as was confirmed by the Clemson group.

This group is also investigating the structure and energetics of liquid electrolyte/cathode interfaces with emphasis on Li desolvation from EC and its intercalation into $LiCoO_2$. Quantum chemistry calculations have been performed on representative $LiCoO_2$ clusters. These calculations form the basis for developing a classical force field for CoO_2 interacting with Li, various anions and liquid electrolytes. The resulting force field will be utilized in simulations of the cathode/electrolyte interface.

***Gel Electrolytes and Ionic Liquids in $LiFePO_4$ Cathodes (Zaghib)* -** This team has evaluated laboratory cells containing $LiFePO_4$ cathodes, graphite anodes based on water soluble binder and ionic liquids [1-methyl-3-ethyl imidazolium bis-trifluoromethanesulfonimide (EMI-FSI) and N-methyl-N-propylpyrrolidinium–FSI (Py13-FSI)]. These cells were compared to those containing conventional electrolytes, EC-DEC-LiFSI. Figure IV-46(left) shows the initial cycles of $LiFePO_4$ with both Li and graphite anodes and different electrolytes. The first-cycle coulombic efficiency was 100%, 93.4% and 94.2%, respectively, for cells with EC/DEC-LiFSI, Py13-FSI and EMI-FSI. The highest reversible capacity was obtained with EC-DEC-LiFSI (160 mA/g), 151 mAh/g was obtained with the IL-containing cells.

Regarding the anode, the coulombic efficiency and reversible capacity were strongly affected by the electrolyte. With Py13-FSI, the first coulombic efficiency was 83%, 80% when EMI-FSI is used. However, the reversible capacity was only 330 mAh/g with PY13-FSI, and 370 mAh/g with EMI-FSI. With the liquid electrolyte, the first coulombic efficiency was 96%, and reversible capacity was close to theoretical at 371 mAh/g.

The power performance is shown in Figure IV-46(right). Both ILs show lower capacity than the cell with EC-DEC-LiFSI. In the range of C/12 to 1C, the capacity fade was 21% for EMI-FSI and 18% for Py13-FSI, compared to 8% for the liquid cell. Moreover, in the rate range between 1C and 10C, the capacity of both cells with ionic liquids drops by more than 80%. In contrast, the liquid cell with LiFSI salt had only 21% fade.

This group has also continued investigating the use of gel polymer electrolytes in an iron phosphate-based cell. A new gel polymer was developed with a minimum polymer content to maintain the high rate performance. The polymer/ (EC-DEC-$LiPF_6$) composition was 2%/98% by weight. No initiator was added to the composition as it is an auto-crosslink polymer. Its performance in the cathode and anode was studied separately with the gel formed at either 25 or 60°C. The initial coulombic efficiency in the anode was 89%, independent of the gel-formation temperatures, compared to 86% for the standard liquid type cell (Figure IV-47). For the reversible capacity, the gel formed at 25°C resulted in a capacity of 360mAh/g, while 342mAh/g was obtained with the gel formed at 60°C. For comparison, the liquid electrolyte cell yielded 358mAh/g.

In the cathode side, the coulombic efficiency was close to 100% for gel-formation electrolytes at either temperature and with the liquid electrolyte. However the reversible capacities were slightly different at 158, 155 and 160 mAh/g for 25 and 60°C gel formation temperature and liquid electrolyte, respectively.

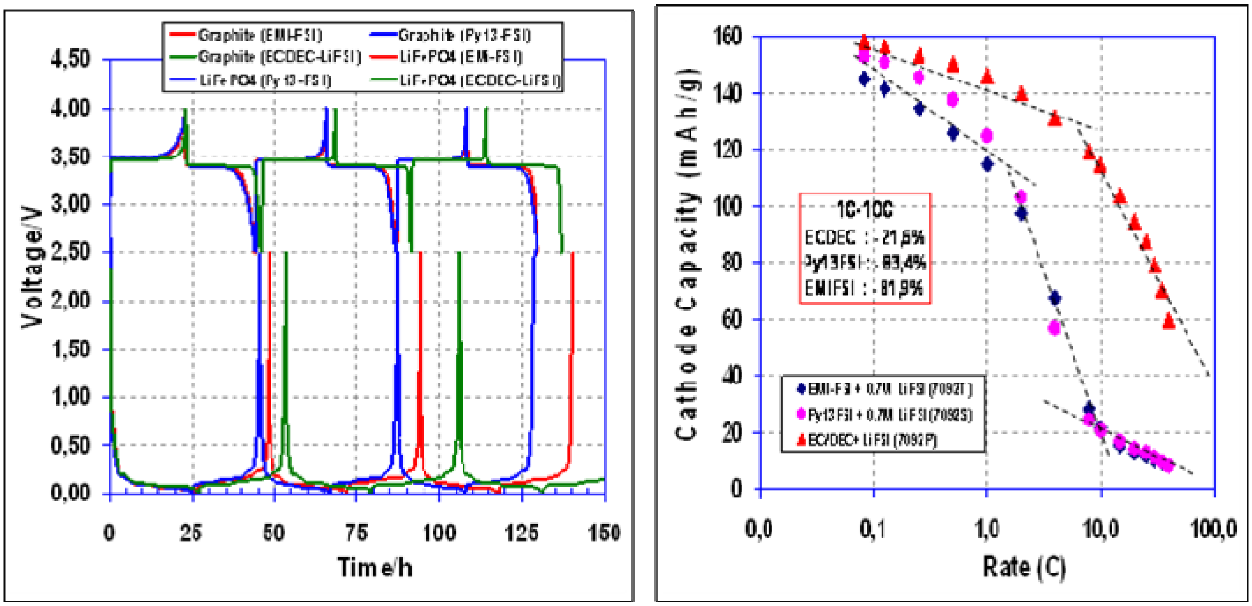

Figure IV-46. Left) Cycling of Li/$LiFePO_4$ and Li/graphite cells with different electrolytes at C/24, Right) Ragone plot of Li/$LiFePO_4$ cells with different electrolytes at 25°C.

The power performance of the $LiFePO_4$ cathode was evaluated and the results are presented in Figure IV-47(right). Very comparable data were obtained for gel-polymer and liquid-type cells from C/12 to 10C rate range. The difference in the discharge capacities is observed at rates above 15C. At 15C, the discharge capacity of the gel-polymer formed at 25°C was 74%, 20% lower than that of the liquid electrolyte. In contrast, only 33 mAh/g was obtained with the gel formed at 60°C, 64% lower than liquid electrolyte. Thus, for rates <15C, the gel polymer electrolyte with this new auto-crosslink polymer in graphite/$LiFePO_4$ cells showed comparable performance to that of cells with liquid electrolyte.

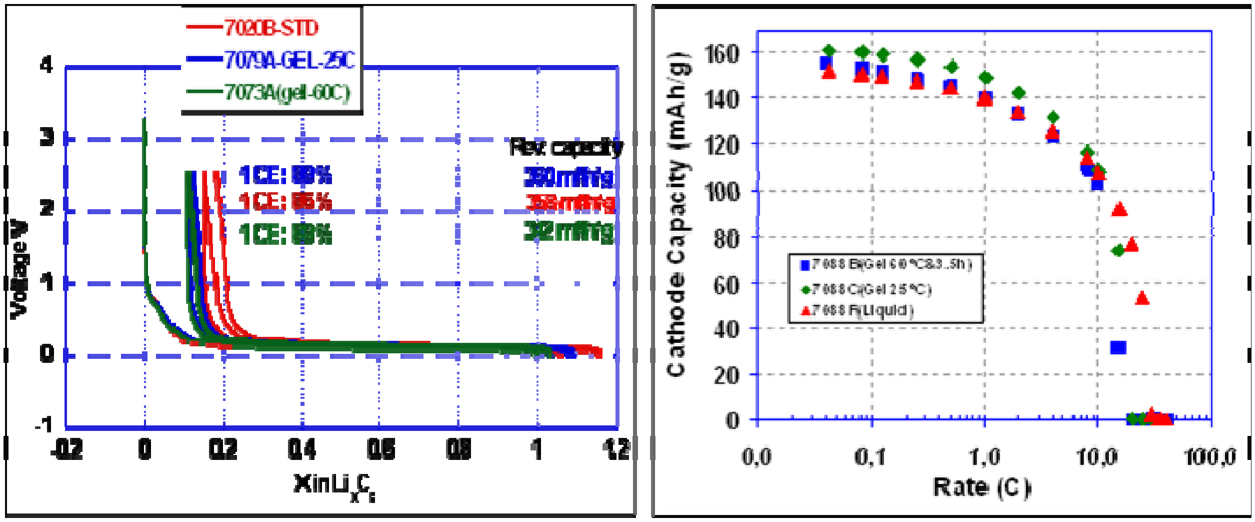

Figure IV-47. Left) Cycling of Li/graphite cells with the new gel polymer electrolytes at C/24. Right) Ragone plot of Li/$LiFePO_4$ cells with new gel polymer formed at 25°C and at 60°C.

Sample Future Plans in Novel Electrolytes

- Carry out measurements of the kinetics of electrolyte reactivity and combine those results with identification of products to obtain insight into how these reactions affect interfacial impedance.

- Continue the investigation of the extended phenyl ionic liquid with studies of voltage limits and reactivity testing.

- Complete calculations needed to develop a classical force field for CoO_2 interacting with Li, various anions and liquid electrolytes. Utilize the resulting force field to simulate the cathode/electrolyte interface.

- Use molecular dynamics to study the free energy barrier associated with Li cation desolvation from electrolyte and its intercalation into graphite. The free energy barrier will be correlated with the activation energy of the charge transfer resistance of cells.

- Identify the factors that govern the transport properties of PS-PEO/LiTFSI mixtures, including microphase morphology. Study the stability of these materials when placed against lithium iron phosphate -based cathodes and Li metal anodes.

IV.D Li-Ion Modeling, Diagnostics, and Cell Analysis

Objectives

The objectives in this section include determining the contributions of electrode material changes, interfacial phenomena, and electrolyte decomposition to cell capacity and power decline. Researchers are also working to obtain a fundamental understanding of the effect of bulk and surface microstructure on transport properties and materials stability, and to determine the composition and processing conditions of electrodes with enhanced conductivity.

Approach

***Diagnostics* -** The microstructure of oxide-electrolyte interfaces with and without nanoparticle coatings and their stability as a function of potential and cycle number is examined *ex situ* and *in situ* by TEM and electrochemical AFM.

Another approach is to build porous electrodes with realistic microstructures, based on results of image analysis of real electrodes. Porosities and dimensions for candidate cells are then used as input to develop optimal combinations of materials from simulations. These will be used to inform electrode design.

***Modeling/Simulation* -** Mathematical models are developed for candidate Li-ion chemistries. Experiments are designed to test theoretical predictions and to estimate properties needed for the models. Researchers then use the models to compare various chemistries to each other and assess their ability to meet EV, HEV, and PHEV goals.

Cell Analysis **-** Perform engineering design analysis of each of the steps of the electrode fabrication process. Specifically, investigate the impact of varying the ratio of conductive additive to binder on the rate and cycling performance of high power cells.

Accomplishments

Cell Making Protocol (Battaglia) **-** One of the goals of this project is to establish and execute standard cell making and testing protocols for evaluating promising materials. The LBNL Cell Making Protocol, specifically focused on Mn-spinel cathodes, was published as an LBNL report, available at http://repositories.cdlib.org/cgi/viewcontent.cgi?article=5114&context=lbnl.

Impact of Conductive Additive to Binder Ratio Cell Performance (Battaglia) **-** This group also focuses on developing low-impedance electrodes through electrode engineering. Previous research into the electronic conductivity of films of varying ratios of carbon to polymer indicated that films with a 0.8:1 carbon to polymer ratio displayed a maximum in conductivity. Below 0.2, the films displayed very little conductivity and above 0.8 the conductivity began to fall. Films with less carbon than 0.2:1 may exhibit reduced conductivity due to lack of percolation between carbon particles. Films with greater carbon content than 0.8:1 may display a reduction in conductivity because the polymer is being spread too thin to hold the carbon particles together.

In a follow on study, three laminates with $LiNi_{0.8}Co_{0.15}Al_{0.05}O_2$ active material with a constant carbon content of 4% and carbon to binder ratios of 0.5:1, 0.8:1, and 1:1 were fabricated. These laminates were calendered to the same porosity and thickness but had different active material loadings. They were then loaded into coin cells with lithium anodes. After a few formation cycles, AC impedance was measured. Surprisingly, the electrodes with the highest binder fraction displayed the lowest impedance. As seen in Figure IV-48, much of the decrease in impedance appears to stem from a reduction in the interfacial charge transfer resistance. Research in the coming year will focus on trying to understand why this is the case.

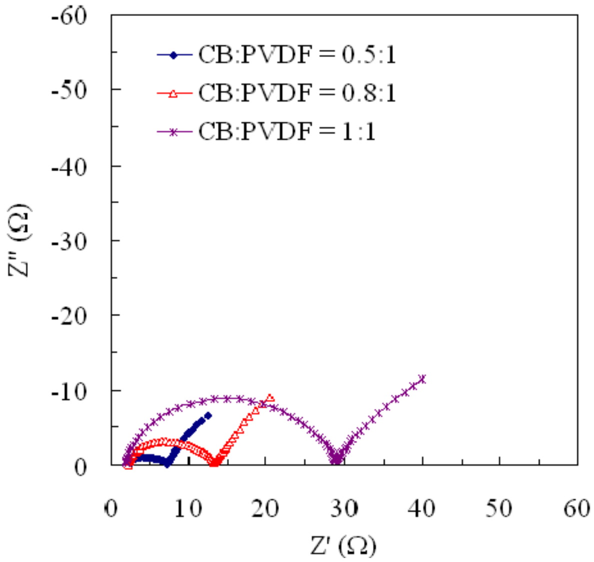

Figure IV-48. Nyquist plot of the ac impedance of films of different ratios of carbon black to poly vinylidenedifluoride binder (CB:PVdF).

***Cathode Surface Coatings for Improved Stability (Shao-Horn)* -** Application of a surface oxide or phosphate such as ZrO_2, Al_2O, TiO_2, or $AlPO_4$ to $LiCoO_2$ particles can significantly improve the degree of capacity retention upon cycling to high voltages without loss in reversible capacity. Among these, "$AlPO_4$"-coated $LiCoO_2$ as reported by Cho et al. has shown superior cycling performance relative to $LiCoO_2$ coated with other oxides. Specifically, the "$AlPO_4$" coating increases the initial reversible discharge capacity from 200 to 210 mAh/g with a 4.8 V upper limit, and "$AlPO_4$"-coated $LiCoO_2$ electrodes retain ~150 mAh/g after 50 cycles. This work employs EDX in a scanning transmission electron microscope (STEM) to obtain the distribution of Co, O, Al and P on the μm- and nm-scale of the powder sample, and uses XPS to analyze the chemical environments of C, Al, P, Co, O and Li in order to provide new insights into the phases on the surfaces of the active particles.

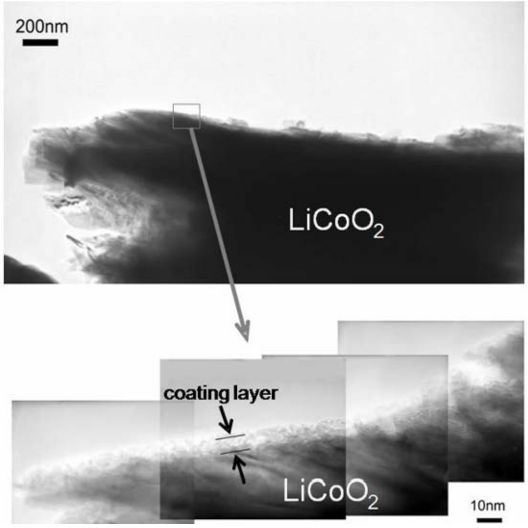

Figure IV-49. Cross-sectional TEM images of the "$AlPO_4$"-coated $LiCoO_2$ show uniform coverage of the particle surface, with a thickness variation of 10-100 nm. High-resolution TEM images of the coating cross-section show a light-dark variation which may indicate regions of varying composition or thickness in the coating.

Bare "$LiCoO_2$" was prepared from stoichiometric amounts of Co_3O_4 and Li_2CO_3 at 1000°C for 4 hours in an oxygen stream. An $AlPO_4$-nanoparticle solution was prepared by slowly dissolving $Al(NO_3)_3{\cdot}9H_2O$ and $(NH_4)_2HPO_4$ in distilled water until a white $AlPO_4$-nanoparticle suspension was observed. The slurry was dried in an oven at 120°C for 6 hours and heat-treated at 700°C for 5 hours, from which the $AlPO_4$-coated $LiCoO_2$ was obtained. The coating layer appeared to cover most of the particle surface but it was found that the thickness was not uniform, with a thickness variation of 10-100 nm. Figure IV-49 shows a typical cross sectional image of the coating layer with a thickness of ~10 nm. XRD analyses showed that major phase is O3 layered in the "$AlPO_4$"-coated $LiCoO_2$ sample, however orthorhombic Li_3PO_4 in the γ-phase, which can form at temperatures above 500°C, was detected as a minor phase, as shown in Figure IV-50. Evidence for the presence of $AlPO_4$ was not found in the diffraction data. It is believed that the $AlPO_4$ coating nanoparticles reacted with excess Li in bare "$LiCoO_2$" particles to form Li_3PO_4 on the particle surface and rendered stoichiometric $LiCoO_2$ in the bulk during the heat-treatment at 700°C. Upon Li_3PO_4 formation, remaining Al^{3+} may form $LiAlO_2$ or $LiCo_{1-y}Al_yO_2$ with high levels of Al substitution on the particle surface and diffuse into the particle interior to form $LiCo_{1-y}Al_yO_2$ solid solutions with small amounts of Al substitution.

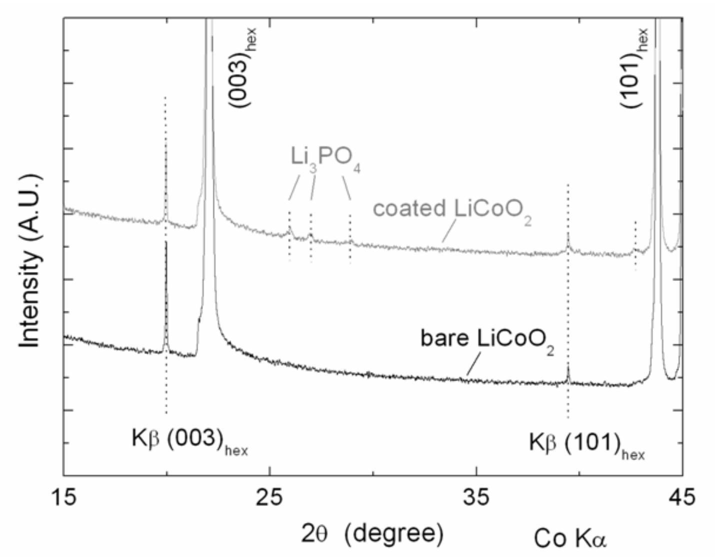

Figure IV-50. XRD patterns of bare $LiCoO_2$ and $AlPO_4$-coated $LiCoO_2$ show the appearance of peaks corresponding to Li_3PO_4 in the coated sample.

These observations were further supported by EDX and XPS study. As can be seen in Figure IV-51, certain features correspond to phosphorus-rich clusters, while the Al is more evenly distributed across the thick coating region and the rest of the particle surface. Figure IV-52 shows XPS spectra of the Al 2p and P 2p photoemission lines for $AlPO_4$-coated $LiCoO_2$ and pure $AlPO_4$ with some of reference materials. The Al 2p and P 2p photoemission peaks were found for $AlPO_4$-coated $LiCoO_2$ but not for bare $LiCoO_2$, as expected. The Al 2p peak occurs at 73.3eV, which differs from the Al 2p peak at 75.0 eV of the reference $AlPO_4$ sample used in this study and the reported value of 74.5 eV for the Al 2p in an $AlPO_4$ thin film. This difference further confirms that the $AlPO_4$ phase is absent from the particle surface of $AlPO_4$-coated $LiCoO_2$. Given a resolution of 0.05 eV for the XPS data, the Al 2p peak found in the $AlPO_4$-coated $LiCoO_2$ is comparable to that of the reference $LiAlO_2$ sample having an Al 2p peak at 73.4 eV but is higher than that of the reference Al-substituted $LiCoO_2$ - $LiAl_{0.1}Co_{0.9}O_2$ sample (72.4 eV). This result is in good agreement with the view that the surface of the coating layer may contain Al-substituted $LiCoO_2$, with substitution levels much higher than that of $LiAl_{0.1}Co_{0.9}O_2$ and close to that of $LiAlO_2$. The P 2p photoemission peak at 133.2 eV for $AlPO_4$-coated $LiCoO_2$ is considerably different from that of the reference $AlPO_4$ at 134.4 eV but agrees very well with that of the reference Li_3PO_4 sample at 133.2 eV, as shown in Figure IV-52b. This result is consistent with the detection of orthorhombic Li_3PO_4 on the surface of $AlPO_4$-coated $LiCoO_2$ as revealed by XRD. Therefore, these comparative studies of Al 2p and P 2p binding energies confirm previous EDX data that the coating layer contains no $AlPO_4$.

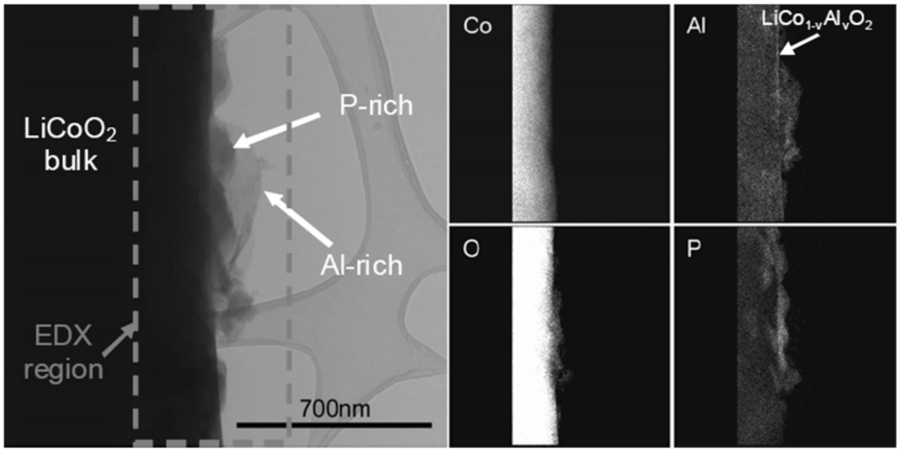

Figure IV-51. EDX mapping of "$AlPO_4$"-coated $LiCoO_2$ particle edge with STEM. Only the center region of the image has been mapped by EDX.

It is proposed that Li_3PO_4 and $LiAl_yCo_{1-y}O_2$ phases on the coated sample can significantly reduce Co dissolution and impedance growth during cycling to high voltages, which leads to superior cycling performance. Moreover, having Li-conducting phases such as Li_3PO_4 and $LiAl_yCo_{1-y}O_2$ on the surface can reduce resistance to Li diffusion at the particle-electrolyte interface, which may lead to enhanced rate capability.

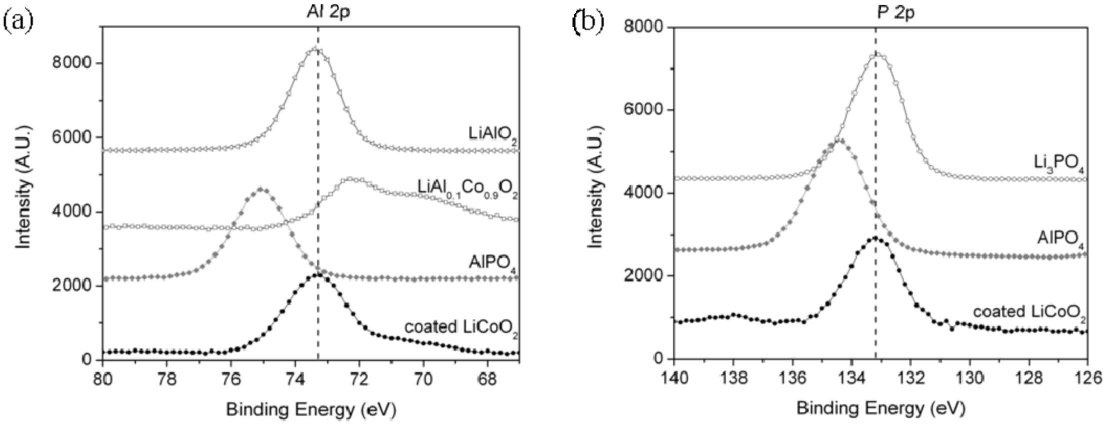

Figure IV-52. XPS spectra of the (a) Al 2p and (b) P 2p photoemission lines for $AlPO_4$-coated $LiCoO_2$ and pure $AlPO_4$. The large shifts to lower binding energy for the coated $LiCoO_2$ relative to the reference $AlPO_4$ for both spectra indicate that the Al and P are not present as $AlPO_4$ in the surface coating. The oxidation states of Al and P on the coated $LiCoO_2$ surface are similar to those of P in Li_3PO_4 and Al in $LiAlO_2$. Dashed lines indicate peak positions in the coated $LiCoO_2$ sample.

Transport-Property Measurement (Newman) **-** A technique for measuring diffusion coefficients in electrolytes for Li-ion batteries has been developed that allows for temperature control in $LiPF_6$ in acetonitrile (ACN) as well as the Gen 2 electrolyte. Results indicate that the diffusion coefficient for $LiPF_6$ is a factor of five higher in ACN than in baseline electrolytes. Exposure time to UV light has been minimized using a shutter in order to prevent localized heating. Figure IV-53 shows the diffusion coefficient as a function of $LiPF_6$ concentration.

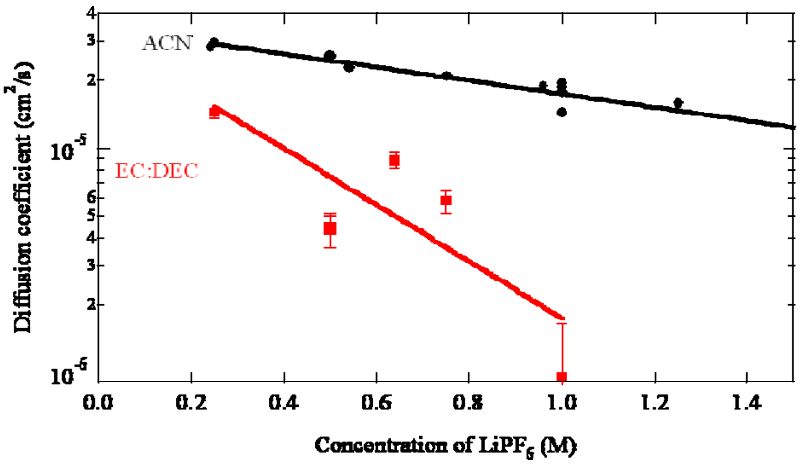

Figure IV-53. Diffusion-coefficient results for $LiPF_6$ in ACN and in EC:DEC at 296 K. The diffusion coefficients are seen to decrease with increasing salt concentration. Results for $LiPF_6$ in EC:DEC at higher concentrations have more error because the diffusion coefficient is approaching the limitations of the technique (ca. 10^{-6} cm^2/s).

The activity coefficient in $LiPF_6$ electrolytes is also being measured using melting-point depression and a concentration-cell experiment. A phase diagram is being experimentally determined using a baseline system.

***Electrodes with a Constant Open-Circuit Potential with SOC (Newman)* -** Work is complete on quantifying the effect that flat open-circuit potential profiles have on increasing the capacity usage of HEV and PHEV batteries. One of the main conclusions is that for HEVs, capacity usage is power-limited rather than energy-limited. This is because of the requirement for short current pulses that amount to little energy. Thus, the battery must be large enough to deal with the high current pulses while remaining within the upper and lower voltage cutoffs, which results in a limited use of the batteries capacity. There is only a slight increase in capacity usage by using electrodes with a constant potential vs. SOC for HEV applications. These results are specific to a driving cycle. Emphasis is now being placed on understanding the battery usage based on changes to the driving cycle.

As batteries become larger, such as for PHEV applications, they become energy limited. They are able to use a greater percentage of their SOC window and the effect of a flat open-circuit potential is more pronounced. An LTO anode and an $LiFePO_4$ cathode (which exhibit two-phase Li intercalation) achieve a significant increase in capacity usage over the graphite—manganese oxide spinel system. However, due to the relatively low open-circuit potential of the former system (1.8 V compared to 3.9 V), its separator area is significantly larger. Cell resistance also plays an important part in determining capacity usage: the lower the cell resistance, the greater the SOC range that can be used. A zero-dimensional model was developed, including the OCP and overall cell resistance as functions of SOC. Figure IV-54 shows that the SOC range is larger for a given driving distance for the LTO/$LiFePO_4$ system (because of the flat potential profile) but the separator area is larger (because of the lower potential).

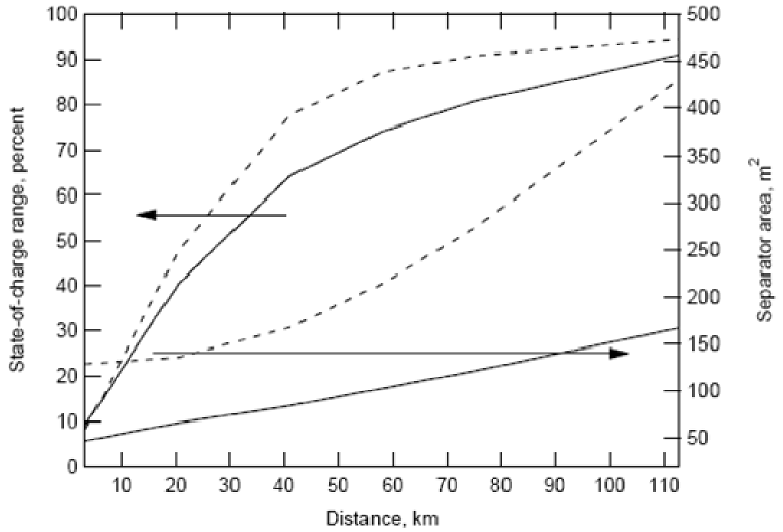

Figure IV-54. Comparison between the graphite – manganese oxide spinel (solid curves) and titanate spinel – iron phosphate (dashed curves) electrode systems for various all-electric driving distances.

***Design of Batteries for HEVs (Srinivasan)* -** This project has focused on describing the complexity of battery behavior in HEVs and PHEVs wherein the battery is not continuously discharged, but is subjected to high power pulses for a short periods (10 s), under both discharge and charge. This usage constrains the battery operation to smaller SOC ranges. This effort complements those in the Newman-group (see above) where battery operation is understood based on a vehicle model associated with a driving cycle. This project aims to understand battery operation by starting with a battery design that is subjected to FreedomCAR testing protocols. Simulations were performed for a high voltage (~4.0 V) low capacity (85 mAh/g) spinel $LiMn_2O_4$ system with high transport rates; for the high capacity (180 mAh/g) and high voltage (~ 4.0 V) layered NMC system with reasonable transport in the solid phase; and the mid-capacity (155 mAh/g) low voltage (3.42 V) $LiFePO_4$ system with small particle size to ensure low solid phase limitations. The $LiFePO_4$ system has a flat discharge voltage allowing use of a larger SOC range, thereby increase the available energy.

The model was used to generate curves of available energy vs. discharge pulse power while keeping the ratio of regeneration to discharge power at 0.8. The design of the battery was then changed to maximize the power at a power to available energy ratio of 83:1 (*i.e.,* the USABC HEV goal). The simulations confirm the advantages of the flat-potential $LiFePO_4$ system where the SOC range of operation was considerably larger (36%) when compared to the spinel and layered systems (~25%). Comparison of this result to that obtained by the Newman-group suggests that the driving profile used in developing the FreedomCAR goals is critical in determining battery usage. Interestingly, although the SOC range is smaller in the layered chemistry, the higher energy (due to the higher voltage and capacity) resulted similar performance to that of the $LiFePO_4$ system. The results are shown in Figure IV-55 where the cell level data is scaled to a pack by dividing by a factor of two. Work will proceed in collaboration with the Cell Analysis group to ensure that the model is compared to experimental pulse data and to provide guidance for designs.

Models have also been adapted to simulate PHEV behavior. Simulations were conducted with both the charge depleting and the charge sustaining modes. The battery design was optimized to maximize the performance for a P/E ratio of 13.25 corresponding to the PHEV-10 goal defined by USABC.

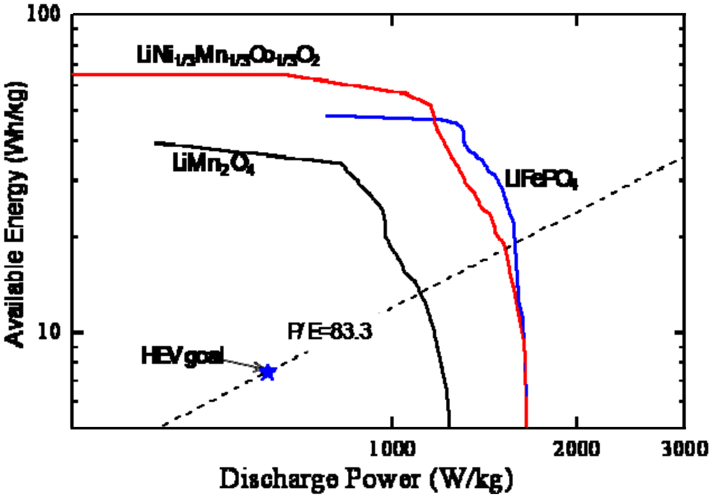

Figure IV-55. Optimal available energy vs. discharge power for baseline chemistries.

Figure IV-56 summarizes the result of the modeling study where the performance of the various chemistries is compared to each other and to the USABC/FreedomCAR Partnership goals. The cell level data is scaled to a pack by dividing by a factor of two. Results show that, as expected, the NMC cathode has the best performance for PHEV's among these three candidates.

A preliminary calculation, assuming intercalative behavior, was performed for the 4.0 V flat-potential system, corresponding to $LiMnPO_4$, with properties similar to $LiFePO_4$. While an increase in performance is seen due to the higher voltage, the increase is not as much as expected from a simple theoretical-energy calculation (~ 15%). This is because the potential of the $LiMnPO_4$ cathode is closer to the potential where electrolyte oxidation could occur (4.3 V), thereby decreasing the regen power capability of this chemistry. This suggests that to truly take advantage of $LiMnPO_4$, its power capability would need to exceed that of $LiFePO_4$. The study points to the importance of understanding the maximum voltage to which cathodes can be cycled without compromising life, and how this voltage translates across various chemistries. The excess spinel cathode modeled in this study has a capacity of 85 mAh/g and has the lowest theoretical energy among all four cathodes (further details can be seen in previous annual reports where optimized Ragone plots for the three presently-used cathodes were generated using these models). Further, the spinel cathode has a slightly lower window of operation arising from the inability to use the battery in the fully charged state owing to closeness of the equilibrium potential to the 4.3 V cutoff potential used in this study.

Simulations were also conducted on the NMC cathode to determine how much of an energy increase could be achieved if the ratio of active to inactive material in the electrodes could be decreased to match that of cell phone batteries (95% by weight active material in the cathode and 98% active material in the anode for a cell phone battery compared to 84% active material in the cathode and 90% active material in the anode used previously). Clearly, the improvements can be dramatic, if power and life can be maintained with this change. Efforts are underway in the Battaglia and Sastry groups to understand these two aspects and to quantify the impact of cycling to higher voltages.

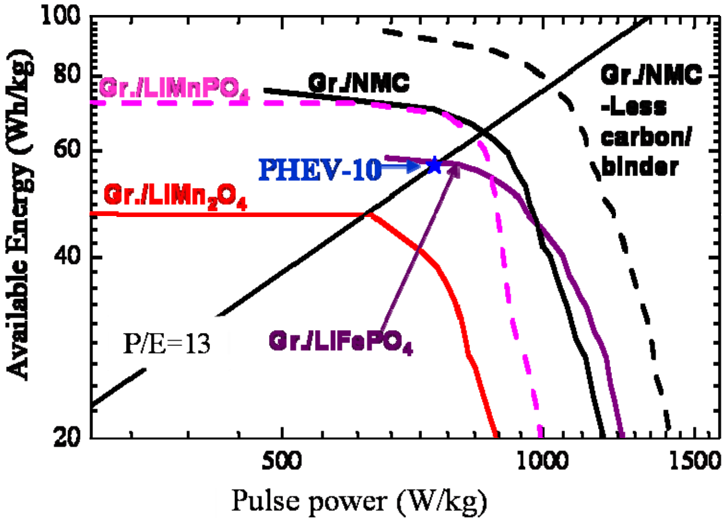

Figure IV-56. Comparison of "best" of chemistries vs. PHEV goals.

Design of EDLCs for HEV Applications (Srinivasan) **-** While the $LiFePO_4$ system has an advantage in HEVs owing to its flat potential, electrochemical capacitors occupy the other extreme with a slopey potential through discharge. However, these systems have significantly higher power due to the small distances over which ions move to store charge and have very good cycle life. Current EDLCs will not meet the HEV performance goals owing to their poor energy density. Simulations have been used to determine the ability of modified or enhanced EDLCs to meet HEV goals. The system modeled was one where concentration polarization was ignored, similar to previous capacitor models. While the operating voltage of the capacitor is 2.7 V, literature reports (see *J. Electrochem. Soc.*, 141, 2989, 1994) suggest that the electrolyte is stable to >5.0 V. A significant increase in the operating voltage (1 V) is needed to achieve energies that bring the EDLC closer to the HEV goals (see Figure IV-57 where all cell level calculations are converted to a pack level by dividing by a factor of two). Research into tuning the surface groups in carbon to change the rest potential could prove useful. In addition, while typical double-layer capacitances are in the order of 5-10 $\mu F/cm^2$, a recent report (Science, **313,** 1760, Sept. 2006) suggests that a three fold increase is possible with the use of nanoporous (~2 nm pores) materials. Model results suggest that such a large increase would indeed make capacitors competitive for HEV applications.

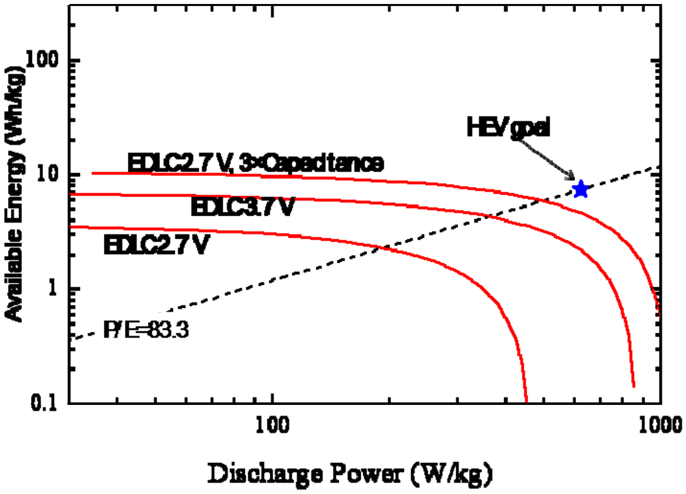

Figure IV-57. Possible UCap improvements vs. HEV goal.

Electrode Modeling (Sastry) **-** This group has developed a suite of numerical tools to determine optimal compositions of Li-ion cathodes, that is, proportions and properties of active material, binder, and conductive additive. Their mathematical models extend the 1D model, developed by Newman's group[17], to full, multiphysics 3D finite element models, to determine the effective material properties of a porous electrode[18]. This approach replaces the Bruggeman correction for porosity in the 1D model with a more realistic 3D finite element model. It accounts for the effects of particle arrangement, types, and density. Varying each, and the ratio of electrolyte ionic conductivity /electrical conductivity of the cathode solid phase, does affect cathode properties.

Extensions of this to a whole cell model have allowed investigation of microstructural features[19] on rate performance. A first case study was completed, comprising Li/$LiPF_6$-(EC:DMC)/ $Li(Ni_{1/3}Co_{1/3}Mn_{1/3})O_2$. The cathode comprised active particles with conductive additives (carbon black with/without graphite), and PVdF. Proportions of each and the size of the cathode particles were systematically altered to determine the energy and power densities under different discharge rates. Moreover, mechanical stresses induced during intercalation have been included in a way that allows seamless incorporation into the finite element analysis, via thermal analogy[20]. Completion of these studies will allow optimization of Li cells for energy or power, and also provide insight on lifetime-limiting mechanical performance.

Although all parameters being studied affect cell performance, cathode porosity, particle size, and the ratio of electrolyte conductivity/cathode electrical conductivity solid phase parameters are being intensively studied, first. It has been found that some conductive additives may reduce electrode conductivity[8] if they are incorporated by penalizing the concentration of more effective

---

[17] M. Doyle and J. Newman, The Use of Mathematical-Modeling in the Design of Lithium Polymer Battery Systems, *Electrochimica Acta*, **40** (13-14), 2191 (1995).

[18] Y.H. Chen, C.W. Wang, G. Liu, X.Y. Song, V.S. Battaglia, and A.M. Sastry, Selection of conductive additives in Li-ion battery cathodes - A numerical study, JECS **154**, (10), A978-A986 (2007).

[19] C.-W. Wang and A.M. Sastry, Mesoscale Modeling of a Li-Ion Polymer Cell, *JECS,* **accepted**, (2007).

[20] Zhang, X.-C., Shyy, W., and Sastry, A.M., 2007, "Numerical Simulation of Intercalation-Induced Stress in Li-Ion Battery Electrode Particles," JECS, v. 154 (10), pp. A910-A916.

additives, thus reducing overall cell energy density. Also, the morphology of the cathode solid phase strongly affects effective ionic conductivity of the electrolyte phase.

The proportions of each constituent of the cathode were systematically altered in simulations, such that effective electronic conductivities were comparable to ionic conductivities of the electrolyte. Completion of these studies will result in identification of cathodes with higher overall electronic conductivity and reduced surface area.

The algorithm for determining the effective conductivity of the cathode has been experimentally verified by using our four-point-probe method[9]. Cathodes prepared by Battaglia's group have been simulated; experimental and simulation results matched closely for uncompressed electrodes. These findings suggest that material properties change due to high compression forces applied during manufacturing. Further investigation is needed to identify whether these material changes are beneficial or detrimental to the performance.

Sample Future Plans for Modeling and Cell Analysis

- Determine why initial cycling leads to a large decrease in interfacial impedance.
- Compare the HEV battery simulation model results with experimental pulse data and provide guidance to cell and electrode designers.
- Focus electrode modeling efforts on describing the $LiMnPO_4$ cathode in greater detail by moving away from the shrinking-core approach.
- Apply additional efforts on developing an alloy anode model.
- Continue collaborations between the cell modeling and development groups to identify and construct cathode compositions which offer acceptable ionic and electronic conductivity.

Focused Long-Term Research Publications

1. A. Appapillai, A., A. Mansour, J. Cho and Y. Shao-Horn, “Microstructure of “$LiCoO_2$” with and without “$AlPO_4$” nanoparticle coating: Combined STEM and XPS Studies,” Chemistry of Materials, in press (2007) - published online ASAP article.
2. A.C. Dillon, A.H. Mahan, R. Deshpande, P.A. Parilla, K.M. Jones and S-H. Lee “Metal Oxide Nanoparticles for Improved Electrochromic and Lithium-Ion Battery Technologies” *Thin Solid Films* vol. 216 (in press).
3. A. Guerfi, S. Duchesne, Y. Kobayashi, A. Vijh and K. Zaghib“$LiFePO_4$ and Graphite Electrodes with Ionic Liquids Based on Bis(fluorosulfonyl)imide [FSI]− for Li-ion Batteries,” JPS, in press.
4. A. Manthiram and W. Choi, “Suppression of Mn Dissolution in Spinel Cathodes by Trapping the Protons within Layered Oxide Cathodes,” Electrochem. Solid State Lett. 10, A228 (2007).
5. C. Johnson, N. Li, C. Lefief and M. Thackeray, “Anomalous Capacity and Cycling Stability of $xLi_2MnO_3\bullet(1-x)LiMO_2$ Electrodes (M=Mn, Ni, Co) in Lithium Batteries at 50°C,” Electrochem. Comm. 9, 787 (2007).
6. D. E. Stephenson, E. M. Hartman, J. N. Harb, and D. R. Wheeler, “Modeling of Particle-Particle Interactions in Porous Cathodes for Lithium-Ion Batteries,” JECS, 154, A1146 (2007).
7. D. Zeng, J. Cabana, J. Breger, W.-S. Yoon, and C. P. Grey, “Cation ordering in $Li[Ni_xMn_xCo_{(1-2x)}]O_2$-Layered Cathode Materials: A Nuclear Magnetic Resonance (NMR), Pair Distribution Function, X-ray Absorption Spectroscopy, and Electrochemical Study,” Chem. Mater., in press (2007).
8. H. Xia, Y.S. Meng, L. Lu, G. Ceder, “Electrochemical Properties of Nonstoichiometric $LiNi_{0.5}Mn_{1.5}O_4$-d Thin-Film Electrodes Prepared by Pulsed Laser Deposition,” JECS 154, p. A737 (2007).
9. H.H. Li, N. Yabuuchi, Y.S. Meng, S. Kumar, J. Bréger, C.P. Grey and Y. Shao-Horn, “Structural Changes of $Li_xNi_{0.5}Mn_{0.5}O_2$ During Electrochemical Cycling to High Voltages: An Electron Diffraction Study, Chemistry of Materials, 19, 2551 (2007).
10. H.H. Li, N. Yabuuchi, Y.S. Meng, S. Kumar, J. Breger, C.P. Grey, Y. Shao-Horn, “Changes in the Cation Ordering of Layered O3 $Li_xNi_{0.5}Mn_{0.5}O_2$ During Electrochemical Cycling to High Voltages: An Electron Diffraction Study,” Chem. Mater., 19, 2551 (2007).
11. J. Bréger, K. Kang, J. Cabana, G. Ceder and C. P. Grey, “NMR, PDF and RMC Study of the Positive Electrode Material $Li(NiMn)_{0.5}O_2$ Synthesized by Ion-Exchange Methods,” J. Mater. Chem., 17, 3167 (2007).
12. J. Bréger, Y.S. Meng, Y. Hinuma, S. Kumar, K. Kang, Y. Shao-Horn, G. Ceder, C.P. Grey, “The Effect of High Voltage on the Structure and Electrochemistry of $LiNi_{0.5}Mn_{0.5}O_2$: A Joint Experimental and Theoretical Study,” Chemistry of Materials, 18, 4768 (2006).
13. J. Chen and M. S. Whittingham, “Hydrothermal Synthesis of Lithium Iron Phosphate,” Electrochem. Commun., 2006, 8: 855.
14. J. D. Wilcox, M. M. Doeff, M. Marcinek, and R. Kostecki, “Factors Influencing the Quality of Carbon Coatings on $LiFePO_4$,” JECS, 154, A389 (2007).
15. J. T. Vaughey, A. M. Geyer, N. Fackler, C. S. Johnson, K. Edstrom, H. Bryngelsson, R. Benedek and M. M. Thackeray, “Studies of Layered Lithium Metal Oxide Anodes in Lithium Cells,” JPS, (2007), in press.
16. J. T. Vaughey, J. Owejan and M. M. Thackeray, “Substituted $M_xCu_{6-x}Sn_5$ Compounds (M=Fe, Co, Ni, Zn) for Lithium Batteries,” Electrochem. and Solid State Lett. 10, A220 (2007).
17. K. Kang, G. Ceder, “Factors that Affect Li Mobility in Layered Lithium Transition Metal Oxides,” Physical Review B, Vol. 74, 094105 (2006).
18. K.Y. Chung, W.-S. Yoon, H. S. Lee, J. McBreen, X.Q. Yang, S. H. Oh, W. H. Ryu, J. L. Lee, W. Il Cho, and B.W. Cho “*In situ* XRD Studies of the Structural Changes of ZrO_2 Coated $LiCoO_2$ during Cycling and Their Effects on Capacity Retention in Lithium Batteries” JPS, Vol. 163 (2006) 185.

19. K.Y. Chung, W.-S. Yoon, J. McBreen, X.Q. Yang, S.H. Oh, H.C. Shin, W.I. Cho, and B.W. Cho "Structural Studies on the Effects of ZrO_2 Coating on $LiCoO_2$ during Cycling using *In situ* X-ray Diffraction Technique" JECS, Vol. 153, (2006) A2152.
20. K.Y. Chung, W.-S. Yoon, J. McBreen, X.Q. Yang, S.H. Oh, H.C. Shin, W.I. Cho, and B.W. Cho "*In situ* X-Ray Diffraction Studies on the Mechanism of Capacity Retention Improvement by Coating at the Surface of $LiCoO_2$" JPS, accepted.
21. L. Wang, F. Zhou, Y. S. Meng, G. Ceder, "A First-principles Study of Surface Properties of $LiFePO_4$: Surface Energy, Structure," Wulff Shape, and Surface Redox Potential, Physical Review B (2007, in press).
22. L. Wang, T. Maxisch, G. Ceder, "A First-Principles Approach to Study the Thermal Stability of Oxide Cathode Materials," Chemistry of Materials, 19(3), pp. 543-552 (2007).
23. L. Wang, T. Maxisch, G. Ceder, "Oxidation Energies of Transition Metal Oxides within the GGA+U Framework," Physical Review B, 73, 195107 (2006).
24. M. Thackeray, S.. Kang, C. Johnson, J. Vaughey, R. Benedek, and S. Hackney, "Li_2MnO_3-stabilized $LiMO_2$ (M=Mn, Ni, Co) Electrodes for High Energy Lithium-Ion Batteries," J. Mater. Chem., 17, 3112 (2007).
25. M. Ma, N. A Chernova, B. H. Toby, P. Y. Zavalij, and M. S. Whittingham, "Structural and Electrochemical Behavior of $LiMn_{0.4}Ni_{0.4}Co_{0.2}O_2$," JPS, 165: 517-534 (2007).
26. M. Morcrette, D. Larcher, J. M. Tarascon, H. Bryngelsson, K. Edström, J. Vaughey and M. Thackeray, "Influence of Electrode Microstructure on the Reactivity of Cu_2Sb with Lithium," Electrochim. Acta. 52, 5339 (2007).
27. M. Sterndahl, H. Bryngelsson, T. Gustafsson, J. T. Vaughey, M. M. Thackeray and K. Edstrom, "Surface Chemistry of Intermetallic AlSb Anodes for Li-ion Batteries," Electrochim. Acta, 52, 4947 (2007).
28. N. A. Chernova, M. Ma, J. Xiao, M. S. Whittingham, J. Breger, and C. P. Grey, "Layered $Li_xNi_yMn_yCo_{1-2y}O_2$ Cathodes for Lithium Ion Batteries: Understanding Local Structure via Magnetic Properties," Chem. Mater., 19, 4682-4693, (2007).
29. N. Yabuuchi, S. Kumar, H.Li, Y.Kim and Y. Shao-Horn, "Changes in the Structural and Transport Properties of Layered O3 $Li_xNi_{0.5}Mn_{0.5}O_2$ during Electrochemical Cycling to High Voltages," JECS. 154, A566 (2007).
30. O. Borodin, G.D. Smith, O. Geiculescu, S.E. Creager, B. Hallac, and D. DesMarteau, "Li+ transport in lithium sulfonylimide-oligo(ethylene oxide) ionic liquids and oligo(ethylene oxide) doped with LiTFSI." Journal of Physical Chemistry B, 2006. 110(47): p. 24266-24274
31. O.E. Geiculescu, R. Rajagopal, S.E. Creager, D.D. DesMarteau, X.W. Zhang, and P. Fedkiw, "Transport properties of solid polymer electrolytes prepared from oligomeric fluorosulfonimide lithium salts dissolved in high molecular weight poly(ethylene oxide)," Journal of Physical Chemistry B, 2006. 110(46): p. 23130-23135.
32. P.B. Hallac, O.E. Geiculescu, R. Rajagopal, C. Topping, S.E. Creager, and D.D. Desmarteau, "Ionic melt electrolytes based on olgomeric PEG functionalized with lithium fluorosulfonates or flurosulfonimide pendants," Chimica Oggi-Chemistry Today, 2007. 25(3): p. 37-41.
33. Q. Fan and M. S. Whittingham, "Electrospun Manganese Oxide Nanofibers as Anodes for Lithium-Ion Batteries," Electrochem. Solid-State Letters, 2007, 10: A48-A51.
34. Q. Fan, P. Chupas and M. S. Whittingham, "Characterization of Amorphous and Crystalline Tin–Cobalt Anodes". Electrochem. Solid State Letters, 2007, 10: A274-A278.
35. S. Indris, J. Cabana, O.J. Rutt, S.J. Clarke and C.P. Grey, "Layered Oxysulfides (m = 1, 2 and 3) as Insertion Hosts for Li-Ion Batteries," J. Am. Chem. Soc., 128, 13354 – 13355 (2006).
36. S.-B. Ma, K.-W. Nam, W.-S. Yoon, X.Q. Yang, K.-B. Kim "A Novel Concept of Hybrid Capacitor Based on Manganese Oxide Materials" Electrochemistry Communications, accepted.
37. S.-H. Kang, P. Kempgens, S. Greenbaum, A. J. Kropf, K. Amine and M. M. Thackeray, "Interpreting the Structural and Electrochemical Complexity of $0.5Li_2MnO_3 \bullet 0.5LiMO_2$ Electrodes for Lithium Batteries ($M = Mn_{0.5-x}Ni_{0.5-x}Co_{2x}$, $0 \leq x \leq 0.5$)," J. Mater. Chem., 17, 2069 (2007).

38. S-H. Lee, Y-H. Kim, E. Whitney, P.A. Parilla, K.M. Jones, S.B. Zhang and A.C. Dillon, “Anomalous Reversible Lithium-Ion Intercalation in Molybdenum Oxide Nanostructures”. *Nature Materials* (submitted).
39. S. Park, S. Kang, C. Johnson, K. Amine and M. Thackeray, “Lithium-Manganese-Nickel-Oxide Electrodes with Integrated Layered-Spinel Structures for Lithium Batteries,” Electrochem. Comm. 9, 262 (2007).
40. W. Choi and A. Manthiram, “Factors Controlling the Fluorine Content and the Electrochemical Performance of Spinel Oxyfluoride Cathodes,” JECS, 154, A792-A797 (2007).
41. W. Choi and A. Manthiram, “Influence of Fluorine on the Electrochemical Performance of Spinel $LiMn_{2-y-z}Li_yZn_zO_{4-\eta}F_\eta$ Cathodes,” JECS 154, A614-A618 (2007).
42. W. Choi and A. Manthiram, “Influence of Fluorine Substitution on the Electrochemical Performance of 3 V Spinel $Li_4Mn_5O_{12-\eta}F_\eta$ Cathodes,” Solid State Ionics (in press).
43. W.-S. Yoon, K.Y. Chung, J. McBreen, D. A. Fischer, and X.Q. Yang “Changes in Electronic Structure of the Electrochemically Li-ion Deintercalated $LiNiO_2$ System Investigated by Soft X-ray Absorption Spectroscopy” JPS, Vol. 163 (2006) 234.
44. W.-S. Yoon, K.Y. Chung, J. McBreen, D. A. Fischer, and X.Q. Yang “Electronic Structural Changes of the Electrochemically Li-ion Deintercalated $LiNi_{0.8}Co_{0.15}Al_{0.05}O_2$ Cathode Material Investigated by X-ray Absorption Spectroscopy,” JPS, accepted.
45. W.-S. Yoon, K.Y. Chung, J. McBreen, D. Wang, X. Huang, L. Chen, and X.Q. Yang “Electronic Structural Changes of the Electrochemically Delithiated $LiFe_{0.5}Co_{0.5}PO_4$ Cathode Material studied by X-ray Absorption Spectroscopy” JPS, accepted.
46. W.-S. Yoon, K.Y. Chung, K.-W. Nam, and K.-B. Kim “Characterization of $LiMn_2O_4$ - Coated $LiCoO_2$ Film Electrode Prepared by Electrostatic Spray Deposition,” JPS, Vol. 163 (2006) 207.
47. W.-S. Yoon, K.Y. Chung, M. Balasubramanian, J. Hanson, J. McBreen, and X.Q. Yang “Time Resolved XRD Study on the Thermal Decomposition of Nickel-Based Layered Cathode Materials for Li-ion Batteries,” JPS, Vol. 163 (2006) 219.
48. Y. H. Chen, C. W. Wang, G. Liu, X. Y. Song, V. S. Battaglia, and A. M. Sastry, “Selection of conductive additives in Li-ion battery cathodes - A numerical study,” JECS 154, A978-A986 (2007)
49. Y. Hinuma, Y.S. Meng, K. Kang and G. Ceder, “Phase Transitions in the $LiNi_{0.5}Mn_{0.5}O_2$ System with Temperature, Chemistry of Materials,” 19(7), pp. 1790-1800 (2007).
50. Y.J. Park and M. M. Doeff, “Effect of Structure on the Storage Characteristics of Manganese Oxide Electrode Materials” JPS, 165, 573, (2007).

Conference Proceedings

51. A.C. Dillon, “Characterization of Nanomaterials to Optimize Renewable Energy Applications,” NIST Workshop on Materials Characterization for Nanoscale Reliability, Boulder, Colorado, August, 14-16, 2007.
52. J. Chen and M. S. Whittingham, “The Hydrothermal Synthesis of Lithium Iron Phosphate”, Mater. Res. Soc. Proc., 2007, 972, AA13-08.
53. J. Saint, J. Wilcox, A. Best, A. Hollenkamp, J. Kerr and M.M. Doeff, “Compatibility of Pyrolidinium-based Ionic Liquid Electrolytes with Manganese Oxide Cathode Materials in Lithium Batteries,” *International Symposium on the Reactivity of Solids*, June 2007, Minneapolis, MN.
54. J. Xiao, N. A. Chernova and M. S. Whittingham, “Influence of Lithium Content on Performance of Layered $Li_{1+z}[Ni_{0.45}Mn_{0.45}Co_{0.1}]_{1-z}O_2$ in Lithium Ion Batteries”, Mater. Res. Soc. Proc., 972: AA06 (2007).
55. K. Zaghib, M. Kikuta, P. Charest, A. Guerfi and M. Kono, “$LiFePO_4$/Graphite Li-ion Technology for Transportation Using New Gel Electrolyte” 211th ECS Meeting, Chicago, Illinois, May 06-10, 2007.
56. K. Zaghib, M. Kikuta, P. Charest, A. Guerfi and M. Kono, “Novel gel electrolyte for $LiFePO_4$ Li-ion technology”, Polymer Batteries Fuel Cells-PABFC-2007 Conference, Rome, Italy, 11-14 June 2007
57. N. A. Chernova, M. Ma, J. Xiao, M. S. Whittingham, J. C. Jiménez, and C. P. Grey, “Magnetic Studies of Layered Cathode Materials for Lithium Ion Batteries”, Mater. Res. Soc. Proc. 2007, 972: AA06-10.

58. Q. Fan and M. S. Whittingham, “Nanosized Amorphous Materials as Anodes for Lithium Batteries”, Mater. Res. Soc. Proc., 2007, 972: AA07-03.
59. Y-H. Kim “Lithium Intercalation in Molybdenum Trioxide Nanoparticle” poster at the 24th International Conference on Defects in Semiconductors, Albuquerque, New Mexico, July 18-24, 2007.

Appendix A – Contributors

Technology Development	
J. Barnes	Naval Surface Warfare Center West Bethesda, MD 20817-5700
J. Deppe[21]	Deppe Consulting Services, LLC PO Box 366 Davidsonville MD 21035 jbdeppe@lbl.gov
A. Pesaran	National Renewable Energy Laboratory 1617 Cole Boulevard Golden, CO 80401-3393

Applied Battery Research	
DOE Program Manager	**David Howell** U.S. Department of Energy Office of Vehicle Technologies 1000 Independence Avenue, SW Washington, DC 20585
National Laboratory Program Manager	**Gary Henriksen** Argonne National Laboratory Chemical Engineering Division, Bldg 205 9700 South Cass Avenue Argonne, IL 60439
Understand Life-Limiting Mechanisms and Enhance Life	
Focus area point of contact	**Gary Henriksen** Chemical Engineering Division Argonne National Laboratory, Building 205 9700 South Cass Avenue Argonne, IL 60439 Phone: 630.252.4591, E-mail: henriksen@cmt.anl.gov
D. Abraham, K. Amine, J. Basco, I. Bloom, D. Dees, A. Jansen, C. Johnson, S.H. Kang, J. Lui, J. Vaughey, L. Walker	Argonne National Laboratory Argonne, IL 60439
J. Hanson, H. S. Lee, J. McBreen, K.Y. Nam, X. Q. Yang, W. S. Yoon, Z. Zhong	Brookhaven National Laboratory P.O. Box 5000, MSD Bldg. 555, Upton, NY 11973-5000

---

[21] Preparer of this report.

Applied Battery Research

C Ashton, J. Christophersen, G. Cole, J. Einerson, K. Gering, C. Ho, D. Jamison, T. Murphy	Idaho National Laboratory Idaho Falls, ID 83415-3830
S. Kawauchi, J. Prakash	Illinois Institute of Technology Department of Chemical and Environmental Engineering, Chicago, IL 60616
V. Battaglia, L. Beer, G. Chen, L. Hardwick, J. Kerr, R. Kostecki, G. Liu, M. Marcinek, F. McLarnon, J. Newman, T. Richardson, J.-H.. Song, V. Srinivasan	Lawrence Berkeley National Laboratory Berkeley CA 94720-8168
E. Thomas	Sandia National Laboratories Albuquerque, NM 87185-0613

Understand and Enhance Low-Temperature Performance

Focus area Point of Contact	**Dennis Dees** Chemical Engineering Division Argonne National Laboratory, Building 205 9700 South Cass Avenue Argonne, IL 60439 Phone: 630.252.7349, E-mail: dees@cmt.anl.gov
D. Abraham, K. Amine, J. Liu , D. Dees, G. Henriksen, A. Jansen, C. Johnson, C. Joyce, H. LaDuca, S-H Kang, J. Muntean, J. Vaughey, N. Veselka	Argonne National Laboratory Argonne, IL 60439
K. Gering, T. Murphy	Idaho National Laboratory Idaho Falls, ID 83415-3830
S. Kawauchi, J. Prakash	Illinois Institute of Technology Department of Chemical and Environmental Engineering, Chicago, IL 60616

Understand and Enhance Abuse Tolerance

Focus area point of contact	**E. Pete Roth** Advanced Power Sources R&D Sandia National Laboratories, MS: 0613 P.O. Box 5800 Albuquerque, NM 87185 Phone: 505.844.3949, E-mail: eproth@sandia.gov
K. Amine, I. Belharouak, Z. Chen, G. Henriksen	Argonne National Laboratory Argonne, IL 60439

Applied Battery Research

S. Amiruddin, H. Joachin, J. Prakash	Illinois Institute of Technology Department of Chemical and Environmental Engineering, Chicago, IL 60616
T. Wunsch	Sandia National Laboratory Mail Stop 0613 Albuquerque, NM 87185

Cell-Level Cost Reduction

Focus area point of contact	**Khalil Amine** Chemical Engineering Division Argonne National Laboratory, Building 205 9700 South Cass Avenue Argonne, IL 60439 Phone: 630.252.3838, E-mail: amine@cmt.anl.gov
K. Amine, D. Abram, J. Lui, M. Katz, A. Jansen, D. Dees, G. Henriksen	Argonne National Laboratory Argonne, IL 60439

Focused Long-Term Battery Research

DOE Program Manager	**Tien Duong** U.S. Department of Energy Office of Vehicle Technologies 1000 Independence Avenue, SW Washington, DC 20585
National Laboratory Program Manager	**Venkat Srinivasan** Lawrence Berkeley National Laboratory One Cyclotron Road, MS 70R-0108B Berkeley, CA 94720
New Cathode Systems, Performance and Limitations	
$LiFePO_4$ System	
J. Harb and D. Wheeler	Brigham Young University Chemical Engineering Department, 350 CB Provo, UT 84602
K.-Y. Chung, J. Hanson, H. S. Lee, J. McBreen, X.-Q. Yang, and W.-S. Yoon	Brookhaven National Laboratory Upton, NY 11973
V. Battaglia, G. Chen, M. Doeff , R. Kostecki, G. Lui, M. Marcinek, T. Richardson, V. Srinivasan, J. Wilcox	Lawrence Berkeley National Laboratory Berkeley CA 94720-8168
J. Goodenough, Y. Huang	University of Texas at Austin 1 University Station C2200 Mechanical Engineering Dept. Austin, TX 78712-0292
$LiMn_2O_4$ Spinel System	
C. Johnson, S-H Kang, M. Thackeray, J. Vaughey	Argonne National Laboratory Chemical Technology Division Argonne IL 60439
V. Battaglia, G. Lui	Lawrence Berkeley National Laboratory Berkeley CA 94720-8168
W. Choi, A. Manthiram	Univ of Texas Texas Materials Institute , ETC 9-104 Austin TX 78712-0292
$LiNi_{1/3}Co_{1/3}Mn_{1/3}O_2$ System	
M. Thackeray, C. Johnson, J. Vaughey	Argonne National Laboratory Chemical Technology Division Argonne IL 60439

Focused Long-Term Battery Research	
K.-Y. Chung, J. Hanson, H. S. Lee, J. McBreen, X.-Q. Yang, and W.-S. Yoon	Brookhaven National Laboratory Upton, NY 11973
M. Doeff, R. Kostecki, M. Marcinek	Lawrence Berkeley National Laboratory Berkeley CA 94720-8168
G. Ceder, Y.S. Meng, Y. Hinuma, K. Kang, F. Zhou, T. Maxisch and L. Wang	Massachusetts Institute of Technology Cambridge, MA 02139-4307
S. Whittingham, J. Chen, J. Xiao, N. A. Chernova	State University of New York at Binghamton Chemistry and Materials Research Center Binghamton, NY 13902-6000
C. P. Grey, J. Breger, D. Zeng, J Cabana	State University of New York at Stony Brook, Department of Chemistry Stony Brook, NY
New Anode Materials	
C. Johnson, M. Thackeray, J. Vaughey	Argonne National Laboratory Chemical Technology Division Argonne IL 60439
O. Crowther, A. West	Columbia University Chemical Engineering 812 Mudd Bldg New York, NY 10027-0000
G. Chen , R. Kostecki, T. Richardson	Lawrence Berkeley National Laboratory Berkeley CA 94720-8168
Q. Fan, S. Whittingham	State University of New York at Binghamton Chemistry and Materials Research Center Binghamton, NY 13902-6000
A. Dillon, A. Frank, D. Gillaspie, Y. –H. Kim, S.-H. Lee, A. Pesaran, Q. Wang, E. Whitney, K. Zhu	National Renewable Energy Laboratory 1617 Cole Boulevard Golden, CO 80401-3393
Novel Electrolytes and their Characterization	
W.-S. Yoon, X.Q. Yang	Brookhaven National Laboratory Upton, NY 11973
S. Creager, D. DesMarteau, P. Hallac, O. Geiculescu, R. Rajagopal	Clemson University Department of Chemistry Clemson, SC 29634-0973.
K. Zaghib, P. Charest, A. Guerfi, P. Hovington	Hydro Quebec Varennes, J3X 1S1 Quebec Canada

Focused Long-Term Battery Research

N. Balsara, M. Doeff, J. Kerr, R. Kostecki, G. Liu, V. Srinivasan	Lawrence Berkeley National Laboratory Berkeley CA 94720-8168
O. Borodin, G. D. Smith	University of Utah Department of Materials Science and Engineering Salt Lake City, UT
Li-Ion Modeling, Diagnostics, and Cell Analysis	
V. Battaglia, G. Liu, F. McLarnon, J. Newman, S. Stewart, V. Srinivasan, X. Song, J. Wilcox	Lawrence Berkeley National Laboratory Berkeley CA 94720-8168
Y.S. Horn	Massachusetts Institute of Technology Mechanical Engineering, 3-158 77 Massachusetts Avenue Cambridge, MA 02139
A. M. Sastry, C-W. Wang	University of Michigan Dept of Mechanical Engineering and Applied Mechanics Ann Arbor, MI 48109-2125

Appendix B – List of Acronyms

ACN	Acetonitrile
AEM	Advanced electrolyte model
AER	All electric range
AFM	Atomic force microscopy
ANL	Argonne National Laboratory
ARC	Accelerated rate calorimetry
ASI	Area specific impedance
ATD	Advanced Technology Development
BATT	Batteries for Advanced Transportation Technologies
BCF	Binder and carbon free
BET	Brunauer, Emmett, and Teller surface area
BF	Binder free
BNL	Brookhaven National Laboratory
CE	Counter electrode
CPI	Compact Power Inc.
CRADA	Cooperative research and development agreement
DCIR	Dynamic Charged Interfacial Regions
DEC	Diethyl carbonate
DL	Double layer
DMC	Dimethyl carbonate
DOD	Depth-of-discharge
DOE	Department of Energy
DOEx	Design of experiment
DSC	Differential scanning calorimetry
E_a	Activation energy
EA	Ethylene acetate
EC	Ethylene carbonate
EDX	Energy dispersive XRD
EIS	Electrochemical impedance spectroscopy
EMC	Ethyl methyl carbonate
EP	Ethyl proprionate
EPD	Electrophoretic deposition
ESR	Electron spin resonance
EV	Electric vehicle
EXAFS	Extended x-ray absorption fine structure
EY	Electron yield
FCV	Fuel cell vehicle
FTIR	Fourier transform infrared
FY	Fluorescence yield
γBL	γ-butyrolactone
GC	Gas chromatography
GITT	Galvanostatic intermittent titration technique

HEBM	High-energy ball milling
HEV	Hybrid electric vehicle
HOPG	Highly oriented pyrolytic graphite
HPPC	Hybrid pulse power characterization
HRTEM	High resolution transmission electron microscopy
HTMI	High temperature melt integrity
HWCVD	Hot-wire chemical vapor deposition
ICL	Irreversible capacity loss
IL	Ionic liquids
IM	Ionic melt
IMC	Isothermal Microcalorimeter
INL	Idaho National Laboratory
JCS	Johnson Controls/Saft
LBNL	Lawrence Berkeley National Laboratory
LCL	Lower confidence limit
LiBOB	Lithium bis(oxolato)borate
LiDFOB	Lithium difluoro(oxalate)borate
LFP	Li iron phosphate
LiTFSI	Lithium bis(trifluoromethane-sulfonyl)imide
LTO	Lithium titanate, $Li_4Ti_5O_{12}$
MAG	Massive activated graphite
MAS	Magic angle spinning
MCMB	Mesocarbon micro beads
MD	Molecular dynamics
M-HEV	Minimum HEV battery requirements
mFEC	Mono-fluoroethylene carbonate
MPA	Microwave plasma assisted
MPACVD	Microwave plasma assisted chemical vapor deposition
MPPC	Minimum pulse power characterization
MW	Molecular weight
NCA	$LiNi_{0.8}Co_{0.15}Al_{0.05}O_2$
ND	Neutron diffraction
NEV	Neighborhood electric vehicle
NiMH	Nickel metal hydride
NMC	$LiNi_{1/3}Co_{1/3}Mn_{1/3}O_2$
NMR	Nuclear magnetic resonance
NREL	National Renewable Energy Laboratory
NT	Nanotubes
OCV	Open circuit voltage
PAn	Polyaniline
PC	Propylene carbonate
PCM	Phase change material
PDF	Pair distribution function
PEG	Polyethylene glycol

PEO	Poly(ethylene oxide)
PEY	Partial electron yield
PHEV	Plug in Hybrid Electric Vehicle
PPY	Polypyrrole
PS	Polystyrene
PFPTFBB	pentafluorophenyl)-tetrafluoro-1,3,2-benzodioxaborole
PTPA	polytriphenylamine
PVdF	Poly(vinylidene fluoride)
RE	Reference electrode
RMC	Reverse Monte Carlo
RPT	Reference performance test
RTIL	Room temperature ionic liquids
RVE	Response variable expressions
SBIR	Small Business Innovative Research
SEI	Solid electrolyte interphase
SEM	Scanning electron microscopy
SEO	PS-b-PEO copolymers
SIC	Single ion conducting
SOC	State of charge
SNL	Sandia National Laboratory
STEM	Scanning transmission electron microscope
STTR	Small Business Technology Transfer Program
TEM	Transmission electron microscopy
TGA	Thermal gravimetric analysis
TLVT	Technology Life Verification Test
TM	Transition metal
TMO	Transition metal oxide
TOF-SIMS	Time of flight secondary ion mass spectrometry
UCV	Upper cutoff voltage
USABC	United States Advanced Battery Consortium
USCAR	United States Council for Automotive Research
VC	Vinylene carbonate
VEC	Vinyl ethylene carbonate
VGCF	Vapor grown carbon fibers
VP	Vinyl propionate
VT	Vehicle Technology
WE	Working electrode
WSB	Water soluble binder
XANES	X-Ray absorption near edge structure
XAFS	X-Ray absorption fine structure
XAS	X-Ray absorption spectroscopy
XPS	X-ray photoelectron spectroscopy
XRD	X-ray diffraction

Appendix C – 2007 Energy Storage Highlights

Li-Ion Cells with Enhanced Abuse Tolerance

Argonne National Laboratory & Sandia National Laboratory

As part of DOE's ATD Program, ANL and SNL are working to improve the abuse tolerance of high-power Li-ion cells. They are collaborating to understand the factors that limit the inherent abuse tolerance of high-power Li-Ion cells and then identifying/ developing more stable cell materials and components that enhance the inherent abuse tolerance characteristics of these cells. Argonne identifies and develops more stable cell materials and components, while Sandia verifies and quantifies the effect of these materials at the cell level, using 18650 cells.

During the last year, Argonne demonstrated that the release of oxygen, due the thermal decomposition of the cathode active material, is proportional to the quantity of heat generated by reactions between these delithiated cathode materials and the electrolyte (via DSC) and that this was the dominate heat generating reaction during a thermal event. This result was validated at the cell level by ARC and thermal block tests conducted by Sandia on 18650 cells. Shown below are the comparative weight loss data obtained by Argonne (via TGA) on different types of delithiated cathode materials, as well as Sandia's ARC data on 18650 cells that incorporate three of these different cathode materials. It can be seen that the quantity of oxygen released by the different cathode materials (below 400ºC) directly correlates to the quantity of internal heat generation in the cells. The relative thermal stability of delithiated cathode materials is:

$$LiFePO_4 > LiMn_2O_4 > LiNi_{1/3}Mn_{1/3}Co_{1/3}O_2 > LiNi_{0.80}Co_{0.15}Al_{0.05}O_2$$

The conclusion of this work is that the inherent thermal abuse tolerance of Li-Ion cells can be significantly enhanced by the use of a cathode material that releases little or no oxygen during thermal excursions to temperatures >180^{o}C.

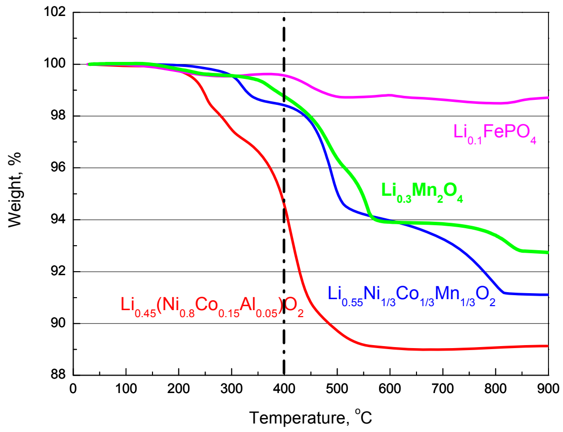

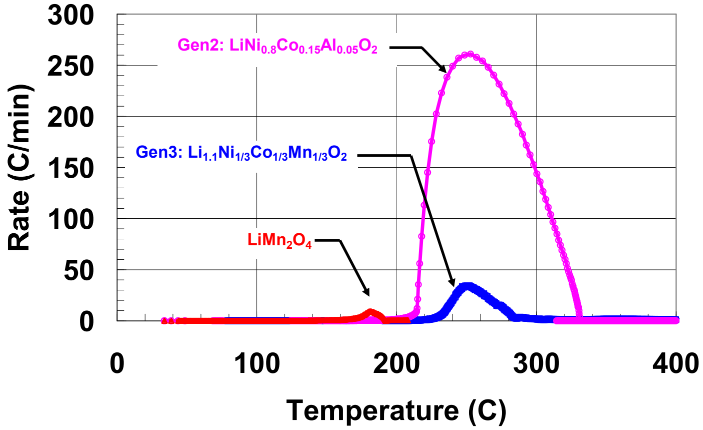

New High-Power Cell Chemistry

Argonne National Laboratory

As part of DOE's ATD Program, ANL evaluates low-cost advanced cell materials and components that offer enhanced stability in Li-ion batteries. The enhanced stability of these materials should aid in simultaneously achieving longer life and enhanced inherent abuse tolerance, which are two key barriers for Li-Ion batteries to become commercially viable for HEV applications.

During the last year, Argonne studied the use of nano-phase lithium titanate, $Li_4Ti_5O_{12}$ (LTO) as a replacement for carbonaceous anode materials. Argonne coupled the titanate anode with a lithium manganese spinel ($LiMn_2O_4$) cathode, which possesses excellent high-rate capabilities, due to its 3-dimensional structure. However, when used with conventional graphite or carbon anodes, cells suffer rather rapid power loss when operated at elevated temperatures, due to Mn^{2+} dissolution from the cathode, which reduces at the anode to form metallic manganese. The metallic manganese is believed to play a catalytic role in the formation of a resistive film on the graphite anode. Use of the titanate anode circumvents this problem, because it is poised at 1.5 volts above metallic lithium, where the Mn^{2+} is not reduced to Mn^o. Argonne evaluated several commercially-available LTO materials and then developed a process for making a more optimal nano-phase material (shown below). Cells employing these materials exhibit extremely high rate capabilities and can be completely discharged in about 1 minute, as shown below. Also, the titanate possess many other attractive characteristics for the HEV application:

- Low cost relative to synthetic graphite
- Limited surface reactivity with the electrolyte for extended life & enhanced inherent abuse tolerance
- No structural or volume changes during cycling (no structural stress)
- No plating of lithium during high-rate regenerative braking at low temperature

This work led to a DOE/USABC-funded Phase I program with EnerDel.

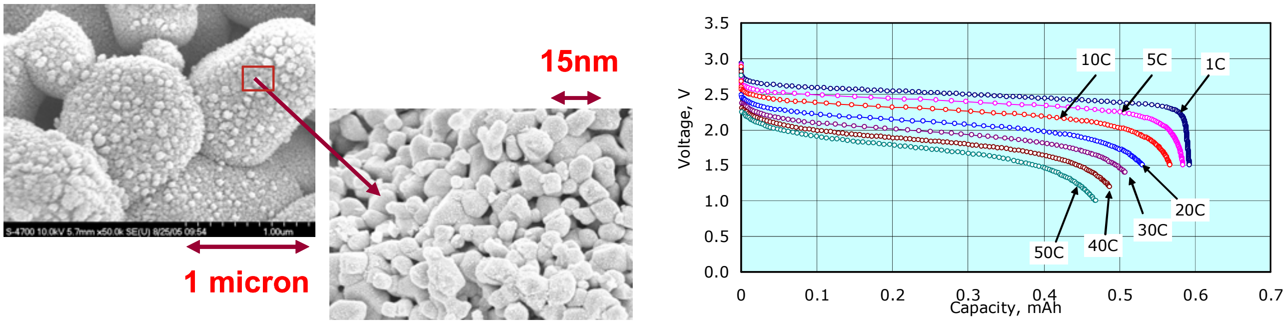

Figure: Cells incorporating Argonne's nano-phase lithium titanate material exhibit extremely high rate capability when coupled with lithium manganese spinel cathode.

Battery Life Prediction Model and Software

Sandia National Laboratory
Argonne National Laboratory
Idaho National Laboratory
Lawrence Berkeley National Laboratory

Participants from four national laboratories combined efforts to develop a calendar life prediction model and a supporting software package that allows for the estimate of the 90% lower confidence limit.

In arriving at the model, high-power cells designed specifically for HEV applications were aged for as much as one year. A model with just three fitting parameters designed to fit all of the testing conditions simultaneously was formulated and fit to the data using an orthogonal regression scheme. A second model was formulated to assess the variance of the data as a function of the relative level of impedance. This model consists of a cell manufacturing variation dependence and a measurement error dependence.

The life model is an explicit function of time and is easily transformed to provide life estimates at any temperature. To arrive at the lower confidence limit, both models are used in a Monte Carlo Simulation. An Excel package has been written specifically for this effort. Below are actual data and the results of the fitting of the model to using a Monte Carlo Simulation after 1000 trials of test conditions meant to simulate the actual cell testing.

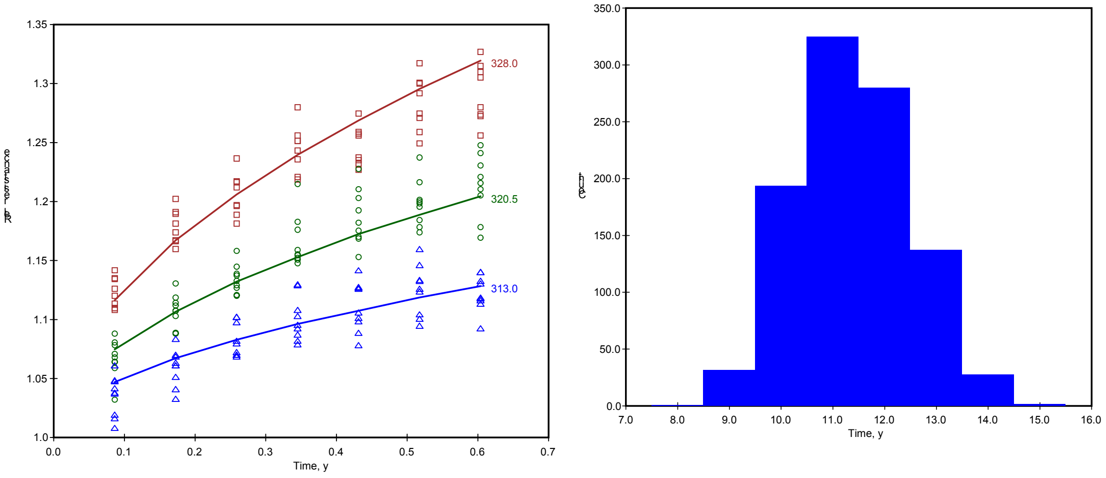

Figure on the left shows a fit of the model to the test data. Temperatures in K are provided in the graph next to the corresponding data. Figure on the right shows the results of the Monte Carlo Simulation that is part of the supporting software package. The ordinate is the number of trials out of 1000 that provide a particular life estimate. The 90% confidence limit of the life estimate is also derived.

Novel High-Capacity Tin-Carbon Composite Anode Synthesized Using a Microwave Technique

Lawrence Berkeley National Laboratory

LBNL has developed a novel microwave technique to synthesize carbon-tin composites that show reversible capacity of 400 mAh/g with long-term cycling stability far exceeding anodes prepared by other techniques. Alloy anodes, like tin, have been the focus of research due to their promise in increasing the energy density of batteries owing to their large capacity (~1000 mAh/g *versus* 372 mAh/g for graphite). However, it is known that tin particles expand upon alloying with Li, resulting in cracking of the particles and capacity fade. One method of alleviating the effect of the volume change is to embed the particles in an inactive matrix like carbon. LBNL's method, which has since been patented, makes use of the microwave technique to embed 1-8 nm sized tin particles in a matrix of carbon. Electrodes made from these materials show reasonable capacity retention with excellent rate behavior, with capacities as high as 300 mAh/g at a 5C discharge. The improvement in cycle life shown using this technique is a big step forward in identifying the next-generation high-energy systems that can meet the needs of plug-in-hybrid-electric vehicles.

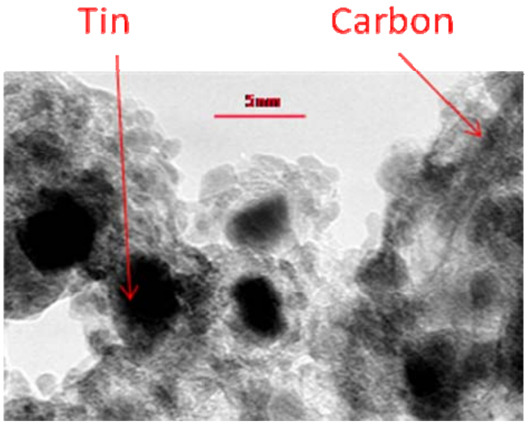

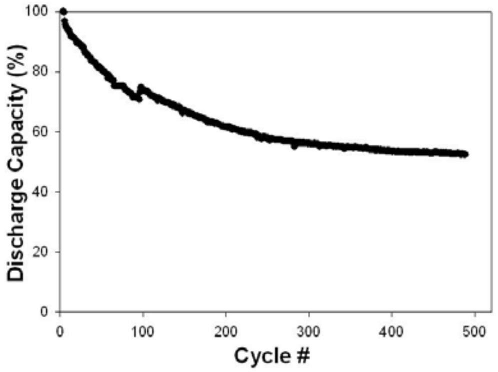

Stabilizing Interfaces with Electrolyte Additives

Argonne National Laboratory

As part of DOE's ATD Program, ANL is developing electrolyte additives that help stabilize the electrode/electrolyte interfaces of lithiated graphite anodes and delithiated metal oxide cathodes. These additives decompose during the initial charge half cycle to produce passivation films that are more stable than the passivation films that form with conventional Li-ion electrolyte systems. By forming more stable passivation films these additives help to stabilize the cell chemistry, leading to reduced rates of capacity and power fade, and thus longer calendar life compared to cells with the same basic chemistry that do not employ the additives. One of the major challenges is to create these more stable passivation films without introducing added impedance into the cells.

One of Argonne's more promising electrolyte additives is difluoro(oxalate)borate. When used as an electrolyte additive, this material helps to stabilize cell chemistries comprised of a graphite anode, an NMC cathode, and several conventional electrolyte systems. Fig. 1 provides accelerated aging data (cell capacity and impedance vs. time and charge/discharge cycles) at elevated temperature (55°C) for cells with and without this electrolyte additive. When used at 2-3 wt percent in the electrolyte, this additive exhibits a significant stabilizing effect on this cell chemistry. Fig. 2 compares AC impedance data for cells with and without the additive. These data show that stabilization with this additive is achieved without significantly increasing the cell impedance.

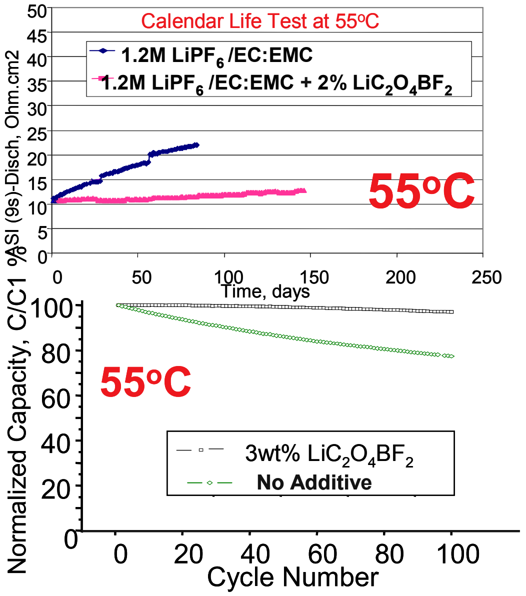

Figure 1. More stable impedance & capacity are achieved with additive.

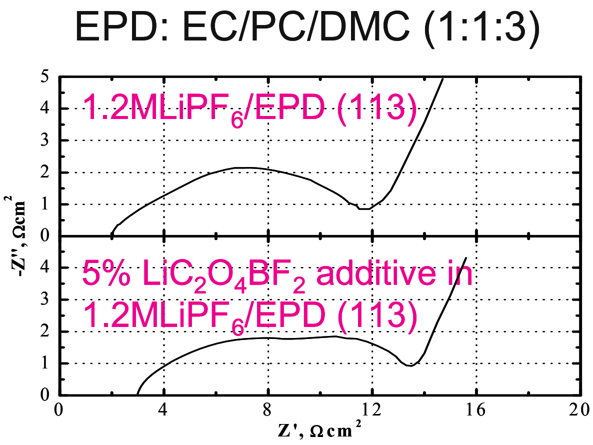

Figure 2. Similar cell impedance values are achieved with & without additive.

More Stable Li-Ion Layered Cathode Materials

Argonne National Laboratory

As part of DOE's ATD and BATT Programs, ANL is developing and refining advanced structurally-integrated layered lithium metal oxide cathode materials that are more structurally and chemically stable than conventional layered lithium metal oxide cathodes. The structural integration of non-electrochemically active Li_2MnO_3 with electrochemically active $LiMO_2$ components, where M=Mn, Ni, and/or Co, produces layered cathode materials that exhibit enhanced structural stability and reduced oxygen surface activity when fully charged (at high levels of delithiation). The core patents cover a family of materials that exhibit these enhanced stability characteristics. Some members of this family exhibit stability at voltages up to 4.6 volts vs. metallic lithium. When delithiated to these high levels, Li_2O is irreversibly removed from some of the non-electrochemically active Li_2MnO_3 component, transforming this portion of material into electrochemically active material. This results in a cathode material that possesses much higher capacity per unit weight (more than 65% more capacity) than conventional Li-Ion cathode materials. This type of new cathode material could significantly increase the energy density of Li-ion batteries, while simultaneously enhancing their inherent thermal abuse tolerance. Materials of this type are being refined to increase their particle density and rate capability, in an effort to enhance their performance, life, and abuse tolerance for PHEV applications. Also, processing conditions are being optimized to achieve these high stable discharge capacities, as shown in the figure below.

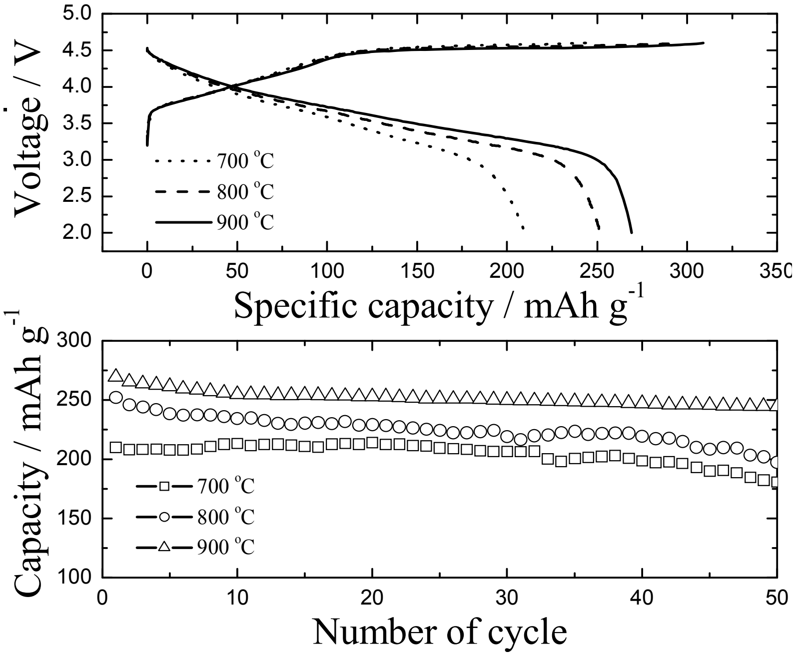

Figure – Stable high capacities achieved by optimizing processing conditions.

A Strong Energy Portfolio for a Strong America

Energy efficiency and clean, renewable energy will mean a stronger economy, a cleaner environment, and greater energy independence for America. Working with a wide array of state, community, industry, and university partners, the U.S. Department of Energy's Office of Energy Efficiency and Renewable Energy invests in a diverse portfolio of energy technologies.

For more information contact:
EERE Information Center
1-877-EERE-INF (1-877-337-3463)
www.eere.energy.gov